

November 2017

## **Pore forming protein assembly and the use in nanopore sensing: a study on E. coli proteins ClyA and OmpG**

Monifa Fahie

Follow this and additional works at: [https://scholarworks.umass.edu/dissertations\\_2](https://scholarworks.umass.edu/dissertations_2)



Part of the [Biochemistry Commons](#), [Biophysics Commons](#), [Biotechnology Commons](#), and the [Molecular Biology Commons](#)

---

### **Recommended Citation**

Fahie, Monifa, "Pore forming protein assembly and the use in nanopore sensing: a study on E. coli proteins ClyA and OmpG" (2017). *Doctoral Dissertations*. 1076.  
[https://scholarworks.umass.edu/dissertations\\_2/1076](https://scholarworks.umass.edu/dissertations_2/1076)

This Open Access Dissertation is brought to you for free and open access by the Dissertations and Theses at ScholarWorks@UMass Amherst. It has been accepted for inclusion in Doctoral Dissertations by an authorized administrator of ScholarWorks@UMass Amherst. For more information, please contact [scholarworks@library.umass.edu](mailto:scholarworks@library.umass.edu).

Pore forming protein assembly and the use in nanopore sensing: a study on *E. coli*  
proteins ClyA and OmpG

A Dissertation Presented

by

MONIFA AKILAH VERNA FAHIE

Submitted to the Graduate School of the  
University of Massachusetts Amherst in partial fulfillment  
of the requirements for the degree of

DOCTOR OF PHILOSOPHY

September 2017

Molecular and Cellular Biology Program

© Copyright by Monifa Akilah Verna Fahie 2017

All Rights Reserved

Pore forming protein assembly and the use in nanopore sensing: a study on *E. coli*  
proteins ClyA and OmpG

A Dissertation Presented

By

MONIFA AKILAH VERNA FAHIE

Approved as to style and content by:

---

Min Chen, Chair

---

Alejandro P. Heuck, Member

---

Craig T. Martin, Member

---

Jennifer L. Ross, Member

---

Lila M. Gierasch, Member

---

Dominique R. Alfandari, Graduate Program Director, Molecular and  
Cellular Biology Program

---

Elizabeth R. Dumont, Director, Interdisciplinary Graduate Programs, CNS

## DEDICATION

*To my maternal and paternal grandmothers, Rupertha Hazell and Beatrice Fahie.*

## ACKNOWLEDGEMENTS

Every person, every word, every action, every celebration, every hardship in my life has challenged me, molded me, been a role model for me and thus have added to the depth and breadth of me. I am privileged and lucky (my first name literally means 'I have my luck' in Yoruba) to have been born into the family and the society I was raised in. It has afforded me knowledge and awareness of not only the good, but also the not-so-good of mankind, and how to navigate through it without nonchalance and ire, but with respect and humility. It is this humility that has greatly impacted the way in which I have lived my life, how I will continue to do so and how I have approached these past six years in graduate school. Egotism has no place in our growth or in our respective careers. Our self-centeredness oftentimes hinders us from moving forward along our destined path.

To my advisor, Min, for guiding me through an unexpected but rewarding maze of scientific discovery and learning. She believes that we can all share in, and from the successes of one other. No man is an island, nor should he have a claim to one. Her conviction has positively impacted my core beliefs.

To my lab-mates, you are a part of my village and you have contributed to my learning and my strive for excellence. I have lived by three mottos during my scholarly life – “*Aim for excellence*” when I was in primary school; “*Decus est sevire*” (Latin for ‘It is an honor to serve’) when I was in secondary school and “*Challenge Convention*” during my undergrad years at Clark University. To truly know the extent of your own abilities, you must become part of a whole.

I give my love to my family – my parents, brother, uncles, aunts, grandparents, adopted grandparents, cousins, friends. Thank you for teaching me to accept myself, my faults and to accept others.

For as long as there is breath in us, let us all continue to grow.

## ABSTRACT

### PORE FORMING PROTEIN ASSEMBLY AND THE USE IN NANOPORE SENSING: A STUDY ON *E. COLI* PROTEINS CLYA AND OMPG

SEPTEMBER 2017

MONIFA AKILAH VERNA FAHIE, B.A. CLARK UNIVERSITY

Ph.D., UNIVERSITY OF MASSACHUSETTS AMHERST

Directed by: Professor Min Chen

Pore forming proteins are typically the proteins that form channels in membranes. They have several roles ranging from molecule transport to triggering the death of a cell. This work focuses on two *E. coli* pore forming proteins that have vastly differing roles in nature. Outer membrane protein G (OmpG) is an innocuous  $\beta$ -barrel porin while Cytolysin A (ClyA) is an  $\alpha$ -helical pore forming toxin.

For OmpG we probed its potential to be a nanopore sensor for protein detection and quantification. A small high affinity ligand, biotin, was covalently attached to loop 6 of OmpG and used to capture biotin-binding proteins. OmpG specifically interacted with target proteins and with a high sensitivity. In addition, we found that OmpG could discriminate among eight target proteins, four avidin homologues and four antibody homologues. Our work was the first revelation that a “noisy” nanopore sensor could not only discriminate among homologous proteins but could maintain this sensitivity and specificity in a serum sample.

Unlike OmpG which is a monomeric pore, the ClyA pore is an oligomer which allowed us to probe its assembly. We found an alternative mechanism of assembly of the ClyA pore from its soluble monomer. Our results revealed an off-pathway oligomerization of ClyA. These oligomers are stable in solution but are less efficient at converting into transmembrane pores in the membrane than monomeric ClyA.

# TABLE OF CONTENTS

	Page
ACKNOWLEDGEMENTS .....	v
ABSTRACT .....	vi
INTRODUCTION.....	1
CHAPTER	
1. RESOLVED SINGLE-MOLECULE DETECTION OF INDIVIDUAL SPECIES WITHIN A MIXTURE OF ANTI-BIOTIN ANTIBODIES USING AN ENGINEERED MONOMERIC NANOPORE .....	21
1.1 Summary .....	21
1.2 Introduction.....	22
1.3 Materials and Methods .....	24
1.3.1 Construction of OmpG D224C mutant.....	25
1.3.2 Cloning, expression and purification of OmpG D224C .....	25
1.3.3 Biotinylation and refolding of OmpG proteins .....	26
1.3.4 Single channel recording of OmpG proteins .....	27
1.3.5 Single-channel current analysis .....	28
1.4 Results.....	28
1.4.1 Detection of Streptavidin by OmpG-PEG <sub>11</sub> -biotin pore .....	28
1.4.2 Shortening the ligand linker to strengthen signal .....	33
1.4.3 Detection of reversible antibody binding .....	35
1.4.4 Influence of voltage on the mAb binding.....	39
1.4.5 Simultaneous detection of mouse mAb and goat polyclonal anti-biotin antibodies.....	42
1.4.6 Power spectrum analysis and fingerprint of analyte protein binding signal.....	44
1.5 Discussion.....	48
1.6 Conclusion .....	52
1.7 References.....	53
2. ELECTROSTATIC INTERACTIONS BETWEEN OMPG NANOPORE AND ANALYTE PROTEIN SURFACE CAN DISTINGUISH BETWEEN GLYCOSYLATED ISOFORMS .....	56
2.1 Summary .....	56
2.2 Introduction.....	57



2.3 Materials and Methods .....	59
2.3.1 Zeta potential Measurement .....	59
2.3.2 Purification of OmpGD224C .....	59
2.3.3 Labeling and refolding of OmpG-biotin proteins .....	60
2.4 Results.....	61
2.4.1 Discrimination among Avidin Homologues .....	61
2.4.2 Influence of Ionic Strength on Binding .....	67
2.4.3 Effect of pH on Binding .....	70
2.4.4 Influence of Applied Voltage on Bound-State Gating Behavior.....	77
2.5 Discussion .....	82
2.6 Conclusion.....	86
2.7 References .....	87
<b>3. SELECTIVE DETECTION OF PROTEIN HOMOLOGUES IN SERUM USING AN OMPG NANOPORE.....</b>	<b>90</b>
3.1 Summary .....	90
3.2 Introduction.....	90
3.3 Materials and Methods .....	92
3.3.1 OmpG biosensor preparation.....	92
3.3.2 Single Channel Recording .....	93
3.3.3 Single Channel analysis.....	95
3.3.4 Analysis of gating characteristics.....	95
3.4 Results.....	96
3.6 Conclusions .....	110
3.7 References .....	111
<b>4. TUNING THE SELECTIVITY AND SENSITIVITY OF AN OMPG NANOPORE SENSOR BY ADJUSTING LIGAND TETHER LENGTH.....</b>	<b>114</b>
4.1 Summary .....	114
4.2 Introduction.....	114
4.3 Materials and Methods .....	117
4.3.1 Cell culture and protein purification.....	117
4.3.2 Single Channel recording.....	118
4.3.3 Single channel data analysis .....	119
4.4 Results.....	120
4.4.1 Effect of PEG linker length on analyte recognition.....	120

4.4.2 Effect of voltage on OmpG-PEG-biotin - avidin interaction .....	129
4.4.3 Effect of salt concentration on the interaction between OmpG-PEG45-biotin and avidin.....	134
4.4.4 Effect of linker length on the binding kinetics .....	137
4.5 Conclusion.....	145
4.6 References .....	146
5. A NON-CLASSICAL ASSEMBLY PATHWAY OF ESCHERICHIA COLI PORE FORMING TOXIN CYTOLYSIN A .....	150
5.1 Summary .....	150
5.2 Introduction.....	151
5.3 Materials and Methods .....	153
5.3.1 Cloning and mutagenesis of ClyA.....	153
5.3.2 Expression and purification of ClyA .....	154
5.3.3 Gel filtration analysis of ClyA oligomerization .....	155
5.3.4 Intrinsic fluorescence studies.....	156
5.3.5 Liposome preparations .....	156
5.3.6 Analysis of pore forming activity by hemolytic activity.....	157
5.3.7 Analysis of pore-forming activity by fluorescence quenching.....	157
5.3.8 Oxidation of ClyA proteins .....	158
5.3.9 Single channel study of ClyA .....	158
5.4 Results.....	159
5.4.1 Assembly of ClyA in the absence of detergent .....	159
5.4.2 Conversion of oligomer 8 and oligomer 9 to the transmembrane pore .....	161
5.4.3 Hemolytic activities of the ClyA proteins .....	163
5.4.4 Conductance of ClyA pores .....	164
5.4.5 Temperature and concentration dependent oligomerization.....	166
5.4.6 Probing the structural arrangement of oligomers by fluorescence.....	168
5.4.7 Effect of lipid composition on pore-forming activity .....	170
5.4.8 Direct conversion of ClyA <sub>O8</sub> and ClyA <sub>O9</sub> to transmembrane pores.....	171
5.4.9 Effect of the redox environment on the activity of ClyA.....	173
5.5 Discussion .....	174
5.6 References .....	179
CONCLUSIONS AND FUTURE WORK.....	182
BIBLIOGRAPHY .....	189

## LIST OF TABLES

Table	Page
1.1 Fingerprint of each type of gating events using the OmpG-PEG <sub>2</sub> -biotin pore.....	47
2.1 Gating characteristics for streptavidin, avidin and extravidin.....	65
2.2 Zeta potential measurements of analyte proteins under various pH conditions.....	66
2.3 Gating characteristics of avidin at various salt concentrations at pH 6.0, +50 mV.....	70
2.4 Fingerprint characteristics of avidin at various salt concentrations at pH 6.0, +50 mV .....	70
2.5 Effect of pH 4 on gating characteristics for streptavidin, avidin and extravidin at 1.0 M KCl pH 4.0, +50mV.....	72
2.6 Effect of pH 4 on fingerprint characteristics for streptavidin, avidin and extravidin at 1.0 M KCl pH 4.0, +50mV .....	73
2.7 Effect of pH 10 on gating characteristics for streptavidin, avidin and extravidin at 0.3 M KCl pH 10.0, +50 mV.....	74
2.8 Effect of pH 10 on fingerprint characteristics for streptavidin, avidin and extravidin at 0.3 M KCl pH 10.0, +50 mV.....	75
2.9 Fingerprint values for bind 1 and bind 2 of streptavidin, avidin and extravidin at 4.0 M KCl pH 10.0, +50 mV.....	76
2.10 Voltage effect on gating characteristics for streptavidin, avidin and extravidin binding at various voltages in 300 mM KCl pH 6.0 buffer.....	80
2.11 Voltage effect on fingerprint characteristics for streptavidin, avidin and extravidin binding at various voltages in 300 mM KCl pH 6.0 buffer.....	81
3.1 The relative change in open probability, gating frequency and open current of OmpG-biotin during type A, B and C binding of SB58C.....	98
3.2 The gating characteristics of the unbound state, the BT and SB bound states in the absence and presence of 10% (v/v) serum.....	104
4.1 Linker effect on the binding kinetics of an anti-biotin mouse monoclonal antibody.....	142
4.2 Summary of the binding effects of streptavidin, avidin and anti-biotin mAb to OmpG-PEG <sub>n</sub> -biotin constructs.....	142

## LIST OF FIGURES

Figure	Page
I.1 Schematic of the classical assembly mechanism for a pore forming toxin (PFT).....	3
I.2 PFTs as drugs to induce cell death or as drug delivery vehicles.....	7
I.3 Side and top views of the OmpG porin structure.....	8
I.4 The structures of the inactive and active ClyA $\alpha$ -PFT.....	10
1.1 SDS-PAGE analysis of OmpG variants.....	26
1.2 Structures of OmpG and its gating activity.....	29
1.3 Point mutation or biotinylation of OmpG does not affect its inherent gating behavior.....	30
1.4 Detection of streptavidin by OmpG-PEG <sub>11</sub> -biotin.....	30
1.5 Characteristic of the two gating event populations of streptavidin binding.....	31
1.6 Effect of streptavidin binding on the bending events.....	32
1.7 Gating behavior due to streptavidin binding is specific.....	33
1.8 Detection of streptavidin by OmpG-PEG <sub>2</sub> -biotin pore.....	34
1.9 BSA does not elicit change in OmpG behavior.....	35
1.10 Detection of monoclonal anti-biotin antibody by OmpG-PEG <sub>2</sub> -biotin pore.....	36
1.11 Monoclonal anti-biotin antibody (mAb) binding is specific.....	37
1.12 Analysis of kinetic parameters of mAb binding to OmpG-PEG <sub>2</sub> -biotin.....	38
1.13 Effect of voltage on the mAb binding.....	40
1.14 Analysis of kinetic parameters of mAb binding to OmpG-Peg2-biotin at various applied voltages.....	41
1.15 Representative traces of single channel recording of OmpG D224C in the presence of polyclonal anti-biotin antibody (pAb).....	42
1.16 A complex mixture of biotin binding proteins elicits no effect on the gating of OmpGwt.....	43
1.17 Detection of mouse mAb and polyclonal Ab binding by OmpG-PEG <sub>2</sub> -biotin pore.....	44

1.18	Detection of streptavidin by OmpG-PEG <sub>2</sub> -biotin pore.....	45
1.19	Comparison of the gating patterns of OmpG-PEG <sub>2</sub> -biotin at analyte binding states.....	46
1.20	Gating events fingerprint analysis.....	46
1.21	Fingerprints of the four biotin binding proteins.....	48
1.22	Schematic model illustrating the interactions between OmpG nanopore and analyte protein.....	50
1.23	Structures of $\alpha$ HL and OmpG.....	51
2.1	Schematic diagram of the OmpG nanopore sensor.....	61
2.2	Single channel current traces of OmpGwt in the presence of streptavidin homologues at various buffer conditions.....	62
2.3	Detection of biotin binding protein homologues by OmpG-PEG <sub>2</sub> -biotin nanopore.....	63
2.4	Detection of extravidin subpopulations by OmpG nanopore.....	64
2.5	Spectral and fingerprint analysis of OmpG nanopore bound to the streptavidin homologues.....	65
2.6	Electrostatic potential map of the extracellular loops (L1-L7) of OmpG.....	67
2.7	Effect of ionic strength on the gating characteristic of OmpG nanopore induced by avidin binding.....	68
2.8	The effect of avidin binding on the five gating characteristics of OmpG-PEG <sub>2</sub> -biotin in various salt concentrations.....	69
2.9	OmpG generates small, closed pores in low salt, low pH buffer.....	71
2.10	Effect of acidic pH on the gating signal of analyte proteins.....	72
2.11	Binding of analyte proteins at pH 10.....	74
2.12	Proximity of the glycosylation site Asn-17 to the biotin binding pocket of the avidin monomer.....	76
2.13	Effect of voltage on the gating characteristics of OmpG at analyte bound.....	78
2.14	Effect of voltages on the gating characteristics of OmpG-PEG <sub>2</sub> -biotin after analyte binding.....	79

2.15 The relative open pore conductance of OmpG-PEG <sub>2</sub> -biotin when bound to the avidin homologues.....	82
2.16 Schematic representation of the sampling mechanism for OmpG nanopore.....	83
3.1 SDS-PAGE analysis of refolding and labeling efficiency of OmpG-biotin.....	93
3.2 Single channel current trace of OmpG D224C.....	94
3.3 Gating characteristics of the OmpG ionic current.....	96
3.4 The open (2I <sub>WV</sub> ) and closed (2I <sub>WW</sub> ) structures of OmpG.....	97
3.5 Detection of SB58C by OmpG-biotin nanopore.....	99
3.6 Detection of SB58C by OmpG-biotin nanopore in high salt.....	101
3.7 The effect of 10% serum added to both chambers on the gating behavior of OmpG-biotin.....	102
3.8 The effect of serum added to one chamber only on the gating behavior of OmpG-biotin.....	103
3.9 Discrimination of two antibodies in the presence of serum.....	105
3.10 Simultaneous detection of two antibodies in serum.....	106
3.11 The effect of serum on the fingerprint pattern of BT and SB.....	107
3.12 Effect of FBS on the kinetics of antibody binding.....	108
4.1 The refolding and labeling efficiency of OmpG-PEG <sub>n</sub> -biotins .....	118
4.2 The design of the OmpG-PEG <sub>n</sub> -biotin constructs.....	120
4.3 Effect of the tethered ligand on OmpG gating.....	121
4.4 Extended electrophysiology traces of OmpG <sub>wt</sub> and OmpG-PEG <sub>n</sub> -biotin constructs.....	122
4.5 Electrophysiology traces showing the effect of biotin binding proteins on OmpG-D224C gating activity.....	123
4.6 The effect of streptavidin binding to the OmpG-PEG <sub>2</sub> -biotin pore.....	124
4.7 Streptavidin binding to OmpG-PEG <sub>n</sub> -biotin constructs.....	125
4.8 Avidin binding to OmpG-PEG <sub>n</sub> -biotin constructs.....	126
4.9 Single channel current traces of OmpG-PEG <sub>n</sub> -biotin.....	127

4.10 Power spectra analysis of noise in the absence and presence of avidin.....	128
4.11 Voltage effect on avidin binding to OmpG-PEG <sub>n</sub> -biotin.....	130
4.12 Comparison of open pore current of the OmpG-PEG <sub>n</sub> -biotin constructs before and after avidin binding at various voltages.....	131
4.13 Electrophysiology traces showing the dwell times of the avidin B2 state of OmpG-PEG45-biotin at various loop voltages.....	132
4.14 First order exponential fitting analysis of B1 and B2 dwell times at various voltages.....	133
4.15 The effect of KCl concentration on the avidin binding states B1 and B2 of the OmpG-PEG45-biotin pore.....	135
4.16 Salt effect on OmpG-PEG45-avidin binding states.....	136
4.17 First order exponential fitting analysis of B1 and B2 dwell times in various salt conditions.....	137
4.18 Detection of an anti-biotin mouse monoclonal antibody (mAb) by the three OmpG-PEG <sub>n</sub> -biotins.....	138
4.19 The binding signal and the defined t <sub>on</sub> and t <sub>off</sub> events of anti-biotin mAb to OmpG-PEG <sub>n</sub> -biotin.....	139
4.20 Statistic analysis to compare the binding of mAb to the OmpG-PEG <sub>n</sub> -biotin constructs.....	140
4.21 First order exponential fitting analysis of t <sub>on</sub> and t <sub>off</sub> dwell times of antibiotic mAb.....	141
5.1 SDS-PAGE of nickel affinity purified ClyAwt protein.....	155
5.2 Gel filtration chromatography of ClyA proteins.....	160
5.3 ClyA oligomerization under reducing conditions.....	161
5.4 Conversion of ClyA <sub>O8</sub> and ClyA <sub>O9</sub> to transmembrane pore.....	162
5.5 SDS-PAGE analysis of ClyA monomer and oligomers.....	163
5.6 Hemolytic activity of ClyA proteins.....	164
5.7 Single channel conductance of ClyA pores.....	165
5.8 Effect of temperature on ClyA assembly.....	166
5.9 Effect of continuous concentration of ClyA on its oligomerization.....	167
5.10 Effect of protein concentration on ClyA assembly.....	168

5.11 Intrinsic fluorescence of ClyA monomer and oligomers.....	170
5.12 Effect of lipid composition on the pore-forming activity of ClyA.....	171
5.13 Examining the pathway of Cly <sub>O8</sub> and Cly <sub>O9</sub> conversion.....	172
5.14 GFC analysis of oxidized ClyA.....	174
5.15 Regulation of the ClyA pore forming activity by redox change.....	174
5.16 Schematic model showing the proposed assembly pathway for the <i>E. coli</i> ClyA.....	178
C.1 Negative stain electron microscopy of ClyA proteins.....	185
C.2 ClyA assembly mechanisms.....	186



## INTRODUCTION

### I.1 Pore forming proteins (PFPs)

Pore-forming proteins (PFPs) are a class of membrane proteins that form a hole across the lipid bilayer.<sup>1-5</sup> These proteins create channels that typically allow the passage of water soluble molecules through the membrane. PFPs are involved in cellular processes such as moving various cargo across the bilayer,<sup>6-8</sup> signaling pathways,<sup>4,9-12</sup> and inducing lytic death in a target cell.<sup>1,13-15</sup> PFPs can make the lipid bilayer permeable to either specific molecules such as a polypeptide,<sup>16</sup> an anion<sup>17</sup> or they can be unspecific allowing molecules equal to or smaller than its exclusion limit to pass through the membrane.<sup>18</sup>

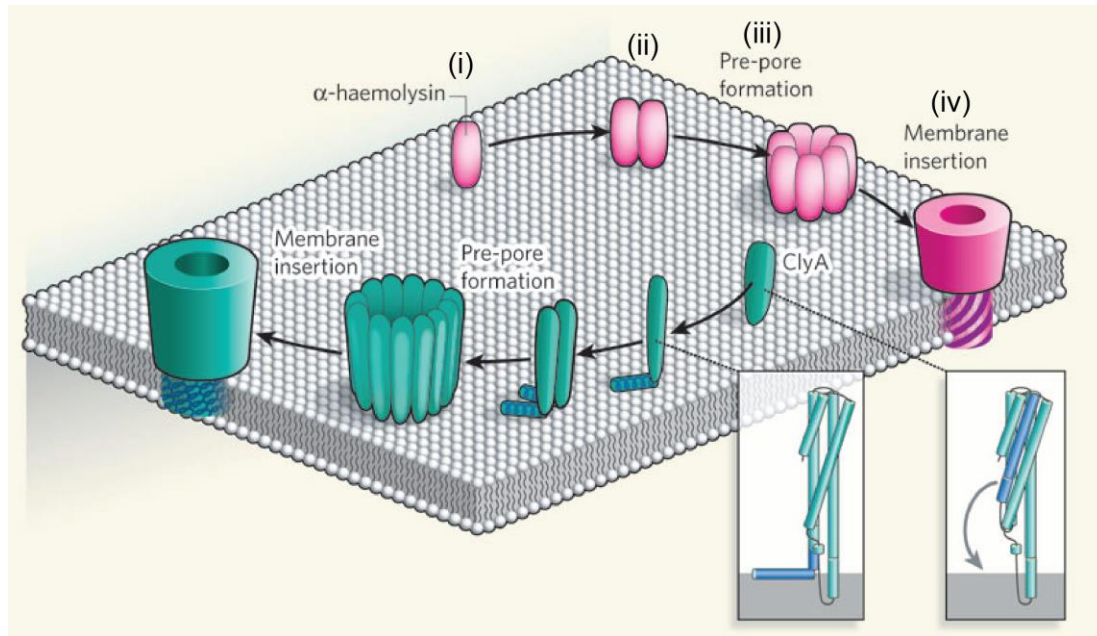
In this dissertation we will focus on two large classes of PFPs which are (i) the membrane porins which can be found in gram negative,<sup>19</sup> mitochondria<sup>6,20-22</sup> and chloroplasts<sup>6,22-24</sup> and (ii) pore forming toxins (PFTs). In the first class, known membrane porins typically have beta-barrel structure<sup>6,8</sup> and create water-filled channels in the membrane. On the other hand, PFTs are proteins that can convert from a soluble monomer into a membrane bound oligomer.<sup>2-4,12,14,15,25-27</sup> PFTs are implicated in infectious disease as a large class of virulence factors,<sup>25</sup> as well as in immunity.<sup>11,12</sup> These proteins are produced as soluble monomers in a wide range of organisms for example bacteria<sup>28</sup>, amoebae,<sup>29</sup> humans,<sup>30</sup> and plants.<sup>9</sup> These monomers are secreted from the organism and then interact specifically with a target cell membrane by binding to a receptor such as lipid domains or cholesterol<sup>31-34</sup> a protein receptor<sup>35-37</sup> or sugar moiety.<sup>26,38</sup> Then they assemble into a membrane bound pore.<sup>14,25,26</sup> Once bound to the target cell membrane PFTs can trigger cell death through lysis<sup>15</sup> or deliver harmful molecules into the cell.<sup>37,39</sup> Because of their significance in a variety of cellular functions, PFPs hold great interest in our fundamental understanding of biological processes and networks. Thus,

there is motivation to study PFPs so that we may better understand and develop ways to manipulate a biological outcome.

## **I.2 Fundamental research on PFPs**

Like all proteins, PFP function depends on their structure. A protein's structure depends on the correct folding mechanisms. The study of protein folding is filled with many questions regarding protein regulation. Our understanding of membrane protein folding, in particular, has been lagging behind that of soluble proteins.<sup>40</sup> Membrane proteins are difficult to study *in vitro* as they are unstable because of their insolubility in aqueous solution and our lack of suitable detergent or lipid mimics to reconstitute them into a native-like membrane environment.<sup>40</sup> Despite this difficulty we have gained some insight into PFP folding and thermodynamics from studies on bacterial outer membrane proteins.<sup>8,41–43</sup>

On the other hand, pore forming toxins (PFTs) represent a unique class of PFPs whose cytotoxic function relies on the assembly into quaternary structures. They undergo significant conformational changes from a soluble protein to a transmembrane pore.<sup>25</sup> Because PFTs are initially soluble, they are less difficult to isolate than membrane porins and their assembly mechanisms can be easily probed. They are classified as either  $\alpha$ -PFTs or  $\beta$ -PFTs depending on their predominant secondary structures.<sup>14</sup> The classical model of PFT assembly includes (i) binding of monomers to membrane, (ii) oligomerization on the membrane, (iii) formation of a pre-pore complex and (iv) membrane insertion of a transmembrane-spanning domain (Figure I.1).<sup>2,14,25,26</sup>



**Figure I.1. Schematic of the classical assembly mechanism for a pore forming toxin (PFT).** Reprinted by permission from Macmillan Publishers Ltd: Nature Publishing Group H. Bayley, "Membrane-protein structure: Piercing insights," *Nature*, vol. 459, pp. 4–5, 2009., copyright (2009)

Although the route of toxin assembly is specific for PFTs, protein complex formation is not unique to them. Many other proteins such as secretion systems (types I to VI),<sup>44</sup> and photosystems I<sup>45</sup> and II<sup>46</sup> are examples of membrane spanning multi-protein complexes. Thus, studying assembly of PFTs which can form either homo-oligomeric or hetero-oligomeric complexes would have wide appeal to many other biological questions that focus on multi-protein complex formation and function.

Some knowledge of PFTs and their assembly has been elucidated while studying infectious diseases,<sup>15</sup> signaling pathways<sup>4,9,11,12,47</sup> and this fundamental knowledge has been exploited in protein engineering and nanopore sensing.<sup>48</sup> To paint a complete picture of PFTs, studying their kinetics of assembly and their thermodynamics is essential. Studying the kinetics of alpha hemolysin ( $\alpha$ HL) assembly revealed that its conversion from monomer to oligomer is too rapid for detecting intermediate states.<sup>49</sup> However atomic force microscopy characterization of MACPF/CDC pores has shown pre-pore,

intermediate pore called arcs and pore states.<sup>50</sup> Thus, studying PFT assembly may be limited to larger pores with slow kinetics. One such toxin is the *E. coli* PFT, Cytolysin A (ClyA) which was recently studied with more direct assays via FRET and cross-linking experiments.<sup>51</sup> ClyA converts from monomer to oligomer in the presence of detergent DDM within minutes.<sup>51–54</sup> which is slow enough to study the oligomerization process. A model for ClyA assembly was proposed highlighting that oligomerization is a concerted cooperative process.<sup>51</sup> This model for ClyA can be extended to other PFTs and can explain the quick assembly kinetics of small toxins.

### **I.3 Applied research on PFPs**

One application of PFPs that has seen a boom is in nanopore technology. Nanopore technology is a field of research focusing on developing sensors based on biological or solid state pores. Solid state nanopores are holes of nm size that are typically fabricated on silica, graphene, borosilicate glass and other materials.<sup>55–57</sup> Biological nanopores are mainly based on membrane pore-forming proteins, although there is increasing success and progress with using nucleic acid based nanopores.[15]–[22] PFP nanopores have been used to detect various molecules ranging from metal ions,<sup>66,67</sup> neurotransmitters,<sup>68</sup> peptides,<sup>69–71</sup> proteins,<sup>72–77</sup> nucleosomes,<sup>78</sup> to even microorganisms.<sup>79–83</sup> In fact, the most significant progress has been in the sequencing of single stranded DNA.<sup>48,57,84–104</sup>

The principle behind nanopore detection and analysis is based on monitoring the changes in ionic flow through the nanopore when an analyte binds.<sup>100,105,106</sup> because of this, analytes can be characterized by their size, their charge and their concentration.<sup>107,108</sup> Analytes can bind directly in the lumen of the nanopore,<sup>92,94,98,107,109,110</sup> or via an adaptor molecule in the lumen,<sup>89,90,111</sup> they can bind to either prevent or promote oligomerization of the nanopore,<sup>112</sup> or they can bind to a non-lumen site on the nanopore.<sup>73</sup> In addition,

nanopores can be used to detect analytes indirectly<sup>72</sup> and study enzyme kinetics.<sup>109</sup> Although there has been much progress in nanopore sensing especially in the sub-field of DNA sequencing, there are some limitations. The most commonly used protein-based nanopores such as  $\alpha$ HL or ClyA range from 1–7 nm in diameter. This means that molecules larger than these diameters cannot enter their lumen. Solid-state nanopores (ss-nanopores) have an advantage to PFPs in their tunable sizes, however, ss-nanopore fabrication lacks the size and shape precision of a biologically produced protein nanopore.<sup>55–57,75,91,95,99,100</sup> In addition, we would need to designate unique ss-nanopores to detect a specific subset of molecules. This is because analytes that are very small will not generate a noticeable change in the ionic current of a large nanopore. To alleviate the nanopore size limitation, researchers have used alternative approaches where large analytes were detected by specifically binding to native receptor sites<sup>113</sup> or engineered sites<sup>114–117</sup> on the nanopore surface where binding altered the ionic flow of the nanopore.

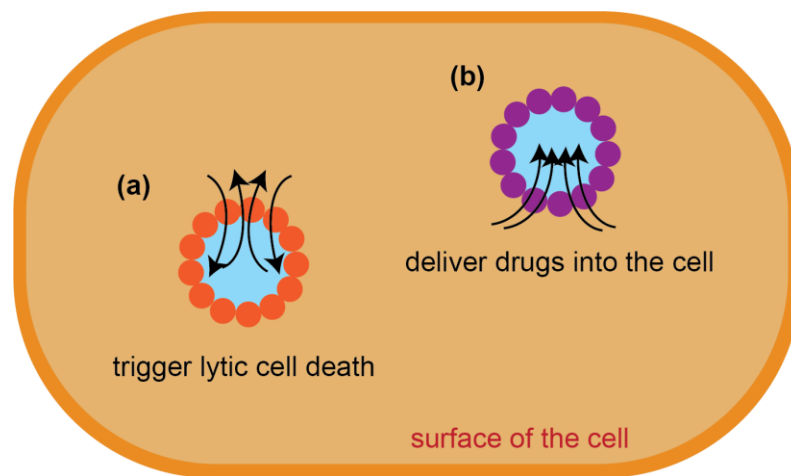
Another big area for nanopores is geared towards protein analytes<sup>118–120</sup> *i.e.* protein/peptide translocation<sup>48,121–125</sup> as well as protein folding/aggregation analysis.<sup>126–132</sup> Protein translocation across the lipid bilayers is ubiquitously found in nature for example in secretion systems<sup>133</sup> or across mitochondria and chloroplasts<sup>23</sup> and the use of nanopores is a suitable *in vitro* platform to probe these mechanisms.<sup>77</sup> Furthermore, nanopores have the potential to be used as analytical tools in protein/peptide sequencing however unlike nucleic acid which have four building blocks, proteins have 20 different amino acids. Currently, nanopores cannot resolve individual amino acids but many works have proven the feasibility of translocating unfolded proteins through nanopores.<sup>74,134–138</sup> The current challenges of protein sequencing using nanopores are quite similar to the early challenges of DNA sequencing. Challenges such as low capture rate due to the heterogeneity of charge on proteins, difficulty of peptide unfolding, rapid protein/peptide translocation<sup>120,136</sup> are all barriers to protein/peptide sequencing. Researchers have

started to address these challenges by adding tags to polypeptide chains to enhance capture rate,<sup>135–138</sup> coupling nanopores with unfoldase enzymes,<sup>135,136</sup> engineering binding sites in the nanopore,<sup>76,123,139,140</sup> and using chaotropic agents to denature proteins.<sup>127,128,131</sup> However, amino acid resolution via nanopores is still a distant dream. Thus, nanopore protein analysis/sequencing research will be thriving for the next several years.

In order to advance nanopore sequencing technology, the next steps will require improving computer software analytical tools.<sup>141</sup> In addition, nanopores with asymmetric properties i.e. geometric asymmetry as well as functional group asymmetry in the lumen could also improve the resolution of molecule detection.<sup>142,143</sup> Solid state nanopores, monomeric protein nanopores and even DNA origami pores have an advantage over oligomeric nanopores based on PFTs to introduce geometric<sup>143</sup> or functional group asymmetry.<sup>142</sup> We currently do not have a large repertoire of monomeric nanopores whose stability rivals that of  $\alpha$ HL nor do we have the precision to repeatedly synthesize an asymmetric solid-state one. However, this limitation will drive researchers to design and engineer new strategies to fill the gap. The nanopore field has many avenues to explore with both solid state and protein nanopores and vibrant research is needed to pinpoint limitations so that we can engineer schemes to overcome them.

In addition to nanopore technology another application for PFPs is in drug development. We can exploit the cytotoxic behavior of PFTs for therapeutic purposes. Malignant cells that resist cell death such as in some cancers<sup>144–146</sup> could undergo death if attacked by a specific and potent PFT<sup>147–153</sup> or peptide<sup>154</sup> (Figure I.2a). Furthermore, PFTs can potentially be used as delivery vehicles to increase the uptake of drugs into a cell,<sup>147</sup> (Figure I.2b) or in delivery vehicles such as outer membrane vesicles<sup>155,156</sup> and can enhance vaccine efficacy.<sup>157</sup> Although there is great potential for PFTs in drug development, the progress has been relatively slow. One major setback in developing PFTs as cytotoxic drugs are due to low toxin specificity which is why some researchers

have proposed to attach the toxin to an antibody to increase specificity.<sup>149</sup> However these large immunotoxins may not survive oral delivery and may be cleared very quickly from the blood. Some research has successfully targeted PFTs to tumor cells in mice models using engineered bacteria,<sup>150–153</sup> however this method is limited to areas where the bacteria can be safely injected. It also raises an ethical and safety concern about administering genetically modified organisms (GMOs) into the human populace. Other limitations are related to toxin potency. For example, PFTs that can efficiently lyse its target cell would be an unlikely candidate to exploit as a drug delivery vehicle. Research on toxin assembly, stability and combinational methods will improve our engineering efforts to create specific and efficacious PFT drugs.



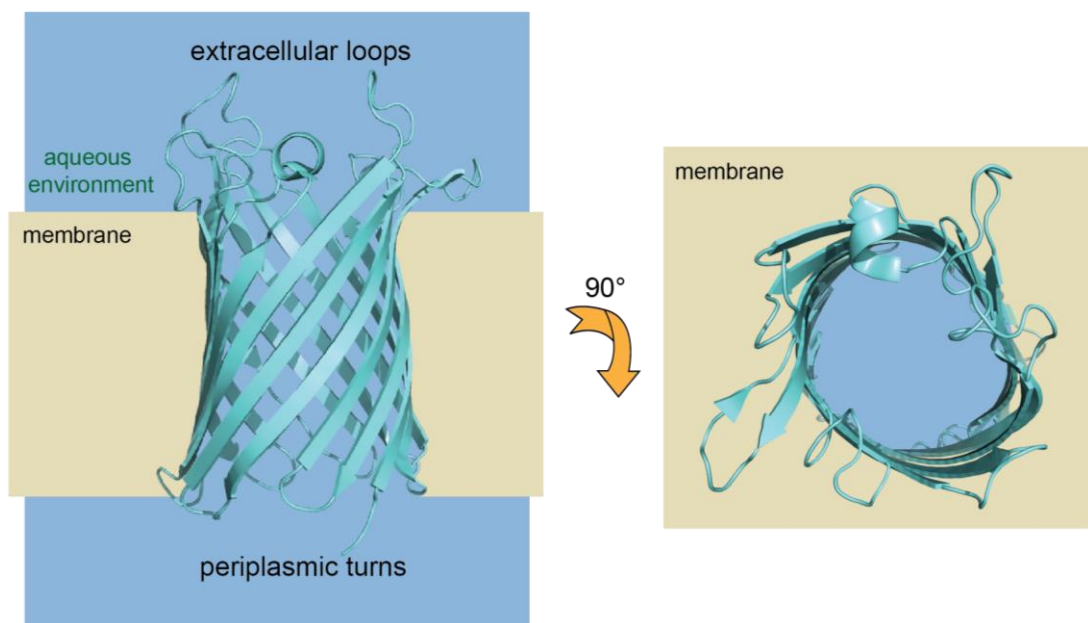
**Figure I.2. PFTs as drugs to induce cell death or as drug delivery vehicles.** (a) A PFT is used to induce cell death by lysis in the malignant cell such as a cancer cell that has become ‘immortal’. (b) A PFT is used as a delivery mechanism to allow beneficial drugs to enter the cell to alleviate the malignancy.

## I.4 Pore forming protein research using OmpG and ClyA

### I.4.1 Outer membrane protein G (OmpG) as a nanopore sensor

One monomeric nanopore that has been recently introduced in the nanopore field is outer membrane protein G (OmpG).<sup>117,158–162</sup> OmpG is a 33 kDa monomeric protein found in the outer membrane of *E. coli*.<sup>18,163</sup> It belongs to the family of bacterial outer

membrane proteins (Omps) which are typically beta barrels and have various functions ranging from enzymatic activity to iron transport.<sup>8</sup> OmpG, in particular, was found to be involved in the uptake of polar molecules such as maltose,<sup>18,163,164</sup> and unlike other typical trimeric Omps it is a monomer.<sup>165–169</sup> OmpG's 14 beta strands are connected by seven long loops which face the exterior of the bacterial cell and seven short turns which face the periplasm<sup>170</sup> (Figure I.3).



**Figure I.3. Side and top views of the OmpG porin structure.** OmpG consists of 14 beta strands, seven periplasmic turns and seven long extracellular loops.

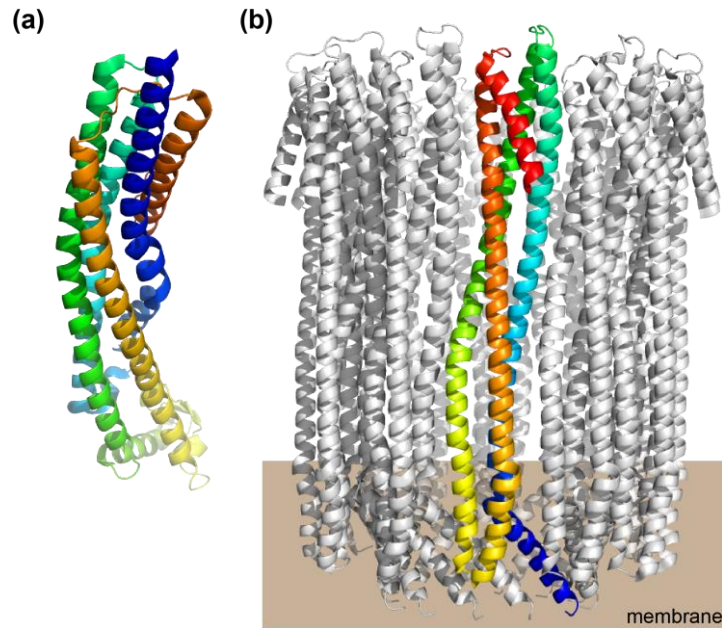
Reconstituted in an artificial planar bilayer, OmpG generates a noisy ionic current fluctuating rapidly between high and low current states when voltage is applied.<sup>158,159,164,166,171</sup> Many structural studies on OmpG under various conditions advanced the understanding of its gating mechanism which is largely due to the movement of its longest loop L6.<sup>168,172–174</sup> Because of this gating property of OmpG, it was deemed undesirable for use as a nanopore sensor.<sup>158</sup> Thus in an attempt to make it more suitable for nanopore sensing researchers stabilized loop 6,<sup>158,175</sup> or shortened it.<sup>176</sup> Thereafter



ADP was successfully detected by Chen et al using a cyclodextrin adaptor in the lumen.<sup>158</sup> Because OmpG is its widest at the periplasmic side with 1.5 nm and narrows to 0.8 nm near the extracellular loop side,<sup>159</sup> thus it is limited to detecting small molecules such as ADP. But the paradigm in nanopore sensing is shifting toward the detection and analysis of proteins. Thus, as will be shown in the following chapters of this dissertation, we exploited this intrinsic gating property to engineer an OmpG nanopore sensor for protein analytes. To do this we covalently attached a high affinity ligand biotin to loop 6 of OmpG which was used to capture biotin-binding proteins. After attaching the biotin ligand, OmpG gained the ability to specifically and sensitively interact with various proteins and generate individual signals for each that could be used to distinguish one from the other.<sup>117,160–162</sup> This was the first report of a single nanopore sensor that would distinguish more than five protein analytes.

#### **I.4.2 Cytolysin A as a model for studying oligomeric protein assembly**

Another protein that has been recently probed in nanopore sensing is the PFT Cytolysin A (ClyA) also known as hemolysin E (HlyE) or silent hemolysin locus A (SheA).<sup>177</sup> It is an  $\alpha$ -PFT and currently is the only one whose monomeric<sup>178</sup> and oligomeric<sup>179</sup> structures are known (Figure I.4). ClyA is found in several bacterial strains such as *Escherichia coli*, *Salmonella enterica* and *Shigella flexneri*<sup>177</sup> and may be involved in the pathogenicity of these strains.<sup>15,180–182</sup> The ClyA toxin is exported to the periplasm<sup>[138],[139]</sup> and studies have found that it is secreted into the extracellular environment via outer membrane vesicles (OMVs).<sup>184–186</sup> Subsequent studies have taken advantage of ClyA secretion into OMVs to engineer particles for cancer therapeutics<sup>150–153</sup> and vaccines.<sup>155–157</sup> ClyA has also been exploited in nanopore sensing and was shown to detect DNA,<sup>86,187</sup> distinguish between homologous proteins,<sup>110,188</sup> trap proteins and reveal conformational changes<sup>189–191</sup> or study protein-ligand interactions.<sup>192</sup>



**Figure I.4. The structures of the inactive and active ClyA  $\alpha$ -PFT.** The soluble ClyA monomer (a) is expressed in the bacteria and the transmembrane oligomeric pore (b) is bound to the target cell and induces them to lyse.

Although, ClyA has now been deemed a bona fide nanopore, our interest in ClyA stems from its ability to assemble into large dodecameric pores on the time scale of minutes.<sup>51–53</sup> Also ClyA tends to assemble into a large distribution of oligomers as suggested in one study.<sup>189</sup> Unlike  $\alpha$ HL,<sup>49</sup> the conversion of the ClyA monomer into the oligomer is a slow process. This is advantageous as we can study the steps in PFT oligomerization using ClyA as a model.<sup>4,7,9</sup> In this dissertation, we have shown that ClyA can undergo an off-pathway assembly into the cytotoxic transmembrane pore through a soluble protein conglomerate. We have shown that ClyA forms multimeric intermediates in the absence of membrane or detergent.<sup>53,193</sup> By revealing this off-pathway folding conglomerate we have sampled a small subset of folding mechanisms in the protein folding landscape of ClyA.

## I.5 References

1. Bischofberger, M., Gonzalez, M. R. & van der Goot, F. G. Membrane injury by pore-forming proteins. *Curr. Opin. Cell Biol.* **21**, 589–595 (2009).
2. Iacovache, I., Bischofberger, M. & van der Goot, F. G. Structure and assembly of pore-forming proteins. *Curr. Opin. Struct. Biol.* **20**, 241–246 (2010).
3. Yamaji-Hasegawa, A., Hullin-Matsuda, F., Greimel, P. & Kobayashi, T. Pore-forming toxins: Properties, diversity, and uses as tools to image sphingomyelin and ceramide phosphoethanolamine. *Biochim. Biophys. Acta - Biomembr.* **1858**, 576–592 (2016).
4. Reboul, C. F., Whisstock, J. C. & Dunstone, M. A. Giant MACPF/CDC pore forming toxins: A class of their own. *Biochim. Biophys. Acta - Biomembr.* **1858**, 475–486 (2016).
5. Ludwig, a, Bauer, S., Benz, R., Bergmann, B. & Goebel, W. Analysis of the SlyA-controlled expression, subcellular localization and pore-forming activity of a 34 kDa haemolysin (ClyA) from *Escherichia coli* K-12. *Mol. Microbiol.* **31**, 557–67 (1999).
6. Benz, R., Popp, B., Petra Wiesner & Schmid, A. The mitochondrial porins. *Prog. Cell Res.* **5**, 107–112 (1995).
7. Kabachinski, G. & Schwartz, T. U. The nuclear pore complex - structure and function at a glance. *J. Cell Sci.* **128**, 423–429 (2015).
8. Schulz, G. E. The structure of bacterial outer membrane proteins. *Biochim. Biophys. Acta* **1565**, 308–317 (2002).
9. Morita-Yamamuro, C. *et al.* The Arabidopsis gene CAD1 controls programmed cell death in the plant immune system and encodes a protein containing a MACPF domain. *Plant Cell Physiol.* **46**, 902–912 (2005).
10. Noutoshi, Y. *et al.* Loss of necrotic spotted lesions 1 associates with cell death and defense responses in *Arabidopsis thaliana*. *Plant Mol. Biol.* **62**, 29–42 (2006).
11. Lukyanova, N. & Saibil, H. R. Friend or foe: the same fold for attack and defense. *Trends Immunol.* **29**, 51–53 (2008).
12. Ota, K. *et al.* MACPF/CDC Proteins - Agents of Defence, Attack and Invasion. *Subcell. Biochem.* **80**, 271–291 (2014).
13. Tilley, S. J. & Saibil, H. R. The mechanism of pore formation by bacterial toxins. *Curr. Opin. Struct. Biol.* **16**, 230–236 (2006).
14. Iacovache, I., van der Goot, F. G. & Pernot, L. Pore formation: An ancient yet complex form of attack. *Biochim. Biophys. Acta - Biomembr.* **1778**, 1611–1623 (2008).
15. Los, F. C. O., Randis, T. M., Aroian, R. V & Ratner, A. J. Role of pore-forming toxins in bacterial infectious diseases. *Microbiol. Mol. Biol. Rev.* **77**, 173–207 (2013).
16. Singh, Y., Klimpel, K. R., Arora, N., Sharma, M. & Leppla, S. H. The Chymotrypsin-sensitive Site , FFD315 , in Anthrax Toxin Protective Antigen Is Required for Translocation of Lethal Factor. *J. Biol. Chem.* **269**, 29039–29046 (1994).
17. Poole, K., Jr, T. R. P. & Hancock, R. E. W. Phosphate-selective porins from the outer membranes of fluorescent *Pseudomonas* sp. *Can. J. Microbiol.* **33**, 63–69 (1987).
18. Misra, R. & Bensont, S. A. A Novel Mutation , cog , which results in production of a new porin protein (OmpG) of *Escherichia coli* K-12. *J. B* **171**, 4105–4111 (1989).
19. Benz, R. & Bauer, K. Permeation of hydrophilic molecules through the outer membrane of gram-negative bacteria. *Eur. J. Biochem.* **171**, 1–19 (1988).

20. Benz, R. Biophysical properties of porin pores from mitochondrial outer membrane of eukaryotic cells. *Experientia* **46**, 131–137 (1990).
21. Weeber, E. J. *et al.* The role of mitochondrial porins and the permeability transition pore in learning and synaptic plasticity. *J. Biol. Chem.* **277**, 18891–18897 (2002).
22. Young, M. J., Bay, D. C., Hausner, G. & Court, D. A. The evolutionary history of mitochondrial porins. *BMC Evol. Biol.* **7**, 31 (2007).
23. Schleiff, E. & Becker, T. Common ground for protein translocation : access control for mitochondria and chloroplasts. *Nat. Rev. Mol. Cell Biol.* **12**, 48–59 (2011).
24. Harsman, A. *et al.* OEP40, a regulated glucose-permeable  $\beta$ -barrel solute channel in the chloroplast outer envelope membrane. *J. Biol. Chem.* **291**, 17848–17860 (2016).
25. Bayley, H. Membrane-protein structure: Piercing insights. *Nature* **459**, 4–5 (2009).
26. Peraro, M. D. & van der Goot, F. G. Pore-forming toxins: ancient, but never really out of fashion. *Nat. Rev.* **14**, 77–92 (2016).
27. Parker, M. W. & Feil, S. C. Pore-forming protein toxins: From structure to function. *Prog. Biophys. Mol. Biol.* **88**, 91–142 (2005).
28. Fagerlund, A., Lindbäck, T., Storset, A. K., Granum, P. E. & Hardy, S. P. *Bacillus cereus* Nhe is a pore-forming toxin with structural and functional properties similar to the ClyA (HlyE, SheA) family of haemolysins, able to induce osmotic lysis in epithelia. *Microbiology* **154**, 693–704 (2008).
29. Leippe, M. Pore-forming toxins from pathogenic amoebae. *Appl. Microbiol. Biotechnol.* **98**, 4347–4353 (2014).
30. Slade, D. J. *et al.* Crystal Structure of the MACPF Domain of Human Complement Protein C8 $\alpha$  in Complex with the C8 $\gamma$  Subunit. *J. Mol. Biol.* **379**, 331–342 (2008).
31. Tweten, R. K. Cholesterol-Dependent Cytolysins , a Family of Versatile Pore-Forming Toxins. *Infect. Immun.* **73**, 6199–6209 (2005).
32. Gilbert, R. J. C., Serra, M. D., Froelich, C. J., Wallace, M. I. & Anderluh, G. Membrane pore formation at protein-lipid interfaces. *Trends Biochem. Sci.* **39**, 510–516 (2014).
33. Rojko, N., Dalla Serra, M., MačEk, P. & Anderluh, G. Pore formation by actinoporins, cytolysins from sea anemones. *Biochim. Biophys. Acta - Biomembr.* **1858**, 446–456 (2016).
34. Schön, P. *et al.* Equinatoxin II permeabilizing activity depends on the presence of sphingomyelin and lipid phase coexistence. *Biophys. J.* **95**, 691–8 (2008).
35. Iacovache, I. & Van Der Goot, F. G. A bacterial big-MAC attack. *Nat. Struct. Mol. Biol.* **11**, 1163–1164 (2004).
36. Cortajarena, A. L., Goñi, F. M. & Ostolaza, H. Glycophorin as a receptor for *Escherichia coli* alpha-hemolysin in erythrocytes. *J. Biol. Chem.* **276**, 12513–9 (2001).
37. Santelli, E., Bankston, L. a, Leppla, S. H. & Liddington, R. C. Crystal structure of a complex between anthrax toxin and its host cell receptor. *Nature* **430**, 905–908 (2004).
38. Rai, A. K., Paul, K. & Chattopadhyay, K. Functional mapping of the lectin activity site on the  $\beta$ -prism domain of *vibrio cholerae* cytolysin: implications for the membrane pore-formation mechanism of the toxin. *J. Biol. Chem.* **288**, 1665–73 (2013).
39. Baran, K. *et al.* The Molecular Basis for Perforin Oligomerization and Transmembrane Pore Assembly. *Immunity* **30**, 684–695 (2009).
40. Booth, P. J. & Clarke, J. Membrane protein folding makes the transition. *Proc. Natl. Acad. Sci. U. S. A.* **107**, 3947–3948 (2010).

41. Tamm, L. K., Hong, H. & Liang, B. Folding and assembly of beta-barrel membrane proteins. *Biochim. Biophys. Acta - Biomembr.* **1666**, 250–263 (2004).
42. Kleinschmidt, J. H. Folding of  $\beta$ -barrel membrane proteins in lipid bilayers - Unassisted and assisted folding and insertion. *Biochim. Biophys. Acta - Biomembr.* **1848**, 1927–1943 (2015).
43. McMorran, L. M., Brockwell, D. J. & Radford, S. E. Mechanistic studies of the biogenesis and folding of outer membrane proteins in vitro and in vivo: What have we learned to date? *Arch. Biochem. Biophys.* **564**, 265–280 (2014).
44. Costa, T. R. D. *et al.* Secretion systems in Gram-negative bacteria: structural and mechanistic insights. *Nat. Rev. Microbiol.* **13**, 343–359 (2015).
45. Mazor, Y., Borovikova, A. & Nelson, N. The Structure of the plant photosystem I supercomplex at 2.6 Å resolution. *Nat. Plants* **3**, 17014 (2017).
46. Young, I. D. *et al.* Structure of photosystem II and substrate binding at room temperature. *Nature* **540**, 453–457 (2016).
47. Westphal, D. *et al.* Apoptotic pore formation is associated with in-plane insertion of Bak or Bax central helices into the mitochondrial outer membrane. *Proc. Natl. Acad. Sci. U. S. A.* **111**, E4076–E4085 (2014).
48. Kasianowicz, J. J. *et al.* Analytical applications for pore-forming proteins. *Biochim. Biophys. Acta - Biomembr.* **1858**, 593–606 (2016).
49. Thompson, J. R., Cronin, B., Bayley, H. & Wallace, M. I. Rapid assembly of a multimeric membrane protein pore. *Biophys. J.* **101**, 2679–83 (2011).
50. Yilmaz, N. & Kobayashi, T. Assemblies of pore-forming toxins visualized by atomic force microscopy. *Biochim. Biophys. Acta - Biomembr.* **1858**, 500–511 (2016).
51. Benke, S. *et al.* The assembly dynamics of the cytolytic pore toxin ClyA. *Nat. Commun.* **6**, 1–13 (2015).
52. Eifler, N. *et al.* Cytotoxin ClyA from *Escherichia coli* assembles to a 13-meric pore independent of its redox-state. *EMBO J.* **25**, 2652–61 (2006).
53. Fahie, M. *et al.* A non-classical assembly pathway of *Escherichia coli* pore forming toxin cytolysin A. *J. Biol. Chem.* **288**, 31042–31051 (2013).
54. Roderer, D. *et al.* Characterization of Variants of the Pore-Forming Toxin ClyA from *Escherichia coli* Controlled by a Redox Switch. *Biochemistry* **53**, 6357–6369 (2014).
55. Kudr, J. *et al.* Fabrication of solid-state nanopores and its perspectives. *Electrophoresis* **36**, 2367–2379 (2015).
56. Dekker, C. Solid-state nanopores. *Nat. Nanotechnol.* **2**, 209–215 (2007).
57. Haque, F., Li, J., Wu, H. C., Liang, X. J. & Guo, P. Solid-state and biological nanopore for real-time sensing of single chemical and sequencing of DNA. *Nano Today* **8**, 56–74 (2013).
58. Burns, J. R. *et al.* Lipid-bilayer-spanning DNA nanopores with a bifunctional porphyrin anchor. *Angew. Chemie - Int. Ed.* **52**, 12069–12072 (2013).
59. Burns, J. R., Stulz, E. & Howorka, S. Self-Assembled DNA Nanopores That Span Lipid Bilayers. *Nano Lett.* **13**, 2351–2356 (2013).
60. Burns, J. R., Al-Juffali, N., Janes, S. M. & Howorka, S. Membrane-spanning DNA nanopores with cytotoxic effect. *Angew. Chemie - Int. Ed.* **53**, 12466–12470 (2014).
61. Messenger, L. *et al.* Biomimetic Hybrid Nanocontainers with Selective Permeability. *Angew. Chemie - Int. Ed.* **55**, 11106–11109 (2016).
62. Seifert, A. *et al.* Bilayer-Spanning DNA Nanopores with Voltage- Switching between Open and Closed State. *ACS Nano* **9**, 1117–1126 (2015).
63. Maingi, V. *et al.* Stability and dynamics of membrane-spanning DNA nanopores.

- Nat. Commun.* **8**, 14784 (2017).
64. Maingi, V., Lelimosin, M., Howorka, S. & Sansom, M. S. P. Gating-like Motions and Wall Porosity in a DNA Nanopore Scaffold Revealed by Molecular Simulations. *ACS Nano* **9**, 11209–11217 (2015).
  65. Burns, J. R., Seifert, A., Fertig, N. & Howorka, S. A biomimetic DNA-based channel for the ligand-controlled transport of charged molecular cargo across a biological membrane. *Nat. Nanotechnol.* **advance on**, 1–16 (2016).
  66. Braha, O. *et al.* Designed protein pores as components for biosensors. *Chem. Biol.* **4**, 497–505 (1997).
  67. Braha, O. *et al.* Simultaneous stochastic sensing of divalent metal ions. *Nat. Biotechnol.* **18**, 1005–1007 (2000).
  68. Boersma, A. J., Brain, K. L. & Bayley, H. Real-time stochastic detection of multiple neurotransmitters with a protein nanopore. *ACS Nano* **6**, 5304–5308 (2012).
  69. Singh, P. R. *et al.* Pulling peptides across nanochannels: Resolving peptide binding and translocation through the hetero-oligomeric channel from nocardia farcinica. *ACS Nano* **6**, 10699–10707 (2012).
  70. Apetrei, A. *et al.* Unimolecular study of the interaction between the outer membrane protein OmpF from *E. coli* and an analogue of the HP(2-20) antimicrobial peptide. *J. Bioenerg. Biomembr.* **42**, 173–180 (2010).
  71. Movileanu, L., Schmittschmitt, J. P., Scholtz, J. M. & Bayley, H. Interactions of peptides with a protein pore. *Biophys. J.* **89**, 1030–45 (2005).
  72. Kasianowicz, J. J., Henrickson, S. E., Weetall, H. H. & Robertson, B. Simultaneous multianalyte detection with a nanometer-scale pore. *Anal. Chem.* **73**, 2268–2272 (2001).
  73. Movileanu, L., Howorka, S., Braha, O. & Bayley, H. Detecting protein analytes that modulate transmembrane movement of a polymer chain within a single protein pore. *Nat. Biotechnol.* **18**, 1091–1095 (2000).
  74. Talaga, D. S. & Li, J. Single-molecule protein unfolding in solid state nanopores. *J. Am. Chem. Soc.* **131**, 9287–9297 (2009).
  75. Firnkes, M. *et al.* Electrically Facilitated Translocations of Proteins through Silicon Nitride Nanopores : Conjoint and Competitive Action of Diffusion ,. *Nano Lett.* **10**, 2162–2167 (2010).
  76. Yusko, E. C. *et al.* Controlling protein translocation through nanopores with bio-inspired fluid walls. *Nat. Nanotechnol.* **6**, 253–60 (2011).
  77. Oukhaled, A., Bacri, L., Pastoriza-Gallego, M., Betton, J. M. & Pelta, J. Sensing proteins through nanopores: Fundamental to applications. *ACS Chem. Biol.* **7**, 1935–1949 (2012).
  78. Ivankin, A., Carson, S., Kinney, S. R. M. & Wanunu, M. Fast, label-free force spectroscopy of histone-DNA interactions in individual nucleosomes using nanopores. *J. Am. Chem. Soc.* **135**, 15350–15352 (2013).
  79. Gurnev, P. A., Oppenheim, A. B., Winterhalter, M. & Bezrukov, S. M. Docking of a Single Phage Lambda to its Membrane Receptor Maltoporin as a Time-resolved Event. *J. Mol. Biol.* **359**, 1447–1455 (2006).
  80. McMullen, A., de Haan, H. W., Tang, J. X. & Stein, D. Stiff filamentous virus translocations through solid-state nanopores. *Nat. Commun.* **5**, 4171 (2014).
  81. Wu, H. *et al.* Translocation of Rigid Rod-Shaped Virus through Various Solid-State Nanopores. *Anal. Chem.* **88**, 2502–2510 (2016).
  82. Darvish, A., Goyal, G. & Kim, M. Sensing, capturing, and interrogation of single virus particles with solid state nanopores. *SPIE Sens. Technol. + Appl.* **9490**, 94900M (2015).
  83. Apetrei, A. *et al.* A Protein Nanopore-Based Approach for Bacteria Sensing.

- Nanoscale Res. Lett.* **11**, 501 (2016).
84. Branton, D. *et al.* The potential and challenges of nanopore sequencing. *Nat. Biotechnol.* **26**, 1146–1153 (2008).
  85. Garrido-cardenas, J. A., Garcia-maroto, F., Alvarez-bermejo, J. A. & Manzano-agugliaro, F. DNA Sequencing Sensors : An Overview. *Sensors (Basel)*. **17 (3)**, 1–15 (2017).
  86. Franceschini, L., Brouns, T., Willems, K., Carlon, E. & Maglia, G. DNA Translocation through Nanopores at Physiological Ionic Strengths Requires Precise Nanoscale Engineering. *ACS Nano* **10**, 8394–8402 (2016).
  87. Barati Farimani, A., Dibaeinia, P. & Aluru, N. R. DNA Origami-Graphene Hybrid Nanopore for DNA Detection. *ACS Appl. Mater. Interfaces* **9**, 92–100 (2017).
  88. Kumar, S. *et al.* PEG-Labeled Nucleotides and Nanopore Detection for Single Molecule DNA Sequencing by Synthesis. *Sci. Rep.* **2**, 1–8 (2012).
  89. Clarke, J. *et al.* Continuous base identification for single-molecule nanopore DNA sequencing. *Nat. Nanotechnol.* **4**, 265–270 (2009).
  90. Reiner, J. E. *et al.* The effects of diffusion on an exonuclease nanopore-based DNA sequencing engine. *J. Chem. Phys.* **137**, 214903 (2012).
  91. Wanunu, M. Nanopores: A journey towards DNA sequencing. *Phys. Life Rev.* **9**, 125–158 (2012).
  92. Derrington, I. M. *et al.* Nanopore DNA sequencing with MspA. *Proc. Natl. Acad. Sci. U. S. A.* **107**, 16060–5 (2010).
  93. Butler, T. Z., Pavlenok, M., Derrington, I. M., Niederweis, M. & Gundlach, J. H. Single-molecule DNA detection with an engineered MspA protein nanopore. *Proc. Natl. Acad. Sci.* **105**, 20647–20652 (2008).
  94. Manrao, E. A., Derrington, I. M., Pavlenok, M., Niederweis, M. & Gundlach, J. H. Nucleotide discrimination with DNA immobilized in the MSPA nanopore. *PLoS One* **6**, 1–7 (2011).
  95. Guo, B. Y., Zeng, T. & Wu, H. C. Recent advances of DNA sequencing via nanopore-based technologies. *Sci. Bull.* **60**, 287–295 (2015).
  96. Xu, J. J. Visualizing nanopore blinkings in parallel: a high-throughput nanopore array potential for ultra-rapid DNA sequencing. *Sci. Bull.* **60**, 2067–2068 (2015).
  97. Howorka, S. & Siwy, Z. Nanopores and Nanochannels: From Gene Sequencing to Genome Mapping. *ACS Nano* **10**, 9768–9771 (2016).
  98. Manrao, E. A. *et al.* Reading DNA at single-nucleotide resolution with a mutant MspA nanopore and phi29 DNA polymerase. *Nat Biotechnol* **30**, 349–353 (2012).
  99. Stoloff, D. H. & Wanunu, M. Recent trends in nanopores for biotechnology. *Curr. Opin. Biotechnol.* **24**, 699–704 (2013).
  100. Kasianowicz, J. J., Robertson, J. W. F., Chan, E. R., Reiner, J. E. & Stanford, V. M. Nanoscopic porous sensors. *Annu. Rev. Anal. Chem. (Palo Alto, Calif)*. **1**, 737–766 (2008).
  101. Stoddart, D. *et al.* Nucleobase recognition in ssDNA at the central constriction of the alpha-hemolysin pore. *Nano Lett.* **10**, 3633–7 (2010).
  102. Benner, S. *et al.* Sequence-specific detection of individual DNA polymerase complexes in real time using a nanopore. *Nat. Nanotechnol.* **2**, 718–24 (2007).
  103. Astier, Y., Kainov, D. E., Bayley, H., Tuma, R. & Howorka, S. Stochastic detection of motor protein-RNA complexes by single-channel current recording. *ChemPhysChem* **8**, 2189–2194 (2007).
  104. Carlsen, A. T. *et al.* Selective Detection and Quantification of Modified DNA with Solid- State Nanopores. *Nano Lett.* **14**, 5488–5492 (2014).
  105. Howorka, S. & Siwy, Z. Nanopore analytics: sensing of single molecules. *Chem. Soc. Rev.* **38**, 2360–2384 (2009).

106. Reiner, J. E. *et al.* Disease detection and management via single nanopore-based sensors. *Chem. Rev.* **112**, 6431–6451 (2012).
107. Reiner, J. E., Kasianowicz, J. J., Nablo, B. J. & Robertson, J. W. F. Theory for polymer analysis using nanopore-based single-molecule mass spectrometry. *Proc. Natl Acad. Sci. USA* **107**, 12080–12085 (2010).
108. Robertson, J. W. F. *et al.* Single-molecule mass spectrometry in solution using a solitary nanopore. *Proc. Natl. Acad. Sci. U. S. A.* **104**, 8207–8211 (2007).
109. Kasianowicz, J. J., Brandin, E., Branton, D. & Deamer, D. W. Characterization of individual polynucleotide molecules using a membrane channel. *Proc. Natl. Acad. Sci. U. S. A.* **93**, 13770–13773 (1996).
110. Soskine, M. *et al.* An engineered ClyA nanopore detects folded target proteins by selective external association and pore entry. *Nano Lett.* **12**, 4895–900 (2012).
111. Gu, L. Q., Braha, O., Conlan, S., Cheley, S. & Bayley, H. Stochastic sensing of organic analytes by a pore-forming protein containing a molecular adapter. *Nature* **398**, 686–690 (1999).
112. Cornell, B. a *et al.* A biosensor that uses ion-channel switches. *Nature* **387**, 580–583 (1997).
113. Halverson, K. M. *et al.* Anthrax biosensor, protective antigen ion channel asymmetric blockade. *J. Biol. Chem.* **280**, 34056–34062 (2005).
114. Xie, H., Braha, O., Gu, L. Q., Cheley, S. & Bayley, H. Single-molecule observation of the catalytic subunit of cAMP-dependent protein kinase binding to an inhibitor peptide. *Chem. Biol.* **12**, 109–120 (2005).
115. Rotem, D., Jayasinghe, L., Salichou, M. & Bayley, H. Protein detection by nanopores equipped with aptamers. *J. Am. Chem. Soc.* **134**, 2781–7 (2012).
116. Harrington, L., Cheley, S., Alexander, L. T., Knapp, S. & Bayley, H. Stochastic detection of Pim protein kinases reveals electrostatically enhanced association of a peptide substrate. *Proc. Natl. Acad. Sci. U. S. A.* **110**, E4417-26 (2013).
117. Fahie, M., Chisholm, C. & Chen, M. Resolved Single-Molecule Detection of Individual Species within a Mixture of anti-Biotin Antibodies Using an Engineered Monomeric Nanopore. *ACS Nano* **9**, 1089–1098 (2015).
118. Movileanu, L. Interrogating single proteins through nanopores: challenges and opportunities. *Trends Biotechnol.* **27**, 333–341 (2009).
119. Howorka, S. & Siwy, Z. S. Nanopores as protein sensors. *Nat. Biotechnol.* **30**, 506–507 (2012).
120. Shi, W., Friedman, A. K. & Baker, L. A. Nanopore Sensing. *Anal. Chem.* **89**, 157–188 (2017).
121. Stefureac, R., Long, Y.-T., Kraatz, H.-B., Howard, P. & Lee, J. S. Transport of alpha-helical peptides through alpha-hemolysin and aerolysin pores. *Biochemistry* **45**, 9172–9 (2006).
122. Fologea, D., Ledden, B., McNabb, D. S. & Li, J. Electrical characterization of protein molecules by a solid-state nanopore. *Appl. Phys. Lett.* **91**, 53901-1-53901–3 (2007).
123. Wolfe, A. J., Mohammad, M. M., Cheley, S., Bayley, H. & Movileanu, L. Catalyzing the translocation of polypeptides through attractive interactions. *J. Am. Chem. Soc.* **129**, 14034–14041 (2007).
124. Goodrich, C. P. *et al.* Single-molecule electrophoresis of  $\beta$ -hairpin peptides by electrical recordings and Langevin dynamics simulations. *J. Phys. Chem. B Lett.* **111**, 3332–3335 (2007).
125. Freedman, K. J. *et al.* Chemical, thermal, and electric field induced unfolding of single protein molecules studied using nanopores. *Anal. Chem.* **83**, 5137–5144 (2011).



126. Sutherland, T. C. *et al.* Structure of peptides investigated by nanopore analysis. *Nano Lett.* **4**, 1273–1277 (2004).
127. Oukhaled, G. *et al.* Unfolding of proteins and long transient conformations detected by single nanopore recording. *Phys. Rev. Lett.* **98**, 158101 (2007).
128. Pastoriza-Gallego, M. *et al.* Dynamics of unfolded protein transport through an aerolysin pore. *J. Am. Chem. Soc.* **133**, 2923–2931 (2011).
129. Wang, H., Ying, Y., Li, Y., Kraatz, H. & Long, Y. Nanopore Analysis of  $\beta$ -Amyloid Peptide Aggregation Transition Induced by Small Molecules. *Anal. Chem.* **83**, 1746–1752 (2011).
130. Wang, H. Y., Gu, Z., Cao, C., Wang, J. & Long, Y. T. Analysis of a single alpha-synuclein fibrillation by the interaction with a protein nanopore. *Anal. Chem.* **85**, 8254–8261 (2013).
131. Freedman, K. J., Haq, S. R., Edel, J. B., Jemth, P. & Kim, M. J. Single molecule unfolding and stretching of protein domains inside a solid-state nanopore by electric field. *Sci. Rep.* **3**, 1638 (2013).
132. Ho, C.-W. *et al.* Engineering a nanopore with co-chaperonin function. *Sci. Adv.* **1**, e1500905 (2015).
133. Deng, W. *et al.* Assembly, structure, function and regulation of type III secretion systems. *Nat. Rev. Microbiol.* (2017). doi:10.1038/nrmicro.2017.20
134. Nir, I., Huttner, D. & Meller, A. Direct Sensing and Discrimination among Ubiquitin and Ubiquitin Chains Using Solid-State Nanopores. *Biophys. J.* **108**, 2340–2349 (2015).
135. Nivala, J., Mulrone, L., Li, G., Schreiber, J. & Akeson, M. Discrimination among Protein Variants Using an Unfoldase-Coupled Nanopore. *ACS Nano* **8**, 12365–75 (2014).
136. Nivala, J., Marks, D. B. & Akeson, M. Unfoldase-mediated protein translocation through an  $\alpha$ -hemolysin nanopore. *Nat. Biotechnol.* **31**, 247–50 (2013).
137. Rodriguez-Larrea, D. & Bayley, H. Protein co-translocational unfolding depends on the direction of pulling. *Nat. Commun.* **5**, 4841 (2014).
138. Rosen, C. B., Rodriguez-Larrea, D. & Bayley, H. Single-molecule site-specific detection of protein phosphorylation with a nanopore. *Nat. Biotechnol.* **32**, 179–181 (2014).
139. Mohammad, M. M. & Movileanu, A. E. L. Excursion of a single polypeptide into a protein pore : simple physics , but complicated biology. *Eur. Biophys. J.* **37**, 913–925 (2008).
140. Kowalczyk, S. W. *et al.* Single-molecule transport across an individual biomimetic nuclear pore complex. *Nat. Nanotechnol.* **6**, 433–438 (2011).
141. Jain, M. *et al.* Improved data analysis for the MinION nanopore sequencer. *Nat. Methods* **12**, 351–356 (2015).
142. Reiß, P. & Koert, U. Ion-channels: Goals for function-oriented synthesis. *Acc. Chem. Res.* **46**, 2773–2780 (2013).
143. Chen, K., Bell, N. A. W., Kong, J., Tian, Y. & Keyser, U. F. Direction- and Salt-Dependent Ionic Current Signatures for DNA Sensing with Asymmetric Nanopores. *Biophys. J.* **112**, 1–15 (2017).
144. Douglas Hanahan & Weinberg, R. A. The hallmarks of cancer. *Cell* **100**, 57–70 (2000).
145. Hanahan, D. & Weinberg, R. A. Hallmarks of cancer: the next generation. *Cell* **144**, 646–674 (2011).
146. Seeger-Nukpezah, T., Geynisman, D. M., Nikonova, A. S., Benzing, T. & Golemis, E. A. The hallmarks of cancer: relevance to the pathogenesis of polycystic kidney disease. *Nat. Rev.* **11**, 515–534 (2015).

147. Panchal, R. G., Cusack, E., Cheley, S. & Bayley, H. Tumor protease-activated, pore-forming toxins from a combinatorial library. *Nat. Biotechnol.* **14**, 852–856 (1996).
148. Potrich, C. *et al.* Cytotoxic Activity of a Tumor Protease-Activated Pore-Forming Toxin. *Bioconjugate Chem* **16**, 369–376 (2005).
149. Tejuca, M., Anderluh, G. & Dalla Serra, M. Sea anemone cytolysins as toxic components of immunotoxins. *Toxicon* **54**, 1206–14 (2009).
150. Ryan, R. M. *et al.* Bacterial delivery of a novel cytolysin to hypoxic areas of solid tumors. *Gene Ther.* **16**, 329–339 (2009).
151. Jiang, S.-N. *et al.* Inhibition of tumor growth and metastasis by a combination of Escherichia coli-mediated cytolytic therapy and radiotherapy. *Mol. Ther.* **18**, 635–42 (2010).
152. Chen, J. Q., Zhan, Y. F., Wang, W., Jiang, S. N. & Li, X. Y. The engineered Salmonella typhimurium inhibits tumorigenesis in advanced glioma. *Onco. Targets. Ther.* **8**, 2555–2563 (2015).
153. Liu, X., Jiang, S., Piao, L. & Yuan, F. Radiotherapy combined with an engineered Salmonella typhimurium inhibits tumor growth in a mouse model of colon cancer. *Exp. Anim.* **65**, 413–418 (2016).
154. Zhong, J. & Chau, Y. Antitumor activity of a membrane lytic peptide cyclized with a linker sensitive to membrane type 1-matrix metalloproteinase. *Mol. Cancer Ther.* **7**, 2933–40 (2008).
155. Kim, J.-Y. *et al.* Engineered bacterial outer membrane vesicles with enhanced functionality. *J. Mol. Biol.* **380**, 51–66 (2008).
156. Chen, D. J. *et al.* Delivery of foreign antigens by engineered outer membrane vesicle vaccines. *Proc. Natl. Acad. Sci. U. S. A.* **107**, 3099–104 (2010).
157. Rosenthal, J. A. *et al.* Mechanistic insight into the Th1-biased immune response to recombinant subunit vaccines delivered by probiotic bacteria-derived outer membrane vesicles. *PLoS One* **9**, 1–24 (2014).
158. Chen, M., Khalid, S., Sansom, M. S. P. & Bayley, H. Outer membrane protein G: Engineering a quiet pore for biosensing. *Proc. Natl. Acad. Sci. U. S. A.* **105**, 6272–7 (2008).
159. Chen, M., Li, Q.-H. & Bayley, H. Orientation of the monomeric porin OmpG in planar lipid bilayers. *Chembiochem* **9**, 3029–36 (2008).
160. Fahie, M. A. & Chen, M. Electrostatic Interactions between OmpG Nanopore and Analyte Protein Surface Can Distinguish between Glycosylated Isoforms. *J. Phys. Chem. B* **119**, 10198–10206 (2015).
161. Fahie, M. A., Yang, B., Mullis, M., Holden, M. A. & Chen, M. Selective detection of protein homologues in serum using an OmpG nanopore. *Anal. Chem.* **87**, 11143–11149 (2015).
162. Fahie, M. A., Yang, B., Pham, B. & Chen, M. Tuning the Selectivity and Sensitivity of an OmpG Nanopore Sensor by Adjusting Ligand Tether Length. *ACS Sensors* **1**, 614–622 (2016).
163. Fajardo, D. A., Cheung, J., Ito, C. & Sugawara, E. Biochemistry and Regulation of a Novel Escherichia coli K-12 Porin Protein, OmpG, Which Produces Unusually Large Channels. *J. Bacteriol.* **180**, 4452–4459 (1998).
164. Conlan, S., Zhang, Y., Cheley, S. & Bayley, H. Biochemical and Biophysical Characterization of OmpG: A Monomeric Porin †. *Biochemistry* **39**, 11845–11854 (2000).
165. Behlau, M., Mills, D. J., Quader, H., Kühlbrandt, W. & Vonck, J. Projection structure of the monomeric porin OmpG at 6 Å resolution. *J. Mol. Biol.* **305**, 71–7 (2001).

166. Conlan, S. & Bayley, H. Folding of a monomeric porin, OmpG, in detergent solution. *Biochemistry* **42**, 9453–65 (2003).
167. Subbarao, G. V & van den Berg, B. Crystal structure of the monomeric porin OmpG. *J. Mol. Biol.* **360**, 750–9 (2006).
168. Yildiz, O., Vinothkumar, K. R., Goswami, P. & Kühlbrandt, W. Structure of the monomeric outer-membrane porin OmpG in the open and closed conformation. *EMBO J.* **25**, 3702–13 (2006).
169. Liang, B. & Tamm, L. K. Structure of outer membrane protein G by solution NMR spectroscopy. *Proc. Natl. Acad. Sci. U. S. A.* **104**, 16140–5 (2007).
170. Visudtiphole, V., Chalton, D. A., Hong, Q. & Lakey, J. H. Determining OMP topology by computation, surface plasmon resonance and cysteine labelling: The test case of OMPG. *Biochem. Biophys. Res. Commun.* **351**, 113–117 (2006).
171. Hwang, W. L., Chen, M., Cronin, B., Holden, M. a & Bayley, H. Asymmetric droplet interface bilayers. *J. Am. Chem. Soc.* **130**, 5878–9 (2008).
172. Damaghi, M. *et al.* pH-dependent interactions guide the folding and gate the transmembrane pore of the beta-barrel membrane protein OmpG. *J. Mol. Biol.* **397**, 878–82 (2010).
173. Korkmaz, F., Köster, S., Yildiz, O. & Mäntele, W. In situ opening/closing of OmpG from *E. coli* and the splitting of  $\beta$ -sheet signals in ATR-FTIR spectroscopy. *Spectrochim. Acta. A. Mol. Biomol. Spectrosc.* **91**, 395–401 (2012).
174. Zhuang, T., Chisholm, C., Chen, M. & Tamm, L. K. NMR-based conformational ensembles explain pH-gated opening and closing of OmpG channel. *J. Am. Chem. Soc.* **135**, 15101–13 (2013).
175. Zhuang, T. & Tamm, L. K. Control of the conductance of engineered protein nanopores through concerted loop motions. *Angew. Chem. Int. Ed. Engl.* **53**, 5897–902 (2014).
176. Grosse, W. *et al.* Structure-Based Engineering of a Minimal Porin Reveals Loop-Independent Channel Closure. *Biochemistry* **53**, 4826–4838 (2014).
177. Hunt, S., Green, J. & Artymiuk, P. J. Hemolysin E (HlyE, ClyA, SheA) and Related Toxins. *Adv. Exp. Med. Biol.* **677**, 116–126 (2010).
178. Wallace, A. J. *et al.* *E. coli* hemolysin E (HlyE, ClyA, SheA): X-ray crystal structure of the toxin and observation of membrane pores by electron microscopy. *Cell* **100**, 265–76 (2000).
179. Mueller, M., Grauschopf, U., Maier, T., Glockshuber, R. & Ban, N. The structure of a cytolytic alpha-helical toxin pore reveals its assembly mechanism. *Nature* **459**, 726–30 (2009).
180. Ludwig, A. *et al.* Molecular analysis of cytolysin A (ClyA) in pathogenic *Escherichia coli* strains. *J. Bacteriol.* **186**, 5311–5320 (2004).
181. Wyborn, N. R. *et al.* Properties of haemolysin E (HlyE) from a pathogenic *Escherichia coli* avian isolate and studies of HlyE export. *Microbiology* **150**, 1495–1505 (2004).
182. Fuentes, J. A., Villagra, N., Castillo-Ruiz, M. & Mora, G. C. The *Salmonella* Typhi hlyE gene plays a role in invasion of cultured epithelial cells and its functional transfer to *S. Typhimurium* promotes deep organ infection in mice. *Res. Microbiol.* **159**, 279–287 (2008).
183. Atkins, A. *et al.* Structure-function relationships of a novel bacterial toxin, hemolysin E. The role of alpha G. *J. Biol. Chem.* **275**, 41150–5 (2000).
184. Wai, S. N. *et al.* Vesicle-mediated export and assembly of pore-forming oligomers of the enterobacterial ClyA cytotoxin. *Cell* **115**, 25–35 (2003).
185. Kouokam, J. C. & Wai, S. N. Outer membrane vesicle-mediated export of a pore-forming cytotoxin from *Escherichia coli*. *Toxin Rev.* **25**, 31–46 (2008).

186. McBroom, A. J., Johnson, A. P., Vemulapalli, S. & Kuehn, M. J. Outer membrane vesicle production by *Escherichia coli* is independent of membrane instability. *J. Bacteriol.* **188**, 5385–92 (2006).
187. Franceschini, L., Soskine, M., Biesemans, A. & Maglia, G. A nanopore machine promotes the vectorial transport of DNA across membranes. *Nat. Commun.* **4**, 2415 (2013).
188. Wloka, C. *et al.* Label-Free and Real-Time Detection of Protein Ubiquitination with a Biological Nanopore. *ACS Nano* acsnano.6b07760 (2017). doi:10.1021/acsnano.6b07760
189. Soskine, M., Biesemans, A., De Maeyer, M. & Maglia, G. Tuning the Size and Properties of ClyA Nanopores Assisted by Directed Evolution. *J. Am. Chem. Soc.* **135**, 13456–63 (2013).
190. Meervelt, V. Van, Soskine, M. & Maglia, G. Detection of Two Isomeric Binding Configurations in a Protein Aptamer Complex with a Biological Nanopore. *ACS Nano* **8**, 12826–12835 (2014).
191. Biesemans, A., Soskine, M. & Maglia, G. A Protein Rotaxane Controls the Translocation of Proteins Across a ClyA Nanopore. *Nano Lett.* **15**, 6076–6081 (2015).
192. Soskine, M., Biesemans, A. & Maglia, G. Single-molecule analyte recognition with ClyA nanopores equipped with internal protein adaptors. *J. Am. Chem. Soc.* **137**, 5793–5797 (2015).
193. Roderer, D., Benke, S., Schuler, B. & Glockshuber, R. Soluble Oligomers of the Pore-forming Toxin Cytolysin A from *Escherichia coli* Are Off-pathway Products of Pore. *J. Biol. Chem.* **291**, 5652–5663 (2016).

## CHAPTER 1

### RESOLVED SINGLE-MOLECULE DETECTION OF INDIVIDUAL SPECIES WITHIN A MIXTURE OF ANTI-BIOTIN ANTIBODIES USING AN ENGINEERED MONOMERIC NANOPORE

Reprinted (adapted) with permission from M. Fahie, C. Chisholm, and M. Chen, “Resolved Single-Molecule Detection of Individual Species within a Mixture of anti-Biotin Antibodies Using an Engineered Monomeric Nanopore,” *ACS Nano*, vol. 9, no. 2, pp. 1089–1098, Jan. 2015. Copyright 2015 American Chemical Society.

#### 1.1 Summary

Oligomeric protein nanopores with rigid structures have been engineered for the purpose of sensing a wide range of analytes including small molecules and biological species such as proteins and DNA. We chose a monomeric  $\beta$ -barrel porin, OmpG, as the platform from which to derive the nanopore sensor. OmpG is decorated with seven flexible loops that move dynamically to create a distinct gating pattern when ionic current passes through the pore. Biotin was chemically tethered to the most flexible one of these loops. The gating characteristic of the loop’s movement in and out of the porin was substantially altered by analyte protein binding. The gating characteristics of the pore with bound targets were remarkably sensitive to molecular identity – even providing the ability to distinguish between homologues within an antibody mixture. A total of five gating parameters were analyzed for each analyte to create a unique fingerprint for each biotin binding protein. Our exploitation of gating noise as a molecular identifier may open new possibilities for more sophisticated sensor design while OmpG’s monomeric structure greatly simplifies nanopore production.

## 1.2 Introduction

Protein nanopores have become powerful single-molecule analytical tools that enable the study of fundamental problems in chemistry and biology,<sup>1,2</sup> including protein folding<sup>3</sup> and unfolding,<sup>4–8</sup> enzymatic activity,<sup>9–11</sup> chemical reactions<sup>12,13</sup> and stability of complex formation.<sup>14</sup> Beyond basic research, nanopores also hold tremendous promise in biotech applications such as DNA sequencing<sup>11,15–17</sup> and biosensing.<sup>1</sup> Molecular detection using a single nanopore works by observing modulations in ionic current flowing through the pore during an applied potential. Typically, binding (or translocation) of an analyte within (or through) the pore's lumen partially blocks the flow of current and provides information about a molecule's size, concentration and affinity.<sup>18</sup> Protein nanopores based on protein toxins, especially  $\alpha$ -hemolysin ( $\alpha$ HL), have been used to detect metal ions,<sup>19,20</sup> organic molecules,<sup>21–23</sup> oligonucleotides<sup>11,17,24</sup> and measure the size of polymers.<sup>25,26</sup>

Although  $\alpha$ HL works well for small analyte detection, molecules larger than 27Å in diameter cannot fit in the pore's lumen. Direct protein detection with nanopores is therefore problematic, though some strategies have been developed to transmit the binding signal from solution to the pore's interior.<sup>27–30</sup> For example, binding of a kinase was performed using an  $\alpha$ HL pore modified with an inhibitor peptide attached to its stem side.<sup>28</sup> The binding of lethal factor to the PA63 pores of the anthrax toxin orients the N-terminal leader sequence towards the pore's lumen.<sup>31,32</sup> In both cases, analyte docking to the binding site on the sensor pore manifest as a current blockage.<sup>28,32</sup> In addition to direct current blockade, target analytes may also be detected indirectly through current modulation. A common strategy involves a nanopore-permeable molecule, e.g. a small chemical ligand or ligand-modified polymer whose partitioning into or translocation through the nanopore was altered after analyte binding. Following this scheme, the detection of streptavidin or avidin was demonstrated by tethering biotin via a PEG

polymer to  $\alpha$ HL<sup>30</sup> or monitoring the translocation of biotinylated poly nucleic acids through  $\alpha$ HL.<sup>33–35</sup>

Another strategy is to use larger nanopores for analyte detect. For example, the bacterial toxin ClyA, with a 70Å diameter, was modified at one end with an aptamer specific to thrombin.<sup>36</sup> So far, ClyA represents the largest protein pore for sensing. Although there are many proteins that form larger pores in nature,<sup>37</sup> e.g. perfringolysin O (~15 nm in diameter),<sup>38</sup> their application as sensors has yet to be realized. Synthetic nanopores do not have the size limitation and are more robust<sup>39–41</sup> and have been applied to identify proteins either during translocation<sup>40–42</sup> or via capture by specific receptors immobilized on the wall of the pore.<sup>39,43–45</sup> However, synthetic nanopores lack the well-controlled geometry common to their protein pore counterparts.

Unlike other multimeric proteinaceous nanopores such as  $\alpha$ HL and ClyA,<sup>27,36</sup> outer membrane protein G (OmpG) from *Escherichia coli* (*E. coli*) is monomeric.<sup>46</sup> Thus, complex and asymmetric alterations by chemical or genetic modifications are straightforward, making OmpG an attractive nanopore platform for developing nanopore-based sensing technology. OmpG is composed of 14  $\beta$ -strands connected by seven flexible loops on the extracellular side and seven short turns on the periplasmic side.<sup>47–49</sup> The extracellular opening is 8 Å in diameter and the periplasmic side is 14 Å.<sup>50</sup> Wild-type OmpG spontaneously gates during an applied potential as revealed by planar bilayer studies.<sup>46,50</sup> Pore gating is attributed to loop 6 which flops in and out of the pore, intermittently blocking the current.<sup>50,51</sup> To reduce gating, a disulfide bond or lipid anchor was introduced into OmpG's structure which effectively pinned the flexible loop 6 in place.<sup>50,51</sup> The resulting quiet OmpG was used to sense ADP in the presence of a cyclodextrin adapter.<sup>50</sup>

So far, a rigid and stable structure is usually sought for protein pores for sensing.<sup>2,52</sup> The protein pores with demonstrated sensing applications include  $\alpha$ HL,<sup>30</sup> MspA,<sup>53</sup> ClyA,<sup>36</sup> aerolysin<sup>54</sup> and phi29 DNA packaging motor<sup>55</sup> all of which are homo-oligomers that possess a rigid structure. Two monomeric outer membrane porins, OmpG<sup>50</sup> and FhuA<sup>56</sup> with flexible loops have also been used for sensing purposes. However in both cases the flexible loops were considered as the major obstacle for sensing. These loops were either fixed or removed to stabilize a single open conformation by protein engineering.<sup>50,56</sup> Here, we directly exploit loop dynamics instead of pore blockage to detect protein interactions. Our results demonstrate that the flexibility of OmpG's structure represents a unique feature, which can be used for resolving subtle differences between the surface properties of highly homologous protein analytes. This capability has not been demonstrated with other nanopores.

### **1.3 Materials and Methods**

The DNA oligos and all chemicals were purchased from Fisher Scientific unless stated otherwise. Streptavidin (Z7041) was purchased from Promega. The biotin-maleimide reagents, Maleimide-PEG2-Biotin and Maleimide-PEG11-Biotin were purchased from Pierce and Warriner (Thermo Scientific). Mouse anti-biotin monoclonal antibody (MS-1048-P1) was purchased from Thermo Scientific. Goat anti-biotin polyclonal antibody (B3640) was from Sigma Aldrich. Mouse anti-His<sub>6</sub> (BSM-0287M) and mouse anti-GAPDH (BSM-0978M) antibodies were obtained from Bioss antibodies. LB media and DL-dithiothreitol (DTT) were purchased from Boston BioProducts. Diphytanoylphosphatidylcholine (DPhPC) were from Avanti polar lipids. Octyl-glucoside (OG) and *tris*(2-carboxyethyl)phosphine (TCEP) were purchased from GoldBio Technology.



### 1.3.1 Construction of OmpG D224C mutant

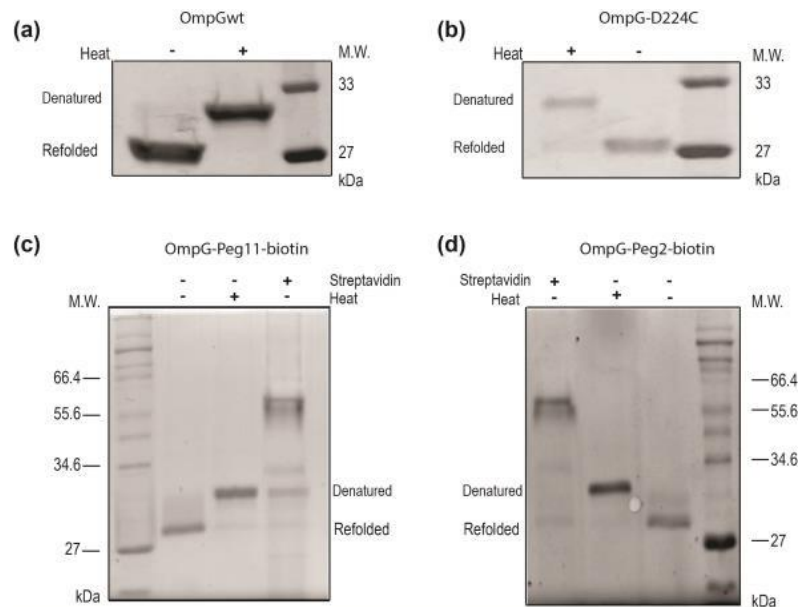
Single cysteine was introduced to replace the aspartic acid 224 by mutagenesis PCR based on the plasmid pT7-OmpG wt.<sup>50</sup> The primers for D224C were 5'-GGGACTGGCAGTGTGATATTGAACGTGAAG (forward) and 5'-GTTCAATATCACACTGCCAGTCCCAGTTAC (reverse). These two primers were used in a pair with the primer SC47: 5'-CAGAAGTGGTCCTGCAACTTTATC (reverse) and SC46: 5'-ATAAAGTTGCAGGACCACTTCTG (forward) which annealed to the middle of the plasmid. The two PCR products were mixed in a 1:1 molar ratio and subjected to DpnI digestion for three hours to degrade the parental plasmid. *E. coli* DH5 $\alpha$  cells were then co-transformed with the PCR mixture and colonies containing the desired mutant construct pT7-OmpG D224C was identified by DNA sequencing.

### 1.3.2 Cloning, expression and purification of OmpG D224C

The OmpG D224C was prepared by following an established protocol.<sup>50</sup> The pT7-OmpG D224C was transformed into the BL21(pLys) *E. coli* cells and cells were grown in LB medium at 37°C until the OD<sub>600</sub> reached 0.6. IPTG (0.5 mM) was added to the culture to induce the protein expression. Cells were harvested 3 hours after induction and lysed in lysis buffer (50 mM Tris·HCl, pH 8.0, 150 mM NaCl, 200  $\mu$ g/ml lysozyme, 1 mM EDTA, 1mM TCEP). Cells were sonicated on ice to break the bacterial membranes. DNAase I (5ul, 2,000 U/ $\mu$ l) and 2 mM MgCl<sub>2</sub> were then added to the mixture to decrease the viscosity. The lysate was centrifuged at 13,000 rpm for 30 min. The pellet was washed once with 30 ml 50 mM Tris·HCl, pH8.0, 1.5 M Urea, 1mM TCEP. Then the OmpG-containing inclusion body was dissolved in 50 ml 50 mM Tris·HCl, pH 8.0, 3 mM Tris(2-carboxyethyl)phosphine (TCEP), 8 M Urea and passed through a 0.45  $\mu$ m filter before FPLC purification. All OmpG proteins were purified using a 5ml Q-ionic exchange column (GE Healthcare).

### 1.3.3 Biotinylation and refolding of OmpG proteins

The purified OmpG D224C was incubated with 10 mM freshly prepared DL-dithiothreitol (DTT) for 30 min on ice to reduce the thiols. The DTT was then removed using a desalting column equilibrated with buffer 50 mM HEPES, pH7.0, 150 mM NaCl, 8M Urea. To label the OmpG D224C with biotin, the protein was incubated with maleimide-PEG-biotin in a molar ratio 1:20 (protein to biotin) at room temperature (~23°C) for 2 hours and then at 4 °C overnight. DTT (10 mM) was added to quench the reaction. The reaction mixture was passed through the desalting column once again to remove the unreacted chemicals. The biotin labelled OmpG was then diluted with the refolding buffer 50 mM Tris·HCl, pH 9.0, 3.25% OG until the final concentration of urea reached 3.0 M. Samples were then incubated at 37 °C for 3 days. The biotinylation and refolding efficiency was determined by SDS-PAGE (Figure 1.1).



**Figure 1.1 SDS-PAGE analysis of OmpG variants.** The refolded OmpG variants were either pre-heated at 95°C for 15 min or directly loaded on a 12.5% SDS-PAGE. Heating denatures the OmpG protein which migrates slower in SDS-PAGE. To determine the labelling efficiency, the OmpG-PEG<sub>11</sub>-biotin and OmpG-PEG<sub>2</sub>-biotin were incubated with streptavidin for 5 minutes which forms an SDS-resistant complex with biotin. Consequently, OmpG shifts to higher-molecular weight and labeling percent can be calculated by the disappearance of the OmpG refolded or denatured band.

#### 1.3.4 Single channel recording of OmpG proteins

Single channel recording of OmpG was similar to the previous study.<sup>50</sup> Briefly, experiments were performed in an apparatus containing two chambers separated by a 25  $\mu\text{m}$  thick Teflon film. An aperture of approximately 100  $\mu\text{m}$  diameter had been made near the center of the film with an electric spark. The aperture was pretreated with a hexadecane/pentane (10% v/v) solution before each chamber was filled with buffers as indicated specifically. An Ag/AgCl electrode was immersed in each chamber with the *cis* chamber grounded. 1,2-Diphytanoyl-sn-glycerol-3-phosphocholine (Avanti Polar Lipids, USA) dissolved in pentane (10mg/ml) was deposited on the surface of the buffer in both chambers and monolayers formed after the pentane evaporated. The lipid bilayer was formed by raising the liquid level up and down across the aperture. OmpG proteins (~1 nM, final concentration) were added to the *cis* chamber and +200mV was applied to facilitate OmpG insertion. After a single OmpG pore inserted, the applied voltage was lowered to 50 mV for recording. OmpG proteins inserted in the planar lipid bilayer bidirectionally with its extracellular loops located at either *cis* or *trans* side. After 10 min recording, the orientation of the OmpG pore in the lipid bilayer was determined by analyzing the asymmetrical gating pattern at positive and negative potentials. Streptavidin or antibodies were added to the *cis* or *trans* chamber depending on the pore orientation and the solution was stirred for 10 s. We define a positive potential as the potential of the chamber where the extracellular loops were exposed to is positive. Current was amplified with an Axopatch 200B integrating patch clamp amplifier (Axon Instruments, Foster City, CA). Signals were filtered with a Bessel filter at 2 kHz (unless otherwise stated) and then acquired by a computer (sampling at 50  $\mu\text{s}$ ) after digitization with a Digidata 1320A/D board (Axon Instruments).

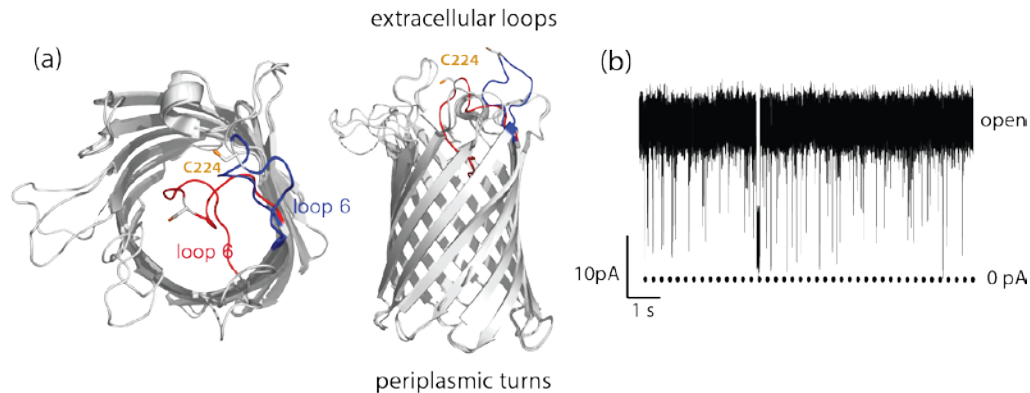
### 1.3.5 Single-channel current analysis

For power spectra analysis, data were recorded with a Bessel filter at 50 kHz and acquired at 250 kHz. Power spectra were calculated from a 20 s recording trace in Clampfit using segment lengths of 32768 samples (spectra resolution 7.62 Hz) by applying Hamming window. Data shown were derived from averaged spectra segments with 50% window overlap. To analyze the mAb and polyclonal antibody binding, power spectra of multiple binding events from a total of 20 s recording time were calculated and averaged. The power spectra densities for all traces were plotted in OriginPro 9.1.

## 1.4 Results

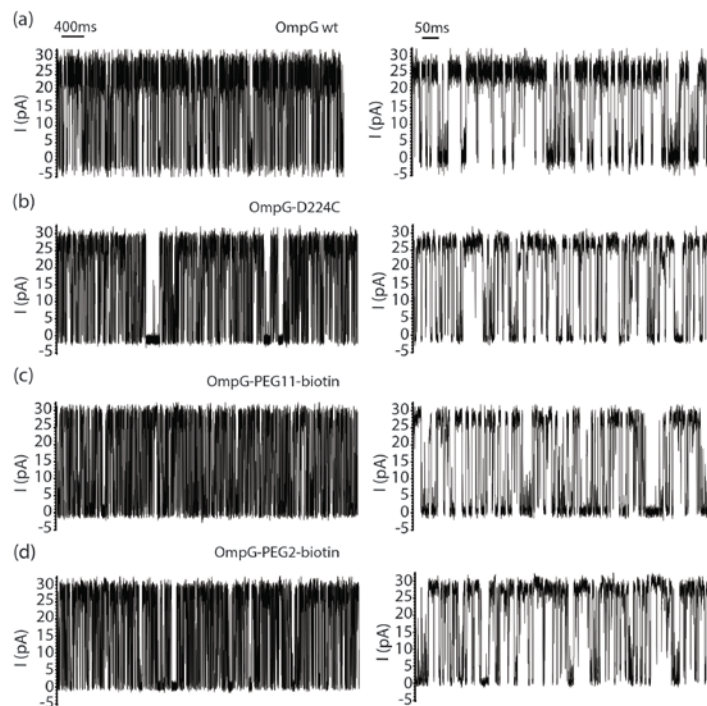
### 1.4.1 Detection of Streptavidin by OmpG-PEG<sub>11</sub>-biotin pore

To detect proteins, we designed an OmpG nanopore with a ligand tethered to loop 6 to “fish” for target proteins. We hypothesized that target binding would alter the flexibility of loop 6 and therefore alter the gating pattern as a recognizable signal to indicate detection. To validate the concept of the OmpG sensor, we first chose biotin and streptavidin as the model ligand and target protein because of its very low dissociation constant of  $\sim 10^{-15}$  M.<sup>57</sup> The OmpG D224C was expressed in *E. coli* as inclusion bodies and purified by ion-exchange chromatography. Purified OmpG D224C proteins were labeled with maleimide-(PEG)<sub>11</sub>-biotin and the resulting OmpG-PEG<sub>11</sub>-biotin construct was refolded to its native structure (Figure 1.1). A single cysteine mutation was introduced to the D224 residue of OmpG by site-directed mutagenesis (Figure 1.2).

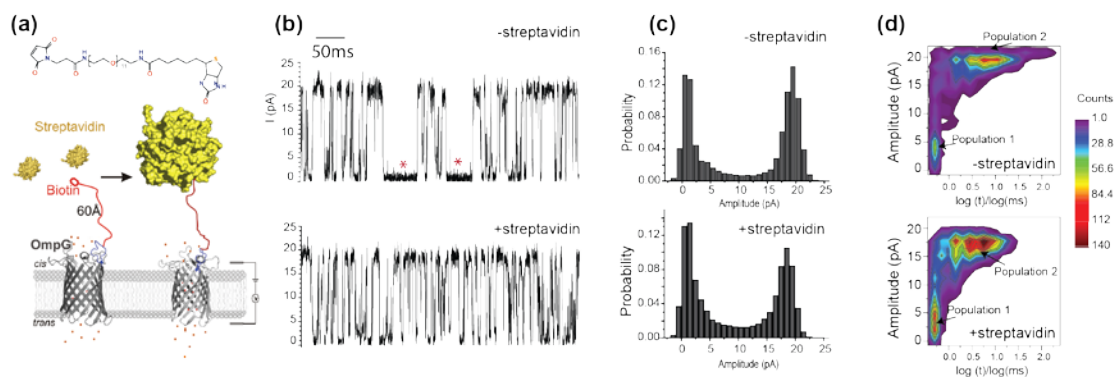


**Figure 1.2. Structures of OmpG and its gating activity.** (a) The top view (left) and side view (right) of the structural alignment of the open and closed states. Loop 6 is highlighted in blue in the open state and red in the closed state. The D224C mutation is shown in ball and stick model. (b) Single channel recording trace of a wild type OmpG pore. The data was obtained in buffer 10 mM Tris-HCl, pH 8.0, 150 mM KCl at +50 mV.

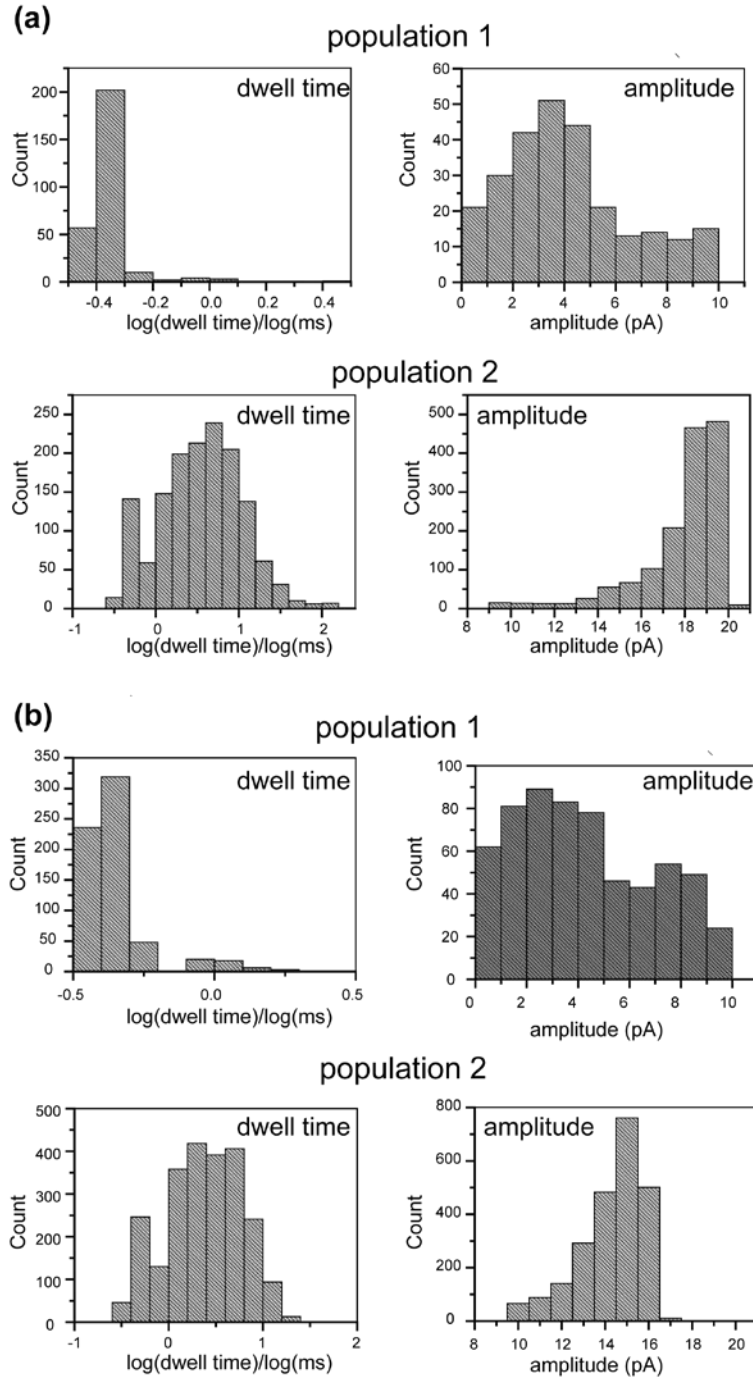
Single-channel recording of OmpG-D224C and OmpG-PEG<sub>11</sub>-biotin pores revealed that neither the mutation nor the tethered biotin group induced a measurable change in the unitary conductance or the gating pattern of OmpG when compared to wild type (Figures 1.3a-1.3c). The maleimide-PEG<sub>11</sub>-biotin ligand could fully extend from loop 6 by approximately 60Å to facilitate the capture of the analyte proteins (Figure 1.4a). Within minutes, the addition of 3 nM streptavidin to the chamber containing loop 6 of the labeled OmpG-PEG<sub>11</sub>-biotin pore could induce an irreversible change in its gating pattern. A marked increase in gating frequency from  $111 \pm 30 \text{ s}^{-1}$  to  $199 \pm 27 \text{ s}^{-1}$  ( $n=3$ ) was observed when streptavidin was bound to OmpG-PEG<sub>11</sub>-biotin labeled pores at pH 5.7 (Figures 1.4b, 1.4c). We plotted all the gating events according to their amplitude (pA) and duration (ms) in a two-dimensional (2D) distribution plot (Figure 1.4d). From the 2D plot analysis, we observe two populations of events. Population 1 only partially blocks the pore with amplitudes between 0 to 7.5 pA and dwell times between 0-0.4 ms (Figure 1.5); population 2 almost fully blocks the pore with amplitudes larger than 10 pA (10-20pA) and dwell times longer than 1ms *i.e.* 1-50 ms (Figure 1.5).



**Figure 1.3. Point mutation or biotinylation of OmpG does not affect its inherent gating behavior.** Single channel recording traces of (a) OmpG wt, (b) OmpG D224C (unlabeled), (c) OmpG-Peg11-biotin and (d) OmpG-Peg2-biotin. Buffer used was 10 mM sodium phosphate buffer, pH 6.0, 300 mM KCl and the applied potential was +50 mV.



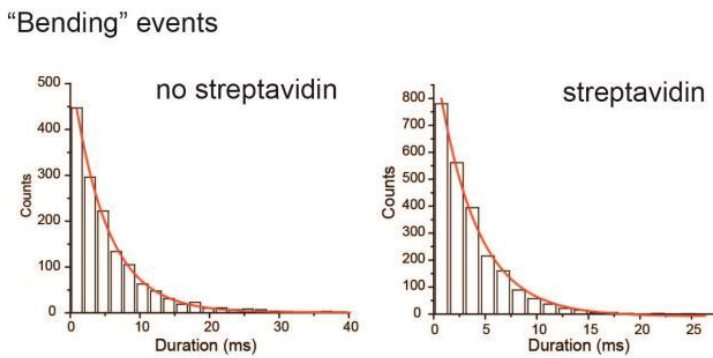
**Figure 1.4. Detection of streptavidin by OmpG-PEG<sub>11</sub>-biotin.** (a) Schematic model showing the OmpG-PEG<sub>11</sub>-biotin. The proteins were generated using PDB files of OmpG (2IWV) and streptavidin (3RY1). The streptavidin was placed approximately 60Å away from the OmpG pore in the model of the bound state. (b) Representative traces of the OmpG pore before and after the addition of the streptavidin (3 nM). The measurements were performed in buffer 10 mM sodium phosphate, pH5.7, 150 mM KCl at +50 mV. (c) All current histogram of the corresponding traces in b. (d) Two dimensional histogram of the gating events. Gating events collected from a 15s recording trace were distributed based on their intensity versus duration.



**Figure 1.5. Characteristic of the two gating event populations of streptavidin binding.** Histograms of amplitude and dwell time of gating events before (a) and after streptavidin binding (b).

From previous studies and known structures of OmpG,<sup>47, 50</sup> we expect that loop 6 cannot fully block the pore on its own as it cannot occupy sufficient space within the

lumen. For complete blockage, we expect that as much as one third of strand 12 must also unfold so that loop 6 is long enough to completely occlude the opening. We give the term “flickering” and “bending” to describe partial vs complete blockages, respectively. This distinction is important when considering the behavior observed in the 2D plots. For example, flickering events (population 1) seem relatively constant in the presence or absence of target, while the bending events (population 2) shorten considerably when the target binds (Figure 1.5d). By contrast, the average dwell time of the bending events decreased from  $5.1 \pm 0.14$  ms to  $3.8 \pm 0.15$  ms ( $n=3$ ) (Figure 1.6) when streptavidin was bound. In particular, those bending events of especially long duration ( $>10$  ms), indicated with red asterisks, were eliminated during the streptavidin-bound state (Figures 1.4b, 1.4d).

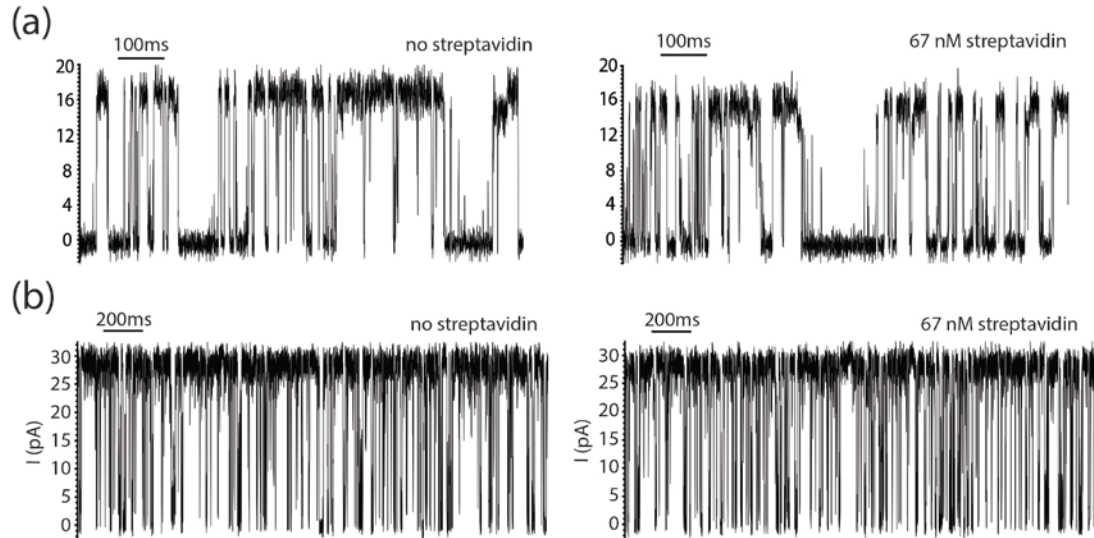


**Figure 1.6. Effect of streptavidin binding on the bending events.** Histogram of the duration time ( $\tau_{off}$ ) of the gating events before and after streptavidin binding to OmpG-Peg11-biotin. Data were fitted with single exponential function yielding an average  $\tau_{off}$  of 5.0 ms before and 3.9 ms after streptavidin binding.

We hypothesize that the bending events are shortened by bound streptavidin by destabilizing the closed state. However, due to the increased gating frequency, the open probability of the OmpG pore actually reduced slightly from  $0.58 \pm 0.09$  to  $0.51 \pm 0.10$  ( $n=3$ ) upon streptavidin binding as revealed by the decrease of the open state peak (Figure 1.4c). As controls, streptavidin has also been added to the unmodified OmpG-D224C pores (15 pores tested), we have not observed any change in the gating pattern (Figure



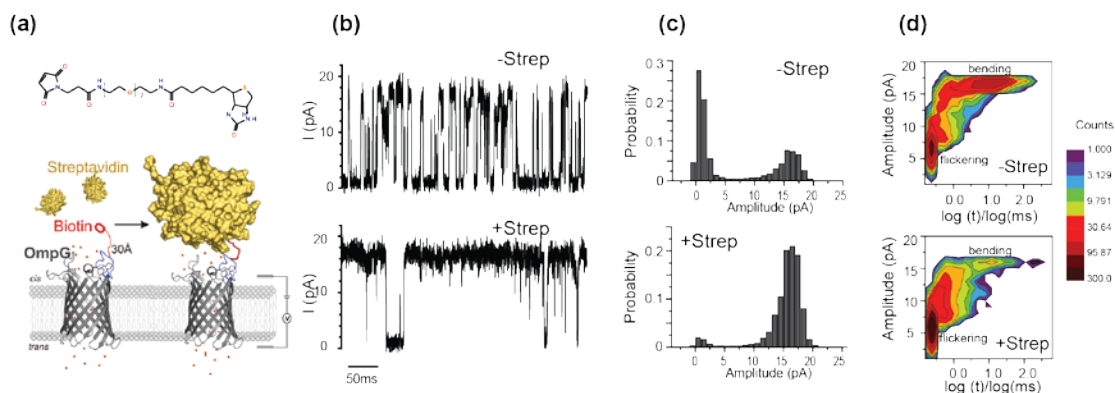
1.7). Thus, specific binding of streptavidin to the tethered biotin induces a clear but slight change in the gating properties of OmpG-PEG<sub>11</sub>-biotin pore.



**Figure 1.7. Gating behavior due to streptavidin binding is specific.** The addition of streptavidin to OmpG D224C does not change the behavior of the pore at either (a) 10 mM sodium phosphate buffer, pH 5.7, 150 mM KCl or (b) 10 mM sodium phosphate buffer, pH 6.0, 300 mM KCl.

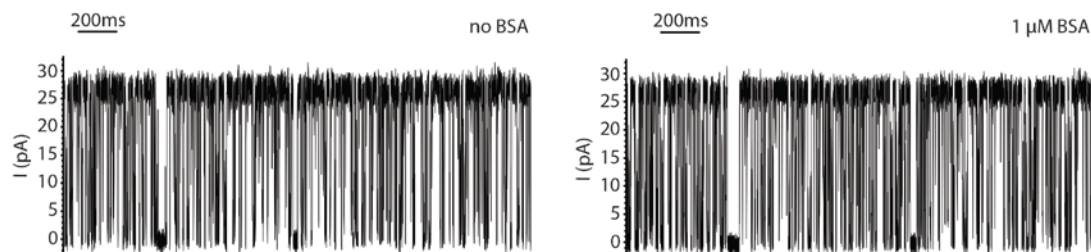
#### 1.4.2 Shortening the ligand linker to strengthen signal

Since the binding between the OmpG-PEG<sub>11</sub>-biotin and streptavidin produced a relatively small effect on the gating, we hypothesized that the polyethylene linker was too long to effectively restrict the dynamic movement of loop 6. Therefore, we shortened the length of the PEG linker to just two units, creating the OmpG-PEG<sub>2</sub>-biotin construct where the biotin could extend ~30 Å into solution (Figure 1.8a). The shortened linker did not affect the gating pattern when compared to OmpG D224C or OmpGwt (Figure 1.3). By shortening the linker, the effect of streptavidin binding was much more pronounced, permanently reducing the frequency and amplitude of gating events (Figures 1.8b,1.8c).



**Figure 1.8. Detection of streptavidin by OmpG-PEG<sub>2</sub>-biotin pore.** (a) Schematic model showing the OmpG nanopore chemically modified with a maleimide-PEG<sub>2</sub>-biotin. The streptavidin is placed around 30Å away from the OmpG pore in the model of the bound state. (b) Representative single channel recording traces of the OmpG pores before and after the addition of the streptavidin (3 nM). The measurements were performed in buffer 10 mM sodium phosphate, pH 5.7, 150 mM KCl at +50 mV. (c) All current histogram of the corresponding traces in (b). (d) Two dimensional histogram of the gating events. Total number of 4000 gating events collected from ~220 s and ~40s recording traces of OmpG pore with and without streptavidin bound were distributed based on their intensity versus duration. The color scale indicates the number of the events.

Quantitative analysis of three OmpG-PEG<sub>2</sub>-biotin pores showed that the gating event frequency was reduced by more than 6 fold from  $104 \pm 6 \text{ s}^{-1}$  to  $16 \pm 2 \text{ s}^{-1}$  ( $n=3$ ). Comparison of the two-dimensional plots of all events reveals that the occurrence of bending events with long duration time ( $>0.1\text{ms}$ ) and high intensity ( $>10 \text{ pA}$ ) were mostly eliminated due to streptavidin binding (Figure 1.8d). Gating events of transient duration time ( $<0.1 \mu\text{s}$ ) and low intensity ( $<10 \text{ pA}$ ) still persist albeit with greatly reduced frequency. The data indicate that streptavidin bound to the PEG<sub>2</sub> linker can strongly restrict bending but not the flickering of loop 6. As a control, streptavidin was added to OmpG D224C pores and no change was observed (10 pores tested). Adding excess BSA ( $1\mu\text{M}$ ) to the OmpG-PEG<sub>2</sub>-biotin pore also did not show any effect (Figure 1.9). These observations confirmed that the alteration of the gating pattern is caused by the specific interaction between the streptavidin and the tethered biotin ligand. In summary, binding of streptavidin to the OmpG-PEG<sub>2</sub>-biotin nanopore can be detected via reduction in gating behavior.

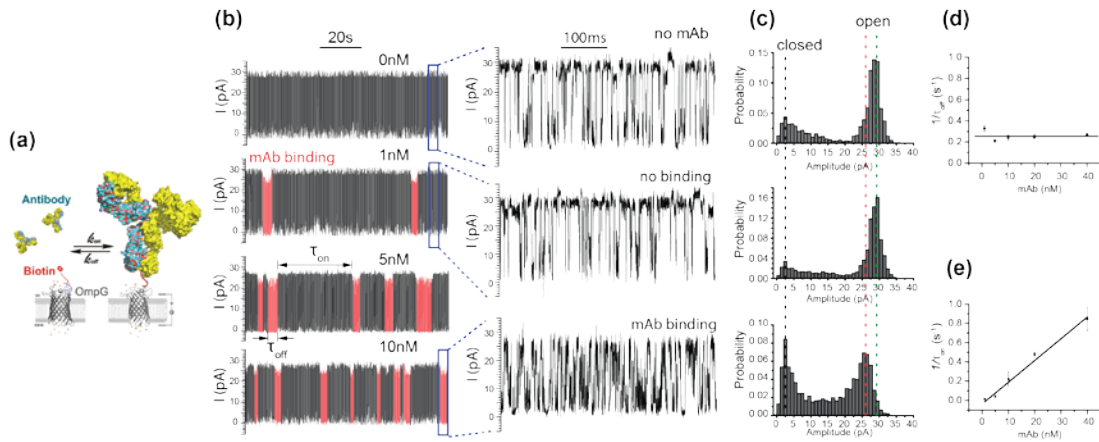


**Figure 1.9. BSA does not elicit change in OmpG behavior.** The addition of BSA to OmpG-Peg2-biotin does not change its gating pattern. This condition was performed in 10 mM sodium phosphate buffer, pH 6.0, 300 mM KCl.

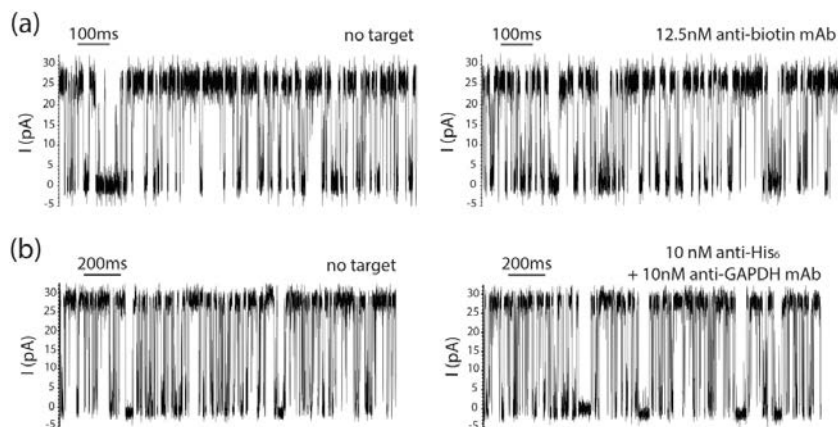
### 1.4.3 Detection of reversible antibody binding

The biotin-streptavidin interaction is effectively irreversible, thus only one binding event can be detected with the nanopore sensor during a 4 hr recording and unfortunately we cannot extract kinetic information from the streptavidin analyte. Here, we introduced proteins with weaker dissociation constants to take a closer look at reversible interactions. Mouse monoclonal anti-biotin antibodies (mAb) were added to a recording chamber with a single OmpG-PEG<sub>2</sub>-biotin (Figure 1.10a). The electrical trace showed that the presence of the anti-biotin antibody induced a dose-dependent gating pattern that was distinct from the unbound state and surprisingly also distinct from the streptavidin bound state (Figure 1.10b). During antibody binding, the pore shifted to more closed conformation as revealed by the larger closed state peak in the all-current histograms (Figures 1.10b, 1.10c). Indeed the calculated open probability was reduced from  $0.73 \pm 0.04$  at the no binding or unbound state to  $0.52 \pm 0.04$  at the bound state ( $n=6$ ). In addition, although the current fluctuates between open and closed states during both the antibody-free and antibody-bound states, the current of the pore in the fully open conformation was slightly reduced by  $3.5 \pm 0.86$  pA or  $13.6 \pm 3.8\%$  ( $n=6$ ) during the antibody bound state compared to the unbound state (Figure 1.10c). This dampening effect on the open conductance was not observed during the experiments using

streptavidin and might suggest that the antibody is in closer proximity to the pore opening when bound and therefore occluding ion flow through the OmpG-PEG<sub>2</sub>-biotin nanopore. As a control, addition of mAb to OmpGwt and unmodified OmpG D224C pores did not induce any detectable binding signal (Figure 1.11a). Neither were mouse anti-histag nor anti-Glyceraldehyde 3-phosphate dehydrogenase (anti-GAPDH) monoclonal antibodies (20 nM) detected by current recording with OmpG-PEG<sub>2</sub>-biotin pores (Figure 1.11b). Thus, these gating events resulted from the specific mAb binding to the tethered biotin.

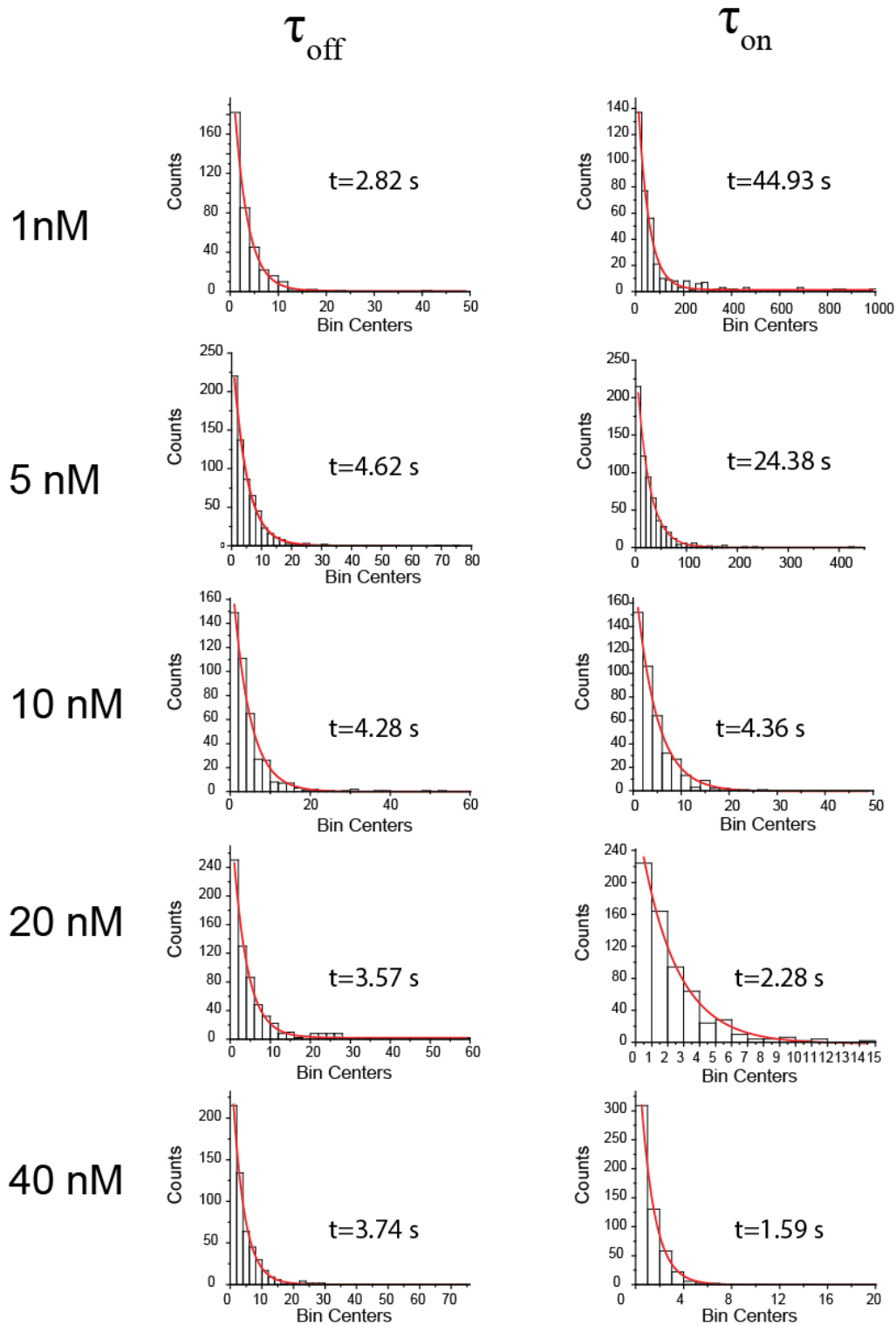


**Figure 1.10. Detection of monoclonal anti-biotin antibody by OmpG-PEG<sub>2</sub>-biotin pore.** (a) Schematic model showing the reversible binding of monoclonal anti-biotin antibody to OmpG-PEG<sub>2</sub>-Biotin pore. The model is generated in Pymol using pdb files of OmpG (2IWV) and a mouse monoclonal anti-phenobarbital antibody (1IGY). The antibody was placed approximately 30Å away from the OmpG pore in the captured model. (b) Representative single channel recording traces at various mAb concentrations. The mAb binding regions in the recording traces are highlighted in red. Increase of the mAb binding frequency was observed with increasing concentration of mAb. The measurements were performed in buffer 10 mM sodium phosphate, pH 6.0, 300 M KCl at +50 mV. (c) All current histogram of the corresponding traces in (b). The green and red dashed lines emphasize the shift of the fully open states in current at unoccupied and mAb bound states respectively. (d) (e) Concentration dependence of the  $1/T_{off}$  and  $1/T_{on}$ . Error bars represent the standard deviations from the measurements of at least three independent pores.



**Figure 1.11. Monoclonal anti-biotin antibody (mAb) binding is specific.** (a) Representative trace of OmpG D224C pore in the absence and presence of mAb. (b) Representative trace of OmpG-Peg2-biotin in the absence and presence of control antibodies anti-GAPDH and anti-His<sub>6</sub>. 10 mM sodium phosphate buffer, pH 6.0, 300 mM KCl was used in both experiments. The applied potential was +50 mV. Neither the addition of mAb to (a) OmpG D224C nor the addition of anti-His, anti-GAPDH mouse mAb to (b) OmpG-Peg2-biotin

Next, the dwell time ( $\tau_{off}$ ) and inter-event intervals ( $\tau_{on}$ ) of mAb binding was calculated (Figure 1.12). The average dissociation rate constant ( $k_{off}=1/\tau_{off}$ ) of the mAb binding events was  $0.25\pm 0.04\text{ s}^{-1}$  ( $n=4$ ) which was independent of the antibody concentration (Figure 1.10d). The observed association constant ( $k_{on}'=1/\tau_{on}$ ) increased linearly with the increasing concentration of antibody (Figure 1.10e). The association rate constant  $k_{on}$  of antibody binding was  $2.30\pm 0.43\times 10^7\text{M}^{-1}\cdot\text{s}^{-1}$  ( $n=4$ ). The equilibrium dissociation constant ( $K_d$ ) of the mouse monoclonal antibody to biotin was  $1.12\pm 0.28\times 10^{-8}\text{M}^{-1}$  ( $n=4$ ). At the lowest mAb concentration tested (1 nM), the mean inter-event interval was  $74.5 \pm 31\text{ s}$  meaning the OmpG-PEG<sub>2</sub>-biotin sensor can detect 1nM anti-biotin mAb within tens of min.

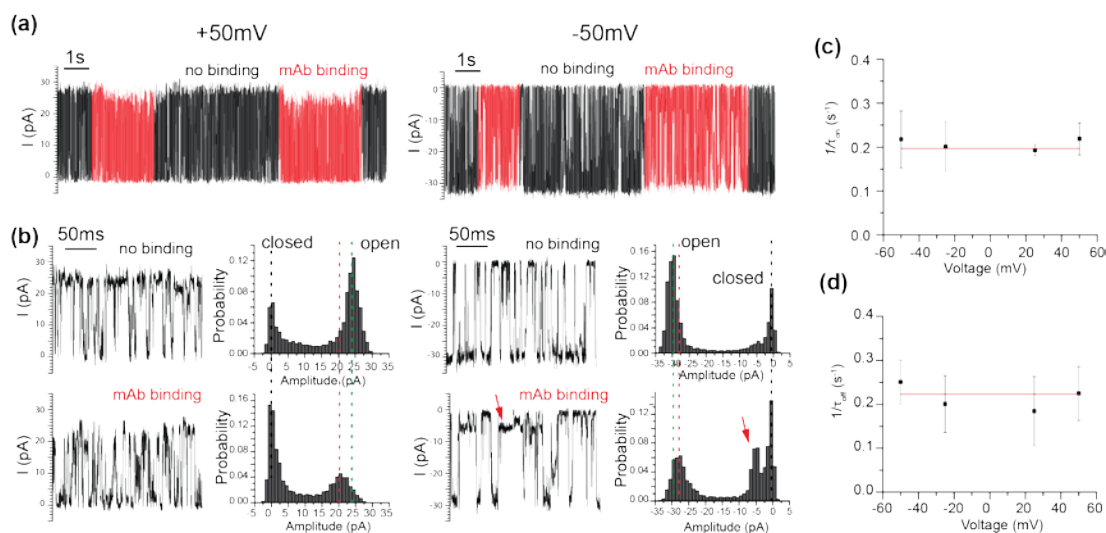


**Figure 1.12. Analysis of kinetic parameters of mAb binding to OmpG-PEG<sub>2</sub>-biotin.** Histograms of the dwell time and the inter-event duration of these events were fitted with single exponential decay function to derive the average time constants.

#### 1.4.4 Influence of voltage on the mAb binding

OmpG exhibits asymmetrical gating pattern at positive and negative voltages, where at one voltage it generates a “quiet” gating pattern while at the opposite voltage it generates a “noisy” pattern.<sup>50</sup> Therefore, we were interested to see if the polarity of the voltage could similarly affect the dynamic motion of loop 6 during the mAb bound state. Figure 1.13a shows that mAb binds to OmpG-PEG<sub>2</sub>-biotin at both +50 mV and -50 mV. The open probability of the mAb bound state at +50 mV and -50 mV is  $0.52 \pm 0.04$  (n=6) and  $0.40 \pm 0.09$  (n=6) respectively, in comparison to  $0.73 \pm 0.04$  (n=6) and  $0.71 \pm 0.01$  (n=3) of the non-binding or unbound state. Thus in the mAb bound state, the pore switched to a more closed state at both negative and positive potentials (Figure 1.13). In addition, the decrease in OmpG open probability was more significant in the mAb bound state when a negative voltage was applied *i.e.* a 30% open probability decrease at negative voltage vs a 20% decrease in open probability at positive voltage.

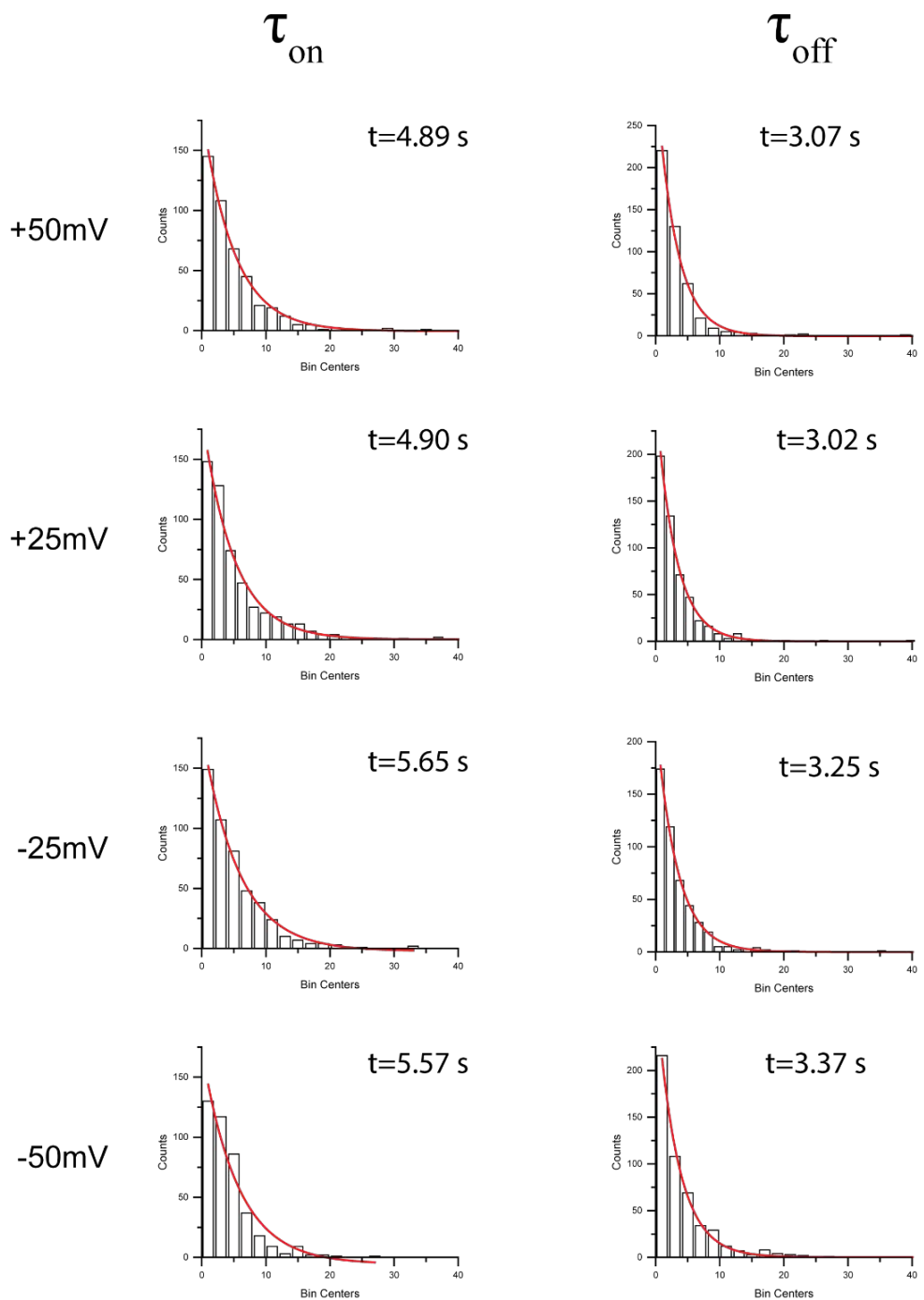
The OmpG-PEG<sub>2</sub>-biotin pore also showed a decreased current (amplitude) by  $1.2 \pm 0.4$  pA (n=3) at its fully open state at -50 mV. This decrease is ~5.4% of the initial current of a non binding state in comparison to the 13.6% decrease in current at the positive potential in the bound state. Moreover it had a partial closure state with 6 pA of residual current as indicated by the red arrow in the recording trace and all current histograms (Figure 1.13b). This result shows that the loop gating during the mAb bound state is still significantly influenced by the polarity of the applied potential. This is a useful feature that can be used for sensing because the asymmetric response of OmpG to target protein binding adds one more parameter for specific analyte protein recognition.



**Figure 1.13. Effect of voltage on the mAb binding.** (a) Representative single channel recording trace of OmpG-PEG<sub>2</sub>-biotin showing reversible binding of mAb at both +50 mV and -50 mV. We define the positive potential as the potential of the chamber where the loops are located is positive. The measurement was performed in buffer, 10 mM sodium phosphate, pH 6.0, 300 mM KCl in the presence of 10 nM mAb. (b) Representative single channel recording traces of OmpG-PEG<sub>2</sub>-biotin at the unoccupied or mAb bound states at +50 mV and -50 mV. All current histogram of the corresponding current recording traces are also shown. The green and red dashed lines emphasize the shift of the fully open states in current at unoccupied and mAb bound states respectively. The positive potential caused a larger shift of the open state current than the negative potential. (c) (d) Voltage independence of  $1/T_{on}$  and  $1/T_{off}$ . The measurements were performed in buffers 10 mM sodium phosphate buffer, pH 6.0, 300 mM KCl in the presence of 10 nM mAb at various applied voltages ranging from -50 mV to +50 mV.

Previous studies on nanopore detection have shown that voltage could alter analyte binding kinetics.<sup>28,43,58</sup> Therefore, single channel recording was performed at applied voltages ranging from -50 mV to +50 mV in the presence of mouse mAbs. The voltage-dependent gating of OmpG prevented us from testing higher potentials as OmpG tends to close completely at  $\pm 75$  mV.<sup>46</sup> Neither  $T_{on}$  nor  $T_{off}$  exhibited a strong dependence on voltages (Figures 1.13c, 1.13d, 1.14). Thus, we concluded that the mAb binding to biotin is not affected at applied potentials ranging from -50mV to +50 mV. The independence of binding from voltage at this range is advantageous since proteins can be analyzed regardless of the applied potential.

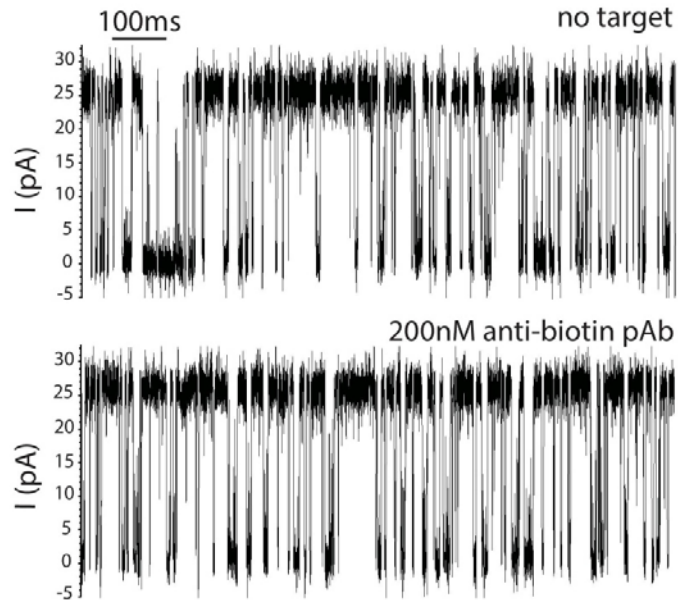




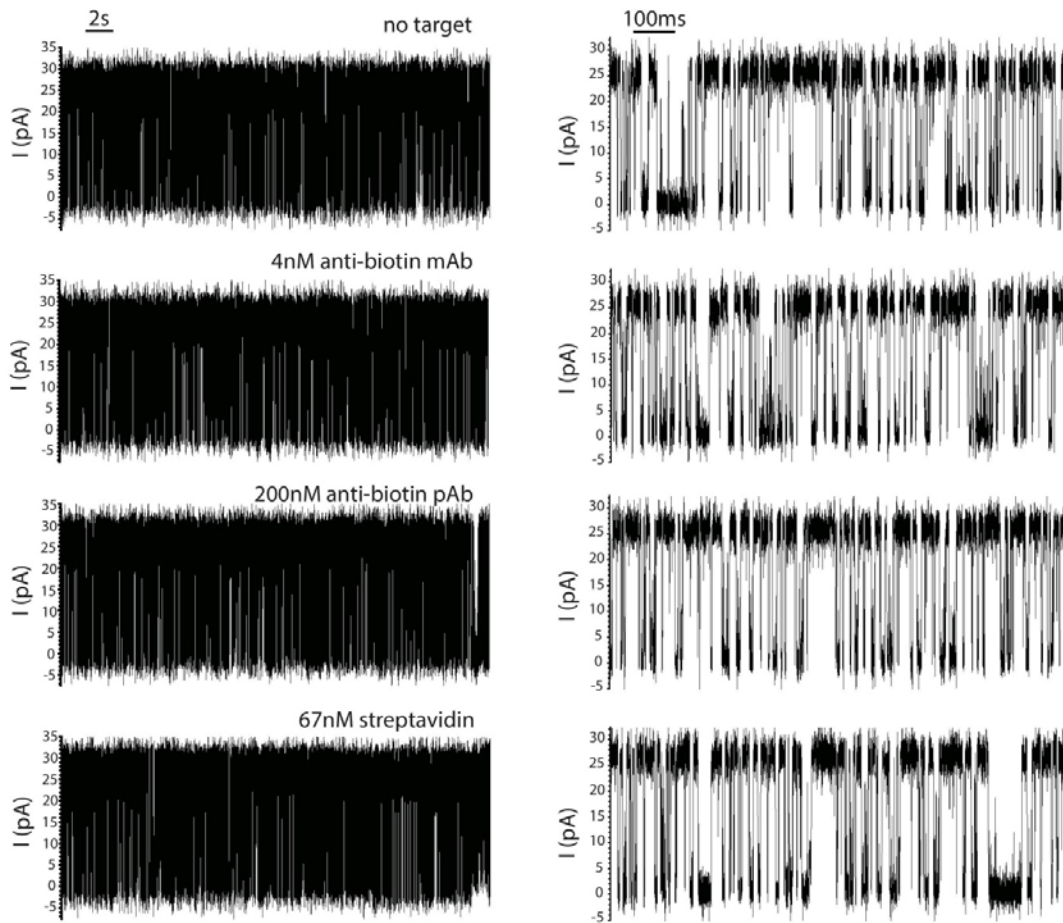
**Figure 1.14. Analysis of kinetic parameters of mAb binding to OmpG-Peg2-biotin at various applied voltages.** Histograms of the inter-event duration ( $\tau_{on}$ ) and dwell time ( $\tau_{off}$ ) of mAb binding events were fitted with single exponential decay function to derive the average time constants.

#### 1.4.5 Simultaneous detection of mouse mAb and goat polyclonal anti-biotin antibodies

Although the antibody and streptavidin both bound the biotinylated OmpG, they produced remarkably unique gating patterns. We wondered how sensitive the OmpG sensor would be to various factors such as a protein's size, shape, surface charge or rigidity. In an attempt to distinguish between these, we analyzed the binding of a polyclonal anti-biotin antibody derived from goat. The polyclonal antibody alone did not induce a change in ionic current of the unmodified OmpG D224C pore (Figure 1.15), also no change in gating patterns were seen when antibodies and streptavidin were added sequentially to unmodified OmpG D224C (Figure 1.16).



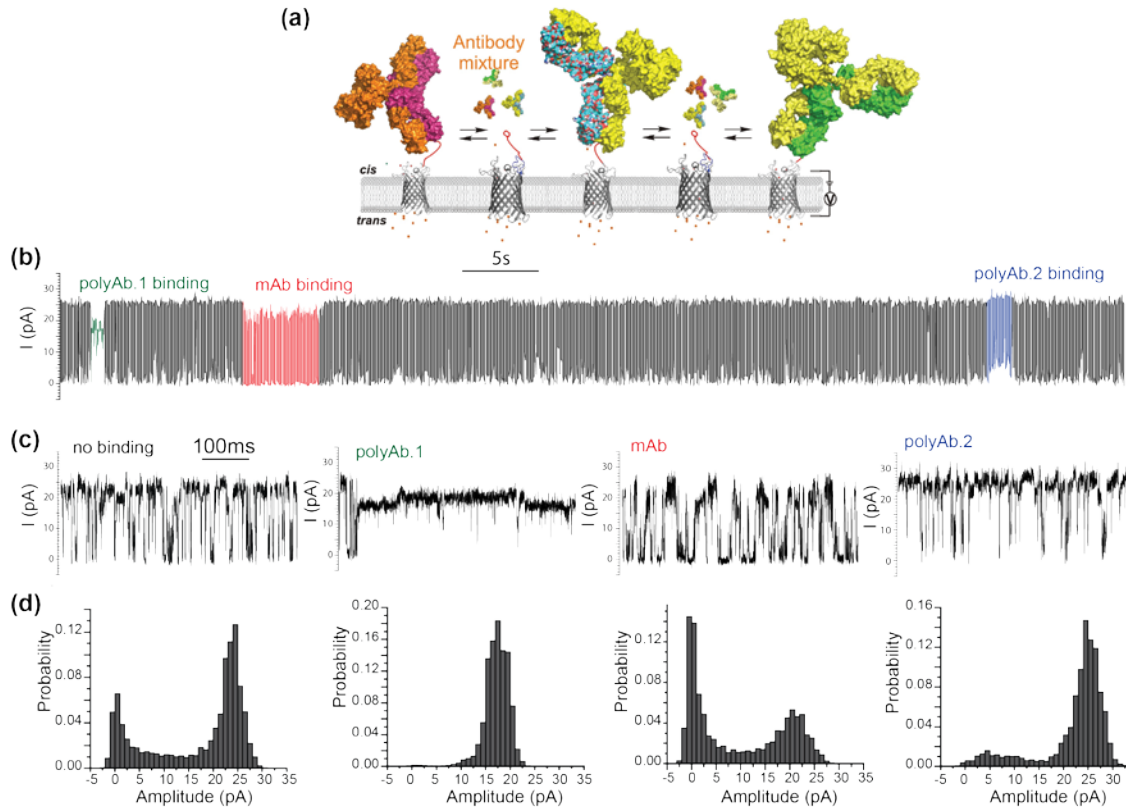
**Figure 1.15. Representative traces of single channel recording of OmpG D224C in the presence of polyclonal anti-biotin antibody (pAb).** OmpG D224C pores were recorded for 2 hours after the addition of 200 nM pAb at +50 and -50 mV. Buffer 10 mM sodium phosphate buffer, pH 6.0, 300 mM KCl was used. No detectable change in the gating pattern of the pore was observed.



**Figure 1.16. A complex mixture of biotin binding proteins elicits no effect on the gating of OmpGwt.** The gating behavior of OmpGwt was recorded after each biotin binding protein was subsequently added to the chamber in which loop 6 was located. As shown in the figure, the gating behavior of OmpGwt never changes even after adding several biotin binding proteins into the same chamber. The behavior was recorded for 1 hour. 10 mM sodium phosphate buffer, pH 6.0, 300 mM KCl was used.

However to our surprise, the polyclonal antibody produced gating patterns distinct from the structurally very similar mAb tested earlier (Figures 1.17a, 1.17b). Furthermore, the polyclonal sample showed clear evidence that at least two readily distinguished populations of antibody were present (Figures 1.17b, 1.17c). We categorized their gating activities into two classes, called type I and type II. During type I binding (pAb.1) the current decreased by 50% and contained few gating events. During type II (pAb.2) binding events, the open state conductance was unchanged but the

gating frequency was slightly reduced (Figures 1.17c, 1.17d). Mouse mAb was then added to the chamber already containing pAb and the binding was observed (Figure 1.17b). All types of antibodies bound with their respective characteristics regardless of the presence of the other antibodies. This is the first example of a nanopore than can distinguish between three antibodies with virtually identical shape in a complex mixture.

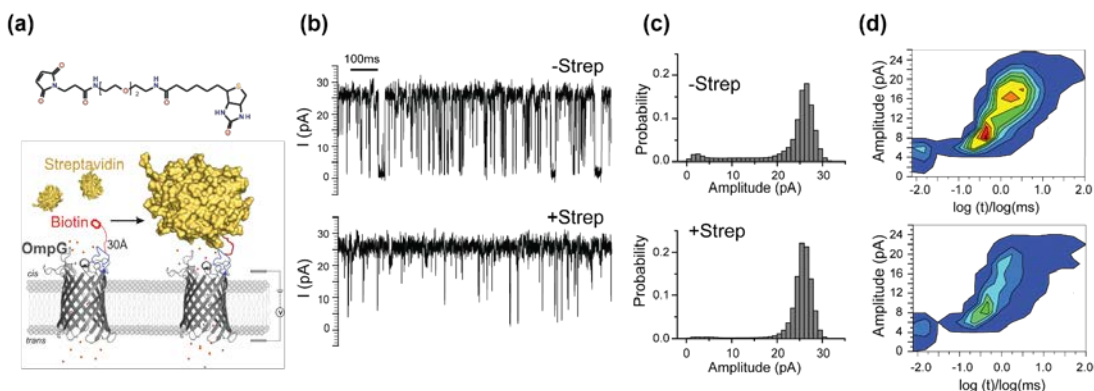


**Figure 1.17. Detection of mouse mAb and polyclonal Ab binding by OmpG-PEG<sub>2</sub>-biotin pore.** (a) Schematic model of simultaneous detection of multiple target proteins by OmpG nanopore. (b) Representative current trace of a single OmpG-biotin. The measurement was performed in the presence of mouse mAb (1 nM) and goat pAb (72 nM) in 10 mM sodium phosphate, pH 6.0, 300 mM KCl at applied potential of +50 mV. The mAb and polyAb binding events were highlighted in colors, i.e. mAb in red, pAb. 1 in green and pAb.2 in blue. (c) Representative current recording trace of OmpG-PEG<sub>2</sub>-biotin pore at the unoccupied and mAb and polyAb bound states. (d) All current histogram of the corresponding current recording traces.

#### 1.4.6 Power spectrum analysis and fingerprint of analyte protein binding signal

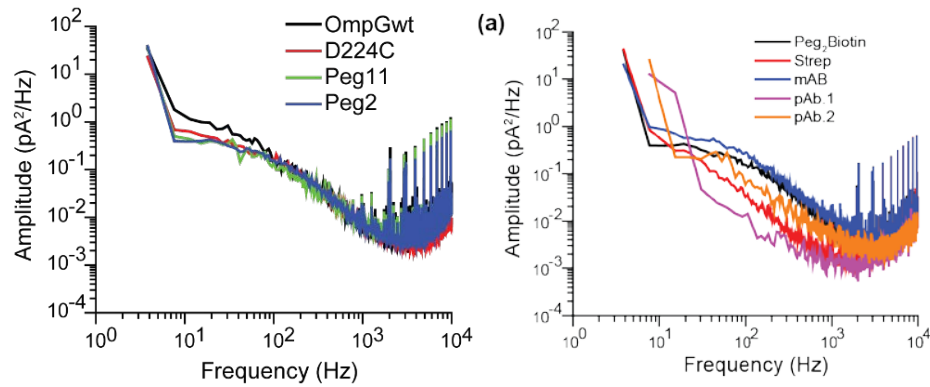
Nanopore sensing often relies on blockade amplitude and/or the mean duration time of binding to discriminating target molecules. For the OmpG nanopore, the binding

of analyte not necessarily induced a current blockage. Instead, alteration of the gating/noise of OmpG was indicative of the interaction. To compare the streptavidin binding with other biotin-binding proteins under the same condition, streptavidin experiments were re-performed in 10 mM sodium phosphate, pH 6.0, 300 mM KCl (Figure 1.18). Electrical traces under this condition were used to derive the power spectra and the fingerprint characteristics.

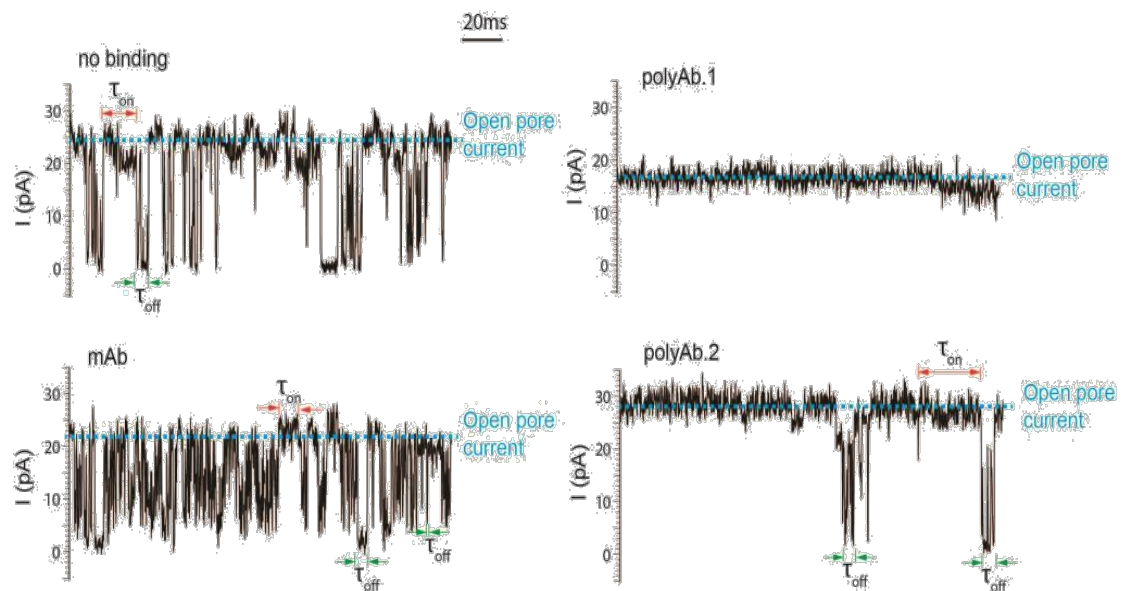


**Figure 1.18. Detection of streptavidin by OmpG-PEG2-biotin pore.** (a) Schematic model showing the OmpG-PEG2-biotin. (b) Representative single channel recording traces of the OmpG pores before and after the addition of the streptavidin (3 nM). The measurements were performed in buffer 10 mM sodium phosphate buffer, pH 6.0, 300 mM KCl at +50 mV. (c) All current histogram of the corresponding traces in (b). (d) 2D histogram of the gating events of the bound and unbound state.

Noise spectral density analysis of all OmpG constructs alone were obtained and showed very small changes in noise (Figure 1.19a). Noise spectral density analysis of each biotin-binding protein in the bound state revealed that mAb showed a higher noise than the unbound state. pAb.1 exhibited the lowest noise while the level of streptavidin and pAb.2 was between that of pAb.1 and the unbound state (Figure 1.19b).



**Figure 1.19. Comparison of the gating patterns of OmpG-PEG<sub>2</sub>-biotin at analyte binding states.** (a) Power spectra of the OmpG constructs. (b) Power spectra of protein-binding states for four biotin-binding proteins with OmpG-PEG<sub>2</sub>-biotin. Electrical recording traces were obtained in 10 mM sodium phosphate buffer, pH 6.0, 300 mM KCl at +50 mV.



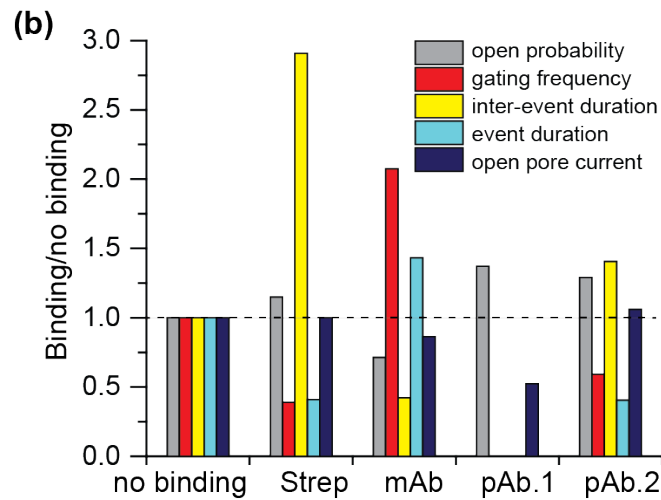
**Figure 1.20. Gating events fingerprint analysis.** The current recording traces were analyzed by Clampfit 10.3 using single channel search to identify gating events which were defined as current blockages larger than 2pA (4% of fully open pore current). The open probability was calculated as the time the pore stays in the open state divided by the recording time. The gating frequency was calculated as the number gating events divided by the recording time. The average inter-event duration ( $\tau_{on}$ ) and event duration ( $\tau_{off}$ ) were obtained by fitting the histogram of these duration values with single exponential function the same as in Figure 1.6 and 1.12. The open pore current is indicated with a blue dashed line.

However, spectral noise analysis alone is insufficient for analyte identification. For example, the mAb-bound state was similar to the unbound state and the open pore current cannot be seen by noise analysis. To thoroughly analyze the characteristics of the traces at the analyte binding state, we analyze five parameters: (i) open probability, (ii) gating events frequency, (iii) inter gating event duration, (iv) duration of gating events and (v) the open state conductance to identify the protein by a specific fingerprint characteristic (Figure 1.20). We quantified the gating characteristics for each biotin-binding protein and summarized the results into Table 1. We then generated a fingerprint graph for each analyte based on the results in Table 1 (Figure 1.21) and found that the OmpG-biotin sensor can unambiguously detect and discriminate between the four biotin-binding proteins that we tested, including three antibody species (two pAb and one mAb) that share highly homologous structures.

**Table 1.1.** Fingerprint of each type of gating events using the OmpG-PEG<sub>2</sub>-biotin pore

	Open probability	Event frequency (s <sup>-1</sup> )	Inter-event duration (ms)	Gating duration (ms)	Relative conductance of open state (%)
No binding	0.73±0.04*	97±3.6	8.68±2.14	2.93±0.52	100
Streptavidin	0.95±0.08	45±7	22.75±3.2	0.62±0.19	100±4.2
mAb	0.52±0.04	201±103	3.67±1.57	4.20±1.90	86.4±1.3
pAb.1	0.99±0.01	7±1	n/a	n/a	52.3±4.7
pAb.2	0.94±0.02	57.5±2	12.2±1.3	1.09±0.21	106.5±6.5

\*Values were calculated from at least three independent experiments. The errors indicate the standard deviation.



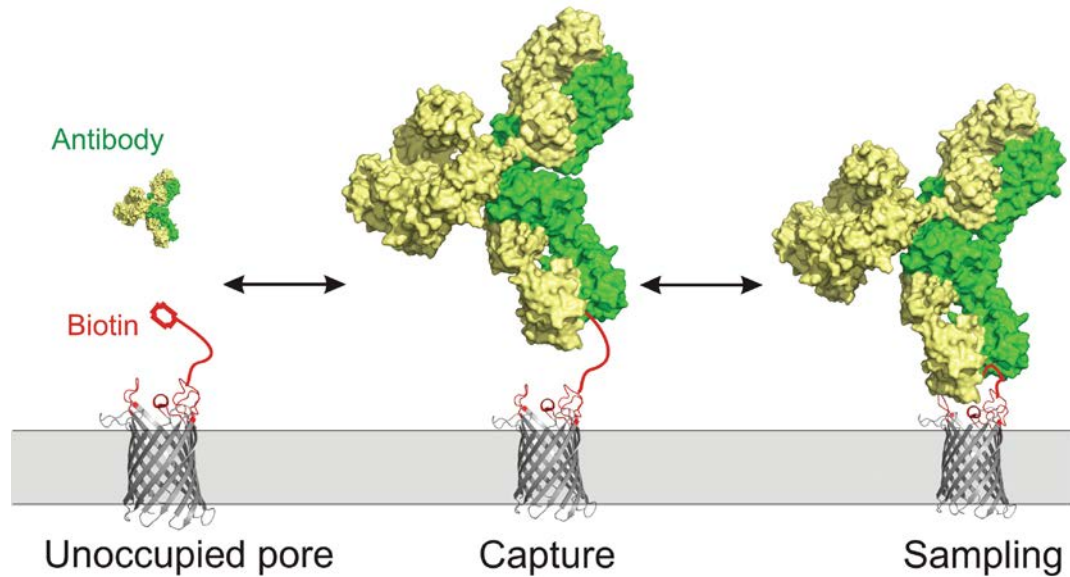
**Figure 1.21. Fingerprints of the four biotin binding proteins.** The gating events of different analyte protein binding states were characterized by five parameters, i.e. open probability, gating frequency, inter-event duration, event duration and the conductance of the open pore state. Changes of these parameters relative to the no binding state generate the fingerprint unique for each protein.

## 1.5 Discussion

Since proteins of the same size and shape produce unique signals, we hypothesize that the OmpG sensor recognizes unique targets based on other factors such as charge, hydrophobicity or perhaps post-translational modification of the surface. The structure of OmpG, along with the data presented here, sheds some light on the possible mechanism of protein detection via the nanopore strategy. Although the four biotin-binding proteins trigger a characteristic gating pattern upon binding to the OmpG nanopore, they can be categorized into two groups. In pAb.2 and streptavidin cause a decreased gating frequency, which suggests binding to the PEG<sub>2</sub> tethered biotin hindered the dynamics of the loop 6. According to the crystal structure, the D224 residue traverses approximately 7.5 Å between the open and closed states.<sup>47</sup> However, a recent NMR study of OmpG shows this residue may migrate as far as 30 Å between the fully open and closed conformers.<sup>49,59</sup> Our results suggest that such a large conformational change is strongly hindered by streptavidin binding and moderately by pAb.2 binding.



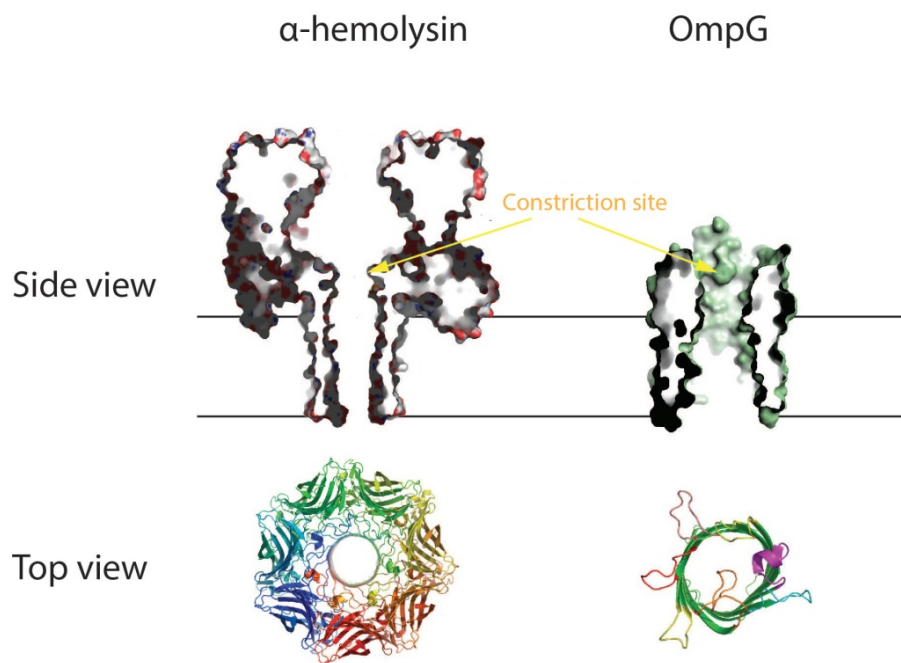
The results also suggest minimal interaction between the streptavidin and pAb.2 with the loops at the opening of OmpG. In another category, mAb and pAb.1 both caused a decrease of current in the fully open state. This observation suggests that the two antibodies obstruct the current flow at the entrance, presumably by partially docking to the extracellular loops of OmpG. Because all seven loops at OmpG's entrance are net negatively charged, the two antibodies are likely positively charged or have a positively charged patch near the biotin-binding site that mediate this interaction. This speculation is supported by the observation of mAb's asymmetrical behavior under an applied potential. Namely, a positive potential might push the mAb closer towards the OmpG pore to cause 13.6% partial block of the current (Figure 1.13). In contrast, at negative potential, the electric field would repel mAb away from the pore entrance. Indeed, we observed that the open pore conductance was less affected, only ~5.4% blockage seen. These results suggest that not only the ligand-tethered loop, but all the loops on the extracellular entrance may be involved in sampling the target proteins, which explains its ability to discriminate between highly structurally homologous proteins. Our data suggests a novel mechanism underlying OmpG nanopore sensing that contains two steps (Figure 1.22). First, OmpG captures the target protein via its tethered high-affinity ligand. Consequently, the bound protein interferes with the movement of loop 6 generating its characteristic gating pattern. Second, the extracellular loops of OmpG may sample the target protein via unspecific interactions which further alters the ionic current providing additional readout. While further study is required to delve deeper into the precise mechanism of protein detection, our sensor's ability to discriminate between structurally homologous antibodies within a multi-component mixture represents a powerful advance over previous approaches.



**Figure 1.22. Schematic model illustrating the interactions between OmpG nanopore and analyte protein.** The proposed principle of OmpG nanopore sampling and detection of a protein analyte via interactions with the OmpG loops.

Previously, the detection of streptavidin and anti-biotin antibody was demonstrated using  $\alpha$ HL that contained a PEG biotin group tethered to its vestibule.<sup>30</sup> In the absence of the target, the PEG polymer traversed through the constriction site from the *cis* and *trans* chamber and back through the pore. This movement was manifest as rapid gating. Analyte protein binding of the biotin group eliminated the gating and provided the readout signal for protein sensing. In contrast to our OmpG nanopore,  $\alpha$ HL-biotin sensor did not differentiate binding events derived from streptavidin and mAb which differ greatly in size, shape and surface properties. Two features of OmpG may contribute to its higher resolution compared to  $\alpha$ HL (Figure 1.23). The first is the location of the constriction site which is the narrowest part of the pore that determines the conductance. The constriction site of OmpG-PEG<sub>2</sub>-biotin is located at the entrance to the pore next to the ligand interaction site while the location of the constriction site of  $\alpha$ HL is

in the middle making it inaccessible for large folded analyte protein. Because of this, analyte protein binding at the pore entrance directly affected the conductance of OmpG but not  $\alpha$ HL. Secondly OmpG has flexible loops at the binding site which allows conformational changes to occur in response to analyte protein binding. Instead,  $\alpha$ HL possesses a rather stable and rigid structure at the two ends.<sup>60</sup> Although the biotin-binding proteins might also interact with the two entrances of  $\alpha$ HL nanopore, the rigidity of the  $\alpha$ HL structure does not allow large conformational changes to occur, so the interaction of different target proteins with the entrance did not induce noticeable changes in the current flow that passed through the constriction site.



**Figure 1.23. Structures of  $\alpha$ HL and OmpG.** The side view shows a cross-section of both proteins to reveal the constriction site. For  $\alpha$ HL, the constriction site is located in the middle of the pore. In contrast, the narrowest site of the pore is located at the top entrance of OmpG. The top view structures show that  $\alpha$ HL has  $\beta$ -strands packing into a highly ordered structure at its entrance while OmpG contains seven flexible loops.

Our study points out an alternative design in the architecture of nanopore sensors. By creating a nanopore with a dynamic structure that changes upon analyte binding, new regions of data may be interpreted that give a greater sensitivity and

selectivity for detecting protein analytes. We have shown that even protein isoforms in a mixture can be clearly distinguished using this new sensing scheme. These features are not available in other nanopore sensing strategies, making the OmpG sensor particularly useful. Further, monomeric proteins such as OmpG are ready to use after refolding and require no further assembly and purification steps compared to other oligomeric nanopores.

## **1.6 Conclusion**

We have shown that binding of target protein to an OmpG-biotin nanopore can be deduced from changes in the gating activity of OmpG. The principle of the OmpG nanopore relies on detecting the modulation of loop dynamics upon target protein binding rather than the occupation in the pore lumen. More importantly, the OmpG nanopore exhibited the ability to resolve protein homologues that share the same high-affinity ligand, making this sensing approach well suitable for screening for homologous disease markers in complex mixtures. In the future, this principle may be extended to a broader spectrum of analytes, such as proteins, viruses, or bacteria without the need to use a far larger nanopore.

## 1.7 References

1. Howorka, S. & Siwy, Z. Nanopore analytics: sensing of single molecules. *Chem. Soc. Rev.* **38**, 2360–2384 (2009).
2. Majd, S. *et al.* Applications of biological pores in nanomedicine, sensing, and nanoelectronics. *Curr. Opin. Biotechnol.* **21**, 439–476 (2010).
3. Stefureac, R. I. & Lee, J. S. Nanopore analysis of the folding of zinc fingers. *Small* **4**, 1646–1650 (2008).
4. Merstorf, C. *et al.* Wild type, mutant protein unfolding and phase transition detected by single-nanopore recording. *ACS Chem. Biol.* **7**, 652–658 (2012).
5. Nivala, J., Marks, D. B. & Akeson, M. Unfoldase-mediated protein translocation through an  $\alpha$ -hemolysin nanopore. *Nat. Biotechnol.* **31**, 247–50 (2013).
6. Oukhaled, G. *et al.* Unfolding of proteins and long transient conformations detected by single nanopore recording. *Phys. Rev. Lett.* **98**, 158101 (2007).
7. Payet, L. *et al.* Thermal Unfolding of Proteins Probed at the Single Molecule Level Using Nanopores. *Anal. Chem.* **84**, 4071–4076 (2012).
8. Rodriguez-Larrea, D. & Bayley, H. Multistep protein unfolding during nanopore translocation. *Nat. Nanotechnol.* **8**, 288–295 (2013).
9. Majd, S., Yusko, E. C., MacBriar, A. D., Yang, J. & Mayer, M. Gramicidin pores report the activity of membrane-active enzymes. *J. Am. Chem. Soc.* **131**, 16119–16126 (2009).
10. Zhao, Q., De Zoysa, R. S. S., Wang, D., Jayawardhana, D. A. & Guan, X. Real-time monitoring of peptide cleavage using a nanopore probe. *J. Am. Chem. Soc.* **131**, 6324–6325 (2009).
11. Kasianowicz, J. J., Brandin, E., Branton, D. & Deamer, D. W. Characterization of individual polynucleotide molecules using a membrane channel. *Proc. Natl. Acad. Sci. U. S. A.* **93**, 13770–13773 (1996).
12. Luchian, T., Shin, S. H. & Bayley, H. Single-molecule covalent chemistry with spatially separated reactants. *Angew. Chemie - Int. Ed.* **42**, 3766–3771 (2003).
13. Shin, S., Luchian, T., Cheley, S., Braha, O. & Bayley, H. Kinetics of a Reversible Covalent-Bond-Forming Reaction Observed at the Single-Molecule Level \*\*. *Current* 3707–3709 (2002).
14. Arnaut, V., Langecker, M. & Simmel, F. C. Nanopore force spectroscopy of aptamer-ligand complexes. *Biophys. J.* **105**, 1199–1207 (2013).
15. Branton, D. *et al.* The potential and challenges of nanopore sequencing. *Nat. Biotechnol.* **26**, 1146–1153 (2008).
16. Wanunu, M. Nanopores: A journey towards DNA sequencing. *Phys. Life Rev.* **9**, 125–158 (2012).
17. Meller, a, Nivon, L., Brandin, E., Golovchenko, J. & Branton, D. Rapid nanopore discrimination between single polynucleotide molecules. *Proc. Natl. Acad. Sci. U. S. A.* **97**, 1079–1084 (2000).
18. Bayley, H. & Cremer, P. S. Stochastic sensors inspired by biology. *Nature* **413**, 226–230 (2001).
19. Braha, O. *et al.* Simultaneous stochastic sensing of divalent metal ions. *Nat. Biotechnol.* **18**, 1005–1007 (2000).
20. Braha, O. *et al.* Designed protein pores as components for biosensors. *Chem. Biol.* **4**, 497–505 (1997).
21. Cheley, S., Gu, L. Q. & Bayley, H. Stochastic sensing of nanomolar inositol 1,4,5-trisphosphate with an engineered pore. *Chem. Biol.* **9**, 829–838 (2002).
22. Wu, H. C. & Bayley, H. Single-molecule detection of nitrogen mustards by covalent reaction within a protein nanopore. *J. Am. Chem. Soc.* **130**, 6813–6819

- (2008).
23. Gu, L. Q., Braha, O., Conlan, S., Cheley, S. & Bayley, H. Stochastic sensing of organic analytes by a pore-forming protein containing a molecular adapter. *Nature* **398**, 686–690 (1999).
  24. Howorka, S., Cheley, S. & Bayley, H. Sequence-specific detection of individual DNA strands using engineered nanopores. *Nat. Biotechnol.* **19**, 636–639 (2001).
  25. Reiner, J. E., Kasianowicz, J. J., Nablo, B. J. & Robertson, J. W. F. Theory for polymer analysis using nanopore-based single-molecule mass spectrometry. *Proc. Natl Acad. Sci. USA* **107**, 12080–12085 (2010).
  26. Robertson, J. W. F. *et al.* Single-molecule mass spectrometry in solution using a solitary nanopore. *Proc. Natl. Acad. Sci. U. S. A.* **104**, 8207–8211 (2007).
  27. Rotem, D., Jayasinghe, L., Salichou, M. & Bayley, H. Protein detection by nanopores equipped with aptamers. *J. Am. Chem. Soc.* **134**, 2781–7 (2012).
  28. Xie, H., Braha, O., Gu, L. Q., Cheley, S. & Bayley, H. Single-molecule observation of the catalytic subunit of cAMP-dependent protein kinase binding to an inhibitor peptide. *Chem. Biol.* **12**, 109–120 (2005).
  29. Howorka, S., Nam, J., Bayley, H. & Kahne, D. Stochastic detection of monovalent and bivalent protein-ligand interactions. *Angew. Chemie - Int. Ed.* **43**, 842–846 (2004).
  30. Movileanu, L., Howorka, S., Braha, O. & Bayley, H. Detecting protein analytes that modulate transmembrane movement of a polymer chain within a single protein pore. *Nat. Biotechnol.* **18**, 1091–1095 (2000).
  31. Zhang, S., Udho, E., Wu, Z., Collier, R. J. & Finkelstein, A. Protein translocation through anthrax toxin channels formed in planar lipid bilayers. *Biophys. J.* **87**, 3842–3849 (2004).
  32. Halverson, K. M. *et al.* Anthrax biosensor, protective antigen ion channel asymmetric blockade. *J. Biol. Chem.* **280**, 34056–34062 (2005).
  33. Henrickson, S. E., Dimarzio, E. A., Wang, Q., Stanford, V. M. & Kasianowicz, J. J. Probing single nanometer-scale pores with polymeric molecular rulers. *J. Chem. Phys.* **132**, (2010).
  34. Henrickson, S. E., Misakian, M., Robertson, B. & Kasianowicz, J. J. Driven DNA transport into an asymmetric nanometer-scale pore. *Phys. Rev. Lett.* **85**, 3057–3060 (2000).
  35. Kasianowicz, J. J., Henrickson, S. E., Weetall, H. H. & Robertson, B. Simultaneous multianalyte detection with a nanometer-scale pore. *Anal. Chem.* **73**, 2268–2272 (2001).
  36. Soskine, M. *et al.* An engineered ClyA nanopore detects folded target proteins by selective external association and pore entry. *Nano Lett.* **12**, 4895–900 (2012).
  37. Rosado, C. J. *et al.* The MACPF/CDC family of pore-forming toxins. *Cell. Microbiol.* **10**, 1765–1774 (2008).
  38. Olofsson, A., Hebert, H. & Thelestam, M. The Projection Structure of Perfringolysin-O (Clostridium-Perfringens Omicron-Toxin). *FEBS Lett.* **319**, 125–127 (1993).
  39. Siwy, Z. *et al.* Protein biosensors based on biofunctionalized conical gold nanotubes. *J. Am. Chem. Soc.* **127**, 5000–5001 (2005).
  40. Han, A. *et al.* Sensing protein molecules using nanofabricated pores. *Appl. Phys. Lett.* **88**, 1–4 (2006).
  41. Li, W. *et al.* Single protein molecule detection by glass nanopores. *ACS Nano* **7**, 4129–4134 (2013).
  42. Fologea, D., Ledden, B., McNabb, D. S. & Li, J. Electrical characterization of protein molecules by a solid-state nanopore. *Appl. Phys. Lett.* **91**, 53901-1-

- 53901–3 (2007).
43. Wei, R., Gatterdam, V., Wieneke, R., Tampé, R. & Rant, U. Stochastic sensing of proteins with receptor-modified solid-state nanopores. *Nat. Nanotechnol.* **7**, 257–63 (2012).
  44. Ding, S., Gao, C. & Gu, L. Q. Capturing single molecules of immunoglobulin and ricin with an aptamer-encoded glass nanopore. *Anal. Chem.* **81**, 6649–6655 (2009).
  45. Yusko, E. C. *et al.* Controlling protein translocation through nanopores with bio-inspired fluid walls. *Nat. Nanotechnol.* **6**, 253–60 (2011).
  46. Conlan, S., Zhang, Y., Cheley, S. & Bayley, H. Biochemical and Biophysical Characterization of OmpG: A Monomeric Porin †. *Biochemistry* **39**, 11845–11854 (2000).
  47. Yildiz, O., Vinothkumar, K. R., Goswami, P. & Kühlbrandt, W. Structure of the monomeric outer-membrane porin OmpG in the open and closed conformation. *EMBO J.* **25**, 3702–13 (2006).
  48. Subbarao, G. V & van den Berg, B. Crystal structure of the monomeric porin OmpG. *J. Mol. Biol.* **360**, 750–9 (2006).
  49. Liang, B. & Tamm, L. K. Structure of outer membrane protein G by solution NMR spectroscopy. *Proc. Natl. Acad. Sci. U. S. A.* **104**, 16140–5 (2007).
  50. Chen, M., Khalid, S., Sansom, M. S. P. & Bayley, H. Outer membrane protein G: Engineering a quiet pore for biosensing. *Proc. Natl. Acad. Sci. U. S. A.* **105**, 6272–7 (2008).
  51. Zhuang, T. & Tamm, L. K. Control of the conductance of engineered protein nanopores through concerted loop motions. *Angew. Chem. Int. Ed. Engl.* **53**, 5897–902 (2014).
  52. Movileanu, L. Interrogating single proteins through nanopores: challenges and opportunities. *Trends Biotechnol.* **27**, 333–341 (2009).
  53. Butler, T. Z., Pavlenok, M., Derrington, I. M., Niederweis, M. & Gundlach, J. H. Single-molecule DNA detection with an engineered MspA protein nanopore. *Proc. Natl. Acad. Sci.* **105**, 20647–20652 (2008).
  54. Pastoriza-Gallego, M. *et al.* Dynamics of unfolded protein transport through an aerolysin pore. *J. Am. Chem. Soc.* **133**, 2923–2931 (2011).
  55. Wendell, D. *et al.* Translocation of double stranded DNA through membrane adapted phi29 motor protein nanopore. *Nat. Nanotechnol.* **4**, 765–772 (2009).
  56. Mohammad, M. M. *et al.* Engineering a rigid protein tunnel for biomolecular detection. *J. Am. Chem. Soc.* **134**, 9521–9531 (2012).
  57. Green, N. M. Avidin and streptavidin. *Methods Enzymol.* **184**, 51–67 (1990).
  58. Gu, L. Q. & Bayley, H. Interaction of the noncovalent molecular adapter, beta-cyclodextrin, with the staphylococcal alpha-hemolysin pore. *Biophys. J.* **79**, 1967–1975 (2000).
  59. Zhuang, T., Chisholm, C., Chen, M. & Tamm, L. K. NMR-based conformational ensembles explain pH-gated opening and closing of OmpG channel. *J. Am. Chem. Soc.* **135**, 15101–13 (2013).
  60. Song, L. *et al.* Structure of staphylococcal alpha-hemolysin, a heptameric transmembrane pore. *Science* **274**, 1859–66 (1996).

## CHAPTER 2

# ELECTROSTATIC INTERACTIONS BETWEEN OMPG NANOPORE AND ANALYTE PROTEIN SURFACE CAN DISTINGUISH BETWEEN GLYCOSYLATED ISOFORMS

Reprinted (adapted) with permission from M. A. Fahie and M. Chen, "Electrostatic Interactions between OmpG Nanopore and Analyte Protein Surface Can Distinguish between Glycosylated Isoforms," *J. Phys. Chem. B*, vol. 119, no. 32, pp. 10198–10206, 2015. Copyright 2015 American Chemical Society.

### 2.1 Summary

The flexible loops decorating the extracellular entrance of the OmpG nanopore especially the longest loop, L6, move dynamically and rapidly during ionic current recording. The current fluctuations or gating caused by these flexible loops are usually altered when a specific target protein is bound. We previously attached a ligand onto L6 and observe changes in OmpG gating when target proteins are bound. The gating is characterized by parameters including frequency, duration and open-pore current and these features combine to reveal the identity of a specific analyte protein. Each analyte protein generates a specific gating fingerprint. Here, we show that OmpG nanopore equipped with a biotin ligand can distinguish glycosylated and deglycosylated isoforms of avidin by their differences in surface charge. Our studies demonstrate that the direct interaction between the nanopore and analyte surface, induced by the electrostatic attraction between the two molecules, are essential for protein isoform detection. Our technique is remarkably sensitive to the analyte surface, which may provide a useful tool for glycoprotein profiling.



## 2.2 Introduction

Conventional nanopore sensing is based on the modulation of ionic current flowing through a nano-scale pore as an analyte translocates through the opening.<sup>1,2</sup> Nanopores come in two main flavors: biological and synthetic. Protein nanopores, which make up the largest class of biological nanopores, are usually derived from pore-forming proteins with well-defined structures at atomic precision. Solid-state nanopores that are fabricated from synthetic material, have the advantage of being robust and easily integrated into microelectronics. Although the technique has been extensively explored for the detection of nucleic acids and single-molecule DNA sequencing,<sup>3–5</sup> nanopores are also particularly useful for detecting protein molecules.<sup>6,7</sup> Nanopore-based detection of protein analytes has used various strategies, including: i) translocation of native analytes through unmodified<sup>8</sup> and modified pores,<sup>9,10</sup> ii) binding of native proteins to nanopores either directly or via tethered high-affinity binding sites such as aptamers,<sup>11–13</sup> ligands<sup>14,15</sup> and peptide binding sequences<sup>16</sup> and iii) binding of proteins to an auxiliary polymer in solution which alters the translocation of polymers through nanopore.<sup>17–19</sup> As a single molecule analytical tool, nanopores have been used to investigate the biochemical and biophysical properties of proteins, e.g. folding<sup>20</sup> and unfolding,<sup>21–23</sup> protein aggregation,<sup>24</sup> ubiquitin linkage type,<sup>25</sup> and enzymatic activity.<sup>17,26</sup> Recently, the unfolding and threading of a protein through a nanopore by an unfoldase demonstrated the unidirectional and processive translocation of a linearized peptide strand which opens the possibility for nanopore-based protein sequencing.<sup>27,28</sup> Another study used a nanopore to identify phosphorylation sites by threading.<sup>29</sup>

Despite these advances, it remains a challenge to detect a single protein in a complex analyte mixture. Bell *et al.* have recently addressed this problem by introducing DNA carriers containing precisely positioned protein binding sites along a double stranded DNA.<sup>18</sup> Binding of target proteins to the DNA carrier altered the current

signature when it translocated through a glass solid-state nanopore. Using this approach, they demonstrated that a single protein species can be identified in a protein mixture. Recently, we have explored an alternate nanopore sensing scheme based on outer membrane protein G (OmpG).<sup>30</sup> OmpG from *Escherichia coli* (*E. coli*) is a  $\beta$ -barrel protein with 14 strands connected by seven short turns on the periplasmic side and seven long loops on the extracellular side (Figure 2.1a).<sup>31–33</sup> Loop 6 moves dynamically, switching the protein between open and closed conformations resulting in gating signal in the current recording (Figure 2.1b).<sup>34–36</sup> Previously we showed that the flexible architecture of the OmpG nanopore can be used to resolve between structurally homologous protein analytes in mixtures.<sup>30</sup> Specifically, upon binding to a biotin group tethered to loop 6, a mixture of anti-biotin antibodies raised from different host species was clearly distinguished. Each antibody species was identified by its unique gating fingerprint and no interference from the other antibodies was observed. So far, no other nanopore has shown the ability to differentiate among a mixture of proteins that bind to the same high affinity ligand and share similar structural organization. The principle behind such high selectivity in OmpG is intriguing. It was previously speculated that the antibodies not only bind the biotin ligand but also non-specifically interact with the OmpG loops.<sup>30</sup> The latter plays an essential role in distinguishing among similar analytes.

Here, we probe the nature of non-specific interactions between OmpG and target proteins. To do so, we interrogate the interaction between the loops of OmpG and three homologous biotin binding proteins, streptavidin, avidin and extravidin. Our results reveal that electrostatic forces may be the dominating inter-molecular interaction between the OmpG nanopore and the target protein. Such interactions between the positively charged target protein surface and the negatively charged loops of the OmpG sensor are essential for discriminating among protein homologous and isoforms.

## 2.3 Materials and Methods

Reagents were purchased from Fisher Scientific and Boston Bioproducts unless otherwise stated. The biotin-peg-maleimide reagent, EZ-Link Maleimide-PEG2-Biotin (Cat# 21902BID), was purchased from Pierce and Warriner (Thermo Scientific). Streptavidin (Cat# Z7041) was purchased from Promega. Avidin (Cat# A9275) and extravidin (Cat# E2511) were purchased from Sigma. Diphytanoylphosphatidylcholine (DPhPC, Cat# 850356P) were from Avanti polar lipids. Octyl-glucoside (OG, Cat# O-110-5) and *tris*(2-carboxyethyl)phosphine (TCEP, Cat# TCEP5) were purchased from GoldBio Technology. Disposable capillary cells (DTS1070) for zeta potential measurement were purchased from Malvern Instruments. Anion exchange columns Hi-Trap QFF (Cat#17-5156-01) and desalting columns (Cat#17-1408-01) were purchased from GE Healthcare. Protein ladder (P7702S) was purchased from New England Biolabs (NEB).

### 2.3.1 Zeta potential Measurement

Proteins (previously dissolved in deionized water at at least 1 mg/ml) were diluted to a final concentration of 0.1 mg/ml in 5 mM buffered solution. Sodium acetate, sodium phosphate and *N*-cyclohexyl-3-aminopropanesulfonic acid (CAPS) buffers were used to obtain the zeta potential values of the proteins at pH 4, 6 and 10 respectively. Protein solutions were passed through a 0.22  $\mu$ m filter to remove any insoluble precipitates prior to analysis with Zetasizer Nano instrument (Malvern Instruments). Three replicates were measured and then averaged. The error values show the standard deviation of the three measurements.

### 2.3.2 Purification of OmpGD224C

OmpGD224C was constructed as previously described.<sup>30</sup> OmpGD224C plasmid was expressed in BL21 (pLys) *E. coli* chemically competent cells and allowed to grow to an optical density (OD<sub>600</sub>) of 0.5-0.6 at 37°C in LB-ampicillin media. The culture was

then induced with 0.5 mM IPTG for 3 hrs at 37°C. After induction, the culture was harvested. The harvested pellet was lysed in buffer containing 50 mM Tris-HCl pH 8.0, 1 mM EDTA, 2 mM TCEP, 200 µg/ml lysozyme at ~23°C for 15 mins and then sonicated on ice for 8 mins. The lysate was centrifuged 15 mins at 13,000 rpm, 4°C and the supernatant was discarded. The inclusion body pellet was resuspended in wash buffer containing 1.5 M Urea, 50 mM Tris-HCl pH 8.0, 2 mM TCEP for 10 mins at ~23°C. Thereafter the pellet was obtained after centrifugation at 13,000 rpm for 15 mins. The inclusion body was then solubilized in binding buffer (8.0 M Urea, 50 mM Tris-HCl pH 8.0, 2 mM TCEP) with constant stirring for 15 mins at ~23°C. This solubilized inclusion body was then centrifuged for 15 mins at 13,000 rpm. The supernatant was passed through a 0.45 µm filter before FPLC purification. OmpG was purified using anion exchange with binding and elution buffer (8.0 M Urea, 50 mM Tris-HCl pH 8.0, 2 mM TCEP, 500 mM NaCl).

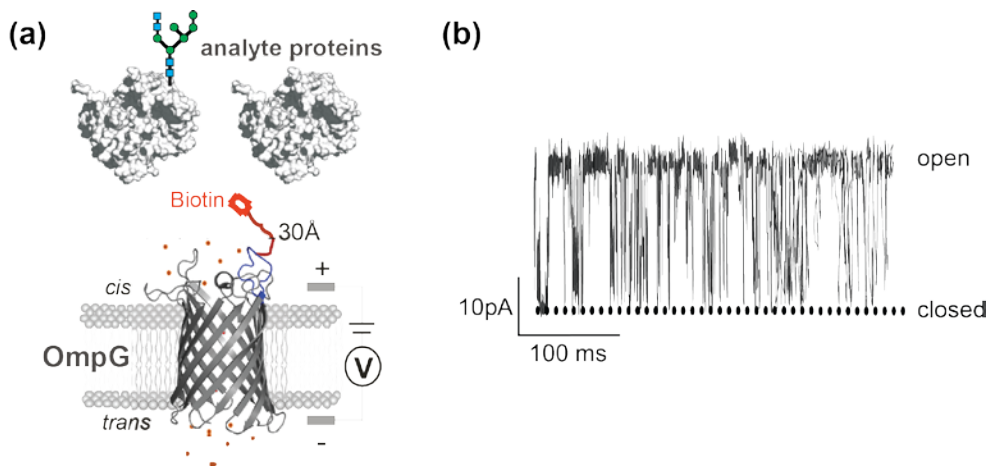
### **2.3.3 Labeling and refolding of OmpG-biotin proteins**

OmpG proteins were desalted in buffer 50 mM HEPES pH 7.0, 200 mM NaCl, 8.0 M Urea to remove the TCEP and Tris-HCl buffer. The protein concentration of OmpG D224C was estimated by Bradford assay and then incubated with maleimide-PEG<sub>2</sub>-biotin in a molar ratio 1:10 (protein to biotin) at room temperature (~23°C) for 1.5-2 hours with constant shaking. The reaction mixture was passed through the desalting column once again to remove the unconjugated biotin. The biotin labeled OmpG was then diluted with refolding buffer 50 mM Tris-HCl, pH 9.0, 3.25% OG in 2:3 volume ratio (OmpG to refolding buffer). Samples were then incubated at 37°C for 3 days. The biotinylation and refolding efficiency was determined by gel shift assay with and without streptavidin and visualized by SDS-PAGE.

## 2.4 Results

### 2.4.1 Discrimination among Avidin Homologues

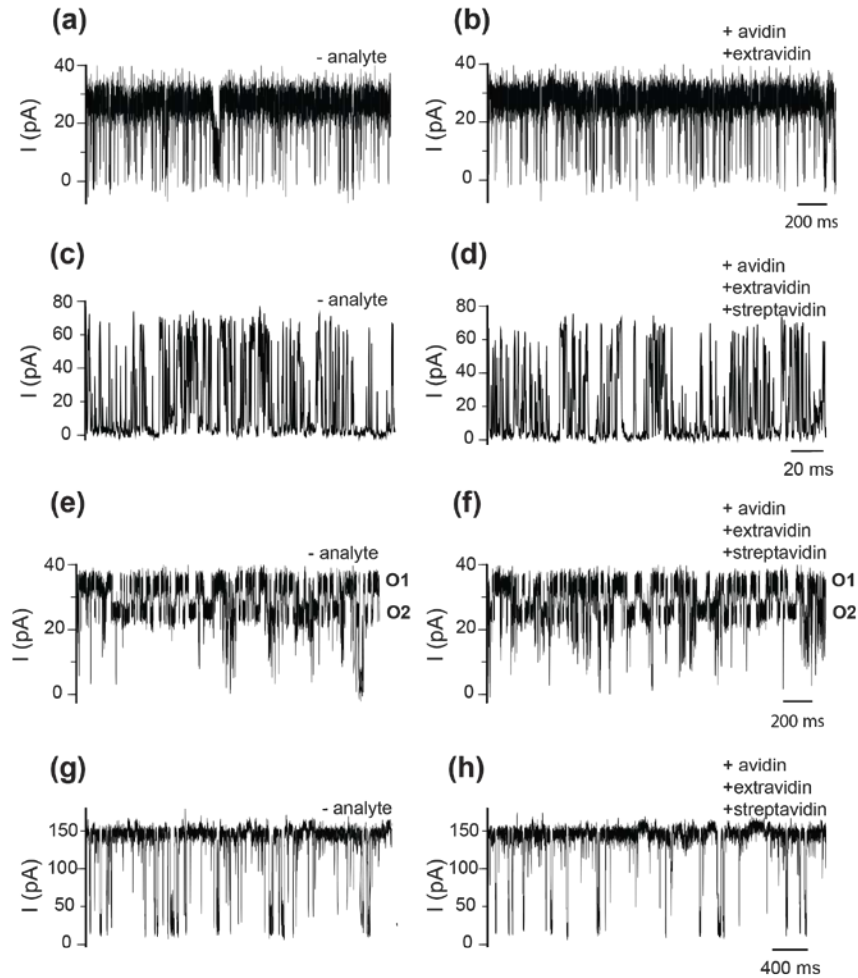
The OmpG-PEG<sub>2</sub>-biotin nanopore was constructed as previously described (Figure 2.1).<sup>30</sup> First, we investigated the ability of OmpG nanopore to detect the three biotin-binding protein homologues. Streptavidin from *Streptomyces avidinii* and avidin from egg white share ~45% sequence similarity. They have very similar structures, molecular weights and both exhibit high affinity (dissociation constant ~ 10<sup>-15</sup> M) for the biotin ligand.<sup>37</sup> Avidin has a basic isoelectric point (pI~10.5) due to its N-linked glycan composed largely of mannose and N-acetylglucosamine.<sup>38</sup> Streptavidin is a non-glycosylated protein with a pI of ~6.3. Extravidin is a commercially available deglycosylated form of avidin with a pI ~6.4, similar to that of streptavidin.



**Figure 2.1. Schematic diagram of the OmpG nanopore sensor.** (a) OmpG-PEG<sub>2</sub>-biotin pore. A biotin was tethered to a cysteine residue located on loop 6 (highlighted in blue) via a polyethylene glycol linker that could extend the biotin away from the nanopore by 30 Å. (b) A representative current trace of OmpG-PEG<sub>2</sub>-biotin nanopore. Buffer used was 10 mM sodium phosphate, pH 6.0, 300 mM KCl.

As a negative control and specificity test, all three biotin binding avidin proteins (unless otherwise stated) were added to unlabeled OmpGwt. Neither of the proteins produced any noticeable change in the wild type OmpG gating behavior indicating that

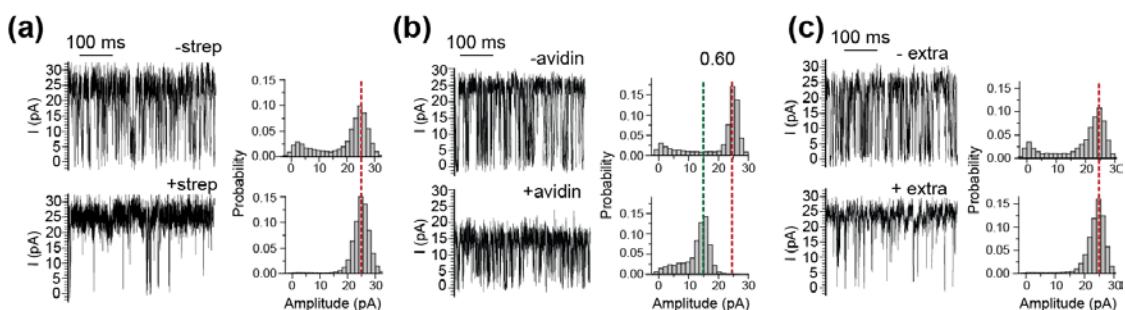
any change in gating signal seen when the OmpG-biotin sensor is used is specific binding of the analyte proteins used (Figure 2.2).



**Figure 2.2. Single channel current traces of OmpGwt in the presence of streptavidin homologues at various buffer conditions.** OmpGwt in the absence (a) and presence (b) of streptavidin homologues in 10mM sodium phosphate, pH 6.0, 300mM KCl buffer. Streptavidin homologues do not affect OmpGwt gating behavior in 10 mM sodium acetate pH 4.0 1.0 M KCl buffer (c, d) 10 mM CAPS pH 10.0, 300 mM KCl (e, f) nor 10 mM CAPS pH 10.0, 4.0 M KCl (g, h) buffers.

As observed previously,<sup>23</sup> streptavidin binding to OmpG-PEG<sub>2</sub>-biotin resulted in an irreversible decrease in OmpG's gating frequency (Figure 2.3a). By contrast, when avidin was bound to OmpG-PEG<sub>2</sub>-biotin the gating frequency increased from  $160 \pm 24 \text{ s}^{-1}$  to  $227 \pm 26 \text{ s}^{-1}$  (Table 2.1). More importantly, avidin binding resulted in a permanent

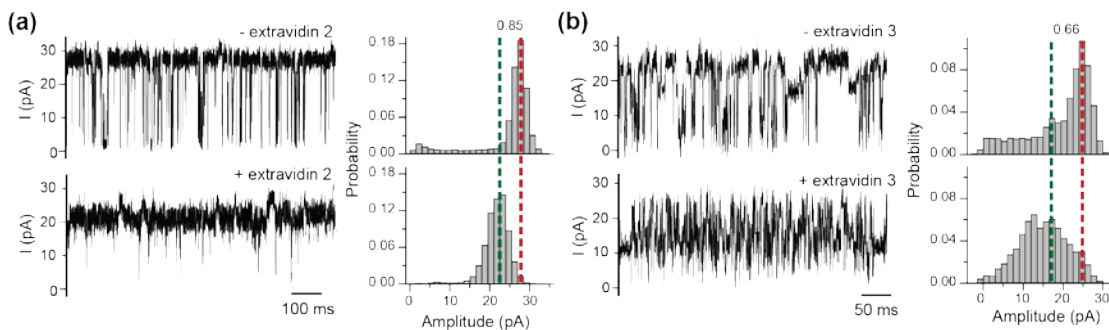
decrease in the open pore current from  $25.8 \pm 2.7$  pA to  $13.8 \pm 1.1$  pA ( $n=3$ ) (Figure 2.3b). When extravidin was tested its addition resulted in three different effects in OmpG gating. These three populations were categorized by their effect on OmpG open pore current specifically. The majority (10 of 19 trials) of extravidin binding events caused a gating behavior that was similar to that of streptavidin (Figure 2.3a, 2.3c): the gating frequency decreased from  $160 \pm 24$  s<sup>-1</sup> to  $30 \pm 9$  s<sup>-1</sup> and unlike avidin, the open-pore current was not affected. We refer to this population of extravidin as E1.



**Figure 2.3. Detection of biotin binding protein homologues by OmpG-PEG<sub>2</sub>-biotin nanopore.** (a, b, c) Typical current recording traces of streptavidin (a), avidin (b) and extravidin (c) bound to OmpG-PEG<sub>2</sub>-biotin at +50 mV in 10 mM sodium phosphate, pH 6.0, 300mM KCl buffer. Red and green dashed line indicates the open pore current before and after analyte protein binding. The relative open pore current of analyte bound state to unbound state is indicated above the dashed line.

Two minor populations, termed extravidin 2 – E2 (6 of 19 trials) and extravidin 3 – E3 (3 of 19 trials), caused a differential decrease in the open pore current with E3 showing an effect similar to that of avidin while E2 showed an effect intermediate between E1 and E3 (Figure 2.4). The E2 population induced a slightly decreased open pore current but reduced OmpG gating in a fashion similar to that of streptavidin (Figure 2.4a). We surmise that the extravidin gating population data may reflect sub-populations in the protein sample that have different levels of deglycosylation. The E3 population for example seems similar to fully intact, fully glycosylated avidin (Figure 2.3b, 2.4b). E1 was most similar to streptavidin and could therefore be fully deglycosylated while E2

may represent several partially deglycosylated forms. Because of the variability of extravidin's gating patterns, we focused mainly on data that represent the E1 characteristics for the following experiments.

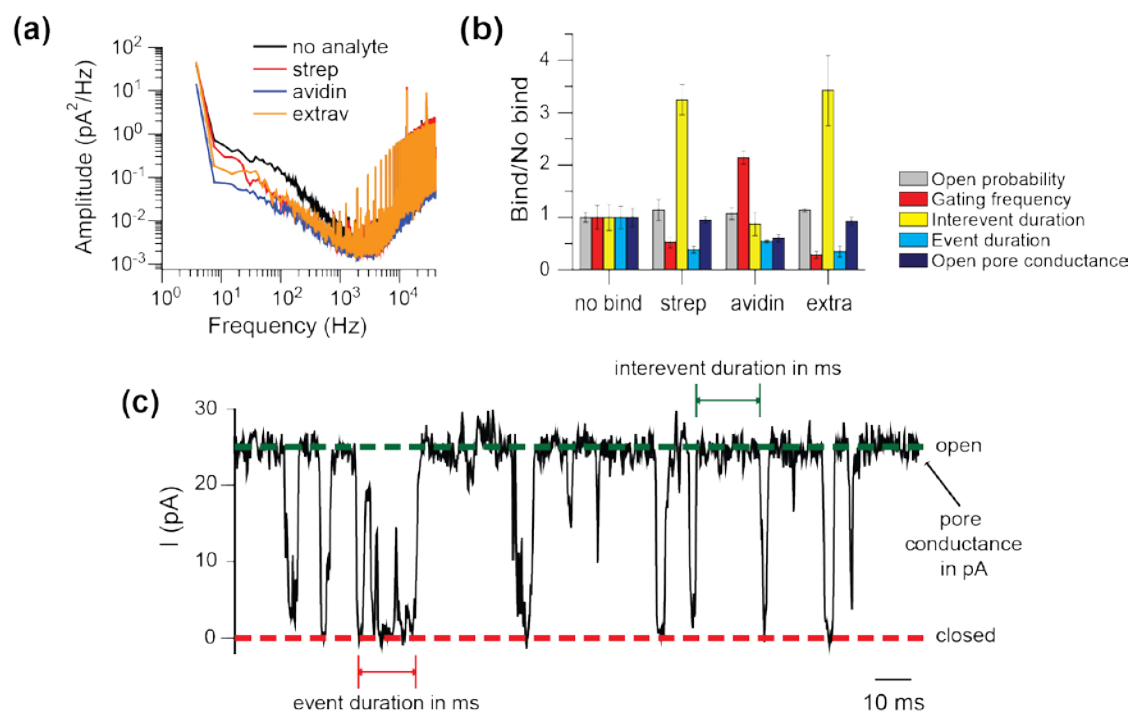


**Figure 2.4. Detection of extravidin subpopulations by OmpG nanopore.** (a) OmpG-PEG<sub>2</sub>-biotin in the absence and presence of extravidin 2 (E2) analyte, where the open pore current reduces to 85%. (b) OmpG-PEG<sub>2</sub>-biotin bound to extravidin 3 (E3) variant, where the open pore current reduces to 66%. All pores were recorded in buffer containing 10mM sodium phosphate pH 6.0, 300mM KCl at +50mV.

Noise spectral density analyses showed that streptavidin (red) and extravidin E1 (orange) had similar spectra which was lower in noise than the unbound pore (black), while avidin binding (blue) induced an even lower noise amplitude which was most likely due to its significantly reduced open pore current compared to the unbound pore (Figure 2.5a).

We then generated a fingerprint profile for each analyte using five parameters of OmpG gating. The relative change of these parameters after analyte binding compared to the unbound state determined the fingerprint of the protein. Clearly, avidin showed a distinct fingerprint in comparison to streptavidin and extravidin E1 (Figure 2.5b). The five parameters of OmpG gating included: open probability, gating frequency, inter-event duration, event duration and open pore current (Figure 2.5c, Table 2.1).<sup>23</sup> To our knowledge, this is the first report that demonstrates the discrimination of glycosylated protein isoforms using protein nanopores.





**Figure 2.5. Spectral and fingerprint analysis of OmpG nanopore bound to the streptavidin homologues.** (a) Power spectra and (b) fingerprint analysis of before and after target bound to OmpG-PEG<sub>2</sub>-biotin. (c) Single channel recording of a representative trace of the gating behavior of OmpG-PEG<sub>2</sub>-biotin in buffer 10mM sodium phosphate pH 6.0, 300mM KCl. Three parameters of OmpG gating behavior are highlighted: event duration (red), interevent duration (green) and open pore conductance. The gating event frequency is defined as the number of events per second. The open probability is the duration of the pore in the open state over unit time. The fingerprints obtained for OmpG in the unbound and bound states (5b) are derived from these five parameters.

**Table 2.1.** Gating characteristics for streptavidin, avidin and extravidin.

	Open probability	Gating frequency (s <sup>-1</sup> )	Inter-event duration (ms)	Event duration (ms)	Open pore conductance (pA)
No binding	0.83±0.08	106±24	8.5±2.1	0.83±0.18	24.8±4.4
Streptavidin	0.95±0.03	56±6	27.6±7.8	0.32±0.01	23.6±3.5
Avidin	0.89±0.08	227±26	7.5±2.1	0.46±0.09	14.6±1.7
Extravidin	0.95±0.03	30±9	29.1±0.4	0.29±0.06	21.7±5.7

Values were calculated from at least three independent experiments that were carried out in buffer 10mM sodium phosphate pH 6.0, 300 mM KCl at +50 mV. The errors indicate the standard deviation.

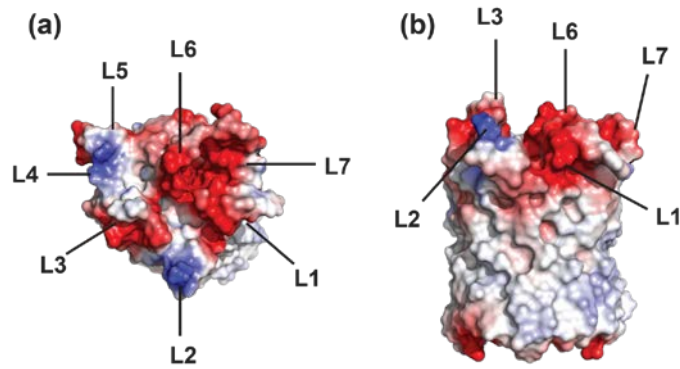
Because avidin has an identical amino acid sequence to extravidin and is homologous to streptavidin with a 41% sequence similarity, their key difference lies in the glycosylated vs non-glycosylated states which directly affects their unique surface charges. At pH 6.0, the zeta potential of avidin is  $7.8\pm 0.9$  mV making it positively charged while streptavidin and extravidin are negatively charged with a zeta potential value of  $-7.0\pm 0.5$  mV and  $-8.0\pm 1.9$  mV respectively (Table 2.2).

**Table 2.2.** Zeta potential measurements of analyte proteins under various pH conditions

pH	Zeta potential value (mV)		
	Streptavidin	Avidin	Extravidin
4.0	$2.5\pm 0.8$	$7.8\pm 1.5$	$1.0\pm 0.5$
6.0	$-7.0\pm 0.5$	$7.8\pm 0.9$	$-8.0\pm 1.9$
10.0	$-18.3\pm 5.0$	$-0.2\pm 0.4$	$-13.3\pm 3.0$

Values were calculated from at least three independent experiments. The errors indicate the standard deviation.

Our experiments suggest that a positive charge on the avidin surface may be the key factor that caused the open-pore current to significantly reduce by ~40% when avidin was bound to OmpG. The seven extracellular loops on OmpG consist of many charged residues including 17 aspartic acid residues (ASP), 8 glutamic residues (GLU) and 5 arginines (ARG) and 4 lysines (LYS). This concentration of charged amino acid residues in an approximate 0.8 nm region of the pore creates a surface rich in negative charge (Figure 2.6). We hypothesize that the negative charges on OmpG pull strongly on a positively charged region of avidin after specific binding to the biotin ligand tethered to loop 6. Thus, the avidin might closely interact with the surface of the pore through electrostatic attractions, partially occluding ionic flow and therefore causing a reduction in open pore current. In addition, the close proximity of avidin might confine the oscillations of loop 6 to a smaller space. This restricted movement might explain why avidin binding causes an increase in gating frequency of the OmpG nanopore.



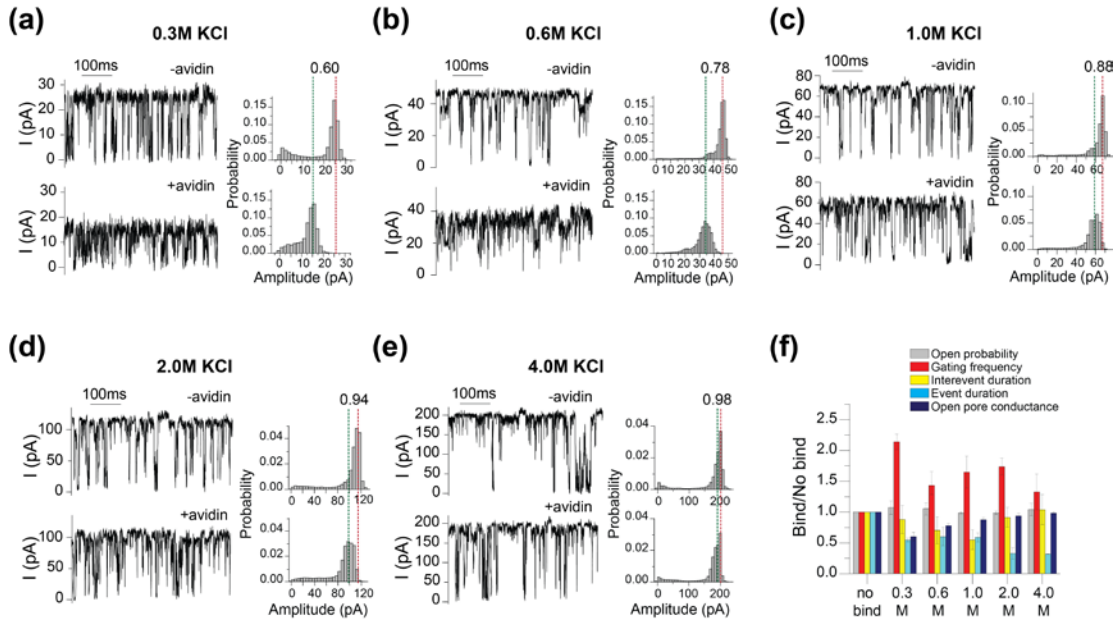
**Figure 2.6. Electrostatic potential map of the extracellular loops (L1-L7) of OmpG.** (a) Top view and (b) side view of the loop environment. PDB file 2IWW was used.

#### 2.4.2 Influence of Ionic Strength on Binding

If the reduction of open pore current is dependent on electrostatic interactions of the bound avidin with OmpG, then we expect this dependence to be reduced under charge screening conditions. Therefore, we investigated avidin binding at various concentrations of salt KCl ranging from 0.3 M to 4.0 M. We also tested 0.15 M KCl, however we could only detect changes in the open pore current before and after avidin bound to the OmpG nanopore (Tables 3.3 & 3.4). After avidin bound to OmpG in 0.15 M KCl solution, the current was too small  $\sim 8$  pA to accurately assign events and inter-events.

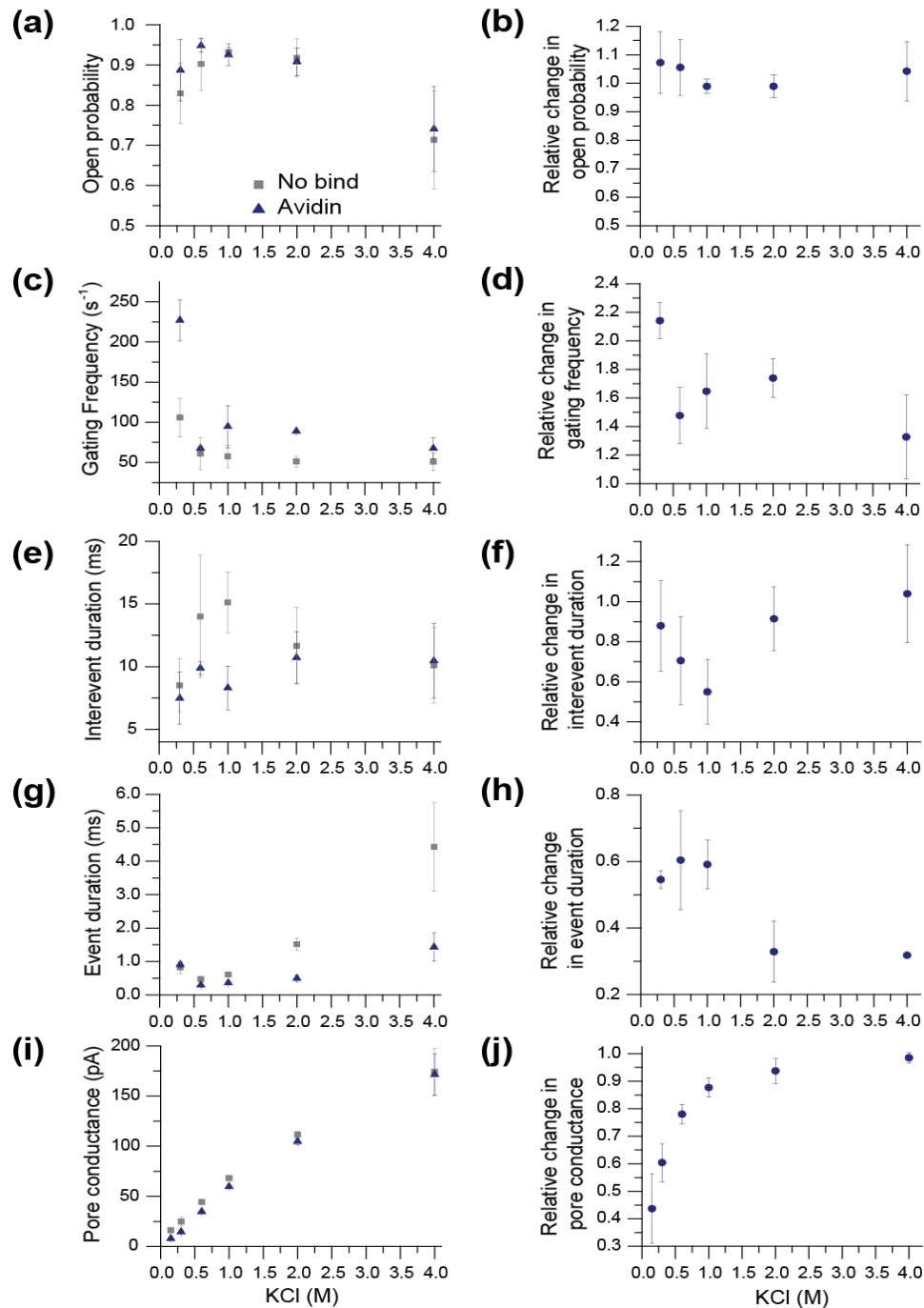
Evidently, with higher salt concentration, the open pore current of the unbound OmpG pore also increased proportionally, however, we found that the gating pattern of OmpG-PEG<sub>2</sub>-biotin after avidin binding was indeed influenced by the concentration of salt. Specifically, as the salt concentration increased, avidin binding induced a less significant reduction in the open pore current (Figure 2.7). The relative open pore current (of the avidin bound state) increased from  $0.6 \pm 0.07$  to  $0.98 \pm 0.18$  with increasing salt concentration (Figure 2.7a-e). Thus at high salt concentrations *i.e.*  $> 1.0$  M KCl the open pore current after avidin binding was similar to that of the unbound state. At 4.0 M

KCl, there was no difference in the open pore current between the avidin bound and unbound states (Figure 2.7e, 2.7f). Thus, our data suggests that electrostatic interactions between avidin and OmpG govern the bound-state open pore conductance because these interactions can be screened with excess salt.



**Figure 2.7. Effect of ionic strength on the gating characteristic of OmpG nanopore induced by avidin binding.** (a-e) Typical current recording traces of OmpG-PEG<sub>2</sub>-biotin before and after avidin binding in buffers containing various KCl concentrations. Relative change in open pore current of OmpG at avidin bound state (green line) to unbound state (red line) is indicated in the histogram. Experiments were performed at +50 mV in 10 mM sodium phosphate at pH 6.0 containing KCl, the concentration of which is indicated in figures. (f) Fingerprint of avidin binding at various KCl concentration.

Clearly, other gating characteristics of OmpG were also influenced by the salt concentration, for example the open probability generally increased with increased salt except at 4.0 M KCl where it decreased, while the gating frequency decreased from 0.15 M to 0.6 M and then plateaued (Figure 2.8, Tables 2.3 & 2.4). However, as opposed to the open pore current, the relative changes in these parameters after avidin binding did not show a strong correlation with increasing ionic strength (Figure 2.8, Tables 2.3 & 2.4).



**Figure 2.8. The effect of avidin binding on the five gating characteristics of OmpG-PEG<sub>2</sub>-biotin in various salt concentrations.** The effect of salt concentration on OmpG gating characteristics in the unbound (grey) and avidin bound (blue) states (a, c, e, g, i). The relative change in open probability (b), gating frequency (d), inter-event duration (f), event duration (h) and pore conductance (j) in the avidin bound state over several KCl concentrations. Values were calculated from at least three independent experiments. The errors indicate the standard deviation.

**Table 2.3.** Gating characteristics of avidin at various salt concentrations at pH 6.0, +50 mV

Salt concentration (M)		Open probability	Gating frequency (s <sup>-1</sup> )	Inter-event duration (ms)	Event duration (ms)	Open conductance (pA)
0.15	No bind	0.84±0.06	125±11	5.2±1.5	0.52±0.08	16.3±1.0
	Avidin	N/D	N/D	N/D	N/D	8.0±1.0
0.30	No bind	0.83±0.08	106±24	8.5±2.1	0.83±0.18	24.8±4.4
	Avidin	0.89±0.08	227±26	7.5±2.1	0.46±0.09	14.6±1.7
0.60	No bind	0.90±0.07	51±6	14.0±4.9	0.48±0.02	44.6±1.6
	Avidin	0.95±0.02	68±3	9.9±0.5	0.29±0.003	34.8±1.0
1.00	No bind	0.93±0.01	58±14	15.1±2.4	0.61±0.01	68.2±1.4
	Avidin	0.92±0.03	95±26	8.3±1.8	0.36±0.05	59.8±1.3
2.00	No bind	0.92±0.05	51±7	11.7±3.1	1.52±0.18	111.8±2.4
	Avidin	0.91±0.03	89±2	10.7±2.1	0.50±0.10	104.7±3.2
4.00	No bind	0.71±0.12	51±11	10.1±3.0	4.40±1.30	174.2±23.3
	Avidin	0.74±0.11	68±13	10.5±2.9	1.40±0.40	171.3±20.8

Values were calculated from at least three independent experiments. The errors indicate the standard deviation.

**Table 2.4.** Fingerprint characteristics of avidin at various salt concentrations at pH 6.0, +50 mV

Salt concentration (M)		Relative open probability	Relative gating frequency	Relative inter-event duration	Relative event duration	Relative open conductance
0.15	No bind	N/D	N/D	N/D	N/D	1.00±0.06
	Avidin	N/D	N/D	N/D	N/D	0.49±0.14
0.30	No bind	1.00±0.09	1.00±0.23	1.00±0.25	1.00±0.22	1.00±0.18
	Avidin	1.07±0.11	2.14±0.13	0.88±0.22	0.54±0.03	0.60±0.07
0.60	No bind	1.00±0.07	1.00±0.11	1.00±0.35	1.00±0.05	1.00±0.04
	Avidin	1.05±0.10	1.33±0.20	0.71±0.22	0.60±0.15	0.78±0.05
1.00	No bind	1.00±0.01	1.00±0.24	1.00±0.16	1.00±0.01	1.00±0.02
	Avidin	0.99±0.02	1.64±0.26	0.55±0.16	0.59±0.07	0.88±0.03
2.00	No bind	1.00±0.05	1.00±0.14	1.00±0.26	1.00±0.12	1.00±0.02
	Avidin	0.99±0.03	1.74±0.14	0.91±0.16	0.33±0.09	0.94±0.04
4.00	No bind	1.00±0.17	1.00±0.22	1.00±0.30	1.00±0.30	1.00±0.13
	Avidin	1.04±0.10	1.33±0.29	1.04±0.24	0.32±0.01	0.98±0.18

Values were calculated from at least three independent experiments. The errors indicate the standard deviation.

### 2.4.3 Effect of pH on Binding

To further support the idea that electrostatic interactions influence the binding of the avidin homologues, we investigated the effect of pH on the gating signal after the analytes bound. Specifically, by protonating or deprotonating the loop residues at the

pore-protein interface, we expect the loop dynamics to change in response to the gain or loss of charges. First, the binding effect of the three analytes to OmpG nanopore was recorded at pH 4.0. For these experiments, we used 1.0 M KCl because the open pore current of OmpG in buffer pH 4.0, 300 mM KCl was on average 8 pA or less which was too small to allow for precise analysis of the gating parameters (Figure 2.9).



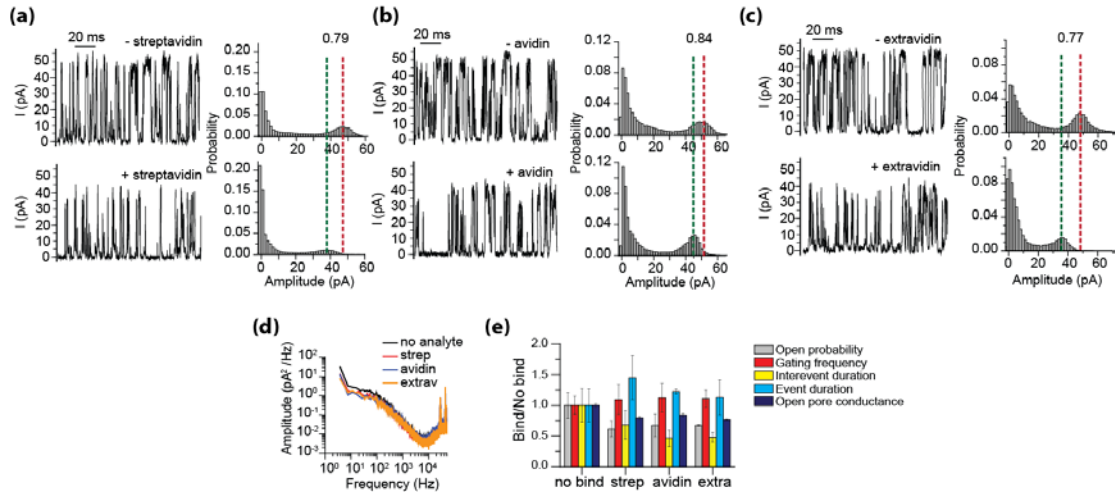
**Figure 2.9. OmpG generates small, closed pores in low salt, low pH buffer.** Representative trace of an OmpG-D224C pore in 10mM sodium acetate pH 4.0, 300 mM KCl and recorded at +50 mV.

Indeed the gating characteristic of the OmpG nanopore was significantly altered at low pH (Figure 2.10) compared to its gating behavior at pH 6. The open probability significantly reduced from  $0.93 \pm 0.01$  at 1.0 M pH 6 to  $0.34 \pm 0.07$  at 1.0 M pH 4. Thus, protonation of the OmpG negatively charged residues on the OmpG loops shifted the gating equilibria from a mainly open pore to a mainly closed pore. However, we were able to detect binding of the three avidin homologues.

At pH 4.0, avidin is strongly positively charged while streptavidin and extravidin have a slight net positive charge on their surfaces as indicated by zeta-potential measurements (Table 2.2). When bound to OmpG all proteins shared similar gating features (Figure 2.10a-c): (i) a decreased open-pore current albeit to a different level and (ii) a significantly reduced open probability due to elongated closure events (Figure 2.10e, Tables 2.5 & 2.6).

As a control, we verified that none of the protein analytes bind to the wild type nanopore under any pH condition (Figure 2.2). At low pH, streptavidin and extravidin

acquire positive charge and, like avidin at pH 6.0, are able to reduce the open pore current when bound (Figure 2.10). As a result, the fingerprints of these three proteins are almost the same, suggesting that the OmpG nanopore is not able to distinguish among these protein analytes under acidic conditions (Figure 2.10d, 2.10e).



**Figure 2.10. Effect of acidic pH on the gating signal of analyte proteins.** (a, b, c) Typical current recording traces and corresponding histograms of OmpG-PEG<sub>2</sub>-biotin nanopore before and after binding of streptavidin (a) avidin (b) and extravidin (c). Relative open pore current of OmpG at avidin bound state (green line) to unbound state (red line) is indicated in the histogram. Experiments were performed in 10mM sodium acetate pH 4.0, 1.0 M KCl at +50 mV. (d) Power spectra and fingerprint analysis (e) of before and after target bound to OmpG-PEG<sub>2</sub>-biotin.

**Table 2.5.** Effect of pH 4 on gating characteristics for streptavidin, avidin and extravidin at 1.0 M KCl pH 4.0, +50mV

	Open probability	Gating frequency (s <sup>-1</sup> )	Inter-event duration (ms)	Event duration (ms)	Open conductance (pA)
No binding	0.34±0.07	189±28	1.44±0.39	3.1±0.8	47.0±1.3
Streptavidin	0.21±0.05	206±39	0.98±0.19	4.5±0.2	37.5±1.0
Avidin	0.25±0.07	211±56	0.64±0.05	3.8±0.8	39.3±1.8
Extravidin	0.25±0.08	209±52	0.69±0.09	3.5±0.5	35.8±1.8

Values were calculated from at least three independent experiments. The errors indicate the standard deviation.



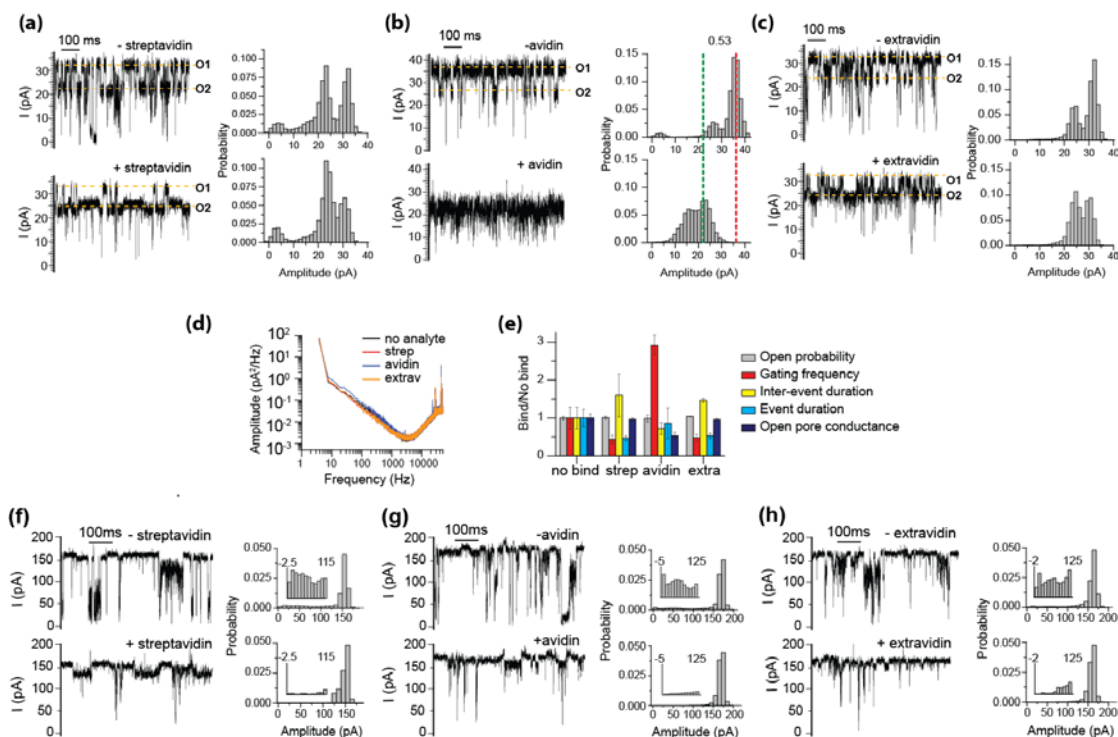
**Table 2.6.** Effect of pH 4 on fingerprint characteristics for streptavidin, avidin and extravidin at 1.0 M KCl pH 4.0, +50 mV

	Relative open probability	Relative gating frequency	Relative inter-event duration	Relative event duration	Relative open pore conductance
No binding	1.00±0.21	1.00±0.15	1.00±0.27	1.00±0.27	1.00±0.03
Streptavidin	0.62±0.14	1.1±0.25	0.68±0.23	1.45±0.36	0.80±0.03
Avidin	0.67±0.18	1.12±0.23	0.47±0.13	1.23±0.04	0.84±0.05
Extravidin	0.67±0.01	1.11±0.14	0.48±0.08	1.13±0.29	0.77±0.07

Values were calculated from at least three independent experiments. The errors indicate the standard deviation.

After observing that all three avidin homologues could not be distinguished by OmpG at acidic conditions, we then tested OmpG's discrimination ability under basic conditions. The OmpG nanopore is mainly in an open state at pH conditions above 5.0 and so we used the original lower salt concentration of 0.3 M KCl. At pH 10.0, OmpG-PEG<sub>2</sub>-biotin pore fluctuates between a fully open (31.5±3.4 pA, O1), a partially open (23.8 pA±3.6, O2) state and gating (closed) states (Figure 2.11a-c). We define the open probability as the probability of the pore staying at either fully open or partially open state.

Power spectral analysis of OmpG-PEG<sub>2</sub>-biotin pore does not show a significant change in the noise of the unbound and analyte bound states (Figure 2.11d) at pH 10. However, streptavidin and extravidin binding slightly increased the open probability due to a 50% reduction in gating frequency and event duration (Figure 2.11e, Tables 3.7 & 3.8). The fingerprint pattern of streptavidin and extravidin binding are similar at pH 6.0 and pH 10.0. This is not surprising as the two proteins are negatively charged at both pH conditions. In contrast, when avidin is bound to OmpG-PEG<sub>2</sub>-biotin the gating frequency increased by three fold and the open probability decreased slightly. The open pore current was reduced from 31.5±3.4 pA to 16.4±4.1 pA at +50mV.



**Figure 2.11. Binding of analyte proteins at pH 10.** (a-c) Typical current recording traces and corresponding histograms of OmpG-PEG<sub>2</sub>-biotin nanopore before and after binding of streptavidin (a) avidin (b) and extravidin (c). Relative open pore current of OmpG at avidin bound state (green line) to unbound state (red line) is indicated in the histogram. Experiments were performed in buffer 10mM CAPS pH 10.0, 300mM KCl at +50 mV. (d) Power spectrum and (e) Fingerprint analysis of the three biotin binding proteins on OmpG-PEG<sub>2</sub>-biotin behavior. (f-h) Binding of analyte proteins at high salt concentration. Typical current recording traces of OmpG-PEG<sub>2</sub>-biotin nanopore and corresponding histograms before and after binding of streptavidin (f) avidin (g) and extravidin (h). Experiments were performed in buffer 10mM CAPS pH 10.0, 4.0 M KCl at +50 mV.

**Table 2.7.** Effect of pH 10 on gating characteristics for streptavidin, avidin and extravidin at 0.3 M KCl pH 10.0, +50 mV

	Open probability	Gating frequency (s <sup>-1</sup> )	Inter-event duration (ms)	Event duration (ms)	Open conductance (pA)
No binding	0.94±0.05	23.4±6.6	35.4±9.8	1.35±0.30	31.5±3.4
Streptavidin	0.95±0.03	10.2±4.2	56.5±13.1	0.63±0.09	28.5±5.9
Avidin	0.93±0.06	68.2±18.3	25.8±8.6	1.16±0.20	16.4±4.1
Extravidin	0.98±0.02	11.2±2.5	51.8±12.7	0.72±0.07	31.4±1.3

Values were calculated from at least three independent experiments. The errors indicate the standard deviation.

**Table 2.8.** Effect of pH 10 on fingerprint characteristics for streptavidin, avidin and extravidin at 0.3 M KCl pH 10.0, +50 mV

	Relative open probability	Relative gating frequency	Relative inter-event duration	Relative event duration	Relative open conductance
No binding	1.00±0.05	1.00±0.28	1.00±0.28	1.00±0.22	1.00±0.11
Streptavidin	1.01±0.03	0.44±0.11	1.6±0.6	0.47±0.07	0.97±0.04
Avidin	0.99±0.09	2.90±0.27	0.73±0.16	0.86±0.40	0.53±0.09
Extravidin	1.04±0.01	0.82±0.16	1.46±0.05	0.53±0.07	0.99±0.08

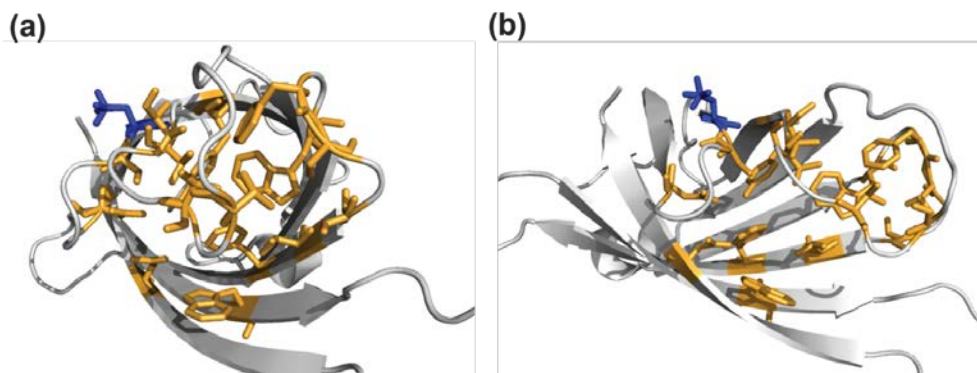
Values were calculated from at least three independent experiments. The errors indicate the standard deviation.

The zeta-potential measurement at pH 10 shows that the charge on the avidin surface approaches zero (Table 2.2). Since the avidin still induced a strong reduction in open pore current at pH 10.0, we suspect that an electrostatic attraction, albeit to a lesser strength than at lower pH conditions, is still present between OmpG and avidin.

One possibility to explain why electrostatic attractions between OmpG and avidin may still exist at pH 10 is that some of the positively charged residues on the OmpG loops may become deprotonated at pH 10.0. For example, there are a total of 2 lysine and 3 arginine residues found in loops L2, L3, L5 and L6 of OmpG and if all are deprotonated, the net result would be a more negatively charged surface. Thus, the loss of positive charge on avidin at high pH may be compensated by a gain of negative charge on OmpG's surface.

Alternatively, the local charge on avidin might still be positive near the biotin binding site even though the total charge on avidin approaches zero. Indeed the glycosylation site of avidin is found on residue Asn-17 (blue), adjacent to residue Ser-16 (gold) which comprises part of the biotin binding pocket<sup>32</sup> (Figure 2.12) and could potentially interact directly with the loops of the OmpG.

Finally, when all proteins were tested at pH 10.0 in the presence of charge screening conditions (4.0 M KCl), the gating pattern of bound avidin was indistinguishable from streptavidin or extravidin (Figure 2.11f-h). The open probability of the OmpG-PEG<sub>2</sub>-biotin increased slightly from 0.87 ±0.05 to around 0.97 ± 0.02 when bound to any of the three protein analytes (Table 2.9). In summary, pH, ionic strength or both can be used to modulate the molecular interactions and hence the gating behavior between the loops of OmpG and bound target proteins. These findings clearly illustrate the role that electrostatic interactions play in OmpG's ability to differentiate between very similar protein analytes.



**Figure 2.12. Proximity of the glycosylation site Asn-17 to the biotin binding pocket of the avidin monomer.** Top view (a) and side view (b) of the biotin binding residues in gold with the Asn-17 residue highlighted in blue. PDB code 1VYO was used to generate the images.

**Table 2.9.** Fingerprint values for bind 1 and bind 2 of streptavidin, avidin and extravidin at 4.0 M KCl pH 10.0, +50 mV

	Open probability	Gating frequency (s <sup>-1</sup> )	Inter-event duration (ms)	Event duration (ms)	Relative open conductance
No binding	0.87±0.05	31.5±7.7	39.9±9.6	3.74±1.08	1.00±0.04
All 3	0.97±0.02	9.5±2.3	92±27	0.45±0.1	0.98±0.02

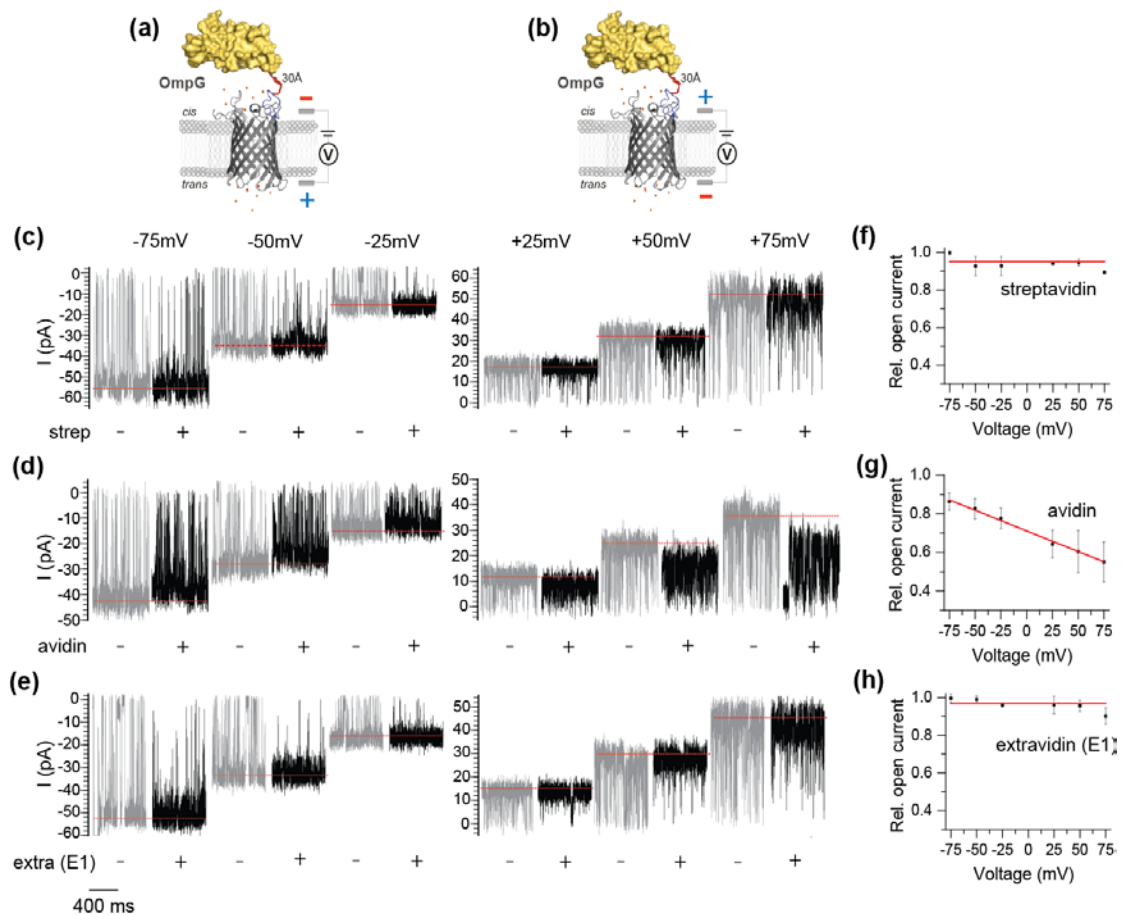
Values were calculated from at least three independent experiments for each analyte protein. The errors indicate the standard deviation.

#### 2.4.4 Influence of Applied Voltage on Bound-State Gating Behavior

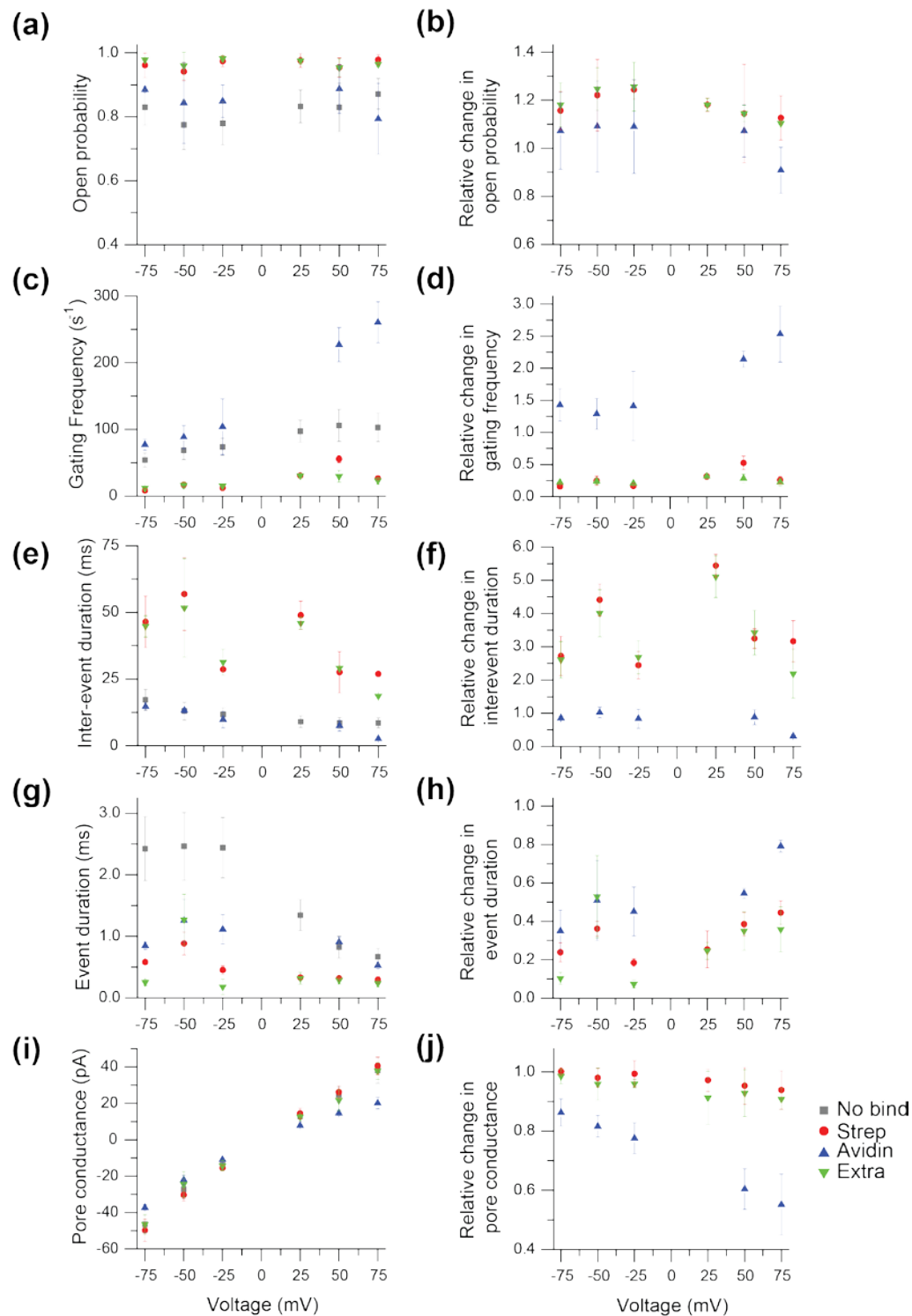
Next, we investigated how the applied potential affects the gating characteristic of the OmpG nanopore during the analyte bound state by varying the applied potential from -75 mV to +75 mV. Here, we define the polarity of the potential relative to the orientation of OmpG's loops. A negative potential is when OmpG's loops are on the negative side of the membrane relative to the positive side (Figure 2.13a). A positive voltage is the opposite scenario (Figure 2.13b). The most significant effect was observed using the open pore current of the avidin bound state which decreased linearly with increasing voltage (Figure 2.13d, 2.13g, Figure 2.14, Tables 2.10 & 2.11). In addition, the gating frequency was higher at positive voltages than at negative voltages (Figure 2.14c, 2.14d). Other avidin-induced changes in the gating characteristics, e.g. open probability, inter-event duration and event duration, appeared to be less dependent on applied voltage. In contrast to avidin, there was no direct correlation between the gating behavior of OmpG in the streptavidin and extravidin bound states at different applied voltages (Figure 2.13c, 2.13e, 2.13f, 2.13h, Figure 2.14, Tables 2.10 & 2.11).

We expect that the following phenomena could explain the dependence of the avidin bound state on the applied potential: electroosmosis, electrophoresis and electrostatics. Molecular dynamics simulation studies indicate that the electric field is strongest in the center of the nanopore and becomes weaker at the entrance and essentially negligible outside of the pore.<sup>39,40</sup> When the avidin molecule is captured by the biotin ligand it may be up to 30 Å away from the pore entrance, thus the electrophoretic effect may likely be negligible compared with the electroosmotic effect at this point. Thus, an electroosmotic flow moving from the loop side to the periplasmic side might be generated at a positive potential which drives the avidin towards the nanopore. At or near the pore entrance, the electrophoretic effect would bring the avidin analyte closer to the OmpG loops, thus promoting the electrostatic interaction between

the two molecules. These three effects combine to force OmpG and avidin together and further decrease the open pore current. On the other hand, a negative potential has an opposite effect where the avidin is pushed away from the loops. In this case the electroosmotic and electrophoretic effects counteract the electrostatics between avidin and OmpG. As a consequence, avidin blocks the open pore current of OmpG to a lesser degree under an applied negative potential.



**Figure 2.13. Effect of voltage on the gating characteristics of OmpG at analyte bound state.** (a, b) Schematic illustration of analyte binding at negative (a) and positive potential (b). (c, d, e) Single channel recording traces of OmpG-PEG<sub>2</sub>-biotin nanopore at the unbound (grey traces) and analyte bound state (black traces). Data were acquired in buffer 10 mM sodium phosphate, pH 6.0, 300 mM KCl at various applied potentials. (f, g, h) Voltage dependence of the open pore current in the streptavidin, avidin and extravidin bound states respectively.



**Figure 2.14. Effect of voltages on the gating characteristics of OmpG-PEG<sub>2</sub>-biotin after analyte binding.** Absolute values of gating characteristics before and after analyte binding (a,c,e,g,i). Relative change in gating characteristics after analyte binding (b,d,f,h,j). Values were calculated from at least three independent experiments. The errors indicate the standard deviation.

**Table 2.10.** Voltage effect on gating characteristics for streptavidin, avidin and extravidin binding at various voltages in 300 mM KCl pH 6.0 buffer

Voltage (mV)		Open probability	Gating frequency (s <sup>-1</sup> )	Inter-event duration (ms)	Event duration (ms)	Open conductance (pA)
-75	No bind	0.83±0.06	54±11	17.2±3.9	2.43±0.52	-46.4±4.6
	Strep	0.96±0.04	8±3	46.5±9.7	0.58±0.003	-49.8±6.0
	Avidin	0.89±0.01	77±8	14.7±0.1	0.85±0.06	-37.3±1.5
	Extrav	0.98±0.01	12±3	44.8±4.0	0.25±0.05	-46.5±5.4
-50	No bind	0.77±0.08	69±14	12.9±3.3	2.46±0.55	-27.2±5.2
	Strep	0.94±0.03	17±3	56.9±13.7	0.89±0.18	-26.7±3.3
	Avidin	0.84±0.13	89±17	13.2±1.1	1.25±0.35	-22.0±2.5
	Extrav	0.96±0.04	16±5	51.7±18.5	1.30±0.40	-24.5±7.1
-25	No bind	0.78±0.07	74±13	11.7±2.5	2.44±0.49	-14.0±2.6
	Strep	0.97±0.02	12±3	28.6±0.3	0.45±0.07	-13.9±1.4
	Avidin	0.85±0.05	104±42	9.8±3.1	1.10±0.20	-11.0±0.8
	Extrav	0.98±0.01	15±1	31.4±4.8	0.18±0.06	-14.3±2.8
+25	No bind	0.83±0.05	97±17	9.0±2.2	1.30±0.25	12.9±2.8
	Strep	0.98±0.02	31±4	48.9±5.4	0.33±0.02	12.5±2.9
	Avidin	N/D*	N/D	N/D	N/D	7.8±0.8
	Extrav	0.98±0.01	31±4	45.9±2.2	0.32±0.09	12.6±1.5
+50	No bind	0.83±0.08	106±24	8.5±2.1	0.83±0.18	24.8±4.4
	Strep	0.95±0.03	56±6	27.6±7.8	0.32±0.01	23.6±3.5
	Avidin	0.89±0.08	227±26	7.5±2.1	0.46±0.09	14.6±1.7
	Extrav	0.95±0.03	30±9	29.1±0.4	0.29±0.06	21.7±5.7
+75	No bind	0.87±0.05	103±21	8.5±1.8	0.67±0.13	38.2±7.1
	Strep	0.98±0.02	27±2	26.9±0.9	0.30±0.05	35.9±4.8
	Avidin	0.79±0.11	261±31	2.6±0.4	0.53±0.06	20.1±3.2
	Extrav	0.96±0.01	23±5	18.6±0.2	0.24±0.06	37.8±4.6

\*Avidin characteristics at +25 mV were not determined because after avidin binding, the conductance was too small to accurately calculate the gating characteristics other than pore conductance.

Values were calculated from at least three independent experiments. The errors indicate the standard deviation.



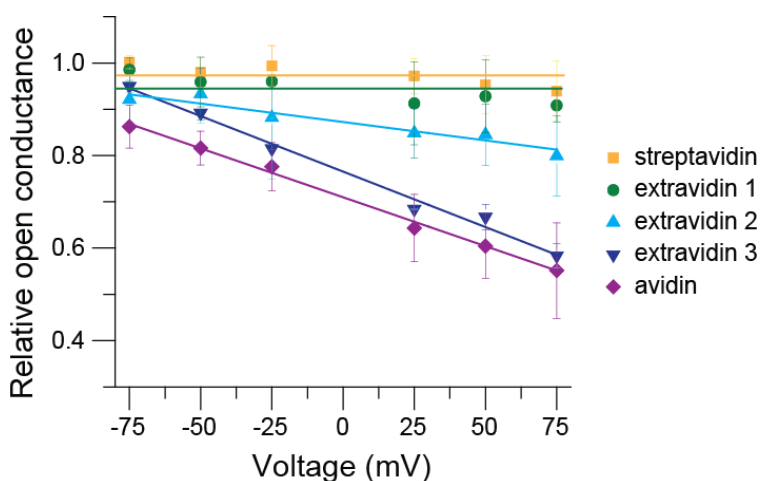
**Table 2.11.** Voltage effect on fingerprint characteristics for streptavidin, avidin and extravidin binding in 300 mM KCl pH 6 buffer

Voltage (mV)		Relative open probability	Relative gating frequency	Relative inter-event duration	Relative event duration	Relative open conductance
-75	No bind	1.00±0.07	1.00±0.19	1.00±0.23	1.00±0.21	1.00±0.10
	Strep	1.16±0.08	0.16±0.05	2.72±0.59	0.24±0.05	1.07±0.10
	Avidin	1.07±0.16	1.42±0.25	0.85±0.07	0.35±0.11	0.86±0.05
	Extrav	1.18±0.09	0.22±0.01	2.60±0.55	0.10±0.03	1.0±0.03
-50	No bind	1.00±0.10	1.00±0.20	1.00±0.26	1.00±0.22	1.00±0.19
	Strep	1.22±0.15	0.25±0.07	4.41±0.49	0.36±0.04	0.98±0.03
	Avidin	1.09±0.19	1.29±0.24	1.02±0.17	0.51±0.21	0.82±0.04
	Extrav	1.25±0.09	0.24±0.04	4.01±0.71	0.53±0.21	0.92±0.05
-25	No bind	1.00±0.09	1.00±0.18	1.00±0.22	1.00±0.20	1.00±0.19
	Strep	1.24±0.04	0.17±0.04	2.44±0.41	0.18±0.02	0.99±0.04
	Avidin	1.09±0.19	1.41±0.54	0.84±0.29	0.45±0.13	0.78±0.05
	Extrav	1.26±0.10	0.21±0.03	2.68±0.50	0.07±0.02	1.02±0.01
+25	No bind	1.00±0.06	1.00±0.17	1.00±0.25	1.00±0.19	1.00±0.21
	Strep	1.18±0.03	0.32±0.05	5.44±0.35	0.25±0.10	0.97±0.04
	Avidin	N/D	N/D	N/D	N/D	0.64±0.07
	Extrav	1.18±0.03	0.32±0.01	3.42±0.67	0.25±0.04	0.98±0.09
+50	No bind	1.00±0.09	1.00±0.23	1.00±0.25	1.00±0.22	1.00±0.18
	Strep	1.14±0.20	0.53±0.10	3.25±0.29	0.39±0.06	0.95±0.06
	Avidin	1.07±0.11	2.14±0.13	0.88±0.23	0.55±0.03	0.60±0.07
	Extrav	1.14±0.04	0.28±0.07	3.42±0.67	0.35±0.10	0.90±0.08
+75	No bind	1.00±0.05	1.00±0.21	1.00±0.22	1.00±0.20	1.00±0.19
	Strep	1.13±0.09	0.26±0.06	3.16±0.62	0.45±0.06	0.94±0.07
	Avidin	0.91±0.10	2.53±0.44	0.31±0.04	0.79±0.03	0.55±0.1
	Extrav	1.10±0.01	0.22±0.06	2.19±0.73	0.36±0.12	0.99±0.04

Values were calculated from at least three independent experiments. The errors indicate the standard deviation.

While the gating behavior of the nanopore with bound avidin was relatively straightforward to understand in terms of electrostatic interactions, our voltage dependent studies using extravidin revealed more subtle information. When we examined the E1 form of extravidin, the gating behavior was not affected by the voltage polarity (Figure 2.13e, 2.13h). However, the E2 and E3 forms of extravidin showed open pore currents that did respond to voltage. Namely, the open pore current of OmpG-PEG<sub>2</sub>-biotin, upon binding to E2 or E3, decreased linearly with increasing voltage from -

75 mV to 75 mV (Figure 2.15). This observation suggests that E2 and E3 population bear net positive charges due to an incomplete removal of glycan from the surface. Notably, the voltage induced a current reduction to similar levels in E3 and avidin while to a lesser extent in E2. This result supports our speculation that E3 was intact avidin and E2 was the intermediate product of the deglycosylation reaction. Taken together, the voltage can influence the binding signal of a charged analyte by either strengthening or weakening the interaction between the OmpG nanopore and the analyte protein.

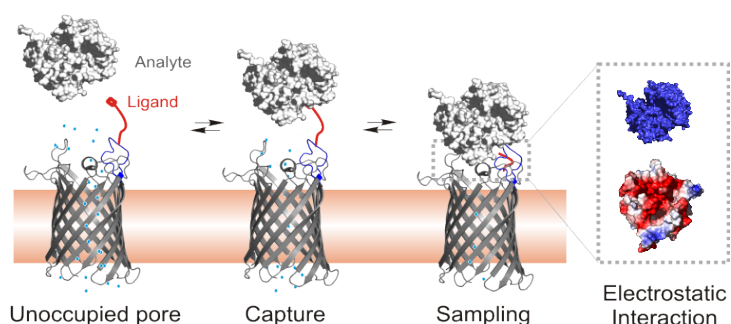


**Figure 2.15. The relative open pore conductance of OmpG-PEG<sub>2</sub>-biotin when bound to the avidin homologues.** Binding of the homologues to OmpG-PEG<sub>2</sub>-biotin affects the open pore current over several voltages. All trials were recorded in buffer containing 10mM sodium phosphate pH 6.0, 300 mM KCl. Values were calculated from at least three independent experiments. The errors indicate the standard deviation.

## 2.5 Discussion

We have demonstrated that analyte proteins with positively charged surfaces are attracted to the negatively charged loops of OmpG. The interaction leads to a reduction of the open-pore current through the nanopore. In control experiments, we showed that our proteins did not induce any significant current change when using wild type OmpG, indicating the interaction of the avidin species only occurs after they bind to the biotin ligand. Therefore, these results strongly support a two-step mechanism for OmpG

nanopore sensing (Figure 2.16). The first step is the capture where the protein binds the ligand on OmpG. The capture of an analyte protein brings it in close proximity to the nanopore opening which then facilitates electrostatic attraction between the two surfaces. In the second step, the analyte interacts directly with the loops of OmpG to obstruct ionic flow through the pore and alter the dynamic movement of the loops. In essence, the flexible loops of OmpG sense and communicate information about the surface of the analyte protein. This process is termed “sampling”.



**Figure 2.16. Schematic representation of the sampling mechanism for OmpG nanopore.** The OmpG loops and protein analyte are attracted electrostatically.

Though all three avidin species were clearly captured by the biotin ligand, some did not undergo the sampling step. For example, streptavidin and extravidin at pH 6.0 do not induce a change in the open pore current which indicates that the loops and target surface are repelled by their like charges. At high salt concentrations (4.0 M KCl), charges were screened and avidin also did not cause a change in open pore current. In scenarios where sampling did not occur, the OmpG nanopore could not distinguish between biotin-binding species. Therefore, system conditions that favor sampling are essential for sensitive analyte discrimination.

Importantly, protein analytes that are sampled by the OmpG loops could induce distinct gating signal. For example, at pH 6.0 in low salt (0.3 M KCl), avidin-OmpG loop interactions increased the gating frequency, indicating that loop 6 oscillates between the

closed and open state more rapidly. However, it caused a reduction in the gating event duration by 30%. The effect of bound avidin on the loops was remarkably different from the effect of a mouse monoclonal anti-biotin antibody (mAb) used in a previous study.<sup>30</sup> Under identical conditions, mAb binding increased both the gating frequency and event duration, which led to a decrease in open probability. Furthermore, one polyclonal anti-biotin antibody eliminated all gating events and resulted in a constantly open pore.<sup>30</sup> The differences in loop interactions between the monoclonal and polyclonal antibodies and the avidin clearly demonstrate that the gating induced by OmpG's loops depends on the unique interaction with the analyte interface. In nature, protein-protein interactions are typically mediated by weak intermolecular forces such as hydrophobic, hydrogen-bonding and electrostatic forces. The OmpG nanopore so far seems predominantly sensitive to attractive electrostatic interactions. Indeed, we note that conditions that leave an avidin species nearly neutral or negatively charged (*i.e.*, conditions that prevent sampling) abolish OmpG's discrimination abilities. The current version of the OmpG nanopore sensor is nearly identical to the wild type save the addition of the biotin ligand. We speculate that further modifications to the loops might allow the use of hydrophobic or hydrogen bond interactions for enhanced sampling of neutral and negative analytes.

We also show that experimental conditions, such as pH, salt concentration and voltage can be tuned to facilitate detection. Sampling process is the key to OmpG's discrimination ability, so parameters that modulate sampling may also be used to enhance sensitivity. This can be accomplished by two general strategies. First, the electrostatic interaction between the analyte and nanopore can be tuned by altering the surface charge of both analyte protein and nanopore. Second, we also showed that voltage could either enhance or weaken the interaction by electrophoretic forces that move the protein closer to or away from the pore entrance. Thus, by optimizing the conditions, we can maximize the relative difference in the fingerprint analysis to generate

unambiguous detection patterns. These strategies may also be particularly useful to ameliorate the effect of interference from other species in complex samples.

Post-translational modifications (PTMs) have an important impact on the physical properties and biological functions of proteins. Altered or missing modifications have profound effects on cellular function and are often associated with human diseases,<sup>41,42</sup> such as neurodegenerative disease,<sup>43</sup> cancer<sup>44</sup> and inflammatory diseases.<sup>45</sup> Mass spectrometry, as the key technology for identifying PTMs, has contributed tremendously our understanding of PTMs in cell.<sup>46–48</sup> However, analysis of PTMs by mass spectrometry can be challenging due to the instability of the modifications during the MS analysis or the effect of the modification of the peptide's ionization efficiency. Single-molecule strategies using nanopore for detecting modifications are especially appealing because it can identify modifications and variants within an intact protein. Along these lines, Rosen *et al.* recently demonstrated the use of  $\alpha$ HL in detecting changes in the phosphorylation of thioredoxin.<sup>22</sup> Here we showed OmpG nanopores can recognize changes in glycosylation patterns of proteins through their differences in surface charge. This is especially important, as many forms of glycosylation *e.g.* sialylation and acetylglucosaminylation add negative or positive charge, respectively. Current glycoprotein profiling methods using mass spectrometry often run in tandem with a separation technique, such as liquid chromatography or gel electrophoresis. Equipped with a specific ligand for the protein of interest, OmpG nanopore could be used for differential profiling of cellular glycoproteins in native states without prior separation procedure or liberation of glycan.

## **2.6 Conclusion**

We demonstrated that an engineered OmpG nanopore can distinguish between protein homologues and post-translationally modified isoforms through their differences in surface charge. This is achieved by the electrostatic interaction between the nanopore loops and analyte proteins and yields a gating fingerprint readout for the analyte.

## 2.7 References

1. Howorka, S. & Siwy, Z. Nanopore analytics: sensing of single molecules. *Chem. Soc. Rev.* **38**, 2360–2384 (2009).
2. Bayley, H. & Cremer, P. S. Stochastic sensors inspired by biology. *Nature* **413**, 226–230 (2001).
3. Branton, D. *et al.* The potential and challenges of nanopore sequencing. *Nat. Biotechnol.* **26**, 1146–1153 (2008).
4. Kasianowicz, J. J., Brandin, E., Branton, D. & Deamer, D. W. Characterization of individual polynucleotide molecules using a membrane channel. *Proc. Natl. Acad. Sci. U. S. A.* **93**, 13770–13773 (1996).
5. Wanunu, M. Nanopores: A journey towards DNA sequencing. *Phys. Life Rev.* **9**, 125–158 (2012).
6. Oukhaled, A., Bacri, L., Pastoriza-Gallego, M., Betton, J. M. & Pelta, J. Sensing proteins through nanopores: Fundamental to applications. *ACS Chem. Biol.* **7**, 1935–1949 (2012).
7. Movileanu, L. Interrogating single proteins through nanopores: challenges and opportunities. *Trends Biotechnol.* **27**, 333–341 (2009).
8. Fologea, D., Ledden, B., McNabb, D. S. & Li, J. Electrical characterization of protein molecules by a solid-state nanopore. *Appl. Phys. Lett.* **91**, 53901-1-53901–3 (2007).
9. Wei, R., Gatterdam, V., Wieneke, R., Tampé, R. & Rant, U. Stochastic sensing of proteins with receptor-modified solid-state nanopores. *Nat. Nanotechnol.* **7**, 257–63 (2012).
10. Yusko, E. C. *et al.* Controlling protein translocation through nanopores with bio-inspired fluid walls. *Nat. Nanotechnol.* **6**, 253–60 (2011).
11. Ding, S., Gao, C. & Gu, L. Q. Capturing single molecules of immunoglobulin and ricin with an aptamer-encoded glass nanopore. *Anal. Chem.* **81**, 6649–6655 (2009).
12. Rotem, D., Jayasinghe, L., Salichou, M. & Bayley, H. Protein detection by nanopores equipped with aptamers. *J. Am. Chem. Soc.* **134**, 2781–7 (2012).
13. Soskine, M. *et al.* An engineered ClyA nanopore detects folded target proteins by selective external association and pore entry. *Nano Lett.* **12**, 4895–900 (2012).
14. Movileanu, L., Howorka, S., Braha, O. & Bayley, H. Detecting protein analytes that modulate transmembrane movement of a polymer chain within a single protein pore. *Nat. Biotechnol.* **18**, 1091–1095 (2000).
15. Howorka, S., Nam, J., Bayley, H. & Kahne, D. Stochastic detection of monovalent and bivalent protein-ligand interactions. *Angew. Chemie - Int. Ed.* **43**, 842–846 (2004).
16. Xie, H., Braha, O., Gu, L. Q., Cheley, S. & Bayley, H. Single-molecule observation of the catalytic subunit of cAMP-dependent protein kinase binding to an inhibitor peptide. *Chem. Biol.* **12**, 109–120 (2005).
17. Zhao, Q., De Zoysa, R. S. S., Wang, D., Jayawardhana, D. A. & Guan, X. Real-time monitoring of peptide cleavage using a nanopore probe. *J. Am. Chem. Soc.* **131**, 6324–6325 (2009).
18. Bell, N. A. W. & Keyser, U. F. Specific Protein Detection Using Designed DNA Carriers and Nanopores. *J. Am. Chem. Soc.* **137**, 2035–2041 (2015).
19. Kasianowicz, J. J., Henrickson, S. E., Weetall, H. H. & Robertson, B. Simultaneous multianalyte detection with a nanometer-scale pore. *Anal. Chem.* **73**, 2268–2272 (2001).

20. Stefureac, R. I. & Lee, J. S. Nanopore analysis of the folding of zinc fingers. *Small* **4**, 1646–1650 (2008).
21. Oukhaled, G. *et al.* Unfolding of proteins and long transient conformations detected by single nanopore recording. *Phys. Rev. Lett.* **98**, 158101 (2007).
22. Talaga, D. S. & Li, J. Single-molecule protein unfolding in solid state nanopores. *J. Am. Chem. Soc.* **131**, 9287–9297 (2009).
23. Rodriguez-Larrea, D. & Bayley, H. Multistep protein unfolding during nanopore translocation. *Nat. Nanotechnol.* **8**, 288–295 (2013).
24. Yusko, E. C. *et al.* Single-particle characterization of A $\beta$  oligomers in solution. *ACS Nano* **6**, 5909–5919 (2012).
25. Nir, I., Huttner, D. & Meller, A. Direct Sensing and Discrimination among Ubiquitin and Ubiquitin Chains Using Solid-State Nanopores. *Biophys. J.* **108**, 2340–2349 (2015).
26. Majd, S., Yusko, E. C., MacBriar, A. D., Yang, J. & Mayer, M. Gramicidin pores report the activity of membrane-active enzymes. *J. Am. Chem. Soc.* **131**, 16119–16126 (2009).
27. Nivala, J., Marks, D. B. & Akeson, M. Unfoldase-mediated protein translocation through an  $\alpha$ -hemolysin nanopore. *Nat. Biotechnol.* **31**, 247–50 (2013).
28. Nivala, J., Mulrone, L., Li, G., Schreiber, J. & Akeson, M. Discrimination among Protein Variants Using an Unfoldase-Coupled Nanopore. *ACS Nano* **8**, 12365–75 (2014).
29. Rosen, C. B., Rodriguez-Larrea, D. & Bayley, H. Single-molecule site-specific detection of protein phosphorylation with a nanopore. *Nat. Biotechnol.* **32**, 179–181 (2014).
30. Fahie, M., Chisholm, C. & Chen, M. Resolved Single-Molecule Detection of Individual Species within a Mixture of anti-Biotin Antibodies Using an Engineered Monomeric Nanopore. *ACS Nano* **9**, 1089–1098 (2015).
31. Liang, B. & Tamm, L. K. Structure of outer membrane protein G by solution NMR spectroscopy. *Proc. Natl. Acad. Sci. U. S. A.* **104**, 16140–5 (2007).
32. Yildiz, O., Vinothkumar, K. R., Goswami, P. & Kühlbrandt, W. Structure of the monomeric outer-membrane porin OmpG in the open and closed conformation. *EMBO J.* **25**, 3702–13 (2006).
33. Zhuang, T., Chisholm, C., Chen, M. & Tamm, L. K. NMR-based conformational ensembles explain pH-gated opening and closing of OmpG channel. *J. Am. Chem. Soc.* **135**, 15101–13 (2013).
34. Conlan, S., Zhang, Y., Cheley, S. & Bayley, H. Biochemical and Biophysical Characterization of OmpG: A Monomeric Porin †. *Biochemistry* **39**, 11845–11854 (2000).
35. Chen, M., Khalid, S., Sansom, M. S. P. & Bayley, H. Outer membrane protein G: Engineering a quiet pore for biosensing. *Proc. Natl. Acad. Sci. U. S. A.* **105**, 6272–7 (2008).
36. Zhuang, T. & Tamm, L. K. Control of the conductance of engineered protein nanopores through concerted loop motions. *Angew. Chem. Int. Ed. Engl.* **53**, 5897–902 (2014).
37. Green, N. M. Avidin and streptavidin. *Methods Enzymol.* **184**, 51–67 (1990).
38. Green, N. M. Avidin. *Adv. Protein Chem.* **29**, 85–133 (1975).
39. Heng, J. B. *et al.* Stretching DNA using the electric field in a synthetic nanopore. *Nano Lett.* **5**, 1883–1888 (2005).
40. Aksimentiev, A. & Schulten, K. Imaging alpha-hemolysin with molecular dynamics: ionic conductance, osmotic permeability, and the electrostatic potential map. *Biophys. J.* **88**, 3745–61 (2005).



41. Hart, G. W., Slawson, C., Ramirez-Correa, G. & Lagerlof, O. Cross talk between O-GlcNAcylation and phosphorylation: roles in signaling, transcription, and chronic disease. *Annu. Rev. Biochem.* **80**, 825–58 (2011).
42. Durand, G. & Seta, N. Protein glycosylation and diseases: Blood and urinary oligosaccharides as markers for diagnosis and therapeutic monitoring. *Clin. Chem.* **46**, 795–805 (2000).
43. Ma, T. *et al.* Suppression of eIF2 $\alpha$  kinases alleviates Alzheimer's disease-related plasticity and memory deficits. *Nat. Neurosci.* **16**, 1299–305 (2013).
44. Lim, Y. P. Mining the Tumor Phosphoproteome for Cancer Markers. *Clin. Cancer Res.* **11**, 3163–3169 (2005).
45. Dube, D. H. & Bertozzi, C. R. Glycans in cancer and inflammation--potential for therapeutics and diagnostics. *Nat. Rev. Drug Discov.* **4**, 477–488 (2005).
46. Mann, M. & Jensen, O. N. Proteomic analysis of post-translational modifications. *Nat. Biotechnol.* **21**, 255–61 (2003).
47. Han, X., Aslanian, A. & Yates, J. R. Mass spectrometry for proteomics. *Curr. Opin. Chem. Biol.* **12**, 483–490 (2008).
48. Silva, A. M. N., Vitorino, R., Domingues, M. R. M., Spickett, C. M. & Domingues, P. Post-translational modifications and mass spectrometry detection. *Free Radic. Biol. Med.* **65**, 925–941 (2013).

## CHAPTER 3

### SELECTIVE DETECTION OF PROTEIN HOMOLOGUES IN SERUM USING AN OMPG NANOPORE

Reprinted (adapted) with permission from M. A. Fahie, B. Yang, M. Mullis, M. A. Holden, and M. Chen, "Selective detection of protein homologues in serum using an OmpG nanopore," *Anal. Chem.*, vol. 87, no. 21, pp. 11143–11149, 2015. Copyright 2015 American Chemical Society.

#### 3.1 Summary

Outer membrane protein G is a monomeric  $\beta$ -barrel porin that has seven flexible loops on its extracellular side. Conformational changes of these labile loops induce gating spikes in current recordings that we exploited as the prime sensing element for protein detection. The gating characteristics - open probability, frequency and current decrease – provide rich information for analyte identification. Here, we show that two anti-biotin antibodies each induced a distinct gating pattern, which allowed them to be readily detected and simultaneously discriminated by a single OmpG nanopore in the presence of fetal bovine serum. Our results demonstrate the feasibility of directly profiling proteins in real-world samples with minimal or no sample pretreatment.

#### 3.2 Introduction

Nanopore sensing is a single molecule technique that measures the ionic current flowing through a nanoscopic pore in a membrane.<sup>1-3</sup> Analytes are detected when they cause transient current blockades as they bind or translocate through the pore. The intensity and duration of the blockades provide information about the structure, size and dynamic properties of analytes while the frequency of the blocking events indicates the concentration. Nanopores have been used to detect a large variety of analytes,<sup>4</sup> ranging

from small molecules, e.g. metal ions,<sup>5</sup> organic chemicals<sup>6,7</sup> and large biological macromolecules, including nucleic acids<sup>8–11</sup> and proteins.<sup>12</sup> For protein sensing, nanopores are usually coupled with a binding site for target proteins to ensure specific detection. The high affinity binding sites used so far have been derived from ligands,<sup>13,14</sup> inhibitors,<sup>15</sup> peptide sequences,<sup>16,17</sup> antibodies<sup>18</sup> and aptamers.<sup>19–21</sup> These binding sites are either introduced inside of the nanopore,<sup>18,21</sup> located at the entrance,<sup>17,19,20</sup> or conjugated with an auxiliary polymer in the solution.<sup>13,22–24</sup> In the latter case, detection is achieved when an analyte binds to a ligand at a polymer and alters the characteristic ionic current signatures derived from the polymer translocation through the nanopore.<sup>22,23</sup>

Outer membrane protein G (OmpG) is a 14 stranded  $\beta$ -barrel protein derived from *Escherichia coli* (*E. coli*).<sup>25–27</sup> Compared to other well studied protein nanopores, e.g.  $\alpha$ HL<sup>28</sup> and MspA<sup>9,29</sup> that are rigid, oligomeric membrane protein channels, OmpG is a monomeric protein with seven long flexible loops decorated at the extracellular entrance (Figure 3.1).<sup>30</sup> Loop 6 is the most flexible loop, causing the OmpG protein pore to oscillate between the open and closed states.<sup>25,31–33</sup> As a result, OmpG exhibits frequent gating in current recordings (Figure 3.1). Although pores exhibiting continuous nongating conductance have been considered a necessity for nanopore sensing, the gating noise/pattern of OmpG has been exploited as a sensing element for protein detection.<sup>34,35</sup> In OmpG sensing, analyte binding induces not only a current decrease by obstructing the pore entrance, but also a significant change in gating patterns by altering the dynamic movement of loop 6.<sup>34</sup> The gating pattern is sensitive to the interface formed between OmpG and analyte proteins.<sup>35</sup> Characteristics of gating, such as open probability, gating frequency, event duration and inter-event duration of the gating events provide multiple parameters for analyte identification. Using this strategy, multiple analytes were identified and simultaneously discriminated using a single OmpG nanopore in buffered solutions.<sup>34</sup>

One of the main challenges of protein sensing using nanopores is to identify target proteins in a complex mixture.<sup>36</sup> Most experiments have been performed under ideal conditions using only pure analytes in buffers. To apply this technique as a diagnostic tool for medical use, it is necessary to test the applicability of nanopores for detecting target analytes in clinically relevant samples, e.g. serum, urine or saliva. In this work, we show that two antibiotin antibodies can be readily detected and simultaneously discriminated by a single OmpG nanopore in the presence of 10-fold diluted serum. Our results demonstrate the feasibility of directly profiling proteins in real-world samples with minimal or no sample pre-treatments.

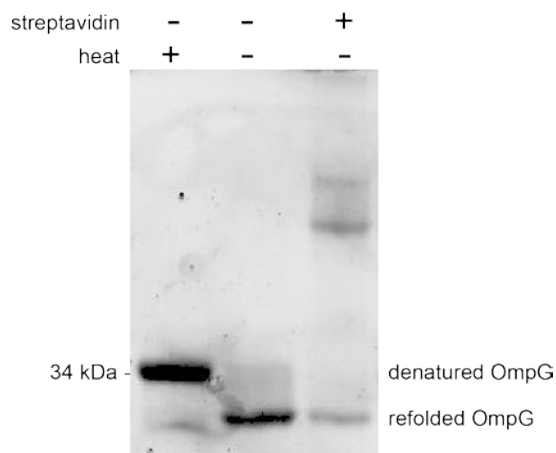
### **3.3 Materials and Methods**

All chemicals were obtained from Fisher Scientific or Boston Bioproducts unless otherwise stated. Chemicals were used without further purification. SB58C mouse monoclonal antibody was obtained from Southern Biotech (Cat# 6406-01) and BTN.4 mouse monoclonal antibody was obtained from Thermo Scientific (Cat# MS-1048-P1). Diphytanyolphosphatidylcholine (DPhPC) lipids were obtained from Avanti Polar Lipids. Teflon film was obtained from Goodfellow. The maleimide-PEG<sub>2</sub>-biotin linker was obtained from Thermo Scientific. Octylglucoside (OG) was obtained from Gold Biotechnology. Hexadecane and pentane were obtained from Sigma Aldrich.

#### **3.3.1 OmpG biosensor preparation**

OmpG D224C was purified and labeled with maleimide-PEG<sub>2</sub>-biotin as previously described.<sup>34, 35</sup> Briefly, OmpG D224C was expressed in BL21 (DE3) *E. coli* as inclusion bodies. The inclusion body pellet was solubilized in 8.0 M Urea, 50 mM Tris-HCl pH 8.0, 2 mM DTT for an hour prior to loading onto a HiTrap Q FF (GE Healthcare Life Sciences). OmpG D224C was then eluted with a gradient of 0-500 mM NaCl, 50 mM Tris-HCl, pH 8.0, 8 M urea and 2 mM DTT over 60 minutes. Purity of OmpG D224C was verified

by SDS-PAGE. Prior to labeling, OmpG D224C was desalted in 50 mM HEPES buffer, pH 7.0 and 8 M Urea to remove DTT and adjust the pH. OmpG D224C was then labeled with maleimide-PEG<sub>2</sub>-biotin by mixing OmpG and ligand in a 1:10 molar ratio for 2 hours with constant shaking at room temperature. OmpG was desalted once more in 50 mM Tris-HCl buffer, pH 8.0 in 8 M Urea to remove excess chemicals. OmpG was then diluted 1.5 times in refolding buffer 20 mM Tris-HCl, pH 9.0 with 3.25% octylglucoside and incubated for three days at 37 °C. Refolding and labeling efficiency was tested via a gel-shift assay as previously described (Figure 3.1).<sup>34</sup> OmpG-biotin was stored at -80 °C in 20% glycerol until further use.

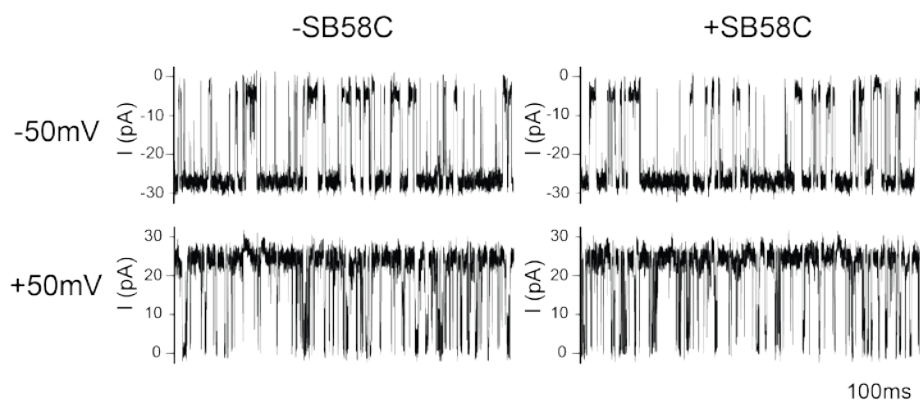


**Figure 3.1. SDS-PAGE analysis of refolding and labeling efficiency of OmpG-biotin.** After three days refolding at 37°C, samples of the OmpG-biotin protein was heated to 95°C for 15 minutes in Laemmli buffer or loaded without boiling to the 15% gel. To determine the labeling efficiency, the sample was mixed with streptavidin in a 1:1 molar ratio for 1 minute and then mixed with Laemmli buffer without boiling. Labeled OmpG forms a SDS-resistant complex with streptavidin which migrate slower in the gel. The intensity of the protein bands were analyzed by gel imager to calculate the labeling efficiency which was about 85%.

### 3.3.2 Single Channel Recording

Single channel recording was done as previously described.<sup>34</sup> Briefly, a 100 µm diameter aperture on a 25 µm thick Teflon film separating two chambers was painted with 10% hexadecane in pentane. The pentane was allowed to evaporate prior to filling the two chambers with buffer (10 mM sodium phosphate pH 6, 300 mM KCl). The bilayer

was formed by adding 15  $\mu\text{L}$  10 mg/mL DPhPC lipids in pentane on the aqueous surface of each chamber. Once the pentane evaporated, the buffer was pipetted up and down to coat the aperture with lipids. An Ag/AgCl electrode, with the *cis* electrode connected to ground, was immersed in each chamber. OmpG was pipetted into the *cis* chamber and 200 mV was applied to promote pore insertion into the bilayer. Once a pore was inserted, the voltage was decreased to 50 mV. Since OmpG inserts into the bilayer bidirectionally, the pore gating behavior was observed at both positive and negative 50 mV for five minutes to determine pore orientation.<sup>37</sup> All analyte proteins were introduced to the chamber where the OmpG loops are located. Unlabeled OmpG D224C was tested with SB analyte and did not generate a change in gating behavior (Figure 3.2). The positive potential is defined as the chamber where the loops are facing is positive. All data was acquired at  $\pm 50$  mV unless otherwise stated. The Axopatch 200B integrating patch clamp amplifier (Axon Instruments) was used to amplify the current and a 2 kHz Bessel filter was applied. Data was digitized with a Digidata 1320A/D board (Axon Instruments) and acquired at a sampling rate of 100  $\mu\text{s}$ .



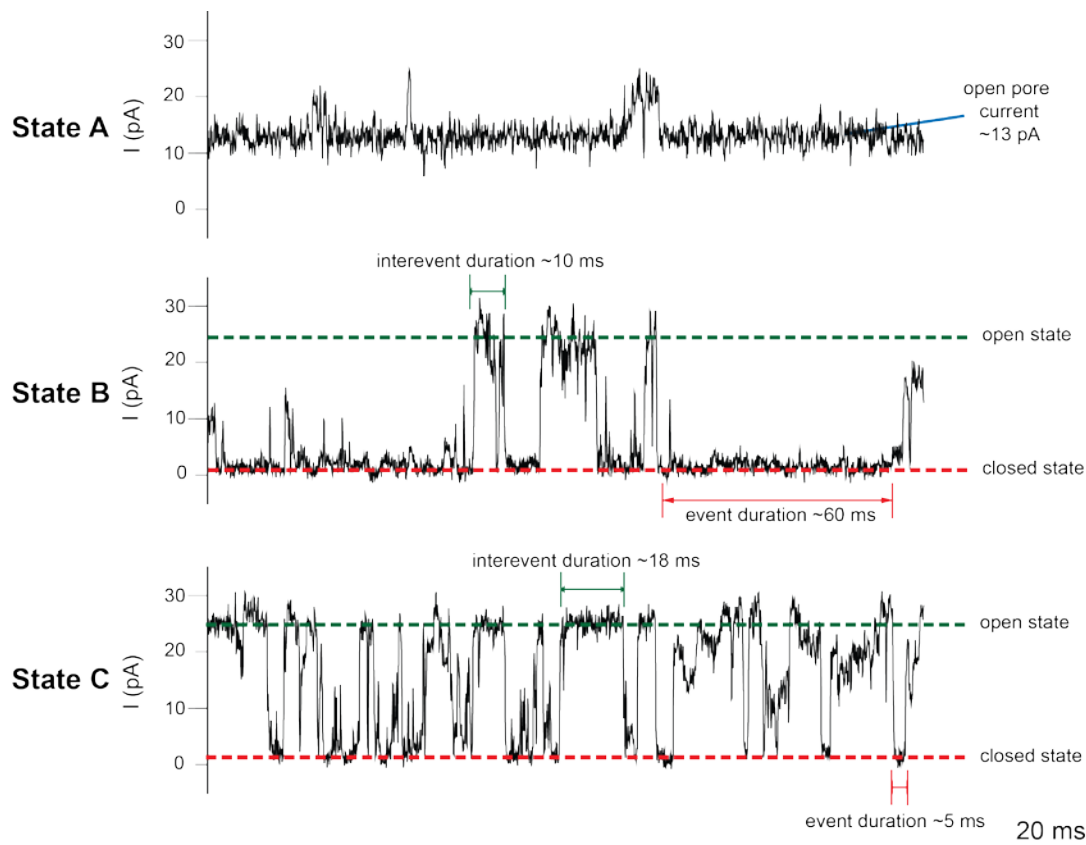
**Figure 3.2. Single channel current trace of OmpG D224C.** SB58C (2 nM) was added to unlabeled OmpG D224C and the ionic current monitored. There was no change in OmpG ionic current behavior. Buffer used was 10 mM sodium phosphate pH 6, 300 mM KCl and the ionic current recorded at both -50 and +50 mV. OmpG was recorded with a 2 kHz Bessel filter at a sampling rate of 100  $\mu\text{s}$ .

### 3.3.3 Single Channel analysis

OmpG gating was analyzed in Clampfit 10.3 software using the single channel search tool from at least 5 s of gating from several independent pores. The extracted dwell times of the open (inter-event) and closed state (event) were used to calculate the open probability, the inter-event duration, event duration, as well as the gating frequency. To determine the open probability, the sum of the open dwell times ( $\tau_{on}$ ) were divided by the total time analyzed, which includes both open and closed states of the OmpG pores. To determine the inter-event duration, the open dwell times ( $\tau_{on}$ ) were plotted in a histogram and fit with a single exponential function. The event duration was similarly calculated, but the closed dwell times ( $\tau_{off}$ ) were fit instead. For gating frequency, the trace was first filtered with a low pass Gaussian filter with a 1 kHz -3dB cut off. The total count of gating events was divided by the total time. To determine the open pore conductance, an all-events histogram of the trace was fit with a Gaussian function.

### 3.3.4 Analysis of gating characteristics

Gating characteristics used for generating the fingerprints of the two antibodies namely – open probability, gating frequency, event duration, inter-event duration and open conductance – are defined as shown in Figure 3.3. To calculate the gating characteristics of SB and BT binding at least 10 binding events with dwell times of at least 1 s from three independent traces or more were analyzed using the single channel search function in Clampfit 10.3. For SB analysis, its gating characteristics were further divided into three different gating types: A, B and C. These three gating types were analyzed independently from one another. Errors represent the standard deviation from the three independent pores (at least 30 events in total).



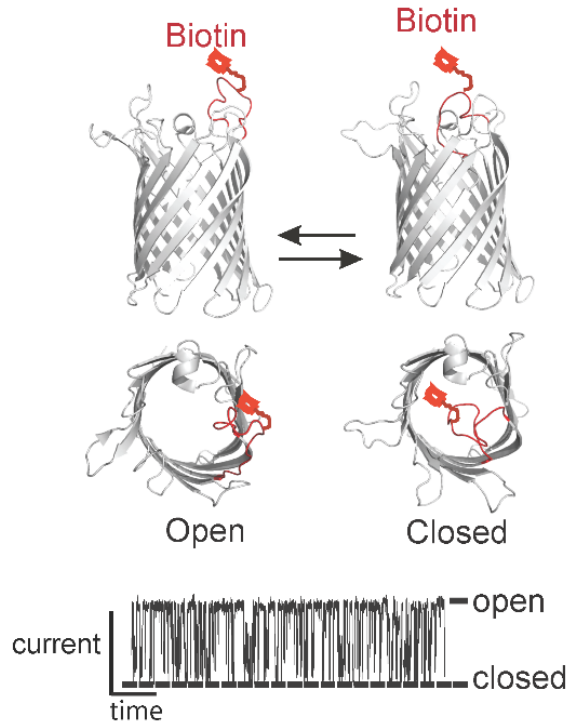
**Figure 3.3. Gating characteristics of the OmpG ionic current.** Three of the five gating parameters are defined in the trace. Open probability is the ratio of the open and closed state while gating frequency is the number of events per second. This trace is the SB binding states in the absence of serum at +50 mV. Buffer used was 10 mM sodium phosphate pH 6, 300 mM KCl. SB binding was recorded with a 2 kHz Bessel filter at a sampling rate of 100  $\mu$ s.

### 3.4 Results

Our OmpG nanopore (OmpG-PEG<sub>2</sub>-biotin) contains a tethered biotin ligand that can potentially extend into the solution up to 30 Å away from the OmpG loop 6 (in red) to which it is attached via a covalent linkage between mutated loop residue C224 and a maleimide moiety on the biotin ligand (Figure 3.4). We previously used this OmpG nanopore to detect and discriminate several biotin-binding proteins namely streptavidin, three anti-biotin antibodies: one mouse monoclonal (BTN.4) and two polyclonal antibodies raised in sheep<sup>34</sup> as well as two streptavidin homologues avidin and extravidin.<sup>35</sup>



Here, we first examined whether the OmpG-PEG<sub>2</sub>-biotin nanopore could also detect an alternative anti-biotin mouse monoclonal, SB58C (SB).



**Figure 3.4. The open (2IWV) and closed (2IWW) structures of OmpG.** The loop 6 is highlighted in red and is covalently attached to the biotin ligand. The ionic current trace was obtained in 10mM sodium phosphate pH 6, 300mM KCl buffer.

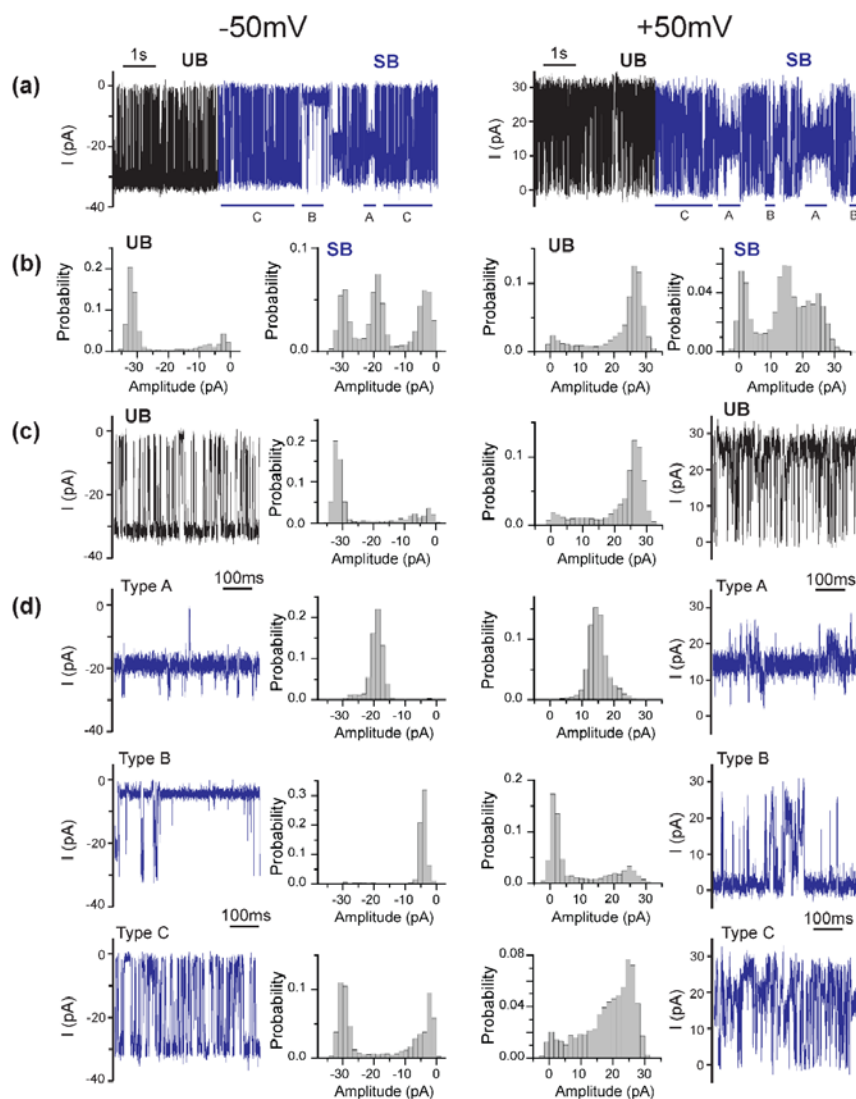
Addition of 1 nM SB to the loop-facing chamber induced a significant change in current traces (Table 3.1, Figure 3.5). At -50 mV, OmpG-biotin nanopore in the SB bound state exhibited the following characteristics: i) the current of the fully open state decreases slightly by 2 pA as shown in the histogram (Figure 3.5a-3.5c); ii) the current traces displayed gating patterns markedly different from that of the unbound states (Figure 3.5a, 3.5b). Interestingly, the gating pattern of the SB bound state is heterogeneous, i.e. a single SB binding event induced three different current fluctuation patterns which we named types A, B and C (Figure 3.5d). We categorize the three types of gating pat-

terns by their open-pore current, open probability and gating frequency (Table 3.1). Type A gating shows that the current was almost constant at  $-18.3 \pm 0.8$  pA which is 62 % of the fully open state current. Due to the lack of full gating events, the open probability is 1 and the gating frequency is 0 (Figure 3.5c, 3.5d). Type B binding shows that OmpG stays mostly closed where the open probability reduces from  $0.76 \pm 0.03$  to  $0.13 \pm 0.04$  with a residual current of  $2.1 \pm 0.5$  pA and a lowered gating frequency of  $32 \pm 4$  s<sup>-1</sup> (Figure 3.5d). Type C gating shows that the current fluctuates rapidly with a gating frequency of  $77 \pm 3$  s<sup>-1</sup>, a 13% increase over that of the unbound state ( $68 \pm 5$  s<sup>-1</sup>) and has an open probability of  $0.60 \pm 0.06$ . Each single SB binding event contains multiple combinations of these three types of gating (Figure 3.5a). This result is interesting as none of the previous biotin-binding protein analytes, including three streptavidin homologues and three biotin antibodies showed such a phenomenon.<sup>34,35</sup>

**Table 3.1.** The relative change in open probability, gating frequency and open current of OmpG-biotin during type A, B and C binding of SB58C

Loop Voltage (mV)	SB58C binding state	Relative Open Probability	Relative Gating Frequency	Relative Open pore current
-50	No bind	$1.00 \pm 0.04$	$1.00 \pm 0.22$	$1.00 \pm 0.05$
	Type A	$1.31 \pm 0.06$	N.D.	$0.62 \pm 0.02$
	Type B	$0.16 \pm 0.05$	$0.46 \pm 0.06$	$0.07 \pm 0.02$
	Type C	$0.79 \pm 0.07$	$1.1 \pm 0.04$	$0.94 \pm 0.04$
+50	No bind	$1.00 \pm 0.02$	$1.00 \pm 0.09$	$1.00 \pm 0.03$
	Type A	$1.22 \pm 0.03$	N.D.	$0.54 \pm 0.03$
	Type B	$0.19 \pm 0.05$	$0.55 \pm 0.10$	$0.04 \pm 0.01$
	Type C	$0.83 \pm 0.06$	$1.38 \pm 0.08$	$0.92 \pm 0.05$

\*The errors indicate standard deviations from at least three independent pores.



**Figure 3.5. Detection of SB58C by OmpG-biotin nanopore.** (a,b) The electrophysiology traces and all events histograms of unbound (UB) and SB-bound states of OmpG-biotin at -50 mV and +50 mV. (c) Zoomed-in electrophysiology traces and all-events histograms of the unbound state and (d) the three independent SB-binding states types A, B and C. Buffer used was 10 mM sodium phosphate pH 6, 300 mM KCl. 1nM SB antibody was added to the recording chamber. SB binding was recorded with a 2 kHz Bessel filter at a sampling rate of 100  $\mu$ s.

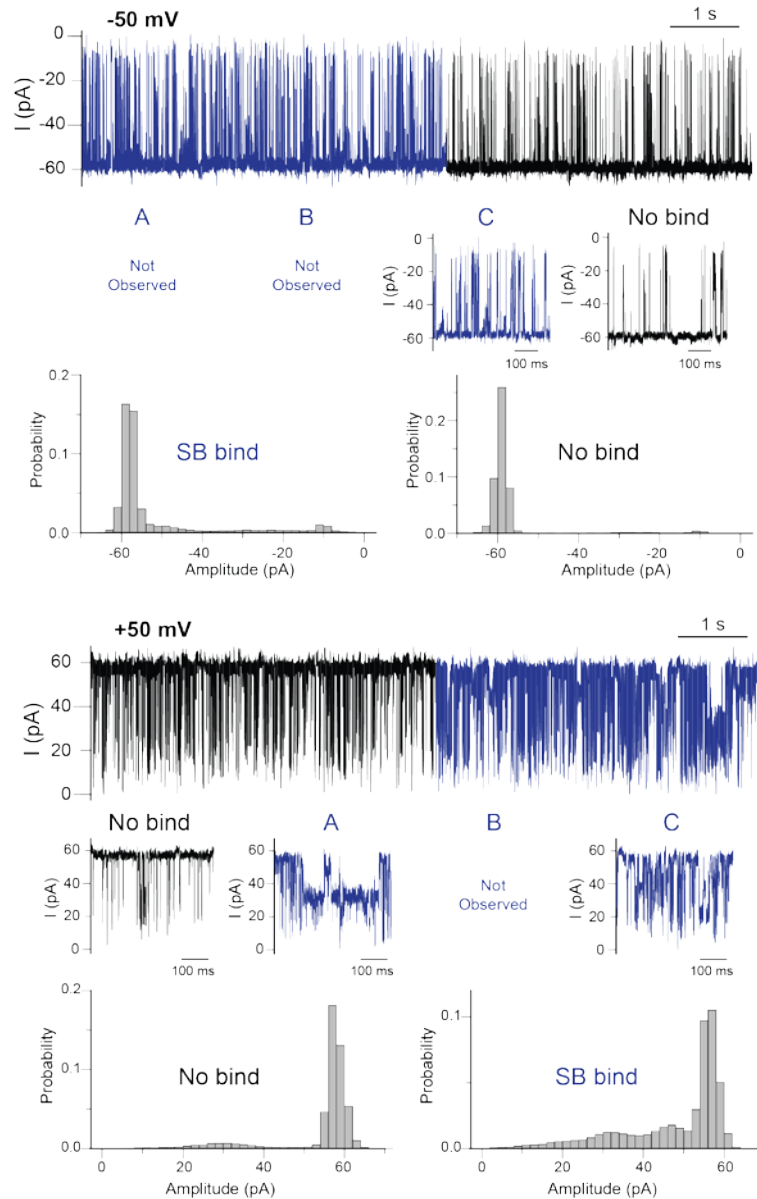
Because the gating pattern of the analyte bound state is dictated by the interaction between analyte and OmpG surface, this result indicates when SB bound to the tethered ligand, it often altered the way in which it interacted with the OmpG surface. Our previous study demonstrated that electrostatic attractions are the dominant force that triggers the interaction between analyte and the OmpG loops.<sup>35</sup> Consistent with our

previous finding, increasing the salt concentration to 1.0 M KCl in the recording buffer almost abolished the type B and A binding while the type C binding became similar to the unbound state (Figure 3.6).

Here, we speculate that the SB antibody might contain multiple positively charged regions separately located in areas close to the biotin-binding site. Each positive region can form a unique binding interface with the negatively charged OmpG loops which triggers a gating pattern different from each other. The ability to trigger multiple gating signatures within one binding event is a great advantage for analyte identification and reveals the sensitivity of our OmpG sensor to subtle changes in the analyte surface.

At +50 mV, we also observed that a single SB induced the three types of gating patterns albeit with slight variations from those at -50 mV. For example, in Type A binding, the open current changes more than at -50 mV, to 54% of the fully open state current (Table 3.1). Type B has essentially no residual current and a gating frequency of  $59 \pm 10 \text{ s}^{-1}$ . Finally, type C gating frequency is  $149.5 \pm 8.2 \text{ s}^{-1}$  (a 38% increase to that of the unbound state) and an open probability of  $0.68 \pm 0.05$  (17% reduction from the unbound state). This observation is consistent with previous finding that the polarity of voltage has a strong influence on the gating characteristics of the analyte bound state. This is due to two factors: i) the polarity of voltage has a strong influence on the gating of OmpG which exhibits asymmetric current gating at positive and negative potential<sup>34</sup> and ii) the voltage could alter the strength of OmpG and analyte interaction through electroosmotic and/or electrophoretic effects. The binding of SB to OmpG-biotin nanopore was specific as no change in behavior occurred with un-biotinylated OmpG D224C (Figure 3.2). The SB antibody appeared to have a high affinity for the biotin ligand as the binding events usually lasted for at least 2 min, 30 times longer than that of a monoclonal antibody BTN.4 that was previously tested, which had a dissociation constant of  $1.12 \pm 0.28 \times 10^8$

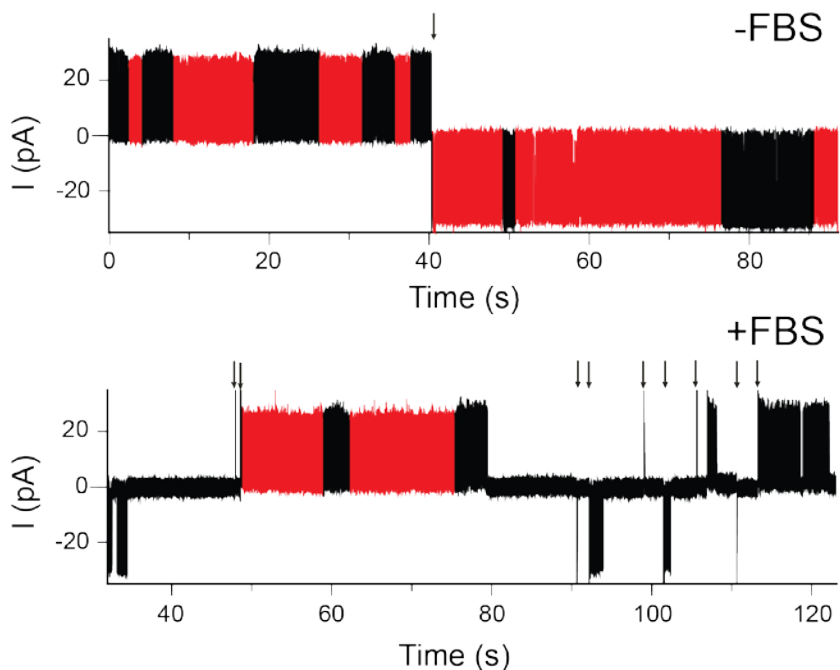
$M^{-1}$ .<sup>34</sup> SB bound for so long that we were not able to calculate the binding kinetics, mainly because the bilayer does not last long to allow to collect enough (~1000) events for accurate data analysis. The lowest concentration of SB we detected was 15 pM within 60 min indicating the high sensitivity of our approach and sensor.



**Figure 3.6. Detection of SB58C by OmpG-biotin nanopore in high salt.** At both -50 and +50 mV, binding state C was the predominant state. Binding state B was completely abolished, while binding state A was periodically seen at +50 mV. Buffer used was 10 mM Tris-HCl pH 8, 1.0 M KCl. Traces were recorded with a 2 kHz Bessel filter at a sampling rate of 100  $\mu$ s.

Previously, we have demonstrated that the OmpG-biotin nanopore could discriminate among three anti-biotin antibodies in an antibody protein mixture.<sup>34</sup> To use OmpG nanopore in clinical applications, OmpG would need to detect analyte and possibly discriminate among homologous proteins in a biological sample such as blood serum. Therefore, we investigated how the presence of serum affected the gating of the OmpG-biotin nanopore.

In the presence of 25% (v/v) fetal bovine serum the bilayer was unstable at  $\pm 50$  mV thus we lowered the concentration to 10% (v/v). We initially added the serum to both chambers, however, under these conditions OmpG could not remain in an open state at any applied potential for long periods of time (Figure 3.7).

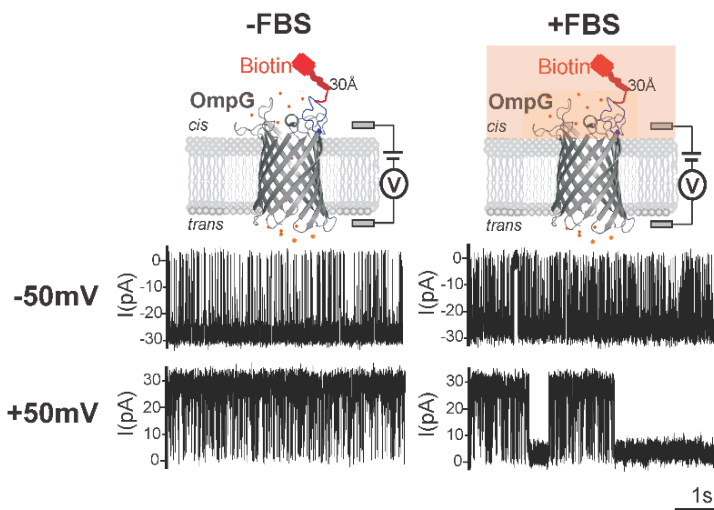


**Figure 3.7. The effect of 10% serum added to both chambers on the gating behavior of OmpG-biotin.** 100  $\mu$ l of FBS was added to both chambers to a final concentration of 10% (v/v). The buffer was 10 mM sodium phosphate pH 6.0, 300 mM KCl. OmpG was recorded with a 2 kHz Bessel filter at a sampling rate of 100  $\mu$ s. Arrows indicate a switch in voltage polarity.

Thus we decided to add 10% (v/v) serum to only the chamber where the loops were located. This induced a noisier gating signal in the OmpG nanopore at both volt-

ages (Figure 3.8). The gating frequency almost doubled at -50 mV (Table 3.2). Also, the inter-event duration was significantly reduced from  $6.37 \pm 1.88$  ms to  $0.96 \pm 0.31$  ms *i.e.* a 6.6-fold reduction. The open probability and event duration were also affected, undergoing a 5% and 61% reduction, respectively (Table 3.2).

At +50 mV, in addition to an increase in gating behavior, frequent full blockage events were observed (similar to when serum was added to both chambers). These blockage events could last from seconds to minutes if the voltage was left unperturbed. Unblocking the pore could be achieved by switching the voltage polarity from +50 to -50 mV. The increased gating frequency and the long closures were likely due to the interaction of serum constituents. These possibly included small molecules and proteins that may have been driven by diffusion, electro-osmosis and electrophoresis near the OmpG loops and into the lumen. Importantly, despite the high protein content in serum, we did not observe any gating pattern changes that were similar to the analyte protein binding, thereby demonstrating the high specificity of OmpG nanopore detection.



**Figure 3.8.** The effect of serum added to one chamber only on the gating behavior of OmpG-biotin. 100  $\mu$ l of FBS was added to the loop-containing chamber to a final concentration of 10% (v/v). The buffer was 10 mM sodium phosphate pH 6.0, 300 mM KCl. OmpG was recorded with a 2 kHz Bessel filter at a sampling rate of 100  $\mu$ s.

**Table 3.2.** The gating characteristics of the unbound state, the BT and SB bound states in the absence and presence of 10% (v/v) serum.

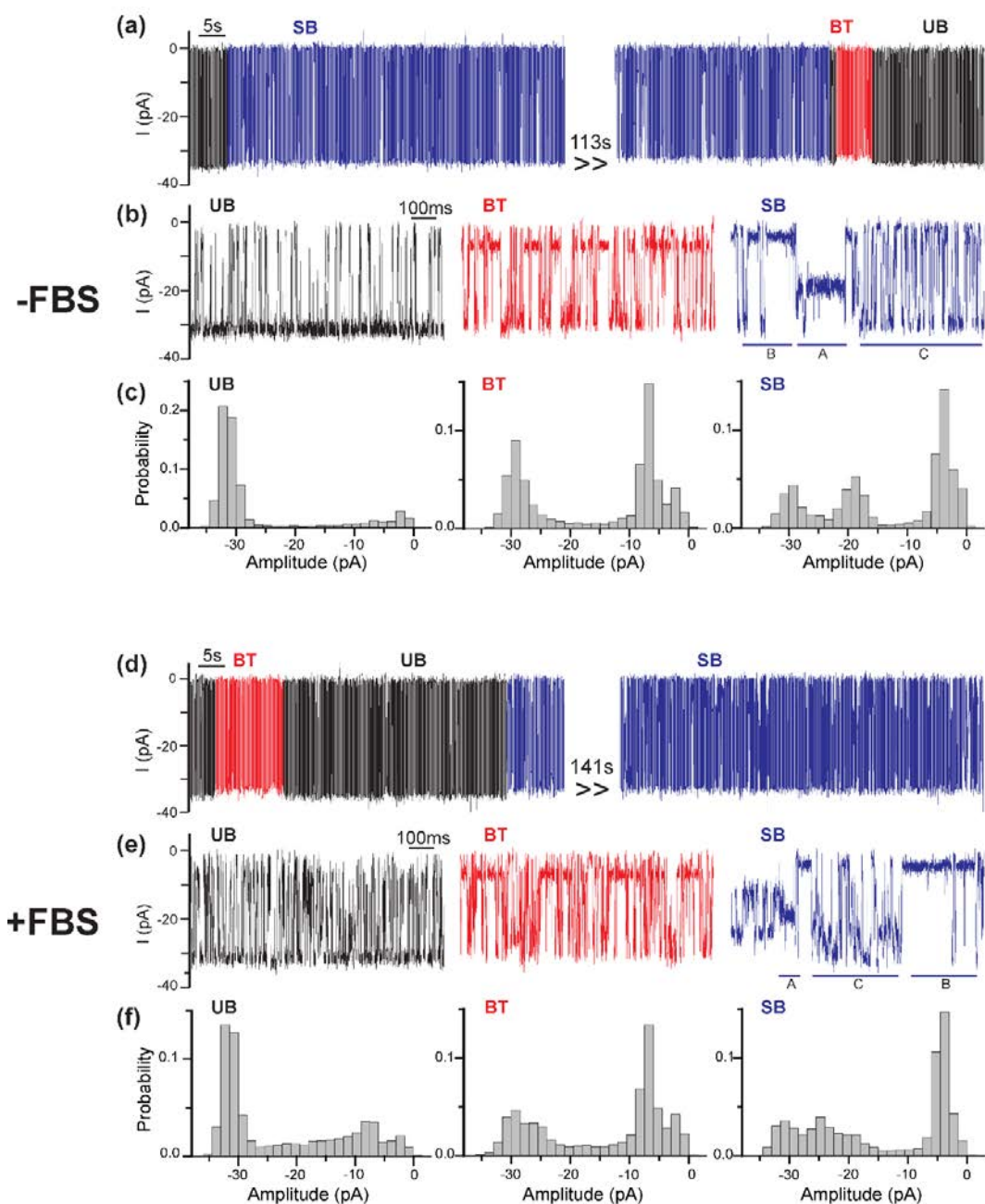
	Open probability	Gating Frequency (s <sup>-1</sup> )	Inter-event duration (ms)	Event duration (ms)	Open pore conductance (pA)
No bind - FBS	0.78 ± 0.03	68 ± 15	6.37 ± 1.88	2.23 ± 0.50	-29.3 ± 1.4
No bind + FBS	0.73 ± 0.06	121 ± 13	0.96 ± 0.31	1.35 ± 0.32	-30.1 ± 2.3
BTN.4 - FBS	0.52 ± 0.08	113 ± 4	0.97 ± 0.21	1.76 ± 0.34	-27.7 ± 1.3
BTN.4 + FBS	0.48 ± 0.16	146 ± 24	0.56 ± 0.19	1.46 ± 0.34	-28.7 ± 2.1
SB58C Type A - FBS	1.00 ± 0.00	0 ± 0	N.D.	N.D.	-18 ± 0.6
SB58C Type A + FBS	1.00 ± 0.00	0 ± 0	N.D.	N.D.	-20.2 ± 1.0
SB58C Type B - FBS	0.13 ± 0.04	32 ± 4	0.70 ± 0.04	3.92 ± 0.23	-2.1 ± 0.5
SB58C Type B + FBS	0.12 ± 0.04	20 ± 5	0.44 ± 0.03	2.16 ± 0.08	-3.8 ± 0.9
SB58C Type C - FBS	0.60 ± 0.06	77 ± 3	1.41 ± 0.07	0.86 ± 0.3	-27.5 ± 1.0
SB58C Type C + FBS	0.60 ± 0.11	121 ± 13	0.39 ± 0.10	0.74 ± 0.21	-29.9 ± 1.2

\*The error bars indicate standard deviations from at least three independent pores.

Because the serum-induced blockages at +50 mV reduced the fraction of time that the OmpG nanopore was able to receive an analyte protein, we focused on testing the discriminatory ability of OmpG-biotin at -50 mV. As shown in Figure 3.9a, the addition of two monoclonal antibodies – clones SB58C (SB) and BTN.4 (BT) – to the recording chamber containing only buffer triggered binding signals with distinct characteristics that can be recognized qualitatively and quantitatively.

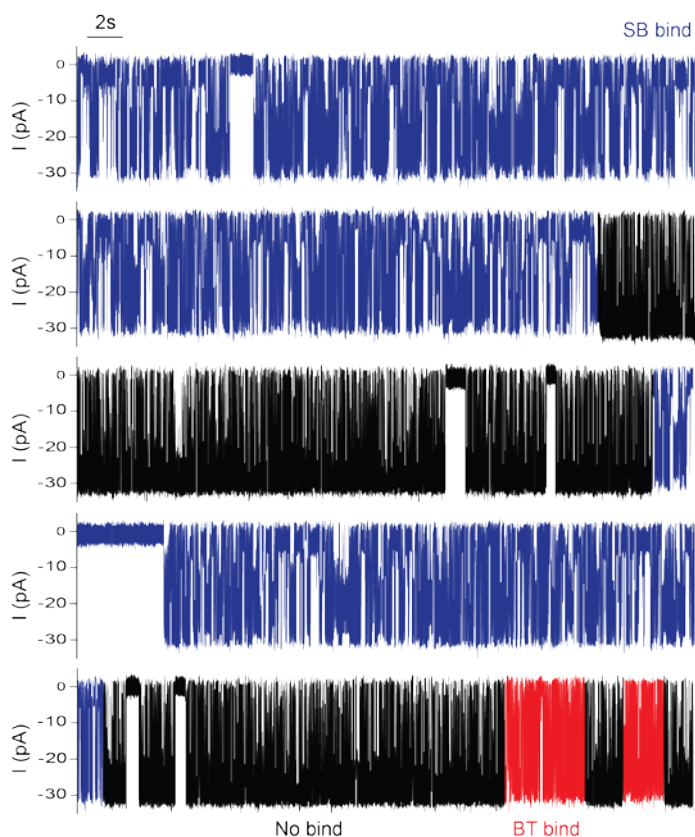
Both proteins induced a slight decrease ~ 6% in open pore current (Table 3.2, Figure 3.9b). The SB-type binding exhibited its typical heterogeneous gating signal while the BT-binding triggered a gating pattern containing a partially closed state with a residual current of 6 pA, which is consistent with previous finding when BT was added to the OmpG-biotin alone.<sup>34</sup> Thus, in the absence of FBS, OmpG could discriminate SB from BT by their respective binding signatures (Figure 3.9a-c).





**Figure 3.9. Discrimination of two antibodies in the presence of serum.** (a) Binding of SB (blue) and BT (red) to OmpG-biotin in the absence of serum. (b) Electrophysiology traces and (c) histograms of the unbound state in comparison with the BT and SB bound states. Buffer used was 10 mM sodium phosphate pH 6.0, 300 mM KCl and recorded at -50 mV. SB (1 nM) and BT (5 nM) were added to the recording chamber. (d) BT and SB binding in the presence of serum. (e) Electrophysiology traces and (f) histograms of BT and SB binding in the presence of serum. In addition to SB and BT, serum (10% v/v) was added to the loop-containing chamber. SB and BT binding were recorded with a 2 kHz Bessel filter at a sampling rate of 100  $\mu$ s.

In the presence of 10% (v/v) serum, the current traces of SB and BT bound states were noisier than those without serum (Figure 3.9a-f). Nevertheless, individual binding signatures of SB and BT were well-preserved; both analytes still induced a decrease in the open pore current. The heterogeneous gating pattern induced by SB was readily visible. Clearly, the different gating patterns between SB and BT allowed us to resolve between two homologues in serum (Figure 3.9).

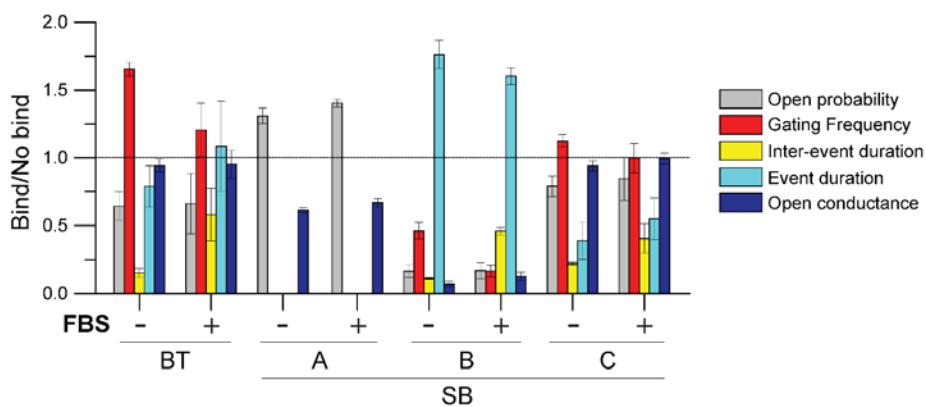


**Figure 3.10. Simultaneous detection of two antibodies in serum.** A continuous trace (170 s) of SB (1 nM, blue) and BT (5 nM, red) binding to OmpG-biotin in the absence of 10% (v/v) serum. Buffer used was 10 mM sodium phosphate pH 6, 300 mM KCl and the ionic current recorded at -50 mV. SB and BT were recorded with a 2 kHz Bessel filter at a sampling rate of 100  $\mu$ s.

Although a previous study has also shown a protein A coated solid-state nanopore can discriminate IgG species, the detection relied on their difference in dwell times, which differ by an order of magnitude.<sup>18</sup> Although BT and SB possessed markedly different dwell times (Figure 3.10), differentiation among the two analytes by OmpG

was achieved through their characteristic binding signals. Therefore, this detection mechanism would allow the differentiation of different analytes that have similar dwell times, an advantage that is beginning to be seen with other engineered nanopores.<sup>20,38</sup>

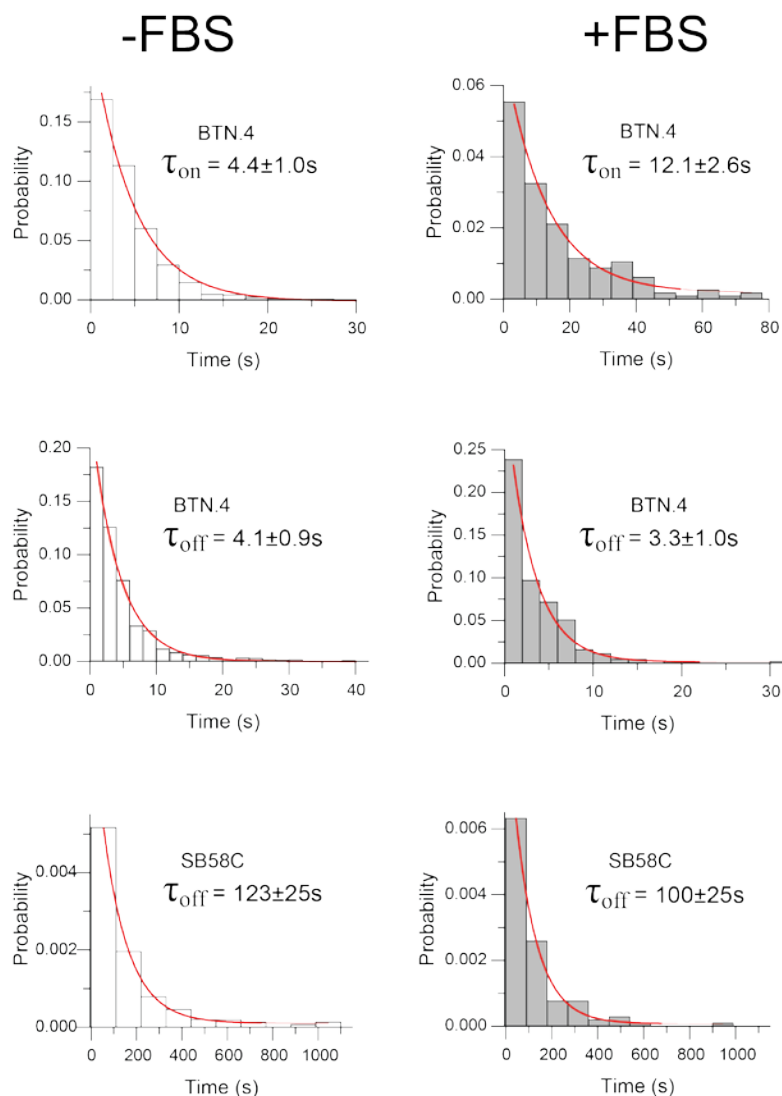
To quantitatively study how serum affected the gating of the analyte-bound state, we calculated five parameters: open probability, gating frequency, event duration, inter-event duration and open pore current in the presence and absence of serum. When BT bound to OmpG-biotin in the presence of serum, the open probability, event duration and open pore current were not significantly different from those in the absence of serum (Figure 3.11, Table 3.2).



**Figure 3.11. The effect of serum on the fingerprint pattern of BT and SB.** The gating events of different analyte protein binding states were characterized by five parameters, i.e. open probability, gating frequency, inter-event duration, event duration and the conductance of the open pore state. Changes of these parameters relative to the no binding state generate the fingerprint unique for each antibody. For SB, the three types of gating pattern were analyzed separately. The error bars indicate standard deviations from at least three independent pores.

The inter-event duration was decreased by ~1.5 times and the gating frequency increased by 1.3 times. Similar to BT, moderate changes were also observed for SB type C binding characteristic in the presence of FBS. FBS showed little effect on the type A and type B signals probably due to the lack of gating in these two types of signals. In previous studies, we used the relative values of bound and unbound states to create a

fingerprint for analyte identification.<sup>34,35</sup> The gating fingerprint of BT in the presence of serum compared to the absence of serum was different. This altered fingerprint in the presence in serum was due mainly to the non-specific effects of serum molecules on OmpG gating, rather than a direct effect on the antibody-OmpG interaction. Despite the effect of serum, the fingerprints of the two analytes are clearly distinguishable.



**Figure 3.12. Effect of FBS on the kinetics of antibody binding.** Histograms of the inter-event duration ( $\tau_{on}$ ) and dwell time ( $\tau_{off}$ ) of mAb binding events were fitted with single exponential decay function to derive the average time constants. Tau-on values for BT were calculated from 10 nM. Buffer used was 10 mM sodium phosphate pH 6, 300 mM KCl and the ionic current was recorded at both -50 mV. Averages and standard deviations were taken from three independent pores.

Next we analyzed the effect of serum on the kinetics of analyte binding. The association rate constant  $k_{on}$  and dissociation rate constant  $k_{off}$  of BT were calculated from the  $\tau_{on}$  and  $\tau_{off}$ , respectively, in the absence and presence of FBS (Figure 3.12). The  $k_{off}$  value slightly increased in serum from  $0.24 \pm 0.05 \text{ s}^{-1}$  to  $0.30 \pm 0.09 \text{ s}^{-1}$  ( $n=3$ ). However, the  $k_{on}$  value decreased from  $2.27 \pm 0.52 \times 10^7 \text{ M}^{-1}\text{s}^{-1}$  to  $0.83 \pm 0.18 \times 10^7 \text{ M}^{-1}\text{s}^{-1}$  by ~3-fold in FBS. The slower  $k_{on}$  of BT in the presence of serum could be due to molecular crowding effects in the high concentration of serum proteins that interact non-specifically with BT (and OmpG) and slow down its diffusion to the pore.<sup>39</sup> This result indicates the serum slightly impedes the sensitivity of OmpG, since detection of the same number of binding events in serum-free buffer would require longer operating and recording time in the presence of serum.

Recently several reports have focused on the issue of sensing specific analytes in protein mixtures.<sup>16,22</sup> Specifically, an engineered phi29 nanopore containing an engineered peptide sequence was shown to detect a target antibody in 1% (v/v) serum.<sup>16</sup> In this study, current blockage histograms of antibody binding in the presence of serum exhibited two slightly overlapping peaks corresponding to the target protein and serum protein, respectively. Because a small portion of serum protein binding events induced current blockades similar to target antibody, detection could be achieved only when the concentration of target protein is significantly above the interfering impurities. Our work shows that the target binding signals are readily distinguishable from that of serum constituents, allowing unambiguous recognition of each target binding events. Moreover, the fact that OmpG could distinguish two homologous analytes in the presence of serum represents an exciting step forward in nanopore sensing. To date, our OmpG-biotin sensor has been able to discriminate among eight analytes: two monoclonal antibodies, two polyclonal antibodies<sup>34</sup> and four avidin glyco-isoforms.<sup>35</sup> To our knowledge, no other nanopore thus far has shown such selectivity towards as many analytes. The flexible struc-

ture of OmpG may adopt distinct conformations for each analyte, which serves as the foundation for generating many unique current gating signals. The high selectivity of the OmpG nanopore can be exploited for profiling of protein homologues or post-translationally modified isoforms. The ability to identify cell-specific isoforms could aid in the discovery of potential therapeutic targets and disease diagnostics.<sup>40,41</sup> Thus, as a complementary approach to mass spectrometry and protein micro-arrays for proteomic study, our OmpG nanopore sensor provides a powerful detection platform that could deliver rapid readouts with little to no sample preparation.

### **3.6 Conclusions**

In this study, we have shown that the OmpG nanopore is able to simultaneously detect multiple homologous antibody analytes in serum with high specificity and selectivity. Our study demonstrates the feasibility of protein isoform profiling in a real-world setting.

### 3.7 References

1. Bayley, H. & Cremer, P. S. Stochastic sensors inspired by biology. *Nature* **413**, 226–230 (2001).
2. Howorka, S. & Siwy, Z. Nanopore analytics: sensing of single molecules. *Chem. Soc. Rev.* **38**, 2360–2384 (2009).
3. Bezrukov, S. M., Vodyanoy, I. & Parsegian, V. A. Counting polymers moving through a single ion channel. *Nature* **370**, 279–281 (1994).
4. Majd, S. *et al.* Applications of biological pores in nanomedicine, sensing, and nanoelectronics. *Curr. Opin. Biotechnol.* **21**, 439–476 (2010).
5. Braha, O. *et al.* Simultaneous stochastic sensing of divalent metal ions. *Nat. Biotechnol.* **18**, 1005–1007 (2000).
6. Gu, L. Q., Braha, O., Conlan, S., Cheley, S. & Bayley, H. Stochastic sensing of organic analytes by a pore-forming protein containing a molecular adapter. *Nature* **398**, 686–690 (1999).
7. Wu, H. C. & Bayley, H. Single-molecule detection of nitrogen mustards by covalent reaction within a protein nanopore. *J. Am. Chem. Soc.* **130**, 6813–6819 (2008).
8. Kasianowicz, J. J., Brandin, E., Branton, D. & Deamer, D. W. Characterization of individual polynucleotide molecules using a membrane channel. *Proc. Natl. Acad. Sci. U. S. A.* **93**, 13770–13773 (1996).
9. Manrao, E. A. *et al.* Reading DNA at single-nucleotide resolution with a mutant MspA nanopore and phi29 DNA polymerase. *Nat. Biotechnol.* **30**, 349–353 (2012).
10. Wanunu, M. Nanopores: A journey towards DNA sequencing. *Phys. Life Rev.* **9**, 125–158 (2012).
11. Branton, D. *et al.* The potential and challenges of nanopore sequencing. *Nat. Biotechnol.* **26**, 1146–1153 (2008).
12. Movileanu, L. Interrogating single proteins through nanopores: challenges and opportunities. *Trends Biotechnol.* **27**, 333–341 (2009).
13. Movileanu, L., Howorka, S., Braha, O. & Bayley, H. Detecting protein analytes that modulate transmembrane movement of a polymer chain within a single protein pore. *Nat. Biotechnol.* **18**, 1091–1095 (2000).
14. Yusko, E. C. *et al.* Controlling protein translocation through nanopores with bio-inspired fluid walls. *Nat. Nanotechnol.* **6**, 253–60 (2011).
15. Xie, H., Braha, O., Gu, L. Q., Cheley, S. & Bayley, H. Single-molecule observation of the catalytic subunit of cAMP-dependent protein kinase binding to an inhibitor peptide. *Chem. Biol.* **12**, 109–120 (2005).
16. Wang, S., Haque, F., Rychahou, P. G., Evers, B. M. & Guo, P. Engineered nanopore of phi29 dna-packaging motor for real-time detection of single colon cancer specific antibody in serum. *ACS Nano* **7**, 9814–9822 (2013).
17. Cheley, S., Xie, H. & Bayley, H. A genetically encoded pore for the stochastic detection of a protein kinase. *ChemBioChem* **7**, 1923–1927 (2006).
18. Wei, R., Gatterdam, V., Wieneke, R., Tampé, R. & Rant, U. Stochastic sensing of proteins with receptor-modified solid-state nanopores. *Nat. Nanotechnol.* **7**, 257–63 (2012).
19. Rotem, D., Jayasinghe, L., Salichou, M. & Bayley, H. Protein detection by nanopores equipped with aptamers. *J. Am. Chem. Soc.* **134**, 2781–7 (2012).
20. Soskine, M. *et al.* An engineered ClyA nanopore detects folded target proteins by selective external association and pore entry. *Nano Lett.* **12**, 4895–900 (2012).
21. Ding, S., Gao, C. & Gu, L. Q. Capturing single molecules of immunoglobulin and ricin with an aptamer-encoded glass nanopore. *Anal. Chem.* **81**, 6649–6655

- (2009).
22. Bell, N. A. W. & Keyser, U. F. Specific Protein Detection Using Designed DNA Carriers and Nanopores. *J. Am. Chem. Soc.* **137**, 2035–2041 (2015).
  23. Plesa, C., Ruitenber, J. W., Witteveen, M. J. & Dekker, C. Detection of Single Proteins Bound along DNA with Solid-State Nanopores. *Nano Lett.* **15**, 3153–3158 (2015).
  24. Kasianowicz, J. J., Henrickson, S. E., Weetall, H. H. & Robertson, B. Simultaneous multianalyte detection with a nanometer-scale pore. *Anal. Chem.* **73**, 2268–2272 (2001).
  25. Yildiz, O., Vinothkumar, K. R., Goswami, P. & Kühlbrandt, W. Structure of the monomeric outer-membrane porin OmpG in the open and closed conformation. *EMBO J.* **25**, 3702–13 (2006).
  26. Liang, B. & Tamm, L. K. Structure of outer membrane protein G by solution NMR spectroscopy. *Proc. Natl. Acad. Sci. U. S. A.* **104**, 16140–5 (2007).
  27. Subbarao, G. V & van den Berg, B. Crystal structure of the monomeric porin OmpG. *J. Mol. Biol.* **360**, 750–9 (2006).
  28. Song, L. *et al.* Structure of staphylococcal alpha-hemolysin, a heptameric transmembrane pore. *Science* **274**, 1859–66 (1996).
  29. Butler, T. Z., Pavlenok, M., Derrington, I. M., Niederweis, M. & Gundlach, J. H. Single-molecule DNA detection with an engineered MspA protein nanopore. *Proc. Natl. Acad. Sci.* **105**, 20647–20652 (2008).
  30. Conlan, S., Zhang, Y., Cheley, S. & Bayley, H. Biochemical and Biophysical Characterization of OmpG: A Monomeric Porin †. *Biochemistry* **39**, 11845–11854 (2000).
  31. Chen, M., Khalid, S., Sansom, M. S. P. & Bayley, H. Outer membrane protein G: Engineering a quiet pore for biosensing. *Proc. Natl. Acad. Sci. U. S. A.* **105**, 6272–7 (2008).
  32. Zhuang, T., Chisholm, C., Chen, M. & Tamm, L. K. NMR-based conformational ensembles explain pH-gated opening and closing of OmpG channel. *J. Am. Chem. Soc.* **135**, 15101–13 (2013).
  33. Zhuang, T. & Tamm, L. K. Control of the conductance of engineered protein nanopores through concerted loop motions. *Angew. Chem. Int. Ed. Engl.* **53**, 5897–902 (2014).
  34. Fahie, M., Chisholm, C. & Chen, M. Resolved Single-Molecule Detection of Individual Species within a Mixture of anti-Biotin Antibodies Using an Engineered Monomeric Nanopore. *ACS Nano* **9**, 1089–1098 (2015).
  35. Fahie, M. A. & Chen, M. Electrostatic Interactions between OmpG Nanopore and Analyte Protein Surface Can Distinguish between Glycosylated Isoforms. *J. Phys. Chem. B* **119**, 10198–10206 (2015).
  36. Howorka, S. & Siwy, Z. S. Nanopores as protein sensors. *Nat. Biotechnol.* **30**, 506–507 (2012).
  37. Chen, M., Li, Q.-H. & Bayley, H. Orientation of the monomeric porin OmpG in planar lipid bilayers. *ChemBiochem* **9**, 3029–36 (2008).
  38. Nir, I., Huttner, D. & Meller, A. Direct Sensing and Discrimination among Ubiquitin and Ubiquitin Chains Using Solid-State Nanopores. *Biophys. J.* **108**, 2340–2349 (2015).
  39. Roosen-Runge, F. *et al.* Protein self-diffusion in crowded solutions. *Proc. Natl. Acad. Sci. U. S. A.* **108**, 11815–11820 (2011).
  40. Nomura, D. K., Dix, M. M. & Cravatt, B. F. Activity-based protein profiling for biochemical pathway discovery in cancer. *Nat. Rev. Cancer* **10**, 630–638 (2010).
  41. Zhao, J., Patwa, T. H., Lubman, D. M. & Simeone, D. M. Protein biomarkers in



cancer: natural glycoprotein microarray approaches. *Curr. Opin. Mol. Ther.* **10**, 602–10 (2008).

## CHAPTER 4

### TUNING THE SELECTIVITY AND SENSITIVITY OF AN OMPG NANOPORE SENSOR BY ADJUSTING LIGAND TETHER LENGTH

Reprinted (adapted) with permission from M. A. Fahie, B. Yang, B. Pham, and M. Chen, "Tuning the Selectivity and Sensitivity of an OmpG Nanopore Sensor by Adjusting Ligand Tether Length," *ACS Sensors*, vol. 1, no. 5, pp. 614–622, 2016. Copyright 2016 American Chemical Society.

#### 4.1 Summary

We have previously shown that a biotin ligand tethered to the rim of an OmpG nanopore can be used to detect biotin-binding proteins. Here, we investigate the effect of the length of the polyethylene glycol tether on the nanopore's sensitivity and selectivity. When the tether length was increased from 2 to 45 ethylene repeats, sensitivity decreased substantially for a neutral protein streptavidin and slightly for a positively charged protein (avidin). In addition, we found that two distinct avidin binding conformations were possible when using a long tether. These conformations were sensitive to the salt concentration and applied voltage. Finally, a longer tether resulted in reduced sensitivity due to slower association for a monoclonal anti-biotin antibody. Our results highlight the importance of electrostatic, electroosmotic and electrophoretic forces on nanopore binding kinetics and sensor readout.

#### 4.2 Introduction

Nanopores sensing is a single molecule approach by which analytes are sensed when they interfere with ionic current flowing through the pore during an applied potential.<sup>1–5</sup> Nanopores are broadly grouped into two classes: solid state nanopores and protein nanopores.<sup>1,4</sup> Solid-state nanopores are fabricated from silicon nitride, glass or

polymer substrates.<sup>6-8</sup> Solid-state nanopores possess several advantages including the physical and chemical robustness, tunable pore size and shape. On the other hand protein nanopores always have the same, atomically precise structure. Generally, nanopores detect proteins by one of two mechanisms: translocation-dependent or translocation-independent. For translocation-dependent sensing, the analyte is drawn into the pore by electrophoresis, which partially blocks the flow of ionic current. Both solid-state and protein nanopores applied this strategy to detect targets including BSA,<sup>9-</sup><sup>11</sup> streptavidin/avidin,<sup>12,13</sup> antibodies,<sup>12,14</sup> and polyarginine peptides.<sup>15</sup> Alternatively, some proteins may be sensed via binding to an auxiliary polymer that threads through the nanopore.<sup>16-18</sup> Because ionic current is sensitive to the size, shape, and surface properties of the analyte protein, as well as analyte-lumen interactions, nanopores are able to distinguish complex protein isoforms,<sup>19-22</sup> e.g. ubiquitin dimeric isoforms<sup>20</sup> and two configurations of aptamer-thrombin complex.<sup>22</sup> In addition, the amino acid composition of a protein may be revealed as an unfolded polypeptide is threaded through a nanopore.<sup>23-27</sup> Nanopores were also used as a single molecule analytical approach to investigate the protein folding,<sup>28,29</sup> unfolding,<sup>23,30</sup> aggregation<sup>12,31</sup> and enzymatic activity.<sup>32,33</sup>

Despite the utility of these methods, the translocation-dependent approach is generally not suited for directly analyzing proteins that are too large to fit into the pore. While it is relatively straightforward to control the size of solid-state nanopores during fabrication, adjusting the size of protein nanopores is challenging due to our limited understanding of the connection between amino acid sequence and protein structure, (i.e. the folding riddle). To overcome this limitation, large proteins have been detected by protein nanopores via a translocation-independent mechanism. Typically, an analyte binds to a high affinity site located on the exterior of the nanopore. The binding site can be (i) a peptide sequence introduced into a region of the protein nanopore,<sup>34-37</sup> or (ii) a

covalently attached ligand in the lumen<sup>38</sup> or on the rim of the nanopore.<sup>7,39,40</sup> Using this approach, a single nanopore can detect proteins of any size, eliminating the need to search for pores or fabricate pores of suitable dimensions. Recently, we have used outer membrane protein G (OmpG) from *Escherichia coli* (*E. coli*) to detect large proteins. For example, we distinguished several structural homologues and isoforms of biotin-binding proteins in complex mixture.<sup>40-42</sup> OmpG contains seven flexible loops on the extracellular side.<sup>43-45</sup> Dynamic loop movement induces current fluctuations (called gating) in ionic current measurements. Our engineered sensor had a biotin covalently attached to the long loop 6 of OmpG.<sup>46,47</sup> Proteins were detected via changes in the gating pattern when they bound to biotin. Eight biotin-binding proteins, including four streptavidin homologues and four anti-biotin antibodies were differentiated by their characteristic current gating signals.<sup>40-42</sup> Compared to other multimeric protein nanopores,<sup>21,36,38,48</sup> such as  $\alpha$ HL,<sup>49</sup> MspA,<sup>50</sup> ClyA<sup>51</sup> and phi29 motor,<sup>52</sup> OmpG is a monomeric protein nanopore with flexible loops at the entrance. OmpG sensing relies on the interaction of its flexible loops with the analyte protein which generates distinct characteristic signal for each analyte. The high selectivity of the OmpG nanopore was attributed to the ability of its loops to undergo distinct conformational changes when interacting with each analyte. Such a high selectivity is rarely observed among other nanopores because their rigid structures are unable to undergo large conformational changes when bound by an analyte.

Electrostatic attractions between the nanopore loops and the analyte played an important role in OmpG selectivity.<sup>41</sup> Such interactions only occurred when the analyte proteins were bound to the tethered ligand and confined in close proximity to the OmpG nanopore. Here, we investigated how the proximity between the ligand and nanopore might affect the sensitivity and selectivity of our detection system. We increased the length of the polyethylene glycol (PEG) biotin linker and measured changes in gating

signals as well as binding kinetics. While a longer linker allowed a greater range of motion and therefore new gating states induced by biotin-bound proteins, this also adversely impacted the kinetics and impaired sensitivity. This work shows that the linker length of a tethered ligand influences the selectivity and sensitivity of the OmpG sensor and is important in the design of future sensors.

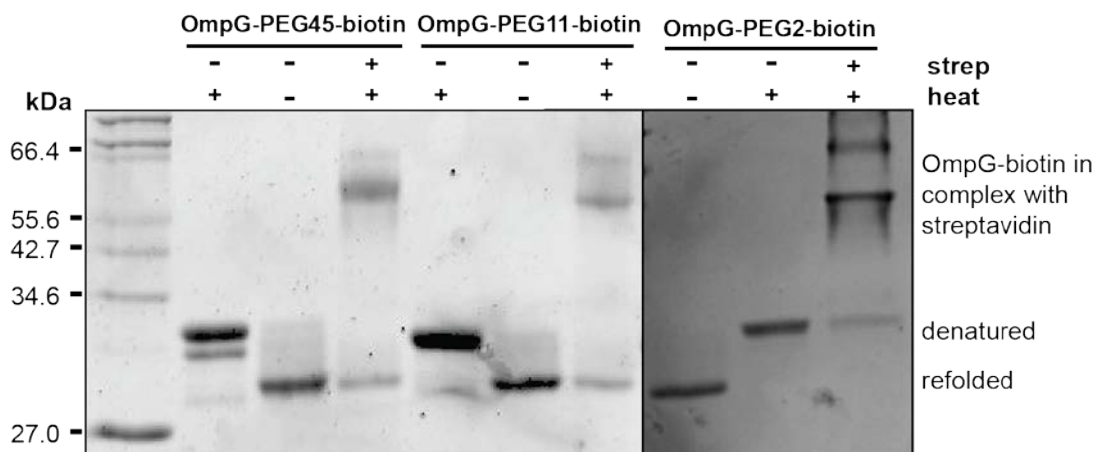
### **4.3 Materials and Methods**

All reagents and materials were purchased from Fisher Sci. or Boston Bioproducts unless otherwise noted. Mouse anti-biotin monoclonal antibody BTN.4 clone (MS-1048-P1) was purchased from Thermo Scientific. Avidin (A9275) was purchased from Sigma. Streptavidin (Z7041) was purchased from Promega. Maleimide-PEG45-biotin molecule was purchased from Creative PEG works (Biotin-PEG-MAL, MW 2k (PJK-1930)). Maleimide-PEG2-biotin and maleimide-PEG11-biotin were purchased from (ThermoFisher Scientific). Diphytanoylphosphatidylcholine (DPhPC) were from Avanti polar lipids. *Tris*(2-carboxyethyl)phosphine (TCEP) and octyl-glucoside (OG) and were purchased from GoldBio Technology.

#### **4.3.1 Cell culture and protein purification**

OmpG mutant D224C was created and expressed in *E. coli* cells as previously described.<sup>42</sup> OmpG was purified from an inclusion body under denaturing conditions in 50 mM Tris-HCl pH 8, 5 mM TCEP, 8 M urea using anion exchange chromatography. Prior to labeling with the MAL-PEG<sub>n</sub>-biotin ligands, OmpG-containing fractions were desalted on a HiTrap column into an 8 M urea, 50 mM HEPES pH 7 buffer to remove the reducing agent TCEP and the amine containing buffer Tris-HCl and to lower the pH for an optimal maleimide-thiol reaction. After desalting, OmpGD224C and MAL-PEG<sub>n</sub>-biotin were immediately mixed in 1:10 (protein to ligand) molar ratio and incubated for 2 hrs at room temperature (~23°C) with constant, gentle shaking. The mixture was desalted a

second time using a HiTrap 5 ml desalting column (GE Healthcare) to remove unconjugated MAL-PEG<sub>n</sub>-biotin. The labeled OmpG was then diluted in refolding buffer (110 mM octyl glucoside, 20 mM Tris-HCl, pH 9) in a 2:3 v/v (OmpG to refolding buffer) ratio and incubated at 37°C for 3 days (no agitation needed). The labeling and refolding efficiency of the OmpG proteins were analyzed by gel-shift assay. Labeling and refolding percentages were both determined to be more than 70% for all constructs (Figure 4.1). Proteins were aliquoted and stored at -80°C in 20% glycerol. Freshly thawed aliquots were used for the experiments.



**Figure 4.1. The refolding and labeling efficiency of OmpG-PEG<sub>n</sub>-biotins.** Denatured OmpG-PEG<sub>n</sub>-biotin migrates slower than refolded protein as shown on the 15% SDS PAGE gel. Labeled OmpG-PEG<sub>n</sub>-biotin shifts to an SDS-resistant high molecular weight complex in the presence of excess streptavidin. OmpG-PEG45-biotin, OmpG-PEG11-biotin and OmpG-PEG2-biotin each have a labeling efficiency of 75%, 83% and 87% respectively.

### 4.3.2 Single Channel recording

Single channel recording experiments were performed as previously described.<sup>42</sup> For recording OmpG-PEG<sub>n</sub>-biotin behavior in planar lipid membranes, signals were filtered with a 2 kHz Bessel filter (unless otherwise stated) and acquired at a sampling rate of 100 μs after digitization with a Digidata 1320A/D board (Axon Instruments). The current was amplified with an Axopatch 200B integrating patch clamp amplifier (Molecular Devices). To create the bilayer, 2 μl of a 10% v/v hexadecane in pentane mix

was applied to both sides of a 25  $\mu\text{m}$  Teflon film with a 100  $\mu\text{m}$  aperture separating two chambers. Buffer (900  $\mu\text{L}$ ) was added to each chamber and approximately 15  $\mu\text{L}$  of 10 mg/ml 1,2-Diphytanoyl-sn-glycerol-3-phosphocholine (DPhPC) lipids dissolved in pentane was dropped onto the surface of the buffer. The pentane was allowed to evaporate for 2 min after the addition of hexadecane and the DPhPC lipids to the chip.

One Ag/AgCl electrode was inserted into each chamber, where one electrode was in the grounded *cis* chamber and the other connected to the *trans* chamber. The liquid level was pipetted slowly in one chamber at a time to form the lipid bilayer in the aperture. Once a stable bilayer formed that could withstand 200-300 mV for at least 5 mins, about 1 nM (final concentration) OmpG proteins were added to the *cis* chamber. A positive voltage of 200-250 mV was applied to induce pore insertion. The voltage was lowered to 50 mV immediately after a single pore was inserted in order to hinder the insertion of multiple pores into the bilayer. The orientation of nanopore was determined based on its asymmetric gating behavior at positive and negative potentials.<sup>53</sup> OmpG behavior was recorded in the absence and presence of analyte proteins that were added to the chamber facing the loop side.

#### **4.3.3 Single channel data analysis**

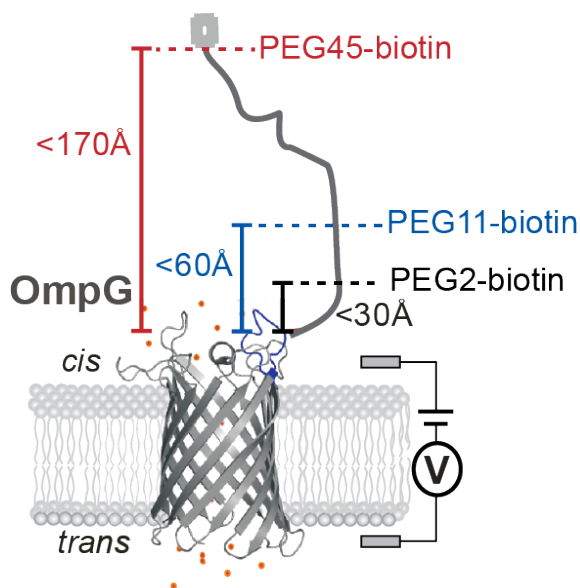
To determine the open probability of OmpG pores, traces were analyzed in Clampfit 10.3 using the single channel search. The open probability was calculated as the sum of the dwell time of open states divided by the total time analyzed. To determine the kinetics of the mouse monoclonal antibody bound and unbound states, the dwell times of 300-500 bound events and 300-500 unbound events were extracted manually and fit with a single standard exponential to derive the averaged inter-event time ( $\tau_{\text{on}}$  from the unbound events) and event duration ( $\tau_{\text{off}}$  from the bound events). To identify when the antibody was binding to the OmpG nanopore, the decrease of the open

pore conductance and the increase in gating frequency were used as clear identifiers to guide accurate data extraction. The dwell times of the binding sub-states of avidin B1 and B2 (when the OmpG-PEG45-biotin sensor was used) were also extracted manually and similarly analyzed as the anti-biotin mAb in order to extract the binding kinetics.

## 4.4 Results

### 4.4.1 Effect of PEG linker length on analyte recognition

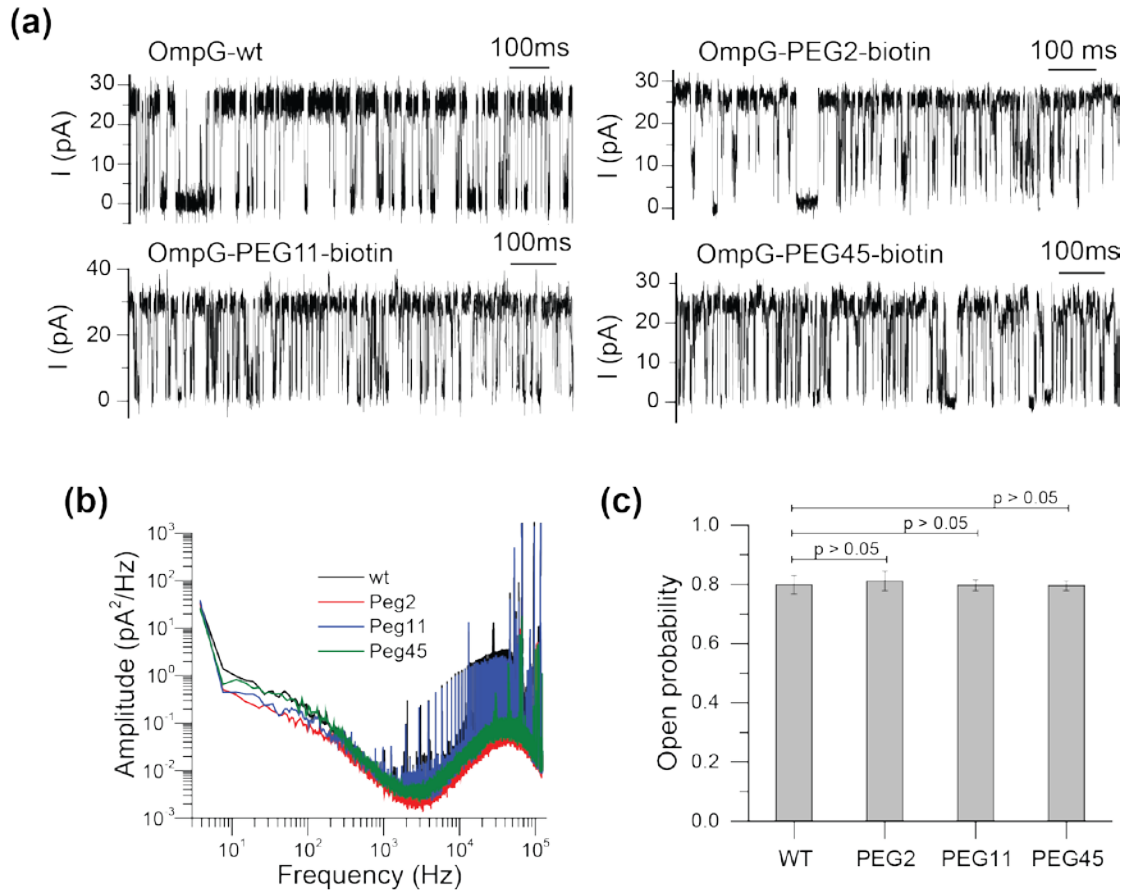
A single cysteine mutant, OmpG (D224C) was purified under denaturing and reducing conditions then labeled with one of the following: maleimide-PEG<sub>n</sub>-biotin, where n is 2, 11 or 45, respectively. The resulting constructs -OmpG-PEG2-biotin, OmpG-PEG11-biotin and OmpG-PEG45-biotin - contained biotin moieties that could fully extend approximately up to 30, 60 and 170 Å from the cysteine, C224, on loop 6 as estimated by chemical linkage (Figure 4.2). However, in reality, the biotin ligand was most likely closer to the OmpG pore entrance, as PEG molecules are not often in a stretched state.



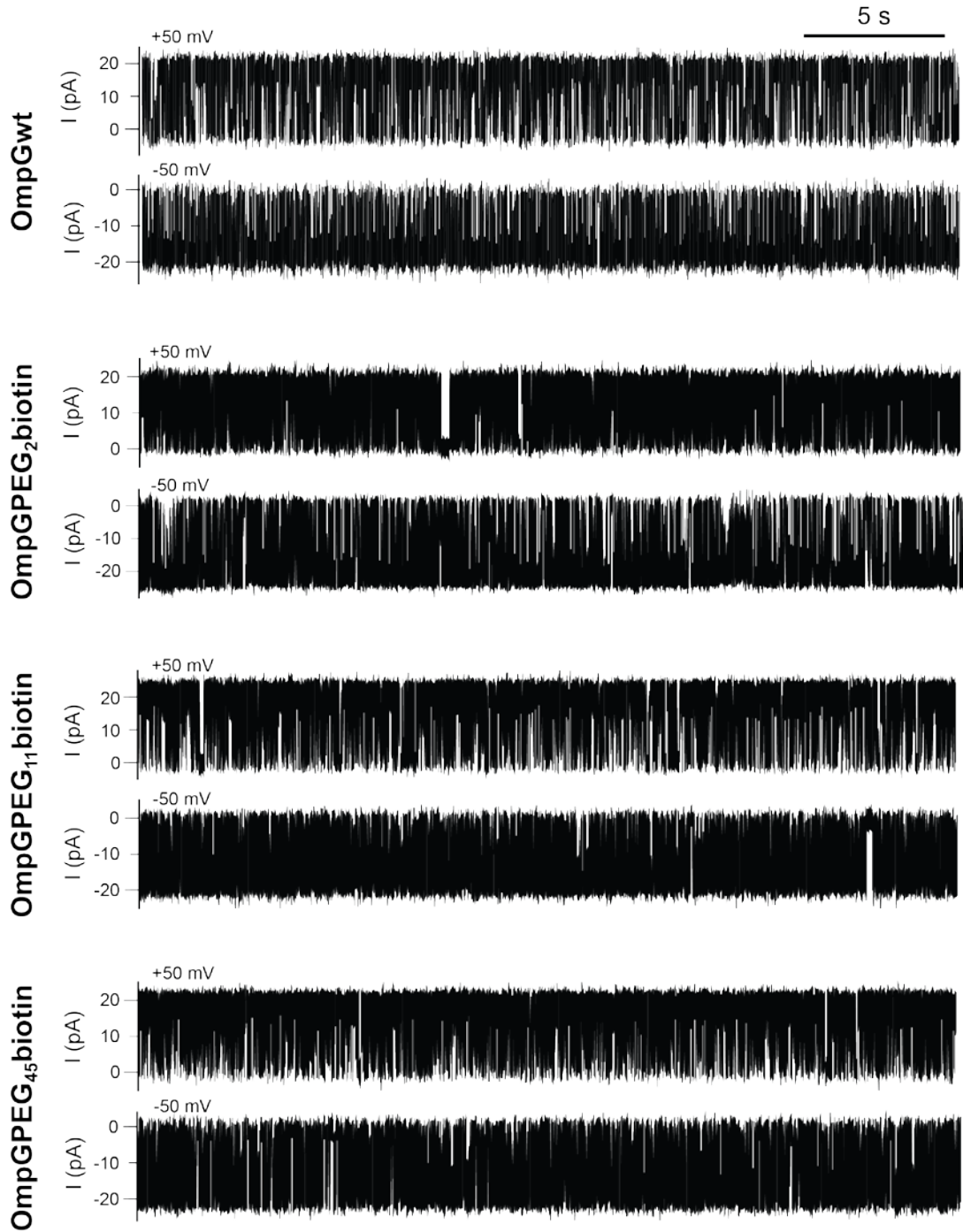
**Figure 4.2. The design of the OmpG-PEG<sub>n</sub>-biotin constructs.** The biotin ligand attached to residue D224C of the OmpG nanopore via PEG2, PEG11 and PEG45 linkers could extend up to 30, 60 and 170 Å away from loop 6 respectively.



The dynamic movement of the loop 6, which moves in and out of the OmpG entrance, contributes to more than 95% of the intrinsic gating signal.<sup>46,47</sup> Chemical modification of the OmpG proteins with biotin reagents had minimal effect on the gating behavior of OmpG (Figures 4.3, 4.4).

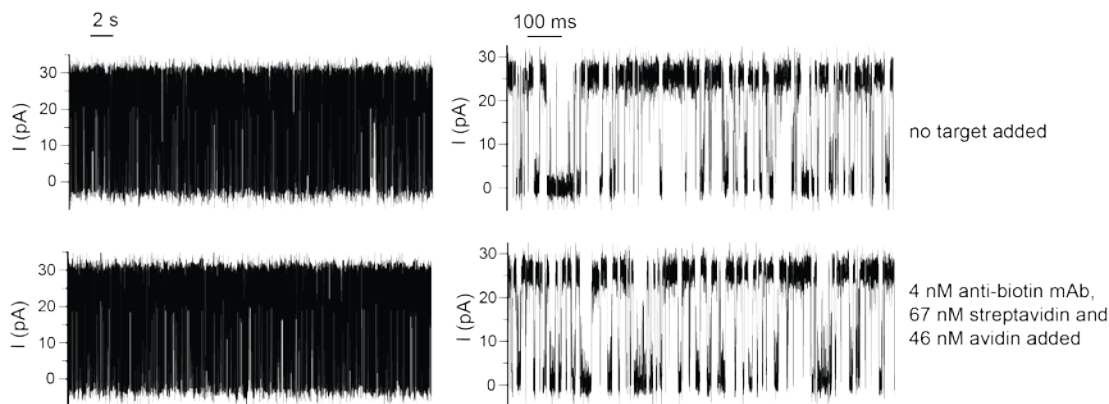


**Figure 4.3. Effect of the tethered ligand on OmpG gating.** The tethered Maleimide-PEG<sub>n</sub>-biotin ligands do not significantly affect the gating behavior of OmpG. (a) Typical electrophysiology traces of OmpGwt, OmpG-PEG2-biotin, OmpG-PEG11-biotin and OmpG-PEG45-biotin in 10 mM sodium phosphate pH 6, 300 mM KCl buffer at +50 mV. (b) Power spectra analysis of OmpGwt, OmpG-PEG2-biotin, OmpG-PEG11-biotin and OmpG-PEG45-biotin. (c) Analysis of the open probability of OmpG pores in 10 mM sodium phosphate pH 6, 300 mM KCl buffer at +50 mV. Averages were calculated from at least three independent pores. Error bars indicate the standard deviation. A p value > 0.05 indicates that the open probabilities of the four proteins are not significantly different from one another. Signals in (a) were filtered with a 2 kHz Bessel filter and acquired at a sampling of 100  $\mu$ s. For power spectra analysis pores were filtered with a 100 kHz Bessel filter and acquired at a sampling of 4  $\mu$ s.



**Figure 4.4 Extended electrophysiology traces of OmpGwt and OmpG-PEG<sub>n</sub>-biotin constructs.** The tethered Maleimide-PEG<sub>n</sub>-biotin ligands do not affect the gating behavior of OmpG. Single channel current traces of OmpGwt, OmpG-PEG2-biotin, OmpG-PEG11-biotin and OmpG-PEG45-biotin were recorded in 10 mM sodium phosphate pH 6, 150 mM KCl buffer at  $\pm 50$  mV applied in the *trans* chamber. Signals were filtered with a 2 kHz Bessel filter and acquired at a sampling rate of 100  $\mu$ s.

Before we tested the biotin binding proteins with the OmpG-PEG<sub>n</sub>-biotin constructs we tested these proteins with unlabeled OmpG pores (OmpG-D224C). These negative control experiments showed that none of the biotin-binding protein analytes could trigger a signal change in the gating behavior of the OmpG-D224C nanopore indicating that non-specific binding of streptavidin, avidin (and the mouse monoclonal anti-biotin antibody) to unlabeled OmpG was negligible (Figure 4.5).

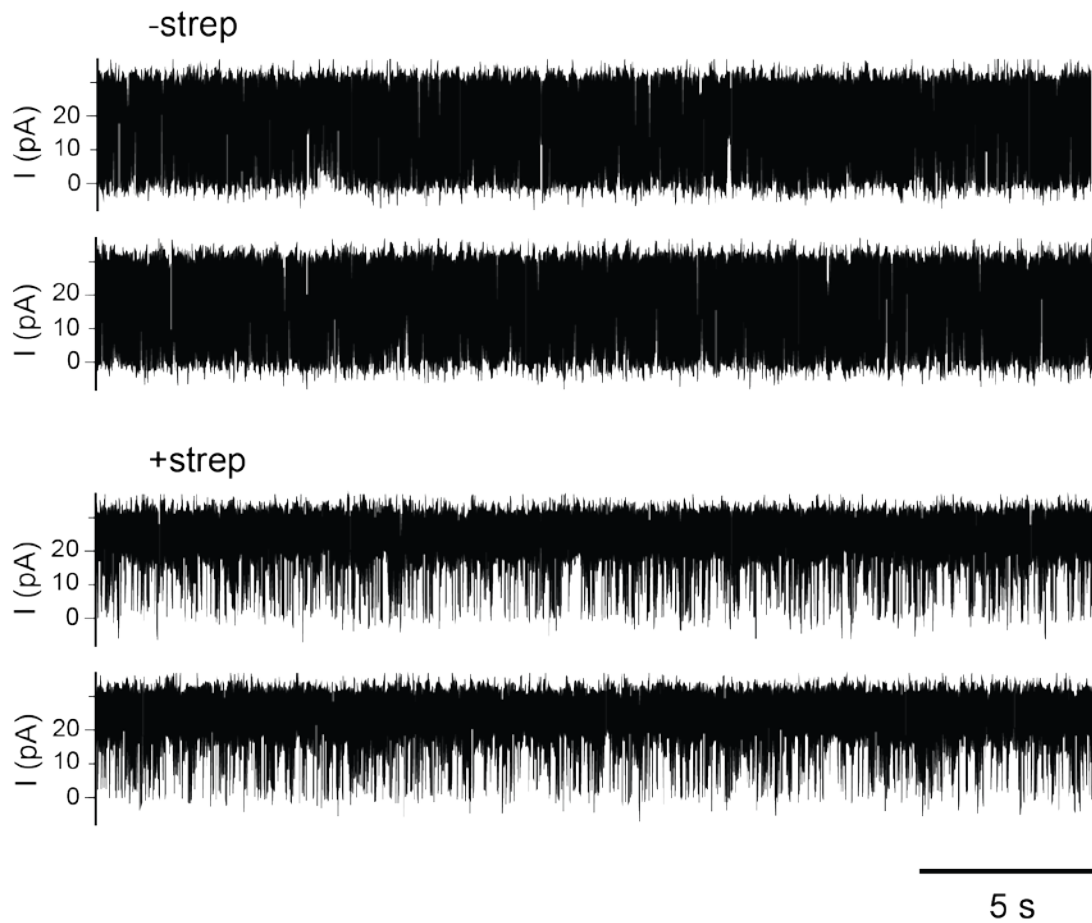


**Figure 4.5. Electrophysiology traces showing the effect of biotin binding proteins on OmpG-D224C gating activity.** The gating behavior of OmpG-D224C is not significantly altered in the presence of a mixture of streptavidin, avidin and anti-biotin mAb. This pore is a representative of four independent pores. 10 mM sodium phosphate pH 6, 300 mM KCl buffer was used at +50 mV. Signals were filtered with a 2 kHz Bessel filter and acquired at a sampling rate of 100  $\mu$ s.

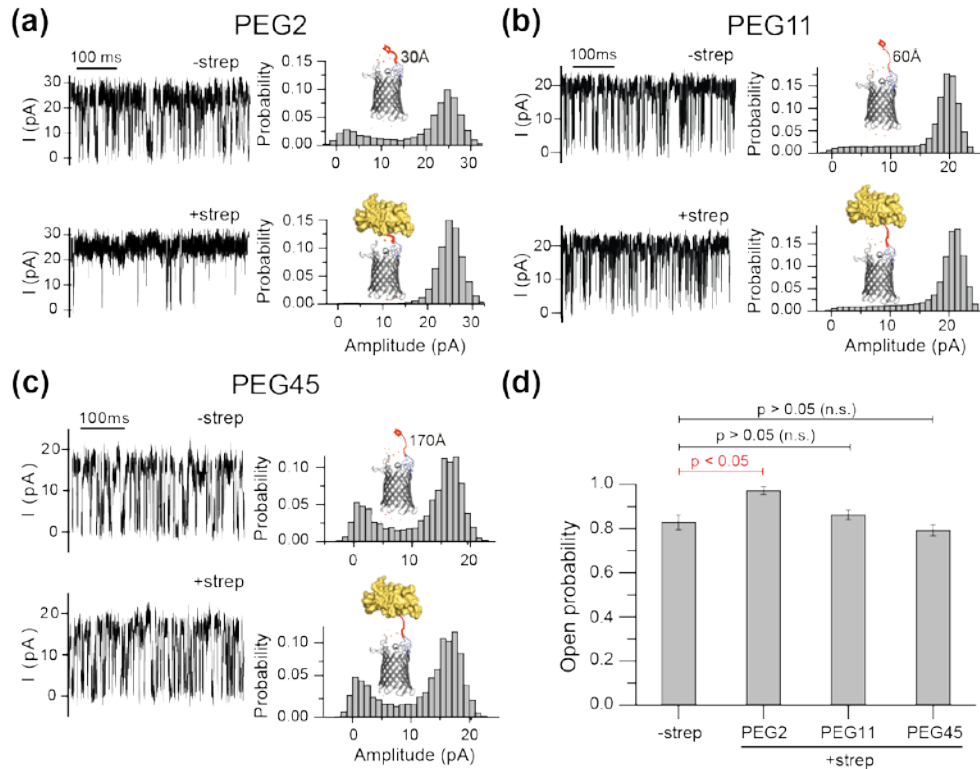
We then examined how the different OmpG-PEG<sub>n</sub>-biotin nanopore constructs responded to the two biotin-binding homologous proteins – streptavidin and avidin. We observed that streptavidin binding resulted in a permanent increase in open probability ( $n = 10$ ,  $p = 0.05$ ) for OmpG-PEG2-biotin (Figure 4.6, Figures 4.7a, 4.7d) as we had previously seen.<sup>40,41</sup> The open probability of the streptavidin bound state increased due to the fact that the gating frequency of the OmpG-PEG2-biotin pore significantly decreased when streptavidin was bound. The duration of the closed events shortened while the duration of the open state increased (Figure 4.6). Furthermore, we did not

observe any dissociation of the bound streptavidin molecule from the OmpG-PEG2-biotin pore during our recordings.

However, the addition of streptavidin to the loop facing chamber of OmpG-PEG11-biotin as well as that of OmpG-PEG45-biotin unfortunately did not induce any quantifiable change in the gating activity of more than 15 OmpG-PEG11-biotin nanopores and 13 OmpG-PEG45-biotin pores (Figure 4.7b-4.7d).<sup>40,41</sup>



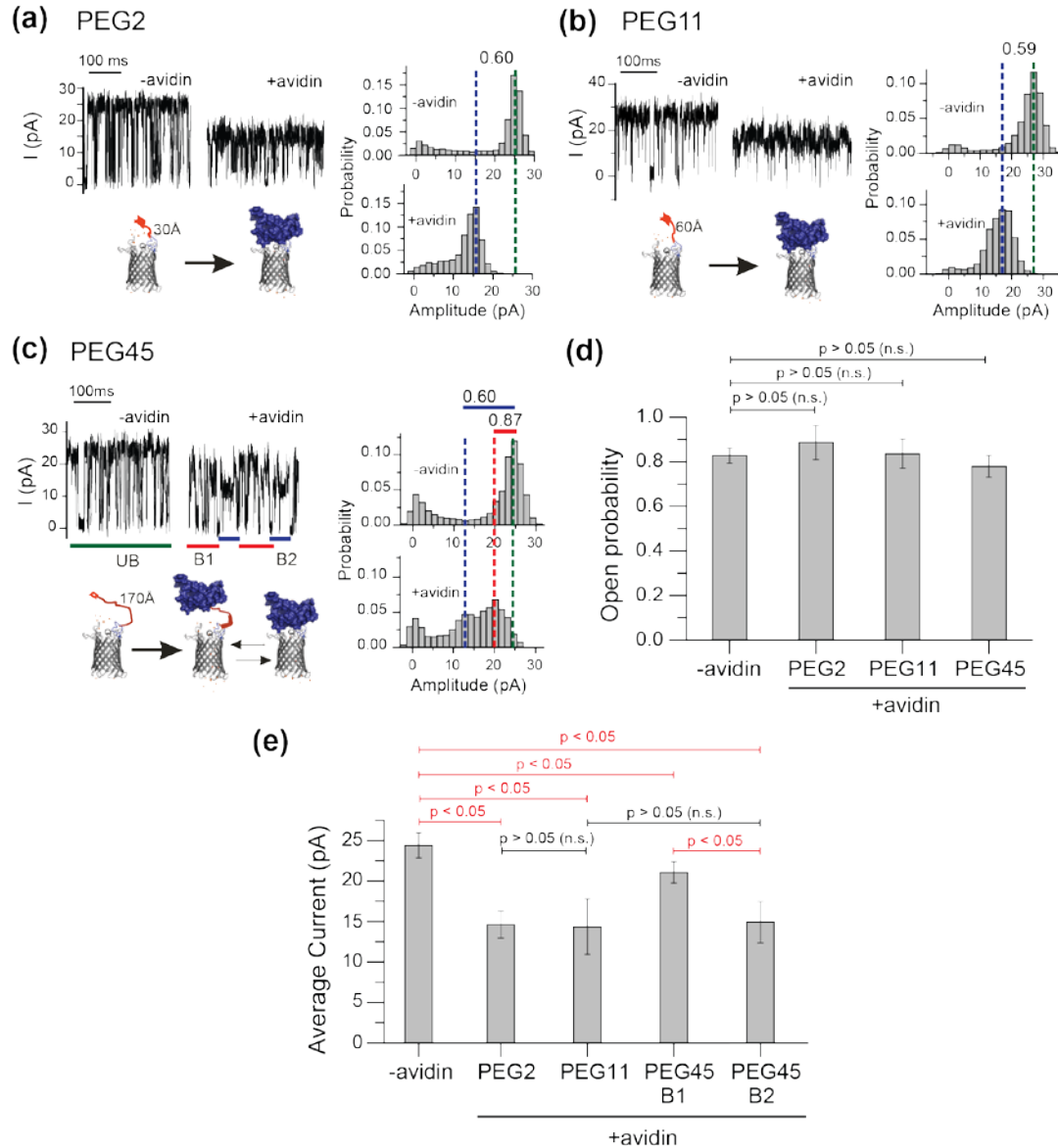
**Figure 4.6. The effect of streptavidin binding to the OmpG-PEG2-biotin pore.** The open probability of the OmpG-PEG2-biotin construct increases. The trace shown is a representative of over 15 pores. The pore was recorded in 10 mM sodium phosphate pH 6, 300 mM KCl buffer at +50 mV. Streptavidin was added to the loop chamber at a final concentration of 5 nM. Signals were filtered with a 2 kHz Bessel filter and acquired at a sampling of 100  $\mu$ s.



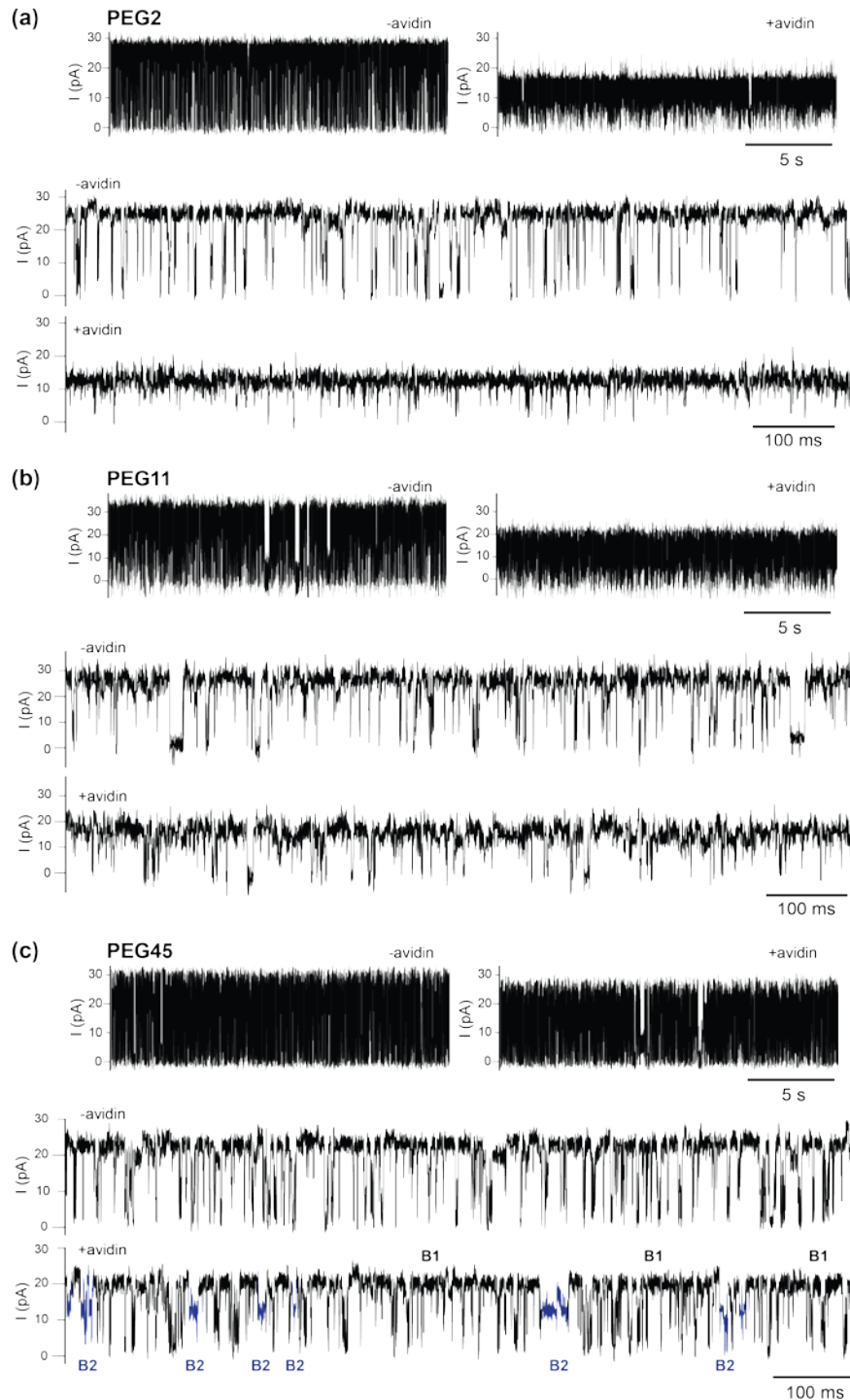
**Figure 4.7. Streptavidin binding to OmpG-PEG<sub>n</sub>-biotin constructs.** Current recordings of (a) OmpG-PEG2-biotin (b) OmpG-PEG11-biotin and (c) OmpG-PEG45-biotin before and after streptavidin binding at +50 mV. Buffer used was 300mM KCl, 10mM sodium phosphate pH 6. (d) Comparison of open probability of OmpG nanopores before and after streptavidin binding. Error bars represent standard errors from at least 5 pores. Statistical analysis was performed with an unpaired two sample t-test (n>5, p = 0.05).

In contrast, significant changes in current traces of all three constructs were observed using avidin (Figures 4.8-4.10). Avidin binding caused a ~45% decrease of the OmpG-PEG2-biotin and OmpG-PGE11-biotin open pore current (Figure 4.8a, 4.b). The open current decreased from  $24.8 \pm 4.4$  pA to  $14.6 \pm 1.7$  pA (n = 6) for OmpG-PEG2-biotin while for OmpG-PEG11-biotin it decreased from  $27.4 \pm 0.9$  pA to  $14.4 \pm 3.4$  pA (n = 4). Interestingly, when avidin bound to OmpG-PEG45-biotin, it induced two distinct current patterns during the bound state (Figure 4.8c). In the predominant pattern, termed B1, the open pore current decreased from  $23.6 \pm 1.0$  pA to  $21.1 \pm 1.3$  pA (n = 6), an 11% decrease in the open state. The minor pattern B2, had an open pore current of  $14.9 \pm 2.5$  pA (n = 6) which was 37% decrease of the unbound state (UB)

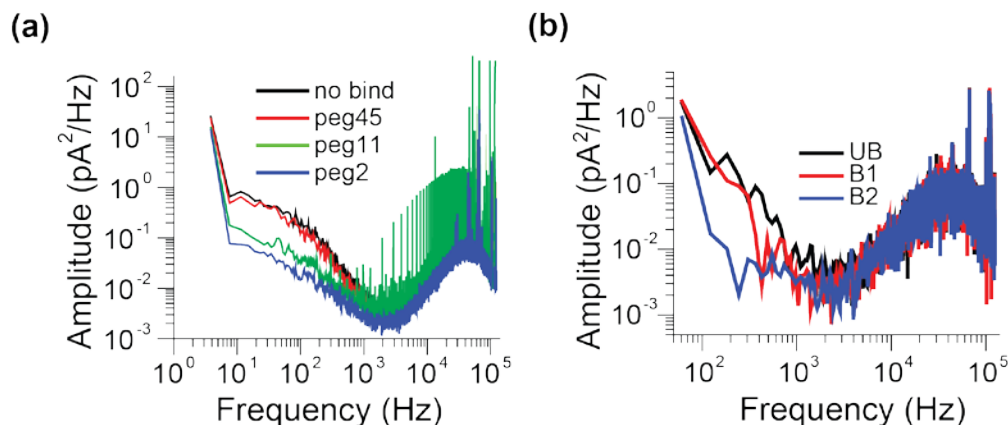
(Figure 4.8c). Notably there were no significant changes to the open probability of either the three OmpG-PEG<sup>n</sup>-biotin pores after avidin was bound (Figure 4.8d), unlike the significant change in open current (Figure 4.8e).



**Figure 4.8. Avidin binding to OmpG-PEG<sup>n</sup>-biotin constructs.** Current recordings and the corresponding histograms of (a) OmpG-PEG2-biotin (b) OmpG-PEG11-biotin and (c) OmpG-PEG45-biotin before and after avidin binding at +50 mV. Buffer used was 300mM KCl, 10mM sodium phosphate pH 6. The relative open pore current of the avidin bound states (blue and red dash lines) to the unbound state (UB, green dash line) are indicated on the top of the histograms. (d-e) Comparison of open probability (d) and open pore current (e) of OmpG nanopores before and after avidin binding. Error bars represent standard errors from at least 4 pores. Statistical analysis were performed with an unpaired two sample t-test ( $n > 4$ ,  $p = 0.05$ ).



**Figure 4.9. Single channel current traces of OmpG-PEG<sub>n</sub>-biotin.** Representative traces of (a) OmpG-PEG2-biotin (b) OmpG-PEG11-biotin and (c) OmpG-PEG45-biotin before and after avidin binding. B1 and B2 states of OmpG-PEG45-biotin are highlighted in black and blue, respectively in (c). Pores were recorded in 10 mM sodium phosphate buffer pH 6, 300 mM KCl at +50 mV. Avidin was added at a final concentration of 5 or 10 nM.



**Figure 4.10. Power spectra analysis of noise in the absence and presence of avidin.** (a) Spectra noise at 5 s of OmpG-PEG45-biotin, OmpG-PEG11-biotin and OmpG-PEG2-biotin after avidin binding. (b) Power spectra analysis of OmpG-PEG45-biotin before and after avidin binds during a 200 ms time scale. 10 mM sodium phosphate pH 6, 300 mM KCl buffer was used and trace recorded at +50 mV. For power spectra analysis recordings were filtered with a 2 kHz Bessel filter and acquired at a sampling of 100  $\mu$ s.

Previous studies using OmpG-PEG2-biotin revealed that analyte proteins could be classified into two categories based on their current signatures. Specifically, some analytes interact with the OmpG pore surface while others do not. We found that non-interacting proteins were either neutral or negatively charged molecules under the experimental conditions used.<sup>41</sup> Typically, a decrease of the gating activity was observed for these proteins which may hinder the dynamic movement of loop 6 through drag or friction forces. One example was streptavidin. The fact that streptavidin binding inhibited gating in OmpG-PEG2-biotin but not OmpG-PEG11-biotin or OmpG-PEG45-biotin suggest that a linker with 11 or more PEG units is flexible enough to allow loop 6 to freely move even with a ~60 kDa protein attached.

On the other hand, proteins that interacted with OmpG's loops usually induced a reduction in the open pore current by occluding ionic flow.<sup>41</sup> Such protein-protein interactions were dominated by electrostatic attraction between the negatively charged OmpG loops and the positively charged analyte protein surface, such as avidin.<sup>41</sup> Avidin binding to OmpG-PEG11-biotin triggered an almost identical effect to that of the OmpG-

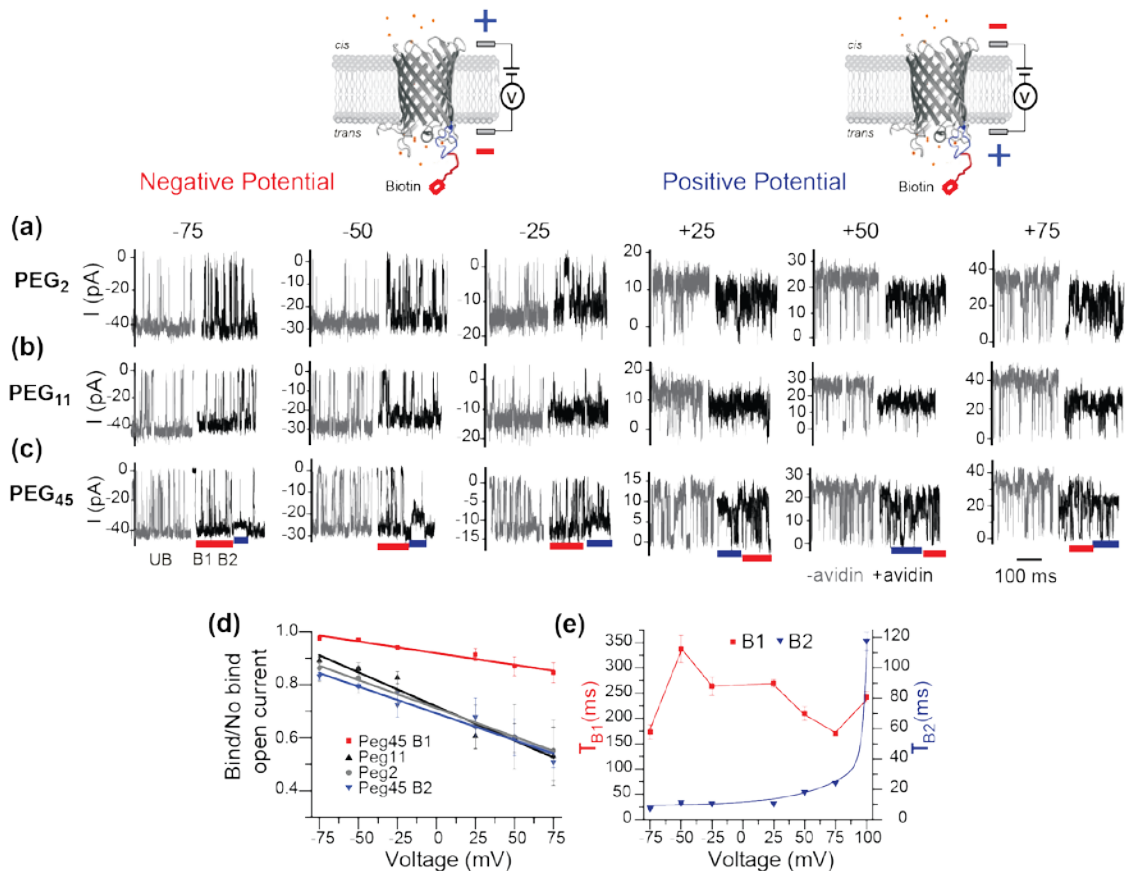


PEG2-biotin, suggesting that the avidin bound states of these two constructs were similar (Figures 4.8e, 4.9-4.10). The avidin bound state of OmpG-PEG45-biotin exhibited two distinct gating signatures with relative open pore current of 87% and 60%. We presume this shows that avidin interacted with OmpG-PEG45-biotin in two different configurations (Figures 4.8e, 4.9-4.10).

Our results show that OmpG lost its ability to detect neutral or negatively charged molecules with an elongated linker but was able to recognize the positively charged protein analytes. This study also suggests that we could adjust the PEG linker to optimize the selectivity of OmpG toward one specific analyte such as a glycosylated protein, like avidin, while removing any interfering signals from related non-glycosylated homologues, like streptavidin.

#### **4.4.2 Effect of voltage on OmpG-PEG-biotin - avidin interaction**

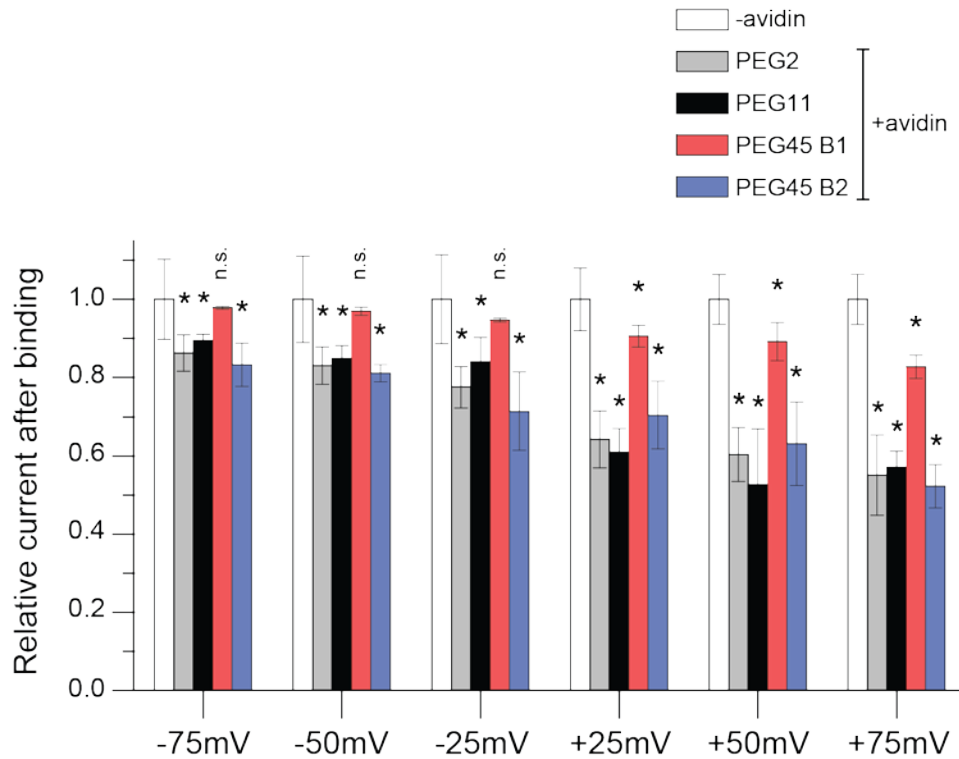
The OmpG-PEG45-biotin is the first variant to show multiple unique bound states, specifically with avidin. Since we suspect that electrostatic forces govern the interactions between the loops and analyte, we tested the effect of applied voltage on the bound states to see if they responded to electric fields. Here, positive potential was defined as the potential of the chamber in which the OmpG loops were facing was positive relative to the other chamber (Figure 4.11). The relative open current of OmpG-PEG2-biotin and that of OmpG-PEG11-biotin showed a significant voltage dependence (Figure 4.11a, 4.11b, 4.11d). The relative open pore current of the B1 state to the unbound state showed a weak voltage dependence (Figures 4.11c, 4.11d). Increasing the potential from -75 mV to 75 mV caused the open pore current to decrease slightly. On the other hand, the relative open current of the B2 state showed a strong dependence.



**Figure 4.11. Voltage effect on avidin binding to OmpG-PEG<sub>n</sub>-biotin.** Current recordings of (a) OmpG-PEG<sub>2</sub>-biotin (b) OmpG-PEG<sub>11</sub>-biotin and (c) OmpG-PEG<sub>45</sub>-biotin before and after avidin binding at various voltages. (d) Effect of voltage on the relative open pore current of the avidin bound states of all three OmpG-PEG-biotins. (e) Effect of voltage on the dwell time of B1 and B2 states of OmpG-PEG<sub>45</sub>-biotin. The B1 and B2 avidin binding states are indicated by the red and blue bars respectively. Buffer used was 300mM KCl, 10mM sodium phosphate pH 6.

Because the open pore current and voltage dependence of the B2 state were similar to the avidin bound states of OmpG-PEG<sub>2</sub>-biotin and OmpG-PEG<sub>11</sub>-biotin (Figures 4.11d, 4.12), we speculated that avidin interacted with OmpG surface in a similar manner in each scenario. The avidin B1 and B2 data suggests that a long PEG linker such as PEG<sub>45</sub> (<170 Å) or longer could allow the analyte (which should have strong electrostatic interaction with the OmpG loops) to sample or interact with more than one binding area of the OmpG loop surface or event a binding distance once it is bound to the tethered ligand. The voltage dependent open pore current of the avidin

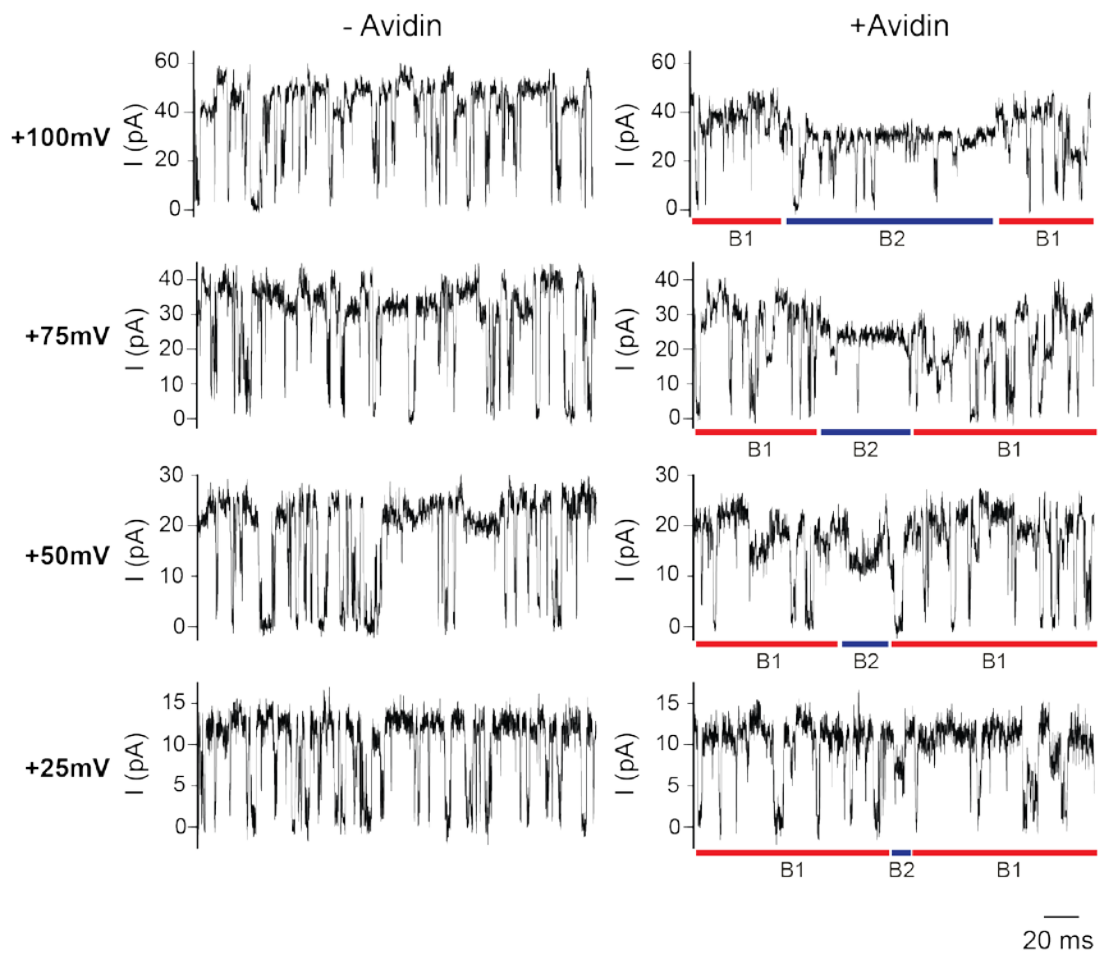
bound B1 and B2 states of OmpG-PEG45-biotin was likely due to the proximity of the bound avidin molecule to the entrance of OmpG under an applied potential.



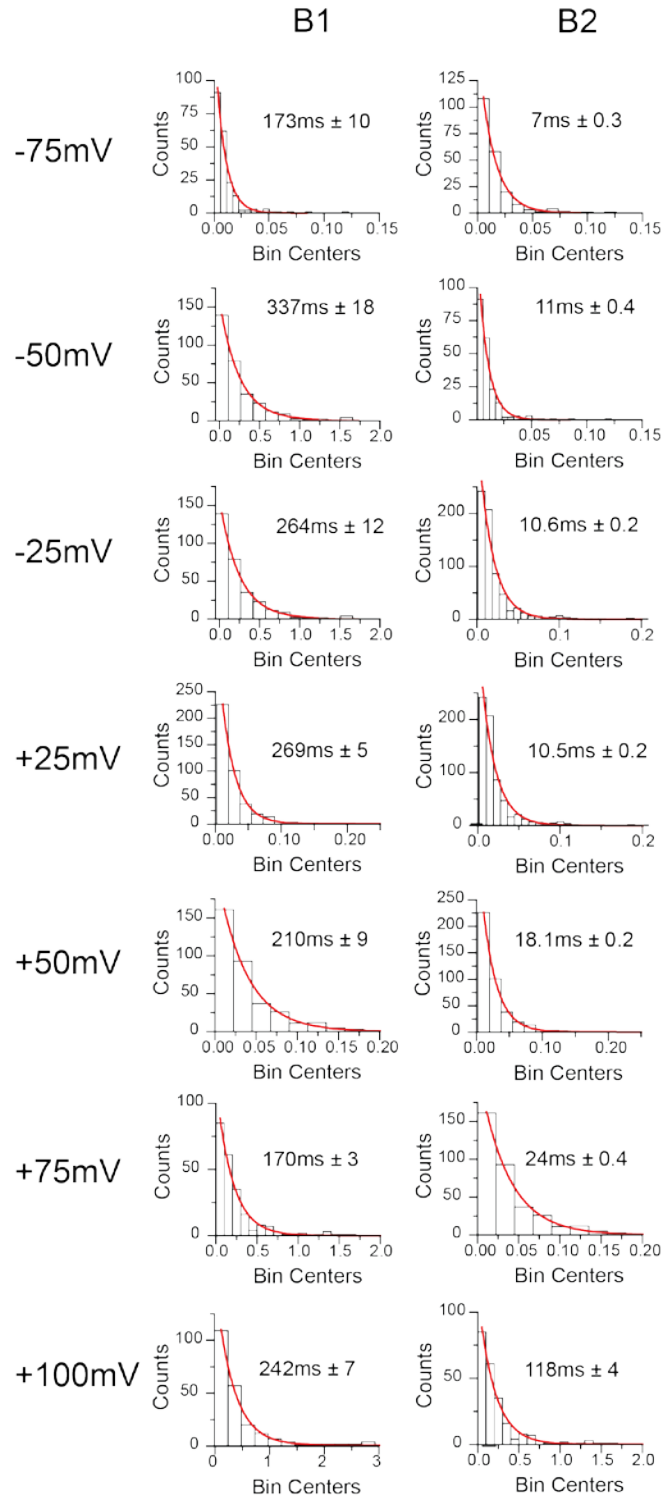
**Figure 4.12. Comparison of open pore current of the OmpG-PEG<sub>n</sub>-biotin constructs before and after avidin binding at various voltages.** Both OmpG-PEG2-biotin and OmpG-PEG11-biotin exhibit a significant change in open pore current from -75mV to +75mV once avidin is bound. The B2 signal of the avidin-bound OmpG-PEG45-biotin is significant at -75mV to +75mV whereas the B1 signal is only significant at positive voltages. At negative voltages, the B1 avidin-bound state is not different from that of the -avidin gating. Asterisks (\*) represent data that have p values < 0.05 compared to the -avidin condition (white bars). Data that have p values > 0.05 are indicated by n.s. signifying that there is no significant difference in the current after avidin is bound. Error bars indicate the standard deviation. More than 15 bound and 15 unbound events from at least three independent pores were analyzed. The pores were recorded in 10 mM sodium phosphate pH 6, 300 mM KCl buffer at +50 mV with a 2 kHz Bessel filter and an acquisition sampling rate of 100  $\mu$ s. Avidin was added at a final concentration of 5 or 10 nM.

We then measured the dwell times of both the B1 and B2 avidin bound states of OmpG-PEG45-biotin at voltages ranging from -75 mV to +100 mV. First, we observed that the B1 dwell time in the 300 mM KCl buffer condition was not voltage dependent where the dwell times fluctuated rather randomly as the voltage varied. On the other

hand, the B2 dwell time initially did not significantly change at negative potential but slowly and exponentially increased after an increasing positive potential was applied (Figures 4.11e, 4.13, 4.14). This result suggests that the avidin and OmpG-PEG45-biotin electrostatic interaction could be strengthened (increase in B2 dwell time) or weakened (decrease in B2 dwell time) by manipulating the applied potential across the bilayer.



**Figure 4.13. Electrophysiology traces showing the dwell times of the avidin B2 state of OmpG-PEG45-biotin at various loop voltages.** The B2 state dwell time (blue line) increases as the loop potential increases. The pores were recorded in 10 mM sodium phosphate pH 6, 300 mM KCl buffer at the indicated loop voltages. Signals were filtered with a 2 kHz Bessel filter and acquired at a sampling of 100  $\mu$ s.



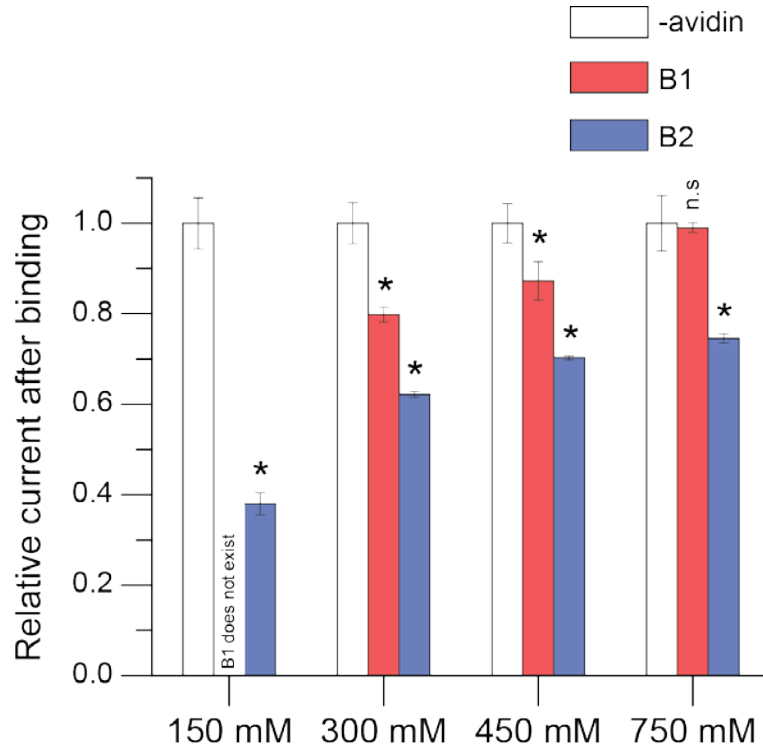
**Figure 4.14. First order exponential fitting analysis of B1 and B2 dwell times at various voltages.** B1 and B2 of OmpG-PEG45-biotin was analyzed from -75 to +100 mV. The histograms are from a single representative pore but the calculated dwell time is the average from at least three independent pores and the error is the standard deviation. 10 mM sodium phosphate pH 6, 300 mM KCl buffer was used.

Because avidin, which bears a positive charge and OmpG's loop surface carries a net negative charge, we expect a strong electrostatic attraction between them and previously confirmed this phenomena.<sup>41</sup> In addition, electrophoretic (EP) and electroosmotic (EO) forces act on the bound avidin in a voltage dependent manner.<sup>41</sup> The OmpG lumen is decorated with 14 positively (12R and 2K) and 16 negatively (13E and 3D) charged residues. At pH 6.0, the lumen had a -2 net negative charge. Thus, at positive potential, EP and EO align to push avidin into the loop surface of the OmpG nanopore. At negative potential, the two forces push in the opposite direction, weakening the electrostatic attraction between the OmpG nanopore and the bound avidin molecule.

In protein nanopores such as  $\alpha$ HL and solid-state nanopores such as glass, simulations have shown that the strength of EO and EP fields peak at the constriction site of the nanopore and diminish rapidly between the nanopore and bulk solution.<sup>54,55</sup> Because the B2 state is voltage dependent, we surmise that during this state, the bound avidin must be close enough to the pore to be influenced by EO and EP forces. On the other hand, avidin in the B1 state might be further away from the pore entrance as it is not affected by voltage. Here, we have shown that the characteristic gating pattern used to identify analytes and homologues can be tuned and possibly optimized to trap desired states by manipulating the voltage.

#### **4.4.3 Effect of salt concentration on the interaction between OmpG-PEG45-biotin and avidin**

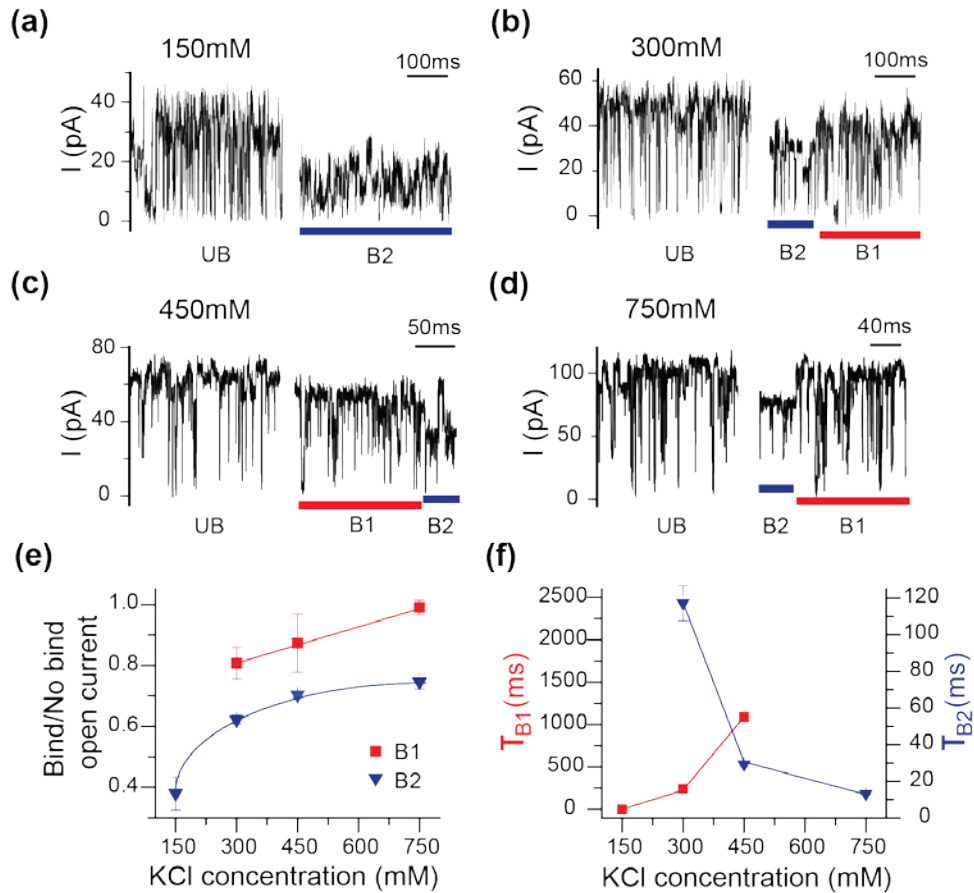
The electrostatic interactions between OmpG-biotin and avidin, EP and EO are sensitive to salt concentration.<sup>41</sup> Thus we observed whether the avidin-bound complex to OmpG-PEG45-biotin responded to changes in salt concentration at +100 mV (Figure 4.15).



**Figure 4.15. The effect of KCl concentration on the avidin binding states B1 and B2 of the OmpG-PEG45-biotin pore.** Pores were recorded in 10 mM sodium phosphate pH 6 buffer at +100 mV in the indicated KCl concentrations. Asterisks (\*) indicate data that have p values < 0.05 which are statistically significant from the -avidin condition. Data that has p value > 0.05 is indicated by n.s. signifying that there is no significant difference in the open current after avidin is bound. Error bars indicate the standard deviation. More than ten B1 and ten B2 events were collected from at least three independent pores to determine the average current reduction.

At 150 mM KCl, only the B2 state was observed (Figure 4.15, 4.16a). At higher salt concentrations, the bound avidin switched between B1 and B2 states (Figures 4.16b-4.16e). The dwell time of the B2 state decreased rapidly with increasing salt concentration with a corresponding increase in B1 dwell time (Figures 4.16f, 4.17). In addition, the relative open current of the avidin B1 and B2 states increased with increasing salt concentration. At 750 mM KCl, the B2 state was still recognizable, while the open current of the B1 state was indistinguishable from that of the unbound state (Figure 4.5d, 4.5e). This suggested that the avidin molecule occluded the ionic flow through OmpG-PEG45-biotin to a lesser degree at higher salt concentration. At 1.0 M

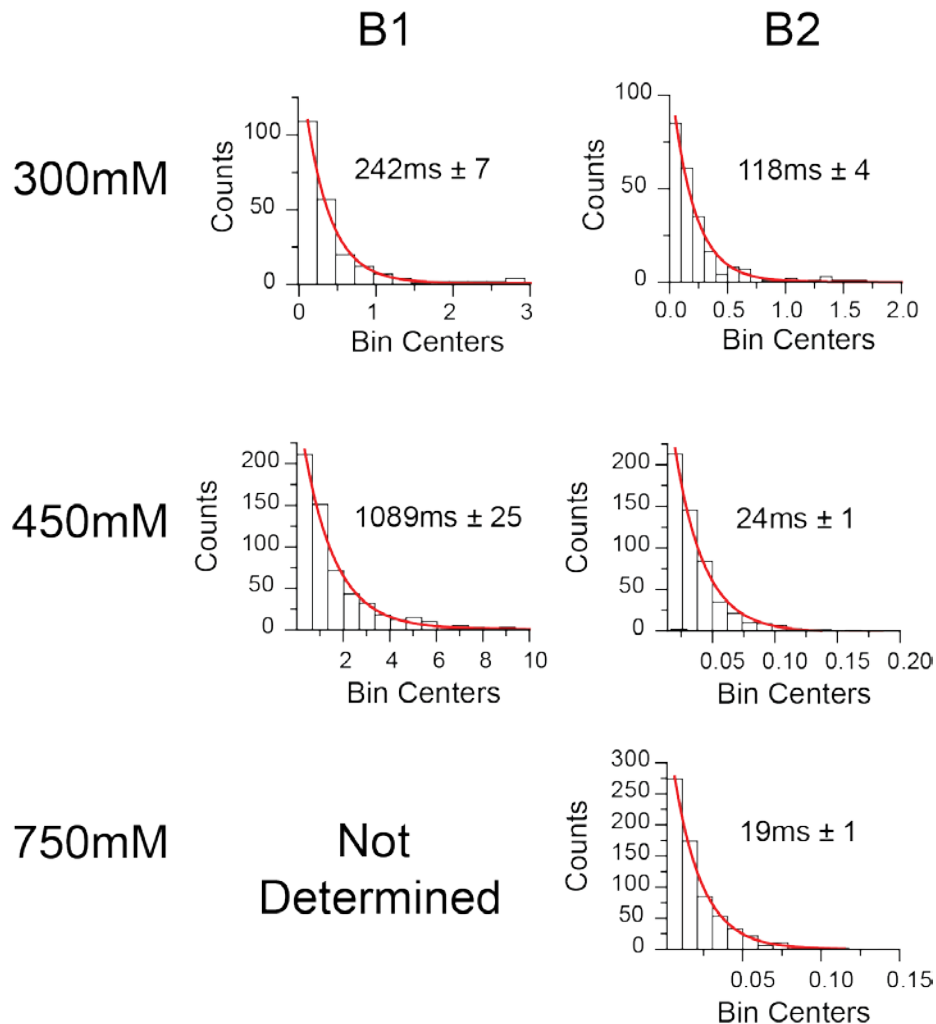
KCl, we did not observe any significant change in gating after the addition of avidin, indicating that avidin no longer interacted electrostatically with the nanopore surface.



**Figure 4.16. Salt effect on OmpG-PEG45-avidin binding states.** Typical current recording of a single OmpG-PEG45-biotin pore at unbound and traces of avidin bound states (B1 and B2). Single channel recording were carried out in 10mM sodium phosphate buffer pH 6 containing KCl ranging from (a) 150mM (b) 300mM (c) 450mM and (d) 750mM KCl. (e) The effect of salt concentration on the relative open pore current and (f) the dwell time duration of avidin B1 and B2 states.

Because salt screens the surface charge of the bound avidin and the OmpG, increasing salt concentration could essentially weaken all three forces that act on avidin. This explains why at low salt concentration (150 mM KCl), avidin stayed tightly bound (B2) while the loosely-bound state (B1) became dominant when salt concentration increased. Thus, the salt concentration of the recording buffer is an important factor to modulate the detection of the binding signature of the chosen target.



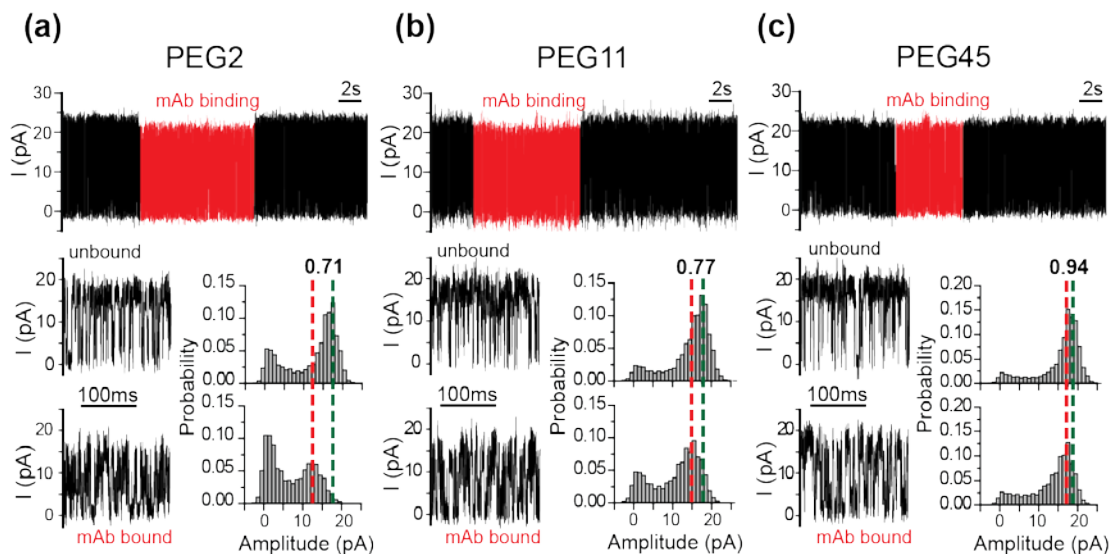


**Figure 4.17. First order exponential fitting analysis of B1 and B2 dwell times in various salt conditions.** B1 and B2 of OmpG-PEG45-biotin in 300 to 750 mM KCl (10 mM sodium phosphate pH 6) buffers was measured at +100 mV. The histograms were generated from at least 300 events from a single representative pore. The average dwell times were calculated from the extracted dwell times of at least three independent pores and the error is the standard deviation.

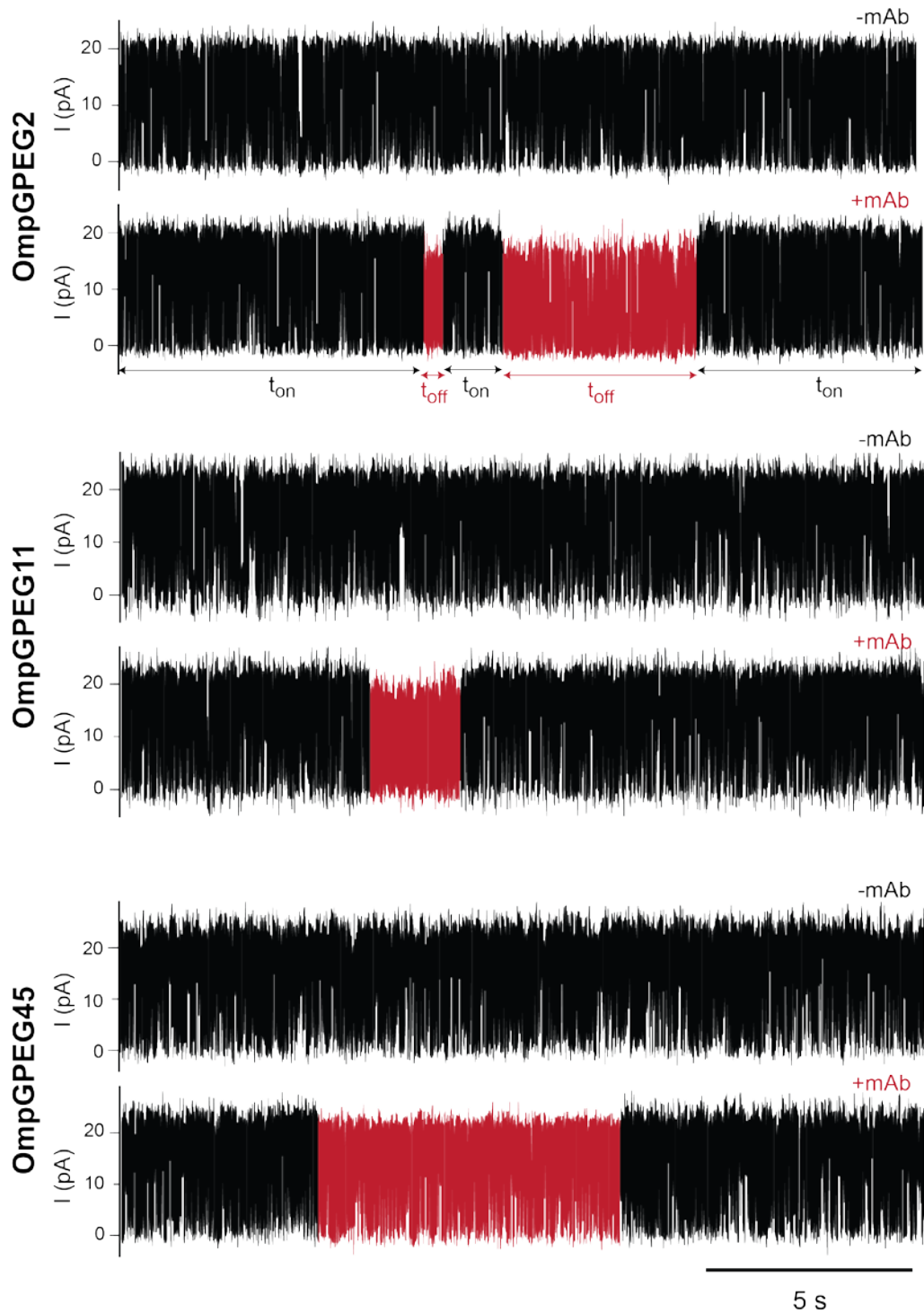
#### 4.4.4 Effect of linker length on the binding kinetics

To assess the effect of PEG linker length on binding kinetics, a reversible-binding mouse monoclonal anti-biotin antibody (mAb) was used in place of streptavidin and avidin. The recording buffer salt was lowered to 150 mM because the gating activity of OmpG-PEG45-biotin pores did not change in the presence of mAb in 300 mM KCl buffer ( $n = 10$ ). The mAb bound all three nanopore constructs and generated gating signatures

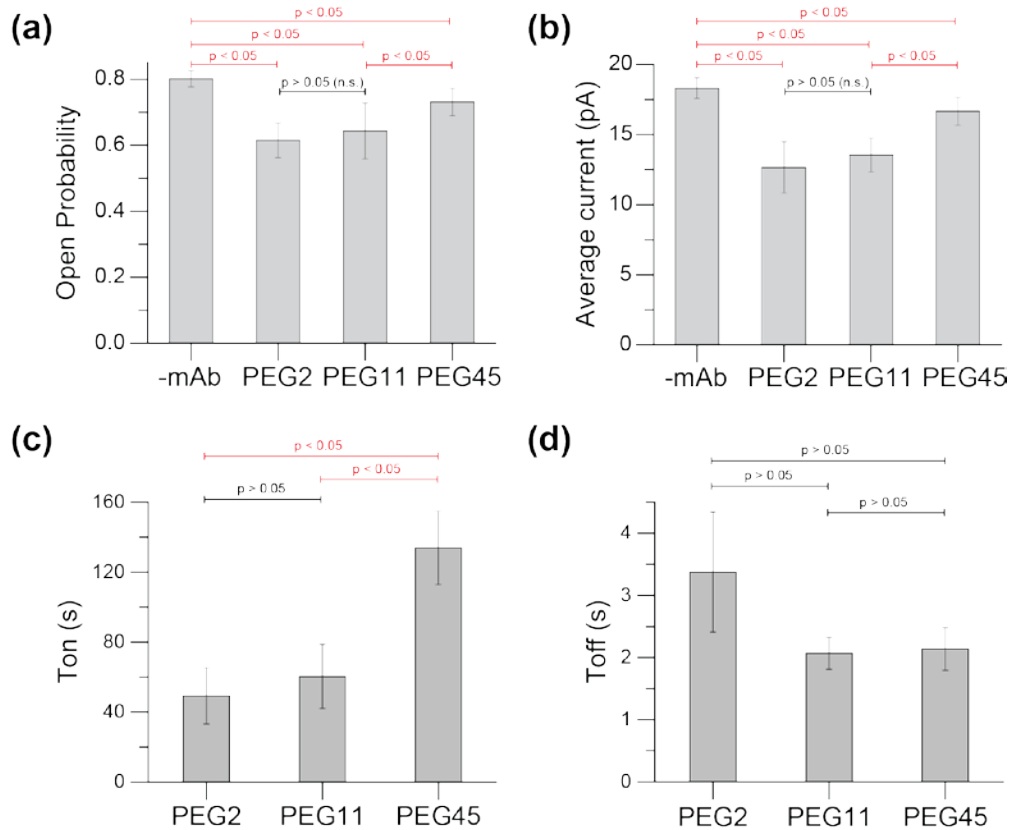
differing in open pore current and gating frequency which lowers the open probability compared to the unbound state (Figure 4.18, 4.19). Although mAb increased the gating frequency for all OmpG-PEG<sub>n</sub>-biotin constructs (Figure 4.20a), the relative open current was  $71 \pm 15\%$  ( $n = 15$ ),  $77 \pm 10\%$  ( $n = 15$ ) and  $94 \pm 7\%$  ( $n = 15$ ) as the length of PEG increased from 2 units to 45 units (Figure 4.20b). Additionally, the three constructs varied in the mAb association ( $k'_{on}$ ) as the longer PEG linker resulted in a slower  $k_{on}$  (Table 4.1, Figures 4.20c, 4.21). The linker length showed less effect on dissociation ( $k_{off}$ ) rates as the differences among the three constructs were insignificant (Table 4.1, Figures 4.20d, 4.21). As a consequence, the observed dissociation equilibrium constant  $K_d$  for OmpG-PEG45-biotin was five times weaker than the OmpG-PEG2-biotin. This result shows the apparent binding affinity of mAb to OmpG-PEG<sub>n</sub>-biotin constructs decreased with the increasing length of the linker (Tables 4.1, 4.2).



**Figure 4.18. Detection of an anti-biotin mouse monoclonal antibody (mAb) by the three OmpG-PEG<sub>n</sub>-biotins.** Current recordings and all events histograms of anti-biotin mAb binding to (a) OmpG-PEG2-biotin (b) OmpG-PEG11-biotin (c) OmpG-PEG45-biotin. Green dashed lines indicate the open current of the pores in the unbound state and red dashed lines indicate the open current in the avidin bound state. Buffer used is 150mM KCl, 10mM sodium phosphate pH 6. The applied voltages were +50 mV.



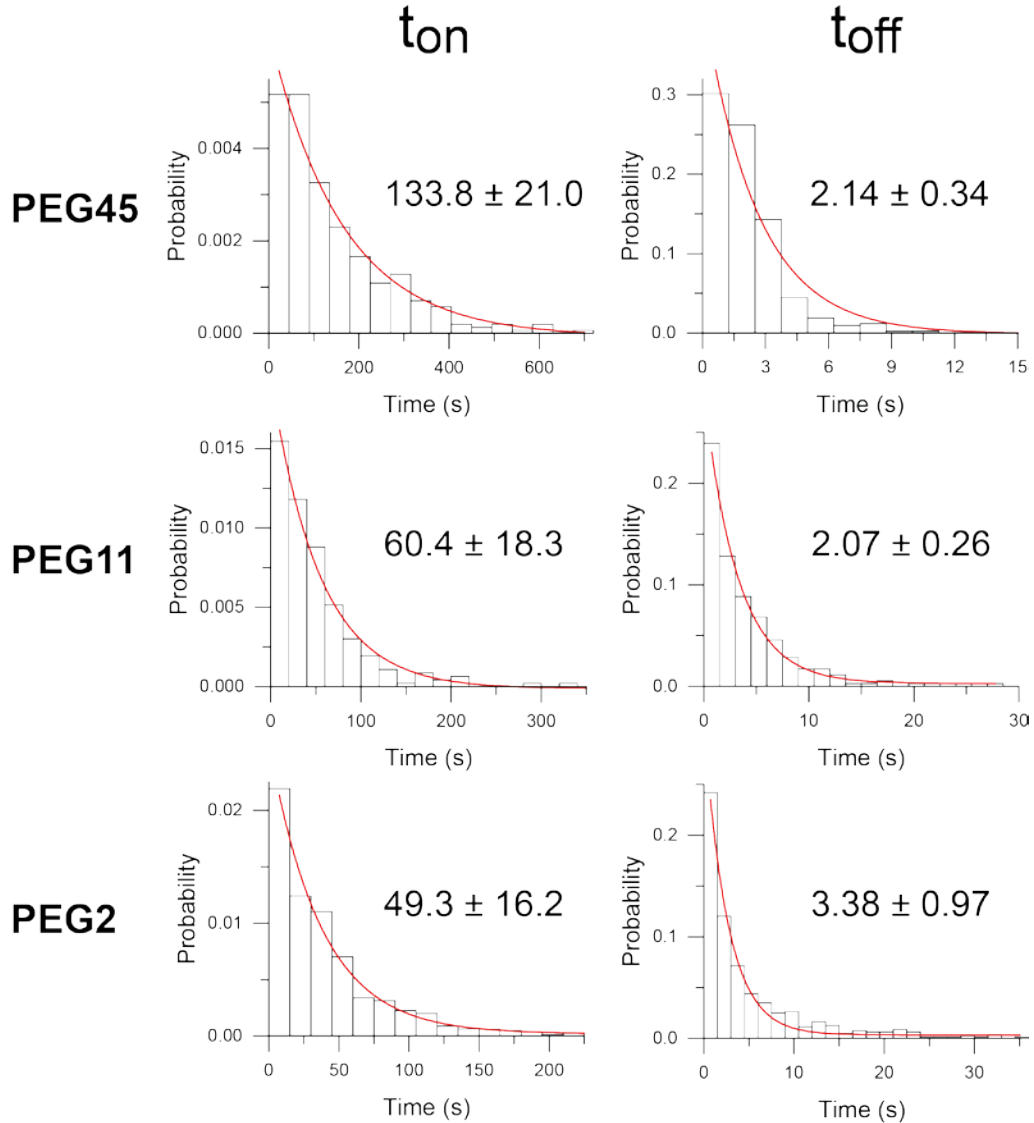
**Figure 4.19. The binding signal and the defined  $t_{on}$  and  $t_{off}$  events of anti-biotin mAb to OmpG-PEG<sub>n</sub>-biotin.** When the mAb binds to the OmpG pore (shown in red) the result is a reduction in the open probability of the pore as well as a reduction in the open current. The pores were recorded in 10 mM sodium phosphate pH 6, 150 mM KCl buffer at +50 mV. Signals were filtered with a 2 kHz Bessel filter and acquired at a sampling of 100  $\mu$ s.



**Figure 4.20. Statistic analysis to compare the binding of mAb to the OmpG-PEG<sub>n</sub>-biotin constructs.** The change in (a) open probability (b) open current (c) on-rate ( $t_{on}$ ) and (d) off-rate  $t_{off}$  when mAb binds to OmpG-PEG2-biotin, OmpG-PEG11-biotin and OmpG-PEG45-biotin are shown. The pores were recorded in 10 mM sodium phosphate pH 6, 150 mM KCl buffer at +50 mV. The average open probabilities were calculated using at least 5000 open and closed events from each pore. At least three independent pores were analyzed. The average open current was determined from at least four independent pores. More than 30 mAb bound and 30 unbound events were extracted from each pore. To determine the  $t_{on}$  and  $t_{off}$ , approximately 1000 events were extracted from each pore. At least three independent pores were analyzed for binding kinetics. P values > 0.05 (highlighted in black) reveal data that has no significant difference (n.s.) while p values < 0.5 (highlighted in red) reveal data that are statistically different.

In nanopore sensing, the electroosmotic flow, electrophoretic force and electrostatic forces strongly influence the molecule's motion within the nanopore and near the entrance.<sup>56,57</sup> Steep potential gradients and strong flow velocity that occur at the constriction site of a nanopore can create an absorbing force to facilitate the capture of the analyte by the nanopore.<sup>58,59</sup> All three forces, when acting on the analyte in the same direction, can potentially promote stronger binding with OmpG-PEG<sub>n</sub>-biotin by

enhancing the mAb association and inhibiting dissociation. Since these forces were strongest in the pore entrance and decrease rapidly with increasing distance, increasing the PEG linker length reduced the binding affinity. Thus, although a longer linker may potentially improve the selective detection, it would compromise the detection sensitivity.

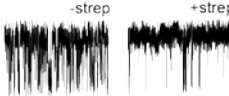
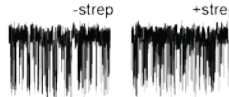
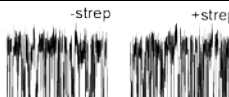
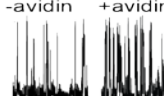
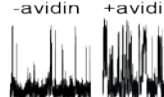
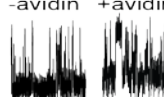
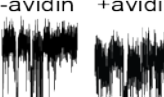

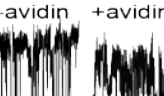


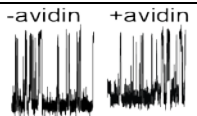
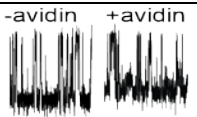
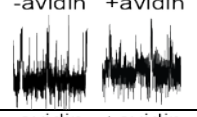
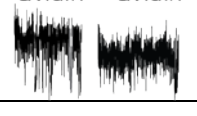
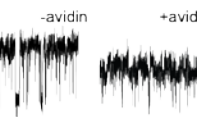
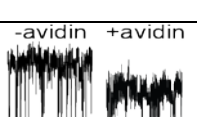
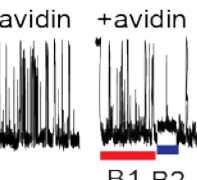
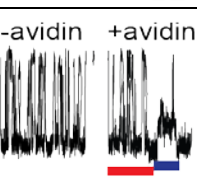
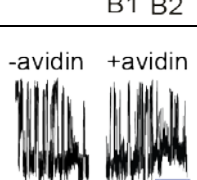
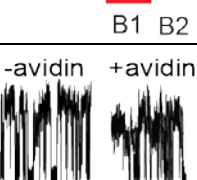
**Figure 4.21. First order exponential fitting analysis of  $t_{on}$  and  $t_{off}$  dwell times of antibiotic mAb.** mAb binding to OmpG-PEG45-biotin, OmpG-PEG11-biotin, OmpG-PEG2-biotin was performed in 10 mM sodium phosphate pH 6, 150 mM KCl buffer and measured at +50 mV. Dwell times are measured in seconds. The histograms were plotted from the dwell times extracted from a single representative pore. The dwell times are the averages from three independent pores and the error is the standard deviation.

**Table 4.1.** Linker effect on the binding kinetics of an anti-biotin mouse monoclonal antibody.

Biotin construct	$k'_{on}$ ( $\times 10^6 \text{ M}^{-1} \text{ s}^{-1}$ )	$k_{off}$ ( $\text{s}^{-1}$ )	$K'_D$ ( $\times 10^{-8} \text{ M}$ )
OmpG-PEG2	$20.3 \pm 6.7$	$0.30 \pm 0.08$	$1.5 \pm 0.6$
OmpG-PEG11	$16.6 \pm 5.0$	$0.48 \pm 0.06$	$2.9 \pm 0.6$
OmpG-PEG45	$7.5 \pm 1.2$	$0.47 \pm 0.07$	$6.3 \pm 1.2$

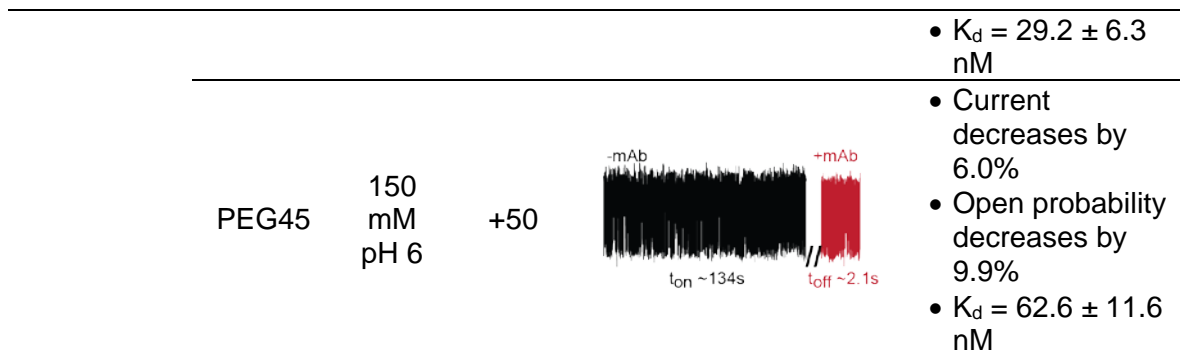
**Table 4.2.** Summary of the binding effects of streptavidin, avidin and anti-biotin mAb to OmpG-PEG<sub>n</sub>-biotin constructs.

Target	OmpG-biotin	Buffer	Voltage (mV)	Binding Signal	Binding Characteristic
Streptavidin	PEG2	300 mM pH 6	+50		• Open probability increases by 17%
	PEG11	300 mM pH 6	+50		• No change in gating activity
	PEG45	300 mM pH 6	+50		• No change in gating activity
Avidin	PEG2	300 mM pH 6	-75		• Current decreases by 13.8%
		300 mM pH 6	-50		• Current decreases by 17.0%
		300 mM pH 6	-25		• Current decreases by 22.4%
		300 mM pH 6	+25		• Current decreases by 35.7%
		300 mM pH 6	+50		• Current decreases by 39.6% • No change in open probability
		300 mM pH 6	+75		• Current decreases by 44.8%

Avidin	PEG11	300 mM pH 6	-75		<ul style="list-style-type: none"> <li>• Current decreases by 10.5%</li> </ul>
		300 mM pH 6	-50		<ul style="list-style-type: none"> <li>• Current decreases by 15.1%</li> </ul>
		300 mM pH 6	-25		<ul style="list-style-type: none"> <li>• Current decreases by 16.0%</li> </ul>
	PEG11	300 mM pH 6	+25		<ul style="list-style-type: none"> <li>• Current decreases by 39.0%</li> </ul>
		300 mM pH 6	+50		<ul style="list-style-type: none"> <li>• Current decreases by 42.8%</li> <li>• No change in open probability</li> </ul>
		300 mM pH 6	+75		<ul style="list-style-type: none"> <li>• Current decreases by 47.3%</li> </ul>
Avidin	PEG45	300 mM pH 6	-75		<ul style="list-style-type: none"> <li>• B1 current indistinguishable from -avidin</li> <li>• B2 current decreases by 16.7%</li> </ul>
		300 mM pH 6	-50		<ul style="list-style-type: none"> <li>• B1 current indistinguishable from -avidin</li> <li>• B2 current decreases by 18.9%</li> </ul>
		300 mM pH 6	-25		<ul style="list-style-type: none"> <li>• B1 current indistinguishable from -avidin</li> <li>• B2 current decreases by 28.5%</li> </ul>
		300 mM pH 6	+25		<ul style="list-style-type: none"> <li>• B1 current decreases by 9.4%</li> <li>• B2 current decreases by 29.5%</li> </ul>

Avidin	PEG45	300 mM pH 6	+50		<ul style="list-style-type: none"> <li>• B1 current decreases by 10.8%</li> <li>• B2 current decreases by 36.8%</li> <li>• No change in open probability</li> </ul>
		300 mM pH 6	+75		<ul style="list-style-type: none"> <li>• B1 current decreases by 17.3%</li> <li>• B2 current decreases by 47.7%</li> </ul>
		300 mM pH 6	+100		<ul style="list-style-type: none"> <li>• B1 current decreases by 20.2%</li> <li>• B2 current decreases by 37.8%</li> </ul>
		150 mM pH 6	+100		<ul style="list-style-type: none"> <li>• Current decreases by 62%</li> </ul>
		450 mM pH 6	+100		<ul style="list-style-type: none"> <li>• B1 current decreases by 12.7%</li> <li>• B2 current decreases by 29.7%</li> </ul>
		750 mM pH 6	+100		<ul style="list-style-type: none"> <li>• B1 current indistinguishable from -avidin</li> <li>• B2 current decreases by 25.4%</li> </ul>
Anti-biotin mAb	PEG2	150 mM pH 6	+50		<ul style="list-style-type: none"> <li>• Current decreases by 28.6%</li> <li>• Open probability decreases by 27.6%</li> <li>• <math>K_d = 14.6 \pm 5.77</math> nM</li> </ul>
		150 mM pH 6	+50		<ul style="list-style-type: none"> <li>• Current decreases by 22.5%</li> <li>• Open probability decreases by 17.4%</li> </ul>





#### 4.5 Conclusion

By varying the length of the tether connecting biotin to OmpG, we showed how distance influenced OmpG's detection selectivity and sensitivity. Our data demonstrated that electrostatic interactions, electroosmotic and electrophoretic forces not only strongly modulate the signal characteristics of the bound state but also affect their binding kinetics. Increasing the linker length weakened these forces resulted in the decrease in sensitivity. On the contrary, a longer linker allowed a bound analyte to sample multiple interactions at the interface with the nanopore, which may enhance analyte identification and differentiation.

## 4.6 References

1. Howorka, S. & Siwy, Z. Nanopore analytics: sensing of single molecules. *Chem. Soc. Rev.* **38**, 2360–2384 (2009).
2. Movileanu, L. Interrogating single proteins through nanopores: challenges and opportunities. *Trends Biotechnol.* **27**, 333–341 (2009).
3. Oukhaled, A., Bacri, L., Pastoriza-Gallego, M., Betton, J. M. & Pelta, J. Sensing proteins through nanopores: Fundamental to applications. *ACS Chem. Biol.* **7**, 1935–1949 (2012).
4. Kasianowicz, J. J., Robertson, J. W. F., Chan, E. R., Reiner, J. E. & Stanford, V. M. Nanoscopic porous sensors. *Annu. Rev. Anal. Chem. (Palo Alto, Calif.)*, **1**, 737–766 (2008).
5. Reiner, J. E. *et al.* Disease detection and management via single nanopore-based sensors. *Chem. Rev.* **112**, 6431–6451 (2012).
6. Li, J. *et al.* Ion-beam sculpting at nanometre length scales. *Nature* **412**, 166–169 (2001).
7. Siwy, Z. *et al.* Protein biosensors based on biofunctionalized conical gold nanotubes. *J. Am. Chem. Soc.* **127**, 5000–5001 (2005).
8. Ding, S., Gao, C. & Gu, L. Q. Capturing single molecules of immunoglobulin and ricin with an aptamer-encoded glass nanopore. *Anal. Chem.* **81**, 6649–6655 (2009).
9. Han, A. *et al.* Sensing protein molecules using nanofabricated pores. *Appl. Phys. Lett.* **88**, 1–4 (2006).
10. Fologea, D., Ledden, B., McNabb, D. S. & Li, J. Electrical characterization of protein molecules by a solid-state nanopore. *Appl. Phys. Lett.* **91**, 53901-1-53901–3 (2007).
11. Sexton, L. T. *et al.* Resistive-pulse studies of proteins and protein/antibody complexes using a conical nanotube sensor. *J. Am. Chem. Soc.* **129**, 13144–13152 (2007).
12. Yusko, E. C. *et al.* Controlling protein translocation through nanopores with bio-inspired fluid walls. *Nat. Nanotechnol.* **6**, 253–60 (2011).
13. Kasianowicz, J. J., Henrickson, S. E., Weetall, H. H. & Robertson, B. Simultaneous multianalyte detection with a nanometer-scale pore. *Anal. Chem.* **73**, 2268–2272 (2001).
14. Wei, R., Gatterdam, V., Wieneke, R., Tampé, R. & Rant, U. Stochastic sensing of proteins with receptor-modified solid-state nanopores. *Nat. Nanotechnol.* **7**, 257–63 (2012).
15. Singh, P. R. *et al.* Pulling peptides across nanochannels: Resolving peptide binding and translocation through the hetero-oligomeric channel from nocardia farcinica. *ACS Nano* **6**, 10699–10707 (2012).
16. Bell, N. A. W. & Keyser, U. F. Specific Protein Detection Using Designed DNA Carriers and Nanopores. *J. Am. Chem. Soc.* **137**, 2035–2041 (2015).
17. Plesa, C., Ruitenbergh, J. W., Witteveen, M. J. & Dekker, C. Detection of Single Proteins Bound along DNA with Solid-State Nanopores. *Nano Lett.* **15**, 3153–3158 (2015).
18. Li, T., Liu, L., Li, Y., Xie, J. & Wu, H. C. A universal strategy for aptamer-based nanopore sensing through host-guest interactions inside a-hemolysin. *Angew. Chemie - Int. Ed.* **54**, 7568–7571 (2015).
19. Niedzwiecki, D. J. *et al.* Observing Changes in the Structure and Oligomerization State of a Helical Protein Dimer Using Solid-State Nanopores. *ACS Nano* **9**, 8907–8915 (2015).

20. Nir, I., Huttner, D. & Meller, A. Direct Sensing and Discrimination among Ubiquitin and Ubiquitin Chains Using Solid-State Nanopores. *Biophys. J.* **108**, 2340–2349 (2015).
21. Soskine, M. *et al.* An engineered ClyA nanopore detects folded target proteins by selective external association and pore entry. *Nano Lett.* **12**, 4895–900 (2012).
22. Meervelt, V. Van, Soskine, M. & Maglia, G. Detection of Two Isomeric Binding Configurations in a Protein Aptamer Complex with a Biological Nanopore. *ACS Nano* **8**, 12826–12835 (2014).
23. Talaga, D. S. & Li, J. Single-molecule protein unfolding in solid state nanopores. *J. Am. Chem. Soc.* **131**, 9287–9297 (2009).
24. Rosen, C. B., Rodriguez-Larrea, D. & Bayley, H. Single-molecule site-specific detection of protein phosphorylation with a nanopore. *Nat. Biotechnol.* **32**, 179–181 (2014).
25. Rodriguez-Larrea, D. & Bayley, H. Multistep protein unfolding during nanopore translocation. *Nat. Nanotechnol.* **8**, 288–295 (2013).
26. Nivala, J., Mulroney, L., Li, G., Schreiber, J. & Akeson, M. Discrimination among Protein Variants Using an Unfoldase-Coupled Nanopore. *ACS Nano* **8**, 12365–75 (2014).
27. Nivala, J., Marks, D. B. & Akeson, M. Unfoldase-mediated protein translocation through an  $\alpha$ -hemolysin nanopore. *Nat. Biotechnol.* **31**, 247–50 (2013).
28. Japrun, D. *et al.* Single-molecule studies of intrinsically disordered proteins using solid-state nanopores. *Anal. Chem.* **85**, 2449–2456 (2013).
29. Stefureac, R. I. & Lee, J. S. Nanopore analysis of the folding of zinc fingers. *Small* **4**, 1646–1650 (2008).
30. Oukhaled, G. *et al.* Unfolding of proteins and long transient conformations detected by single nanopore recording. *Phys. Rev. Lett.* **98**, 158101 (2007).
31. Wang, H., Ying, Y., Li, Y., Kraatz, H. & Long, Y. Nanopore Analysis of  $\beta$ -Amyloid Peptide Aggregation Transition Induced by Small Molecules. *Anal. Chem.* **83**, 1746–1752 (2011).
32. Kasianowicz, J. J., Brandin, E., Branton, D. & Deamer, D. W. Characterization of individual polynucleotide molecules using a membrane channel. *Proc. Natl. Acad. Sci. U. S. A.* **93**, 13770–13773 (1996).
33. Zhao, Q., De Zoysa, R. S. S., Wang, D., Jayawardhana, D. A. & Guan, X. Real-time monitoring of peptide cleavage using a nanopore probe. *J. Am. Chem. Soc.* **131**, 6324–6325 (2009).
34. Cheley, S., Xie, H. & Bayley, H. A genetically encoded pore for the stochastic detection of a protein kinase. *ChemBioChem* **7**, 1923–1927 (2006).
35. Xie, H., Braha, O., Gu, L. Q., Cheley, S. & Bayley, H. Single-molecule observation of the catalytic subunit of cAMP-dependent protein kinase binding to an inhibitor peptide. *Chem. Biol.* **12**, 109–120 (2005).
36. Wang, S., Haque, F., Rychahou, P. G., Evers, B. M. & Guo, P. Engineered nanopore of phi29 dna-packaging motor for real-time detection of single colon cancer specific antibody in serum. *ACS Nano* **7**, 9814–9822 (2013).
37. Harrington, L., Cheley, S., Alexander, L. T., Knapp, S. & Bayley, H. Stochastic detection of Pim protein kinases reveals electrostatically enhanced association of a peptide substrate. *Proc. Natl. Acad. Sci. U. S. A.* **110**, E4417-26 (2013).
38. Movileanu, L., Howorka, S., Braha, O. & Bayley, H. Detecting protein analytes that modulate transmembrane movement of a polymer chain within a single protein pore. *Nat. Biotechnol.* **18**, 1091–1095 (2000).
39. Rotem, D., Jayasinghe, L., Salichou, M. & Bayley, H. Protein detection by nanopores equipped with aptamers. *J. Am. Chem. Soc.* **134**, 2781–7 (2012).

40. Fahie, M., Chisholm, C. & Chen, M. Resolved Single-Molecule Detection of Individual Species within a Mixture of anti-Biotin Antibodies Using an Engineered Monomeric Nanopore. *ACS Nano* **9**, 1089–1098 (2015).
41. Fahie, M. A. & Chen, M. Electrostatic Interactions between OmpG Nanopore and Analyte Protein Surface Can Distinguish between Glycosylated Isoforms. *J. Phys. Chem. B* **119**, 10198–10206 (2015).
42. Fahie, M. A., Yang, B., Mullis, M., Holden, M. A. & Chen, M. Selective detection of protein homologues in serum using an OmpG nanopore. *Anal. Chem.* **87**, 11143–11149 (2015).
43. Liang, B. & Tamm, L. K. Structure of outer membrane protein G by solution NMR spectroscopy. *Proc. Natl. Acad. Sci. U. S. A.* **104**, 16140–5 (2007).
44. Subbarao, G. V & van den Berg, B. Crystal structure of the monomeric porin OmpG. *J. Mol. Biol.* **360**, 750–9 (2006).
45. Yildiz, O., Vinothkumar, K. R., Goswami, P. & Kühlbrandt, W. Structure of the monomeric outer-membrane porin OmpG in the open and closed conformation. *EMBO J.* **25**, 3702–13 (2006).
46. Chen, M., Khalid, S., Sansom, M. S. P. & Bayley, H. Outer membrane protein G: Engineering a quiet pore for biosensing. *Proc. Natl. Acad. Sci. U. S. A.* **105**, 6272–7 (2008).
47. Zhuang, T. & Tamm, L. K. Control of the conductance of engineered protein nanopores through concerted loop motions. *Angew. Chem. Int. Ed. Engl.* **53**, 5897–902 (2014).
48. Butler, T. Z., Pavlenok, M., Derrington, I. M., Niederweis, M. & Gundlach, J. H. Single-molecule DNA detection with an engineered MspA protein nanopore. *Proc. Natl. Acad. Sci.* **105**, 20647–20652 (2008).
49. Song, L. *et al.* Structure of staphylococcal alpha-hemolysin, a heptameric transmembrane pore. *Science* **274**, 1859–66 (1996).
50. Faller, M., Niederweis, M. & Schulz, G. E. The Structure of a Mycobacterial Outer-Membrane Channel. *Science (80-. )*. **303**, 1189–1192 (2004).
51. Mueller, M., Grauschopf, U., Maier, T., Glockshuber, R. & Ban, N. The structure of a cytolytic alpha-helical toxin pore reveals its assembly mechanism. *Nature* **459**, 726–30 (2009).
52. Simpson, A. A. *et al.* Structure of the bacteriophage phi29 DNA packaging motor. *Nature* **408**, 745–750 (2000).
53. Chen, M., Li, Q.-H. & Bayley, H. Orientation of the monomeric porin OmpG in planar lipid bilayers. *Chembiochem* **9**, 3029–36 (2008).
54. Aksimentiev, A. & Schulten, K. Imaging alpha-hemolysin with molecular dynamics: ionic conductance, osmotic permeability, and the electrostatic potential map. *Biophys. J.* **88**, 3745–61 (2005).
55. Laohakunakorn, N. & Keyser, U. F. Electroosmotic flow rectification in conical nanopores. *Nanotechnology* **26**, 275202 (2015).
56. Wang, Y. *et al.* Nanopore sensing of botulinum toxin type B by discriminating an enzymatically cleaved peptide from a synaptic protein synaptobrevin 2 derivative. *ACS Appl. Mater. Interfaces* **7**, 184–192 (2015).
57. Firnkes, M. *et al.* Electrically Facilitated Translocations of Proteins through Silicon Nitride Nanopores : Conjoint and Competitive Action of Diffusion . *Nano Lett.* **10**, 2162–2167 (2010).
58. Wong, C. T. a & Muthukumar, M. Polymer capture by electro-osmotic flow of oppositely charged nanopores. *J. Chem. Phys.* **126**, 1–6 (2007).
59. Wanunu, M., Morrison, W., Rabin, Y., Grosberg, A. Y. & 1D, A. M. Electrostatic Focusing of Unlabeled DNA into Nanoscale Pores using a Salt Gradient. *Nat.*

*Nanotechnol.* **5**, 160–165 (2010).

## CHAPTER 5

### A NON-CLASSICAL ASSEMBLY PATHWAY OF *ESCHERICHIA COLI* PORE FORMING TOXIN CYTOLYSIN A

Reprinted (adapted) with permission from M. Fahie, F. Romano, C. Chisholm, A. P. Heuck, M. Zbinden, and M. Chen, "A non-classical assembly pathway of *Escherichia coli* pore forming toxin cytolysin A.," *J. Biol. Chem.*, vol. 288, no. 43, pp. 31042–31051, Sep. 2013. Copyright 2013 Journal of Biological Chemistry.

#### 5.1 Summary

Cytolysin A (ClyA) is an alpha-helical pore forming toxin ( $\alpha$ -PFT) from pathogenic *Escherichia coli* (*E. coli*), *Shigella* and *Salmonella enteric* strains. PFTs are virulent factors secreted as monomers by bacteria but can assemble to oligomeric pores when they encounter their target cell membrane. Here, we report that *E. coli* ClyA can assemble into an oligomeric structure in solution at physiological temperature in the absence of either bilayer membranes or detergents. These soluble ClyA oligomers can rearrange to create transmembrane pores when in contact with detergents or biological membranes. Intrinsic fluorescence measurements revealed that the oligomers adopted an intermediate state found during the transition between monomer and transmembrane pore. These results suggest that the water-soluble oligomers represent a prepore intermediate state. Furthermore, our data suggests that ClyA does not form transmembrane pores on reconstituted *E. coli* lipid membranes. Since ClyA can be delivered to the target host cell in an oligomeric conformation within outer membrane vesicles (OMVs), our findings support a model that suggests that ClyA forms a prepore oligomeric structure independently of the lipid membrane within the OMV. This proposed model for ClyA represents a non-classical PFT assembly pathway to attack eukaryotic host cells.

## 5.2 Introduction

Pore-forming toxins (PFTs) represent the largest family of bacterial protein toxins and constitute important bacterial virulence factors.<sup>1,2</sup> Their cytolytic function operates by introducing a large, water-filled pore into target cell membranes. These pores either deliver toxic effector proteins to the target cell or lead to cell lysis through leakage.<sup>3</sup> Most bacterial PFTs are secreted into the extracellular environment in a water-soluble form, where they subsequently diffuse and assemble on host cell membranes. Pore-forming toxins are classified as  $\alpha$ -PFTs or  $\beta$ -PFTs depending on the predominant secondary structure of the transmembrane pore, i.e.  $\alpha$ -PFTs contain  $\alpha$ -helical transmembrane domains and  $\beta$ -PFTs form a  $\beta$ -barrel.<sup>1,2</sup>

Cytolysin A (ClyA), also known as silent hemolysin A (SheA) or hemolysin E (HlyE), is a cytolytic  $\alpha$ -PFT that causes the hemolytic phenotype of several *Escherichia coli* (*E. coli*) strains.<sup>4-9</sup> Its homologues are also found in other pathogenic organisms, including *Salmonella typhi* and *Shigella flexneri*.<sup>10,11</sup> The *E. coli* ClyA monomer is a 34-kDa soluble protein that has a rod shape formed by a core bundle of four long  $\alpha$ -helices (~90 Å long).<sup>10</sup> At the end of the bundle that contains the N-terminal region, an additional shorter (~30 Å long) helix from the C-terminal region packs against the core bundle, forming a five-helix bundle for about one-third the length of the molecule. The structure of the transmembrane pore shows a hollow funnel consisting of 12 subunits (protomers).<sup>12,13</sup> Each protomer contributes one amphipathic  $\alpha$ -helix that packs in an iris-like structure to form the transmembrane barrel. The narrowest opening of the channel at the transmembrane site has a diameter of 35 Å while the top or widest part of the funnel is 70 Å.<sup>12</sup>

The general model for multimeric PFT attack action involves three steps<sup>1</sup>: (i) docking of the soluble monomer to the target cell membrane; (ii) assembly of the monomer into a ring-like prepore structure that lacks the transmembrane domain structure at the membrane surface; (iii) penetration of the transmembrane domain across the target cell membrane. In the first step, cholesterol, carbohydrates or membrane proteins on the host's cell surface may serve as receptors for the association of the toxins with the membrane.<sup>14-18</sup> ClyA toxin is also believed to follow a similar strategy when attacking host cells.<sup>1</sup> However, unlike the well-studied  $\beta$ -toxins  $\alpha$ -hemolysin and protective antigen from anthrax toxin (PA), which are secreted by gram-positive bacteria into the extracellular environment as a soluble monomer,<sup>19,20</sup> ClyA is secreted from *E. coli* via a vesicle-mediated pathway.<sup>21-23</sup> Similar to the budding of yeast cells, the outer membrane of *E. coli* bubbles out and pinches off to form the outer membrane vesicles (OMVs).<sup>24</sup> During the formation of the OMV, many outer membrane proteins as well as periplasmic proteins (of which ClyA is a member) are incorporated into the OMV. The vesicle-mediated pathway has been found to deliver several toxins, including heat-labile enterotoxin and Shiga toxin.<sup>25-27</sup> So far, it remains unclear how these toxins are released from the OMVs to carry out their cytolytic function.<sup>25</sup>

Of note, Wai et al. discovered that ClyA in the OMV adopted a ring-like oligomeric structure when viewed under an electron-microscope.<sup>21</sup> This observation contradicts the typical PFT strategy of assembling pores from water-soluble monomers at the surface of the target cell. These ClyA oligomers were speculated to represent transmembrane pores, thus raising a question about how transmembrane pores already embedded in *E. coli* lipid membranes could then transfer to the host cellular membrane. Nevertheless, its secretion pathway is distinct from the well-studied  $\beta$ -toxins, which suggests that ClyA may have an unexpected mechanism to carry out its cytolytic function.



In this study, we report that ClyA assembles into soluble hemolytically active oligomers in the absence of lipid bilayers or detergents. The water-soluble oligomer may represent a prepore intermediate undergoing the transition from the monomer to the transmembrane pore. This data could provide important evidence to elucidate the structural organization of the oligomeric ClyA proteins in the OMV, which is a step further towards understanding the attack mechanism for the ClyA toxin.

### **5.3 Materials and Methods**

All the chemicals were purchased from Fisher Scientific unless otherwise specified. Luria Broth (LB) Miller version medium was purchased from Boston BioProducts.

#### **5.3.1 Cloning and mutagenesis of ClyA**

The *E. coli* ClyA gene was amplified from the *E. coli* K-12 genome (ATCC) and cloned into a pT7 vector with a C-terminal hexa-histidine tag XhoI and HindIII restriction cut sites to insert the gene into the multiple cloning site. The cysteine-less ClyA (C87S, C285S) was obtained by the overlap PCR method using the plasmid containing the C-terminal hex-histidine tagged ClyAwt gene (pT7-ClyAwt) as a template. The PCR was performed using Phusion polymerase reaction (New England Biolabs). The primers for C87S were 5'- ATGAATGGTCTGGTGTTCGACGCAATTG (forward) and 5'- CGTCGCAACACCAGACCATTCATACACTG (reverse). These two primers were used in a pair with the primers SC47: 5'-CAGAAGTGGTCCTGCAACTTTATC (reverse) and SC46: 5'-ATAAAGTTGCAGGACCACTTCTG (forward) which annealed to the middle of the plasmid in the Ampicillin resistance cassette. The two PCR products were then mixed in an approximate 1:1 molar ratio and subjected to DpnI digestion for three hours at 37°C to degrade the parental plasmid. Competent *E. coli* DH5α cells were then co-transformed with the PCR mixture and colonies containing the desired mutant construct pT7-ClyA C87S were identified by DNA sequencing. The same procedure was repeated

to generate pT7-ClyA  $\Delta$ Cys (C87S C285S) construct using the pT7-ClyA C87S as template. The two primers used for introducing the C285S mutation into the C87S mutant plasmid were 5'-AACACCTCTAATGAGTATCAGAAAAGAC (forward) and 5'-ACTCATTAGAGGTGTTAATCATTTTTTTGG (reverse). The single cysteine mutant pT7-ClyA C304 was constructed in the same way by using pT7-ClyA  $\Delta$ Cys as a template for PCR. Primers were 5'-CTGAAGTCTGCCACCATCACCATCACC (forward) and 5'-TGGTGGCAGACTTCAGGTACCTCAAAG (reverse). All primers were obtained from Fisher Scientific.

### **5.3.2 Expression and purification of ClyA**

The resulted plasmids were transformed into *E. coli* BL21. Cells were grown in LB medium at 37°C to OD<sub>600</sub> 0.5. Isopropyl  $\beta$ -D-1-thiogalactopyranoside (0.5 mM) was then added to the cell culture to induce protein expression. Cells were grown for 3 hours and then harvested by centrifugation. To purify the ClyA protein, cell pellets (1.0 L culture) were resuspended in 50 ml 50 mM Tris•HCl, pH 8.0, 200  $\mu$ g/ml lysozyme and 1 mM EDTA, 0.1 mM phenylmethanesulfonylfluoride (Sigma). The cell lysate was incubated on ice for 30 minutes. To reduce the viscosity, 50 kU DNase I and 3 mM MgCl<sub>2</sub> were added to the mixture and incubated for 30 minutes at room temperature. The lysate was centrifuged at 20,000 g for 30 min. After passing through a 0.45  $\mu$ m filter, the supernatant sample was loaded onto the Ni-NTA affinity column that was equilibrated with buffer A which contained 50 mM Tris•HCl, pH 8.0, 150 mM NaCl. His-tagged ClyA proteins were eluted under a gradient with buffer A and buffer B which contained the same Tris buffer and NaCl but included 0.5 M imidazole. The ClyA protein eluted in around 30% buffer B or ~150 mM imidazole. ClyA was then further purified to remove aggregates and the excess imidazole by Superdex 200 10/300 gel filtration column (GE Healthcare) that was equilibrated with 25mM Tris•HCl, pH 8.0, 150 mM NaCl. The mon-

omeric ClyA proteins were collected and stored at  $-80^{\circ}\text{C}$  at a concentration of 0.7 mg/ml or less. The purity of the protein (>95%) was verified by 15% SDS-PAGE (Figure 5.1).



**Figure 5.1. SDS-PAGE of nickel affinity purified ClyAwt protein.** The ClyA protein eluted in 150 mM imidazole from the nickel affinity column and was then run through gel filtration as a further purification step. The protein purity is > 95%.

### 5.3.3 Gel filtration analysis of ClyA oligomerization

Gel filtration chromatography (GFC) analysis of proteins was performed at room temperature ( $22-23^{\circ}\text{C}$ ) using an analytical Superdex 200 10/300 gel filtration column (GE healthcare). For detergent-triggered oligomerization of ClyA, samples were incubated in 0.1% DDM at the indicated temperature and time. The proteins were then injected onto the column equilibrated in buffer 50 mM Tris•HCl, pH 8.0, 150 mM NaCl, 0.01% (w/v) n-Dodecyl  $\beta$ -D-maltoside (DDM) at room temperature. For detergent independent oligomerization, samples were incubated with buffer containing no DDM at the indicated temperature for 2 hours prior to GFC analysis. The buffer used to analyze and collect the soluble oligomers from GFC was 50 mM Tris•HCl, pH 8.0, 150 mM NaCl.

#### 5.3.4 Intrinsic fluorescence studies

ClyA proteins contained two tryptophan residues (W37 and W85) and were analyzed at a concentration of  $\sim 3 \mu\text{M}$  at  $25^\circ\text{C}$ . For intrinsic fluorescence measurements the excitation wavelength was 280 nm and emission spectra were collected at 290–410 nm using a Fluorolog-3 spectrofluorimeter. The fluorescence emission spectra of corresponding buffers were subtracted from the emission spectrum of each ClyA sample. For DDM-induced oligomerization studies, 15  $\mu\text{l}$  of DDM stock solution (10% w/v) was added to 1.5 ml ClyA monomer at a final concentration of 0.1% (w/v). Subsequently, the emission fluorescence spectra were recorded at 3 minute intervals. The resulting spectra after DDM was added to the sample were adjusted according to the dilution factor as well as the buffer blank.

#### 5.3.5 Liposome preparations

All lipids were purchased from Avanti Polar Lipids (Alabaster, AL). *E. coli* total extract lipids or pig brain total extract lipids in chloroform at 25 mg/ml was dried at  $20\text{--}23^\circ\text{C}$  under dry nitrogen and then kept under vacuum for at least 3 hours. Lipids were re-hydrated in buffer 50 mM Tris•HCl, pH 8.0, 150 mM NaCl to a 25 mg/ml final concentration of total lipids, and incubated for 30 minutes at  $20\text{--}23^\circ\text{C}$  with vortexing at 5 minute intervals. The re-suspended lipid mixture was flash frozen in liquid nitrogen and thawed at  $37^\circ\text{C}$  for a total of three freeze-thaw cycles to reduce the number of multi-lamellar liposomes. Hydrated lipids were extruded 21 times through a  $0.4 \mu\text{m}$  pore size polycarbonate filter (Whatman) using an Avanti Mini-Extruder (Alabaster, AL). The resultant liposomes were stored at  $4^\circ\text{C}$  and used within 2 weeks of production.

Tb(DPA) $_3^{3-}$  loaded liposomes were prepared as above, except that HBS buffer (50 mM HEPES, 100 mM NaCl pH 7.5) including 3 mM TbCl $_3$ , 9 mM 2,6-pyridinedicarboxylic acid (DPA) was added to rehydrate 6.4 mg dried lipids to yield a fi-

nal total lipid concentration of approximately 30 mM (final volume, 0.30 ml). The resulting liposomes loaded with Tb(DPA)<sub>3</sub><sup>3-</sup> were separated from non-encapsulated Tb(DPA)<sub>3</sub><sup>3-</sup> by gravity mediated gel filtration (Sepharose CL-6B-200, 0.7 cm inner diameter X50 cm) in HBS buffer and the resulting concentration (~2 mM) was estimated by measuring the absorbance (light scattering) at 400 nm .

### **5.3.6 Analysis of pore forming activity by hemolytic activity**

The liquid hemolysis assay with sheep defibrinated blood cells was used to measure the hemolytic activity of the ClyA proteins.<sup>28</sup> Briefly, Remel sheep defibrinated blood (Thermo Scientific) was washed with HyClone Dulbecco's phosphate-buffered saline (DPBS) buffer (Thermo Scientific) and diluted four fold in DPBS buffer. ClyA proteins (7 µg) were added to 250 µl of blood cells and incubated at 37°C for 15 minutes. Samples were then centrifuged at 22,000 x g at 4°C for 8 minutes. The absorbance of the supernatant at 540 nm was measured to estimate the concentration of released hemoglobin. The total hemolysis (100%) positive control was defined by incubation of red blood cells in MilliQ water, in place of buffer.

### **5.3.7 Analysis of pore-forming activity by fluorescence quenching**

The pore-forming activity of ClyA proteins was also assessed by using a Tb(DPA) fluorescence quenching assay. Tb(DPA)<sub>3</sub><sup>3-</sup> loaded liposomes (6 µL of ~ 2 mM giving a final concentration of ~12.5 µM total lipids) were added to 994 µL of quenching buffer (100 mM NaCl, 50 mM HEPES, 5 mM EDTA pH 7.5) containing 250 nM protein just before the measurement. Samples were excited at 278 nm and the net initial emission intensity ( $F_0$ ) at 544 nm was determined after equilibration of the sample at 25 °C for 2 minutes. The samples were then incubated for 1 hour at 37°C. After re-equilibration at 25°C for 10 minutes, the final net emission intensity ( $F_i$ ) of the sample

was determined and the fraction of quenched fluorophore was calculated using  $1 - F_i/F_0$ . Measurements were repeated 4 times for each condition.

### 5.3.8 Oxidation of ClyA proteins

The formation of intramolecular disulfide bonds were catalyzed using the oxidizing reagent Cu(phenanthroline)<sub>2</sub> following a previous protocol.<sup>29</sup> ClyA proteins were incubated with 1.5 mM Cu(phenanthroline)<sub>2</sub> at room temperature for 30 minutes with gentle shaking. EDTA (5 mM, final concentration) was then added to quench the oxidation reaction. All the chemicals were then diluted to a negligible level by buffer exchange using a Centricon (Millipore) with a 3kDa cut-off. To reduce the sample, oxidized proteins were incubated with 20 mM reducing agent dithiothreitol (DTT) for 60 min at room temperature with continuous gentle agitation. DTT was then removed by buffer exchange before the analysis of hemolytic activity.

### 5.3.9 Single channel study of ClyA

Planar lipid bilayer experiments were performed in an apparatus partitioned into two chambers with a 25  $\mu\text{m}$ -thick Teflon film. An aperture of approximately 100- $\mu\text{m}$  diameter had been made near the center of the film with an electric arc. About 2  $\mu\text{l}$  of 10% v/v hexadecane dissolved in pentane was added to both sides of the Teflon film and the pentane was allowed to evaporate for 2 minutes. Each chamber was filled with 900  $\mu\text{l}$  of 25 mM Tris•HCl, pH 8.0, 1.0 M KCl. An Ag/AgCl electrode was immersed into each chamber with the *cis* chamber grounded. A positive potential indicates a higher potential in the *trans* chamber. 20-30  $\mu\text{l}$  of 1,2-diphytanoyl-sn-glycerol-3-phosphocholine at a concentration of 10 mg/ml (Avanti Polar Lipids, USA) dissolved in pentane was deposited on the surface of the buffer in both chambers and monolayers formed after the pentane evaporated. The lipid bilayer was formed by raising the liquid level up and down across the aperture, which had been pretreated with a hexadecane/pentane (1:10 v/v)

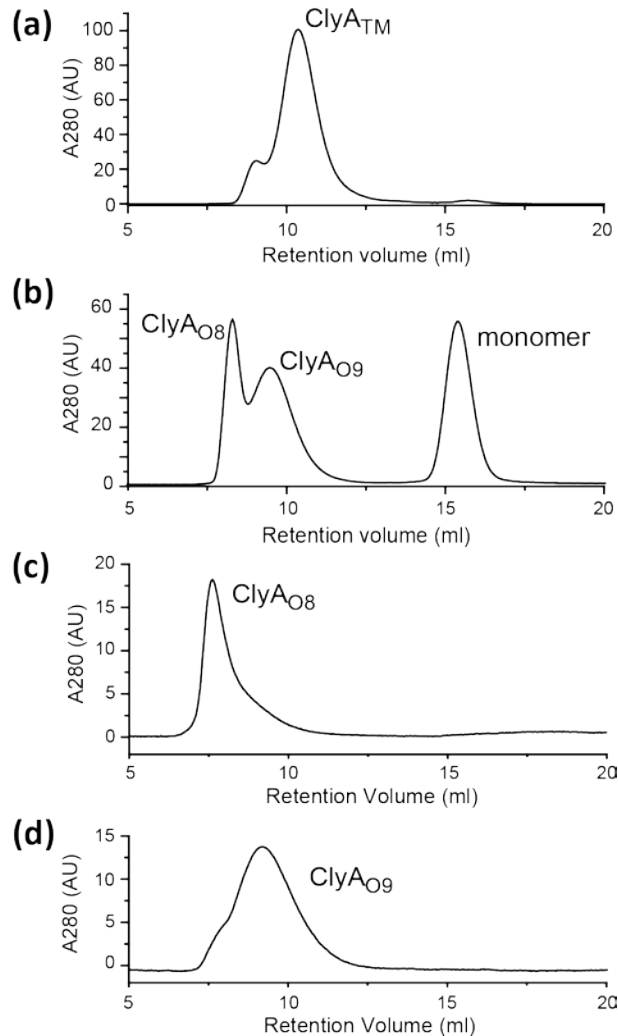
solution to prevent buffer solution exchange between the chambers. The current was amplified with an Axopatch 200B integrating patch clamp amplifier (Axon Instruments, Foster City, CA). A voltage potential of about 10 mV was applied for ClyA pore insertion unless otherwise stated. Signals were filtered with a Bessel filter at 2 kHz (unless otherwise stated) and then acquired by a computer (sampling at 50  $\mu$ s) after digitization with a Digidata 1320A/D board (Axon Instruments). Data were analyzed with Clampex 10.0 software.

## 5.4 Results

### 5.4.1 Assembly of ClyA in the absence of detergent

It is often observed that PFT monomers assemble to form the oligomeric transmembrane pores upon contacting with detergents or lipid vesicles.<sup>30–32</sup> Similar to these previous findings, the retention volume of ClyA monomers shifted from 15 ml to 10 ml by gel filtration chromatography (GFC) after incubation with 0.1% (w/v) DDM overnight at 4°C (Figure 5.2a).<sup>12,33</sup> This high molecular weight oligomer was previously shown to represent the transmembrane pore structure and is termed ClyA<sub>TM</sub> here.<sup>12,33</sup> During the purification, we noticed that the ClyA protein showed a tendency to form high molecular weight oligomers even in the absence of detergent or lipids. We therefore explored the oligomerization of ClyA in the absence of detergent or membranes using GFC. Two peaks with retention volumes of 8.5 ml and 9.5 ml appeared in chromatograms after incubation of the ClyA monomer at 37°C in buffer containing 50 mM Tris•HCl, pH 8.0, 150 mM NaCl for 2 hours (Figure 5.2b). Fractions corresponding to the two peaks were named oligomer 8 (ClyA<sub>O8</sub>) and oligomer 9 (ClyA<sub>O9</sub>) based on their respective retention volumes. Notably, these two fractions migrated faster in the GFC column than ClyA<sub>TM</sub> (Figure 5.2a, 5.2b). The ClyA<sub>O8</sub> and ClyA<sub>O9</sub> were pooled separately and re-analyzed by GFC. The two proteins still eluted at their original retention volumes of 8.5 ml and 9.5

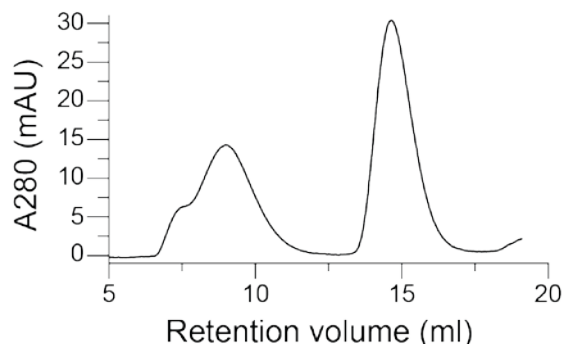
ml, respectively (Figure 5.2c, 5.2d). No monomer was observed in the chromatogram, suggesting that ClyA<sub>O8</sub> and ClyA<sub>O9</sub> did not dissociate under our conditions tested. Because the ClyAwt monomer contains two cysteines, it is possible that ClyA could have formed oligomers through disulfide bond formation during the incubation at 37°C.



**Figure 5.2. Gel filtration chromatography of ClyA proteins.** (a) Oligomerization of the ClyA proteins in the presence of DDM. ClyA monomers were incubated with 0.1% (w/v) DDM overnight at 4°C and then analyzed by GFC with a running buffer 50 mM Tris•HCl, pH 8.0, 150 mM NaCl and 0.01% DDM. (b) Oligomerization of the ClyA protein in the absence of DDM. ClyA monomer was incubated at 37°C for 2 hrs. The running buffer of GFC was 50 mM Tris•HCl, pH 8.5, 150 mM NaCl. Figure 3: GFC of ClyA<sub>O8</sub> and ClyA<sub>O9</sub> oligomers. Running buffer used was 50 mM Tris•HCl pH 8.0, 150 mM NaCl.



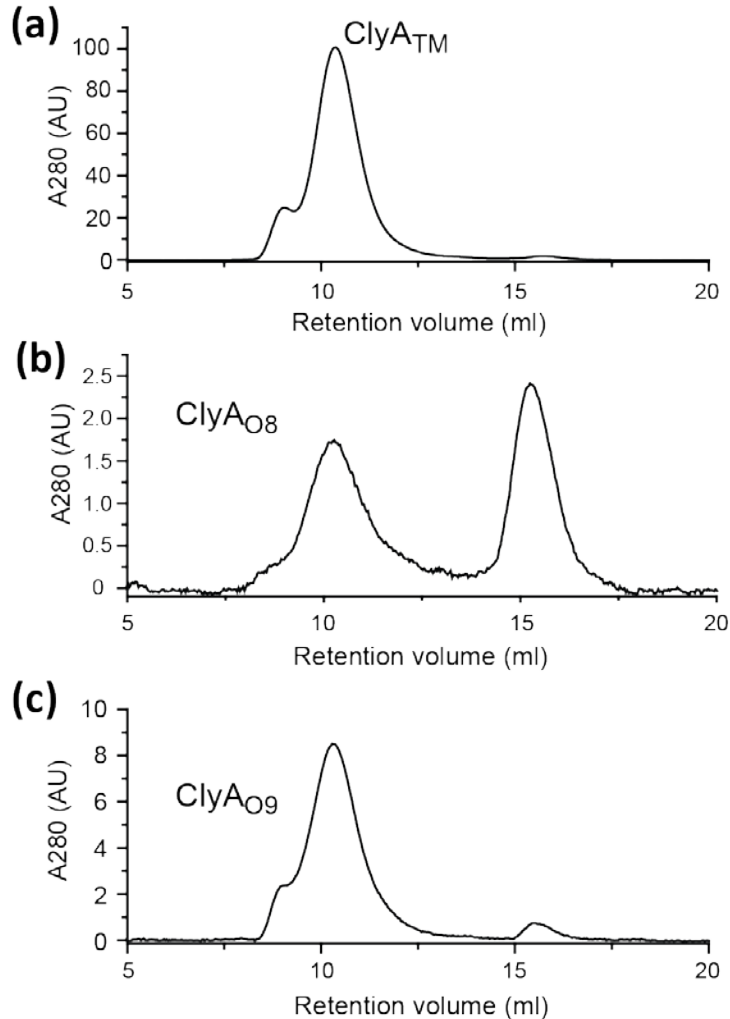
To assess this, the same experiment was repeated in buffers containing freshly prepared 10 mM DTT at 37°C. The presence of DTT did not modify the elution profile of ClyA oligomers, excluding the involvement of disulfide bridges (Figure 5.3). Thus, we conclude that ClyA was able to oligomerize in the absence of detergents/membranes and that the isolated oligomers were stable in solution.



**Figure 5.3. ClyA oligomerization under reducing conditions.** Purified ClyA protein was incubated at 42°C for 2 hrs in the presence of 10 mM DTT and subjected to GPC analysis. The running buffer was 50 mM Tris•HCl, pH 8.0, 150 mM NaCl, 10 mM DTT.

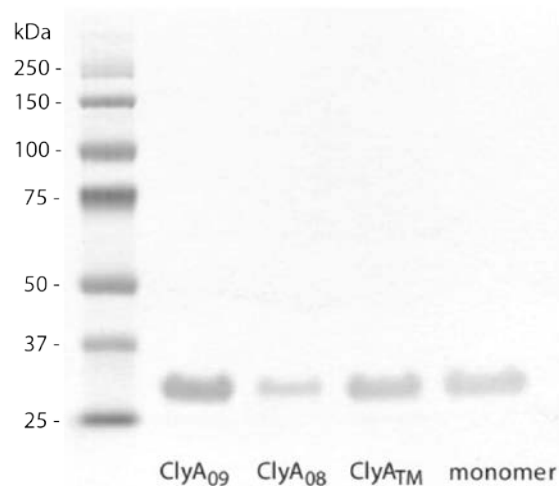
#### 5.4.2 Conversion of oligomer 8 and oligomer 9 to the transmembrane pore

To investigate whether ClyA<sub>O8</sub> and ClyA<sub>O9</sub> can convert to the transmembrane pore, we incubated them with 0.1% DDM overnight at 4°C. The ClyA<sub>O8</sub> shifted to a peak eluted at 15ml, corresponding to the monomer, and a peak at 10ml, corresponding to the fully-assembled transmembrane pore (Figure 5.4a, 5.4b). The ClyA<sub>O9</sub> also shifted to peak at 10ml but little monomer is observed during this process (Figure 5.4c). These results indicate that ClyA<sub>O8</sub> may contain loosely packed monomers that can be solubilized by DDM. By contrast, ClyA<sub>O9</sub> had a more stable structure that did not disassemble in detergent solution. Rather, DDM triggered a conformational change in ClyA<sub>O9</sub> that transformed it into the transmembrane pore. Because a portion of ClyA<sub>O8</sub> also appeared to have converted to ClyA<sub>TM</sub>, it may contain a mixture of ClyA<sub>O9</sub>-like oligomers with a stable structure and loosely packed monomers.



**Figure 5.4. Conversion of ClyA<sub>O8</sub> and ClyA<sub>O9</sub> to transmembrane pore.** The purified ClyA protein (a) ClyA<sub>O8</sub> (b) and ClyA<sub>O9</sub> (c) were incubated with 0.1% (w/v) DDM overnight at 4°C and then analyzed by GFC with a running buffer 50 mM Tris•HCl, pH 8.0, 150 mM NaCl and 0.01% DDM.

Many assembled  $\beta$ -toxin oligomers have shown tolerance to sodium dodecyl sulfate (SDS) treatment and remain as oligomers on SDS-PAGE.<sup>31,34–36</sup> We were interested to see if ClyA oligomers would have different stabilities in SDS and migrate differently in the SDS-PAGE. We found that all three oligomeric forms of ClyA dissociated to monomer on SDS-PAGE (Figure 5.5). This result suggests that the interaction in the oligomeric interface of ClyA is not as strong as those in  $\beta$ -PFTs.

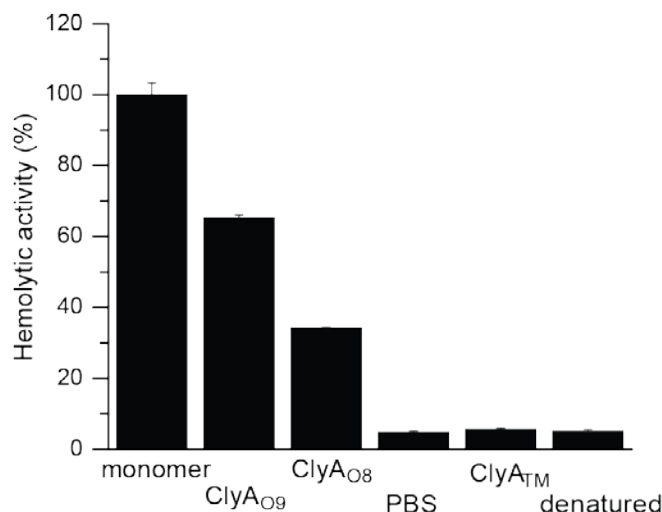


**Figure 5.5. SDS-PAGE analysis of ClyA monomer and oligomers.** ClyA oligomers ClyA<sub>09</sub>, ClyA<sub>08</sub>, ClyA<sub>TM</sub> and ClyA monomer all run with the same MW in SDS-PAGE indicating that the ClyA oligomers are not SDS-resistant.

#### 5.4.3 Hemolytic activities of the ClyA proteins

The cytolytic activity of the oligomeric forms, ClyA<sub>08</sub> and ClyA<sub>09</sub> was determined using a hemolytic assay. We also quantitatively compared its functionality to the ClyA monomer. Sheep blood cells were incubated with ClyA proteins of the same weight concentration at 37°C for 15 min. The release of the hemoglobin associated with cell lysis was then measured. As a negative control, a denatured ClyA sample, which were pre-heated at 95°C for 30min prior to the hemolytic assay, was tested. A sample of PBS buffer was included to define zero activity. Results show that thermally-denatured ClyA has no hemolytic activity while the monomer has the highest activity (Figure 5.6). ClyA<sub>09</sub> and ClyA<sub>08</sub> exhibited 65% and 30% of the monomer activity, respectively. The transmembrane pore (collected as peak 10 from GFC) only exhibited a background level of hemoglobin release, supporting the notion that this population had lost its ability to lyse cells. This result is in agreement with previous observations that transmembrane ClyA pores formed in detergent octyl-glucoside solution showed no pore-forming activity on cell membranes.<sup>37</sup> Because both ClyA<sub>09</sub> and ClyA<sub>08</sub> were still functional in forming pores

on erythrocyte membranes, we concluded that they might be oligomeric states with an ordered structure instead of disordered aggregates.

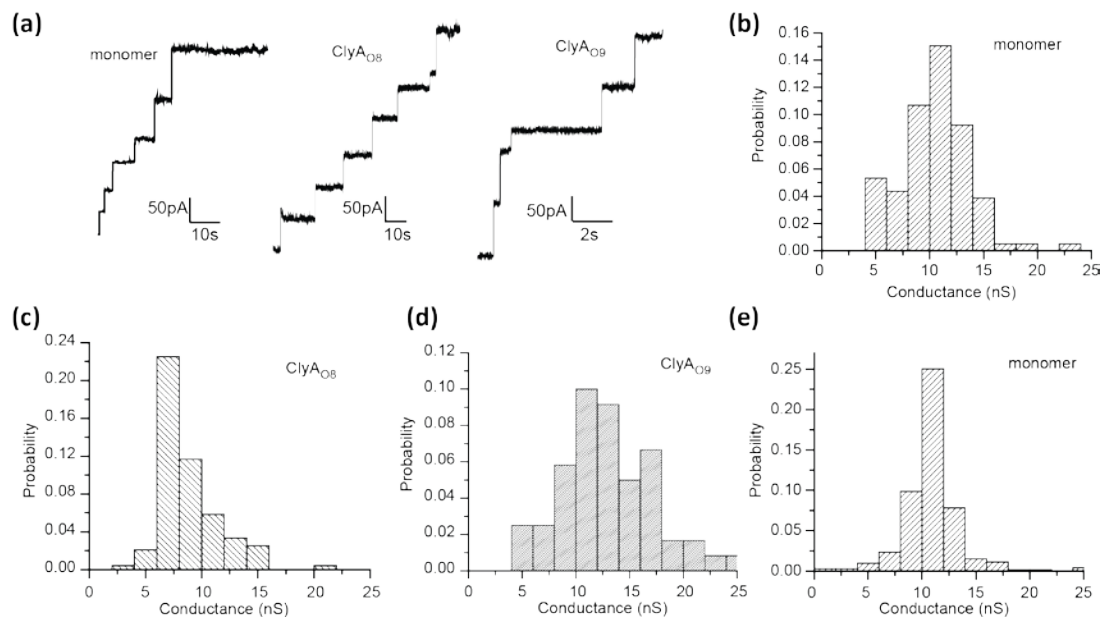


**Figure 5.6. Hemolytic activity of ClyA proteins.** Sheep blood cells were incubated with 7  $\mu\text{g}$  of ClyA at 37°C for 15 min. The hemolytic activity was determined by measuring the absorbance of the released hemoglobin at 540 nm. The plotted values are the average of three independent samples and bars show the standard deviation.

#### 5.4.4 Conductance of ClyA pores

Since ClyA can form transmembrane pores by converting the monomer or oligomer ClyA<sub>O9</sub> in the presence of detergents, we asked if the stoichiometry of the transmembrane pores formed from these two pathways are the same. Because the ion conductance of a membrane channel is proportional to the pore size, which, in turn, is determined by the number of protomers in the transmembrane pore,<sup>38</sup> we could address this question by comparing the conductance of ClyA channels formed in two different pathways. Here, single channel insertion of ClyA proteins into planar lipid bilayers was monitored by bilayer current recording experiments (Figure 5.7a). Similar to the results of the electrophysiological studies of *E. coli* ClyA and its homologs from *Salmonella typhi*,<sup>6,39,40</sup> the ClyA channels formed by monomer show a broad distribution from 5-15 nS with a major peak at around 11 nS (Figure 5.7b), suggesting that ClyA might create

pores of variable size. The broad distribution of conductance observed by electrophysiology agrees with the cryo-EM data showing ClyA pores of variable size in detergent solution.<sup>12</sup> The ClyA channels formed by ClyA<sub>O9</sub> and ClyA<sub>O8</sub> exhibited similar conductance distribution patterns with the majority of ClyA<sub>O8</sub> pores exhibiting a conductance between 6-10 nS and ClyA<sub>O9</sub> pores a conductance between 9-16 ns (Figure 5.7c, 5.7d). The population of ClyA<sub>O9</sub> channels shifted to slightly larger pores than those formed directly from monomer while ClyA<sub>O8</sub> pores appeared smaller. So far, it is unclear why the conductance of the ClyA<sub>O8</sub>, ClyA<sub>O9</sub> and ClyA<sub>TM</sub> pores are different considering that they migrate at the similar retention volume by GFC (Figure 5.4). Further detailed structural studies will be carried out to address this issue in future.

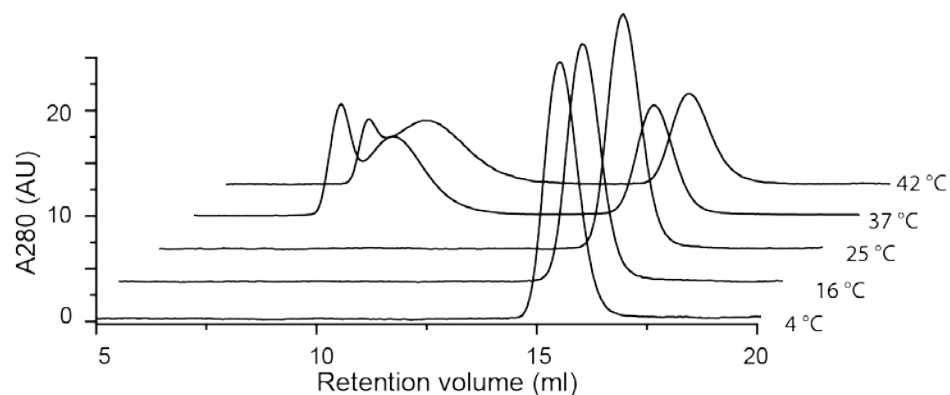


**Figure 5.7. Single channel conductance of ClyA pores.** (a) Single channel insertion of ClyA proteins. After overnight incubation with 0.1% (w/v) DDM, ClyA proteins (~0.5  $\mu\text{g/ml}$ , final concentration) were added to the *cis* chamber. A voltage of 10 mV was applied to monitor the single channel insertion events, manifested as stepwise increases of ionic current with time in 25 mM Tris•HCl, pH8.0, 1M KCl. (b, c, d) Histogram of the conductance of ClyA pores. Samples analyzed were monomer ClyA (b) (105 single channel insertion steps) or ClyA<sub>O8</sub> (c) (118 steps) or ClyA<sub>O9</sub> (d) (76 steps) after overnight incubation with 0.1% (w/v) DDM at 4°C. In (e), the sample contained monomer ClyA (112 steps) after incubation with 0.1% (w/v) DDM at 4°C for 7 days.

Interestingly, when we measured the conductance of the ClyA monomer sample after seven days of incubation at 4°C in 0.1% DDM, the histogram of conductance showed almost a single population of 11 nS pores (Figure 5.7e). This suggests that the 11 nS pore is the most stable form, since it survives a long-time incubation in detergent. By contrast, many other forms of ClyA lose the ability to insert into the lipid bilayer, probably due to aggregation or degradation. The dodecameric structure of the transmembrane pore determined by x-ray crystallography was also obtained from a DDM sample which contained a large variety of ClyA pores of different sizes.<sup>12</sup> We suggest that the ClyA transmembrane pore with dodecameric structure might correspond to the 11 nS pores observed in the electrophysiology recordings.

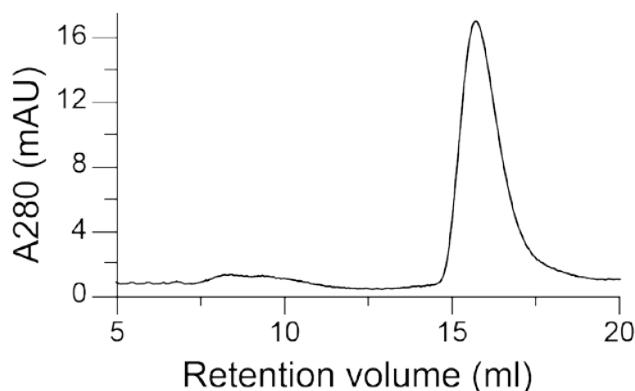
#### 5.4.5 Temperature and concentration dependent oligomerization

We were interested in how the temperature and the protein concentration affect ClyA assembly in solution. ClyA monomer was incubated at temperatures ranging from 4-42°C for 2 hrs. At a temperature lower than 37°C, little ClyA oligomerization was observed (Figure 5.8). Unlike the assembly in the detergent micelles which proceeded to completion at 4°C for 30 min, the detergent-independent assembly was strictly temperature-dependent and was a much slower process relative to the former.



**Figure 5.8. Effect of temperature on ClyA assembly.** ClyA (0.3 mg/ml) was incubated at different temperatures for 2 hrs and subjected to GFC analysis. The running buffer was 50 mM Tris•HCl, pH 8.0, 150 mM NaCl.

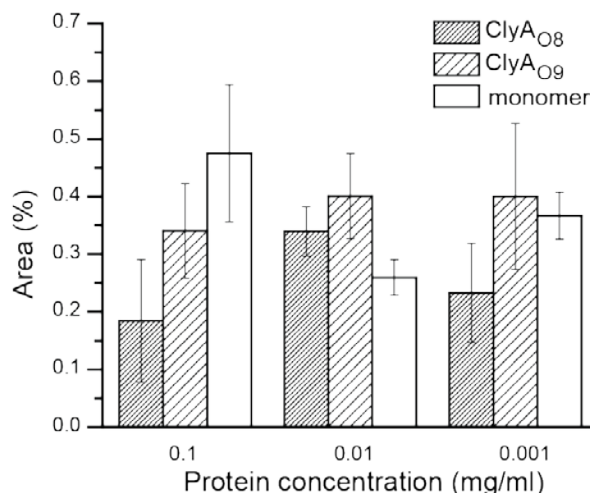
To see if oligomerization was also concentration dependent, we incubated 0.1 mg ClyA protein at concentrations ranging from 1  $\mu\text{g/ml}$  to 0.1 mg/ml at 42°C for 2 hours and samples were then analyzed by GFC. In order to load enough protein sample to the GFC column for detection, the two lower concentration samples, 10  $\mu\text{g/ml}$  and 1  $\mu\text{g/ml}$ , were concentrated to 1 ml using an Amicon centrifuge concentrator at 4°C. To eliminate the possibility that oligomerization or aggregation might also be induced during the centrifugation concentrating procedure, we incubated 100 ml of 1  $\mu\text{g/ml}$  at 4°C for 2 hrs and concentrated the sample to 1 ml and loaded it to the GFC column as a control. We found that ClyA remained mainly as a monomer and a small amount of protein was eluted at around 8 to 9 ml retention volume demonstrating the concentration step does not significantly induce oligomer formation (Figure 5.9).



**Figure 5.9. Effect of continuous concentration of ClyA on its oligomerization.** ClyA (100 ml of 1  $\mu\text{g/ml}$ ) was incubated at 4°C for 2 hrs and then concentrated to 1 ml on a concentrator. Thereafter the protein was subjected to GFC analysis. The running buffer was 50 mM Tris•HCl, pH 8.0, 150 mM NaCl.

The percentage of each population (ClyA<sub>O8</sub>, ClyA<sub>O9</sub> and monomer) was calculated from the area under the peaks eluted at 8.5ml, 9.5ml and 15ml in the chromatogram that were analyzed by the Unicorn software (GE) and are summarized in Figure 5.10. Even at the lowest concentration (1  $\mu\text{g/ml}$ , ~30 nM), the ratio of the oligomer to monomer was not reduced compared those of the higher concentrations, suggesting the oli-

gomerization was independent of the protein concentration (Figure 5.10). Due to the detection limit of GFC, we were not able to investigate lower concentrations. This result demonstrates that ClyA has a strong tendency to oligomerize even at a low concentration (1  $\mu\text{g/ml}$ ) at physiological temperature.



**Figure 5.10. Effect of protein concentration on ClyA assembly.** ClyA at concentrations ranging from 1  $\mu\text{g/ml}$  to 0.1 mg/ml were incubated at 42°C for 2 hours and then analyzed by GFC. The percentage of each population (ClyA<sub>O8</sub>, ClyA<sub>O9</sub> and monomer) was calculated from the area of the peaks eluted at 8.5ml, 9.5ml and 15ml in the chromatogram. The error bars indicate the standard deviation of three independent trials.

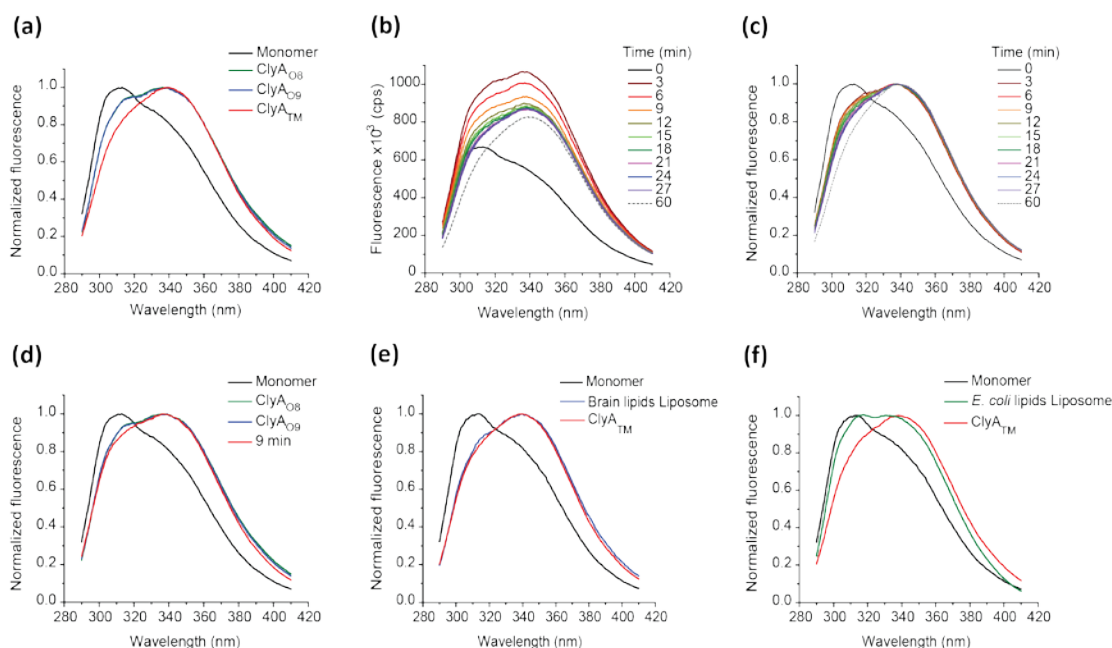
#### 5.4.6 Probing the structural arrangement of oligomers by fluorescence

To understand the structural arrangement of ClyA<sub>O8</sub> and ClyA<sub>O9</sub>, we measured their intrinsic fluorescence spectra. The ClyA monomer contains two tryptophan and 13 tyrosine residues. As shown in Figure 5.7a, the monomer had a fluorescence maximum at 315 nm while the fully assembled pore ClyA<sub>TM</sub> had a red-shifted emission maximum at 340 nm. The fluorescence emission spectra of the ClyA<sub>O8</sub> and ClyA<sub>O9</sub> were very similar to each other with the fluorescence maxima also at 340 nm, close to that of the ClyA detergent-induced transmembrane pore. The spectra of the ClyA<sub>O8</sub> and ClyA<sub>O9</sub> samples from 345-400 nm overlapped well with that of the transmembrane pore while there is a blue shift of 2 nm in the spectra from 300-340 nm (Figure 5.11a). Because the spectra



of ClyA<sub>O8</sub> and ClyA<sub>O9</sub> appeared to be in between that of the monomer and transmembrane pore, we suspected they might be an intermediate state. To test this, we studied a series of intermediate states of ClyA proteins during the DDM-triggered transition to transmembrane pores. Here, DDM was added to ClyA monomer to a final concentration of 0.1% (w/v) of DDM at 23°C to trigger the pore formation. The spectrum was taken every 3 minutes until the spectra stabilized at around 30 minutes. Figure 5.11b shows that the fluorescence intensity rose sharply immediately after the addition of detergent and the wavelength of the peak maximum shifted from 315 to 340 within the first 3 minutes of measurement. After the initial fluorescence jump, the fluorescence intensity gradually decreased and became stable after 30 min. The normalized spectra of these intermediates revealed the peak maxima undergo subtle blue-shift during the transition (Figure 5.11c). Interestingly, the spectrum taken 9 min after the addition of the DDM overlaid well with the spectrum of ClyA<sub>O8</sub> and ClyA<sub>O9</sub> (Figure 5.11d), indicating that the structure of ClyA<sub>O8</sub> and ClyA<sub>O9</sub> might mimic an intermediate state of the oligomerization process.

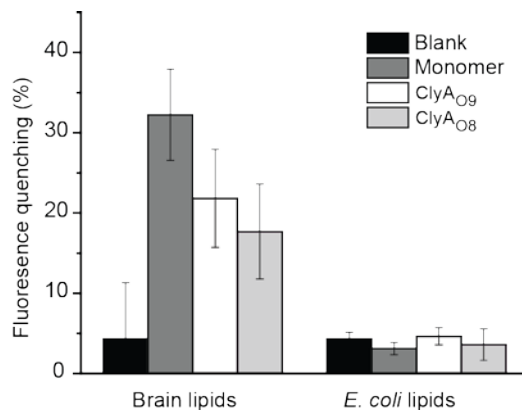
We also investigated how the composition of the lipid membrane could affect the assembly of a ClyA oligomer. To avoid the occurrence of oligomerization in solution that would contribute to fluorescence spectrum, the ClyA monomers were incubated with liposomes prepared from porcine brain lipids or *E. coli* lipids extract at room temperature in an approximate 1:50 protein to lipid molar ratio. The spectrum of the brain lipid liposomes sample overlapped very well with the spectrum of ClyA<sub>TM</sub> (Figure 5.11e), which demonstrated that ClyA proteins have transformed into transmembrane pores on the brain lipid liposomes. In contrast, the spectrum of the ClyA incubated with *E. coli* liposomes did not resemble the DDM treated sample (Figure 5.11f). Instead, it was located in between the monomer and the spectrum of the ClyA<sub>O9</sub>, suggesting that ClyA does not form the transmembrane pore on *E. coli* lipid membranes.



**Figure 5.11. Intrinsic fluorescence of ClyA monomer and oligomers.** (a) Normalized fluorescence emission spectra of monomer, ClyA<sub>O8</sub>, ClyA<sub>O9</sub> and ClyA<sub>TM</sub>. (b) DDM-triggered assembly of ClyA monitored by fluorescence. DDM (0.1% w/v, final concentration) was added to ClyA monomer (1 μM) solution and the fluorescence spectra were recorded every 3 min for 60 min. (c) Normalized spectra from Figure 6b. (d) Comparison of the spectra of ClyA<sub>O8</sub>, ClyA<sub>O9</sub> and the intermediate state taken at 9 min after the addition of DDM. (e, f) Normalized fluorescence spectra of monomer, transmembrane pore and ClyA proteins after incubation with liposomes. ClyA was incubated with liposomes prepared from porcine brain lipids (e) and *E. coli* lipids (f) at room temperature for overnight.

#### 5.4.7 Effect of lipid composition on pore-forming activity

To further examine the pore-forming activity of ClyA proteins on liposomes, we used a fluorescence quenching assay. The liposomes with Tb(DPA)<sup>3-3</sup> encapsulated inside were added to buffers containing the fluorescence quencher EDTA. EDTA can diffuse into the liposome through ClyA pores on the liposome membrane and quench the fluorescence. Figure 5.12 shows that ClyA monomer caused a significant fluorescence decrease in the brain lipid liposomes. Consistent with our hemolytic assay, ClyA<sub>O9</sub> and ClyA<sub>O8</sub> also induced fluorescence quenching but with reduced activity. On the contrary, no fluorescence quenching was observed with any of the ClyA protein samples incubated with *E. coli* liposomes. This experiment confirms that ClyA proteins do not form transmembrane pores on *E. coli* lipid membranes.

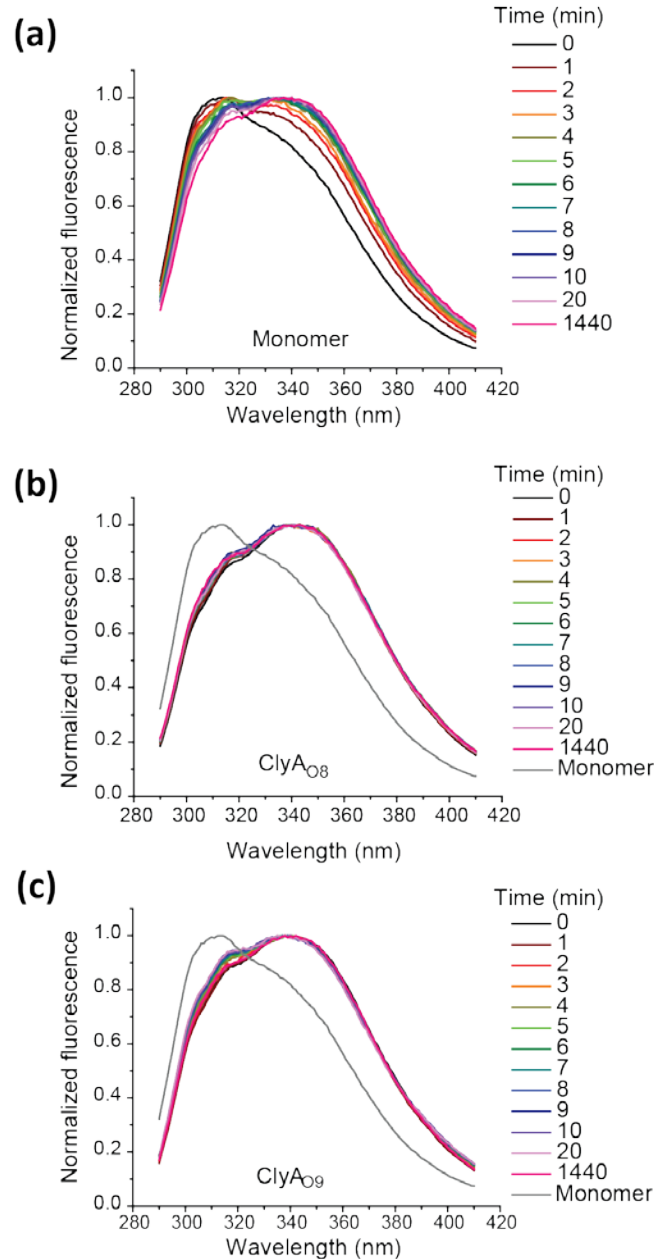


**Figure 5.12. Effect of lipid composition on the pore-forming activity of ClyA.** ClyA proteins (0.034mg/ml, final concentration) were added to liposomes (5  $\mu$ M) containing 3 mM encapsulated Tb(DPA)<sub>3</sub><sup>3-</sup>. The buffer used was 50 mM HEPES, pH 7.5, 100 mM NaCl, 5 mM EDTA. Fluorescence quenching occurred when EDTA diffused across the liposome membrane through transmembrane pores formed by ClyA. Data shows the percentage of the quenched fluorescence signal that was an average of quadruplet measurements with the error bar indicating the standard deviation.

#### 5.4.8 Direct conversion of ClyA<sub>08</sub> and ClyA<sub>09</sub> to transmembrane pores

The data above revealed that Cly<sub>08</sub> and Cly<sub>09</sub> can convert to the transmembrane pore when in contact with detergent micelles or lipid membranes. This could be achieved through two possible pathways: (i) ClyA<sub>08</sub> and ClyA<sub>09</sub> dissociate into monomers then re-assemble in the micelles/ lipid membrane or, (ii) ClyA<sub>08</sub> and ClyA<sub>09</sub> directly convert to the transmembrane pore without undergoing the dissociation step. To distinguish between these pathways, we monitored the conversion of ClyA<sub>08</sub> and ClyA<sub>09</sub> in the presence of brain lipid membranes by intrinsic fluorescence. Liposomes were added to monomer and the fluorescence was recorded (Figure 5.13a). After 5 min, the spectrum showed two peak maxima at 314 nm and 340 nm indicating there was still monomer remaining in the sample. This result suggests the association process of the ClyA monomers to oligomers on the lipid membrane occurs on the time scale of minutes, which is much slower than the  $\alpha$ HL toxin (<5ms).<sup>41</sup> If ClyA<sub>08</sub> and ClyA<sub>09</sub> dissociate into monomers, we expect to observe the spectrum of the monomeric species due to the relatively slow association process of ClyA monomers. Adding liposomes to ClyA<sub>08</sub> and ClyA<sub>09</sub>

induced a slight change at the 300-340 nm range (Figure 5.13b, 5.13c), however we did not observe a significant shift of the spectrum towards the monomer peaks. Thus, this experiment suggests that ClyA<sub>O8</sub> and ClyA<sub>O9</sub> directly convert to the transmembrane pore on the lipid membrane without first dissociating to monomers.

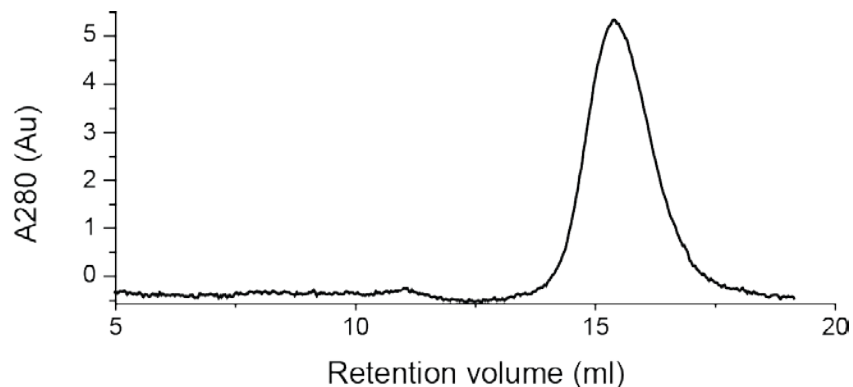


**Figure 5.13. Examining the pathway of Cly<sub>O8</sub> and Cly<sub>O9</sub> conversion.** Brain lipid liposomes (0.025 mg/ml, final concentration) were added to ClyA proteins (0.025 mg/ml): monomer (a), Cly<sub>O8</sub> (b) and Cly<sub>O9</sub> (c) solution at 25 °C. The fluorescence spectra were recorded at the indicated time intervals.

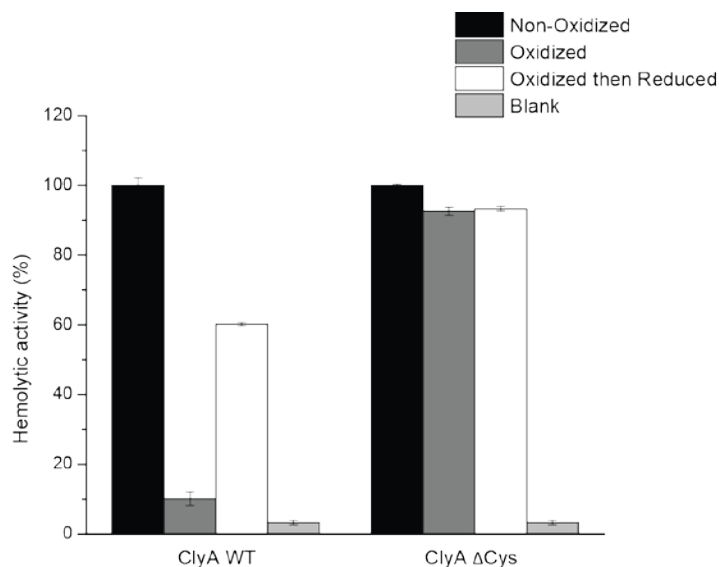
#### 5.4.9 Effect of the redox environment on the activity of ClyA

ClyA monomer contains two cysteines (C87, C285). The structure of ClyA monomer revealed that these cysteines were located within 5.2 Å (Ca to Ca), a distance that would allow a disulfide bond to form. In the transmembrane pore structure, the cysteines move away from each other to be about 6.8 Å apart, which is the longest possible distance for a disulfide bond could form between two cysteine residues.<sup>42</sup> This raised the question that a possible disulfide bond formed between the cysteine residues might act as a redox switch to control ClyA oligomerization and cytolytic activity on its target cell *in vivo*.

To test this theory, we induced the disulfide bond formation of the two cysteine residues in ClyA wild type proteins by incubating the proteins with Cu(phenanthroline)<sub>2</sub> for 0.5 hours at room temperature (22-23°C). GFC analysis of the oxidized sample showed ClyA proteins remained monomeric, indicating that the protein did not form any inter-molecular disulfide bonds during the oxidation reaction (Figure 5.14). The oxidized ClyA was subjected to the hemolytic activity assay. Figure 5.15 shows that the oxidized ClyA (dark grey) lost around 90% of its hemolytic activity compared to that of the untreated control (black). Incubation in 20 mM DTT for an hour could recover about 60% the hemolytic activity. The incomplete recovery of the activity could be likely due to the close packing of the alpha helix bundles of ClyA that may occlude the disulfide bond from the reducing chemical DTT. As a control, the double cysteine knock out mutant ClyA  $\Delta$ Cys exhibited no response to the oxidation/reduction procedure. These results indicated that formation of the intra-molecular disulfide bond could inhibit the pore-forming activity presumably by preventing the occurrence of conformational change necessary for the formation of oligomeric transmembrane pore. The periplasm of *E. coli* is an oxidizing environment and thus an oxidized ClyA protein could exist in this environment preventing ClyA from oligomerizing before being secreted in OMVs.



**Figure 5.14. GFC analysis of oxidized ClyA.** ClyA (30  $\mu$ g) was oxidized with 1.5 mM Cu(phenanthroline)<sub>2</sub> for 30 min at room temperature. Reaction was quenched with 5 mM (final concentration) EDTA. Sample was analyzed by GFC without prior desalting. Running buffer used was 50 mM Tris•HCl pH 8.0, 150 mM NaCl.



**Figure 5.15. Regulation of the ClyA pore forming activity by redox change.** The pore-forming activity of various proteins was examined by hemolytic assay. The oxidized sample contained wild type ClyA (ClyAwt) and ClyA double cysteine mutant C87S, C285S (ClyA  $\Delta$ Cys) incubated with Cu(phenanthroline)<sub>2</sub>. The reduced samples were obtained by DTT treatment of oxidized proteins. Blank samples were phosphate buffer saline.

## 5.5 Discussion

Previous work on ClyA has also shown that ClyA oligomerizes in solution without detergent at 37°C.<sup>43</sup> In this example, monomer, dimers and high molecule-weight oligomers (8-10mers as speculated by the authors) were observed by GFC.<sup>43</sup> The 8-10mer

fraction lacked hemolytic activity. However, our data clearly demonstrated that both ClyA<sub>O8</sub> and ClyA<sub>O9</sub> lysed blood cells while the thermally denatured ClyA did not.

Because ClyA<sub>O8</sub> and ClyA<sub>O9</sub> retains both a stable structure and hemolytic activity, we expect that they are not a disordered aggregate but rather an active oligomeric form of ClyA proteins. In addition, the intrinsic fluorescence of these soluble oligomers matched that of an intermediate state. This suggests the detergent-independent oligomer resembles an intermediate state between the monomer and fully assembled transmembrane pore. Since ClyA<sub>O8</sub> and ClyA<sub>O9</sub> were formed in solution, it is unlikely that the  $\alpha$ -helical transmembrane barrel has formed, as this would expose the hydrophobic outer surface of the barrel to aqueous solution. Therefore, we believe that ClyA<sub>O8</sub> and ClyA<sub>O9</sub> could be oligomeric forms without the hydrophobic transmembrane barrel domain, i.e. the prepore structure. Also, we have shown that Cly<sub>O8</sub> and ClyA<sub>O9</sub> can convert directly to transmembrane pore. In summary, we propose that ClyA<sub>O8</sub> and ClyA<sub>O9</sub> are intermediate states between the monomer and transmembrane ClyA channel. Since these two populations were eluted earlier than transmembrane pores in GFC, it might have a less compact structure than the transmembrane pore.

Although many PFTs require detergents or lipid bilayers for assembly to oligomeric prepore, the protective antigen of anthrax toxin also oligomerizes to a prepore structure in the absence of detergents or lipid membranes.<sup>35,44</sup> In fact, the water-soluble prepore was formed by the oligomerization of protective antigen 63 which derives from the proteolytic removal of a 20 kDa fragment from the full length anthrax monomer. Similarly, Monalysin, a PFT from the *Drosophila* pathogen *Pseudomonas entomophila*, forms a multimeric structure in solution after proteoactivation.<sup>45</sup> Therefore, not all PFTs require lipid membranes or similar environments to form prepore structures. Although in vitro the PA63 and Monalysin undergo oligomerization in solution after protease treatment, in na-

ture the oligomerization of the PA63 and Monalysin is triggered by the proteases expressed on the host plasma membrane, where they subsequently assemble.

The activation of ClyA may be regulated by the change of its redox status during the secretion of ClyA into OMVs.<sup>10,21,43</sup> ClyA in the periplasm contains a C87–C285 disulfide bond,<sup>6,21,46</sup> whereas ClyA within OMV is reduced.<sup>21</sup> The disulfide bond may prevent assembly of functional pore complexes, as oxidized ClyA showed a decreased hemolytic activity than compared to reduced ClyA, which is consistent with previous studies.<sup>10,21,43</sup> This notion is further supported by the observation that ClyA expressed in an *E. coli* (dsbA<sup>-</sup> and dsbB<sup>-</sup>) strain, which is deficient in periplasmic disulfide bond formation, displays a significant hemolytic activity on blood agar plates, an effect that is not detectable for ClyA expressed in wild-type strain.<sup>21</sup> Therefore, the secretion of ClyA to OMVs where DsbA and DsbB are absent may reduce the intracellular disulfide bonds and activate the toxin for oligomerization<sup>21</sup>.

Some speculate that ClyA forms transmembrane pores upon interaction with the membrane of the OMV.<sup>21</sup> However, this contradicts two observations: i) the pre-formed ClyA transmembrane pore lacks hemolytic activity as demonstrated by our study and previous data.<sup>37</sup> A transmembrane ClyA pore embedded in the OMV membrane loses functionality for further attack. ii) the pore-forming activity of ClyA is strongly dependent on cholesterol in the membrane, which suggests that cholesterol may facilitate the transmembrane domain insertion.<sup>46</sup> Since bacterial outer membranes contain no cholesterol, the transformation of ClyA into the transmembrane pore inside of the OMV should be very slow. Our intrinsic fluorescence analysis supports this notion: the spectra of ClyA with liposomes reveal transmembrane pores in brain lipids but ClyA cannot transform in the presence of *E. coli* liposomes. The Tb fluorescence quenching assay further confirmed that ClyA cannot form transmembrane pores on *E. coli* lipid membranes. Thus, it

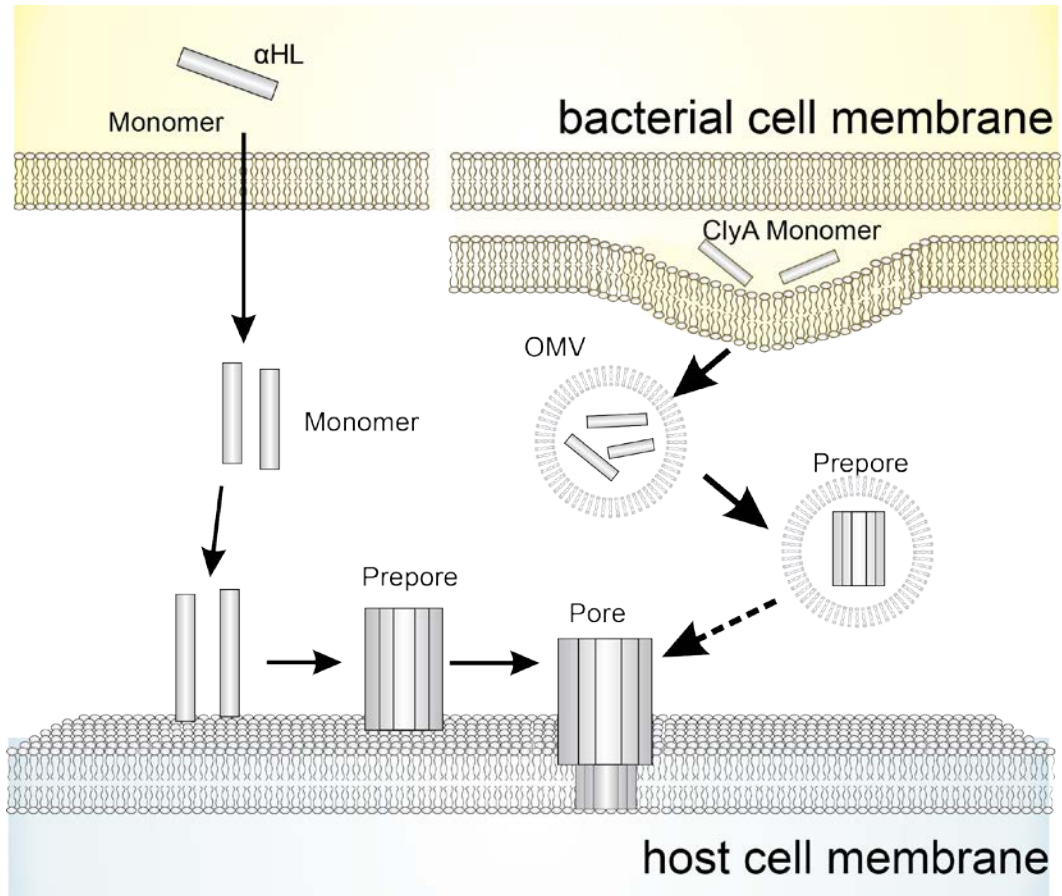


is reasonable to believe the oligomeric structure of ClyA in the OMV may not be the transmembrane pore.

The average expression level of a protein in *E. coli* is approximately 1000 copies, roughly 1  $\mu$ M in the cytosol.<sup>47</sup> Our data demonstrated that ClyA forms oligomers at 37°C at concentrations as low as 30 nM. Under physiological conditions ClyA can associate into ClyA<sub>O9</sub>-like prepore structures once activated in the OMV and this process can occur independently of lipid membrane. Taken together, these data strongly suggest that the secreted ClyA proteins oligomerize to a prepore structure instead of the transmembrane pore inside the OMV before they reach the target cell membrane.

We propose that ClyA adopts a non-classical assembly pathway including the following steps (Figure 5.16): (i) ClyA is expressed as a monomer in the cytosol and exported to the periplasmic space where it remains inactive in an oxidized form; (ii) ClyA is secreted in outer membrane vesicles in monomer form; (iii) Cleavage of the disulfide bond in the OMV activates ClyA monomers which subsequently oligomerize to the prepore structure. How the OMV then delivers the active ClyA prepore to the host cell remains unknown. One plausible mechanism involves internalization of the vesicle and subsequent release of the cargo proteins to the cytoplasm of the target cells<sup>25</sup>. Further studies are underway to identify how ClyA is released.

In conclusion, we have shown that ClyA protein assembles into a functional oligomer in the absence of detergents and membranes. The oligomeric form represents a prepore intermediate state that may resemble the ClyA oligomer structure in the OMVs. These data provide insight regarding the oligomeric state of ClyA proteins in the OMV, which represents an important step toward resolving the overall mechanism of ClyA. High-resolution crystal structures of the prepore might be obtained in the near future and they will be essential for determining how the prepore becomes the hemolytic pore.



**Figure 5.16. Schematic model showing the proposed assembly pathway for the *E. coli* ClyA.** The classical PFT attacking mechanism involves the secreted monomer docking to the host membrane, followed by rapid assembly to the prepore structure. A conformational change triggers the formation of the transmembrane domain. By contrast, monomeric ClyA is secreted in OMVs where the redox environment cleaves intramolecular disulfide-bonds and activates ClyA. ClyA then assembles to a prepore structure in the vesicle. Through an unknown mechanism, OMV release ClyA which then form a transmembrane pore on the host cell.

## 5.6 References

1. Iacovache, I., Bischofberger, M. & van der Goot, F. G. Structure and assembly of pore-forming proteins. *Curr. Opin. Struct. Biol.* **20**, 241–246 (2010).
2. Parker, M. W. & Feil, S. C. Pore-forming protein toxins: From structure to function. *Prog. Biophys. Mol. Biol.* **88**, 91–142 (2005).
3. Tilley, S. J. & Saibil, H. R. The mechanism of pore formation by bacterial toxins. *Curr. Opin. Struct. Biol.* **16**, 230–236 (2006).
4. Reingold, J., Starr, N., Maurer, J. & Lee, M. D. Identification of a new Escherichia coli She haemolysin homolog in avian E. coli. *Vet. Microbiol.* **66**, 125–134 (1999).
5. Oscarsson, J., Mizunoe, Y., Uhlin, B. E. & Haydon, D. J. Induction of haemolytic activity in Escherichia coli by the slyA gene product. *Mol. Microbiol.* **20**, 191–199 (1996).
6. Ludwig, a, Bauer, S., Benz, R., Bergmann, B. & Goebel, W. Analysis of the SlyA-controlled expression, subcellular localization and pore-forming activity of a 34 kDa haemolysin (ClyA) from Escherichia coli K-12. *Mol. Microbiol.* **31**, 557–67 (1999).
7. Hlye, H. E., Hunt, S., Green, J. & Artymiuk, P. J. Hemolysin E (HlyE, ClyA, SheA) and Related Toxins. *Adv. Exp. Med. Biol.* **677**, 116–126 (2010).
8. del Castillo, F. J., Leal, S. C., Moreno, F. & del Castillo, I. The Escherichia coli K-12 sheA gene encodes a 34-kDa secreted haemolysin. *Mol. Microbiol.* **25**, 107–115 (1997).
9. Lai, X. *et al.* Cytocidal and Apoptotic Effects of the ClyA Protein from Escherichia coli on Primary and Cultured Monocytes and Macrophages. *Infect. Immun.* **68**, 4363–4367 (2000).
10. Wallace, A. J. *et al.* E. coli hemolysin E (HlyE, ClyA, SheA): X-ray crystal structure of the toxin and observation of membrane pores by electron microscopy. *Cell* **100**, 265–76 (2000).
11. Oscarsson, J. *et al.* Characterization of a Pore-Forming Cytotoxin Expressed by Salmonella enterica Serovars Typhi and Paratyphi A. *Infect. Immun.* **70**, 5759–5769 (2002).
12. Mueller, M., Grauschopf, U., Maier, T., Glockshuber, R. & Ban, N. The structure of a cytolytic alpha-helical toxin pore reveals its assembly mechanism. *Nature* **459**, 726–30 (2009).
13. Tzokov, S. B. *et al.* Structure of the hemolysin E (HlyE, ClyA, and SheA) channel in its membrane-bound form. *J. Biol. Chem.* **281**, 23042–9 (2006).
14. Tweten, R. K. Cholesterol-Dependent Cytolysins , a Family of Versatile Pore-Forming Toxins. *Infect. Immun.* **73**, 6199–6209 (2005).
15. Bradley, K. A., Mogridge, J., Mourez, M., Collier, R. J. & Young, J. A. Identification of the cellular receptor for anthrax toxin. *Nature* **414**, 225–229 (2001).
16. Bradley, K. A. & Young, J. A. T. Anthrax toxin receptor proteins. *Biochem. Pharmacol.* **65**, 309–314 (2003).
17. Olson, R. & Gouaux, E. Crystal structure of the Vibrio cholerae cytolysin (VCC) pro-toxin and its assembly into a heptameric transmembrane pore. *J. Mol. Biol.* **350**, 997–1016 (2005).
18. Heuck, A. P., Moe, P. C. & Johnson, B. B. The cholesterol-dependent cytolysin family of gram-positive bacterial toxins. *Subcell. Biochem.* **51**, 551–577 (2010).
19. Young, J. A. & Collier, R. J. Anthrax toxin: receptor binding, internalization, pore formation, and translocation. *Annu Rev Biochem* **76**, 243–265 (2007).
20. Bhakdi, S. & Tranum-Jensen, J. Alpha-Toxin of Staphylococcus aureus. *Microbiol. Rev.* **55**, 733–751 (1991).

21. Wai, S. N. *et al.* Vesicle-mediated export and assembly of pore-forming oligomers of the enterobacterial ClyA cytotoxin. *Cell* **115**, 25–35 (2003).
22. Chen, D. J. *et al.* Delivery of foreign antigens by engineered outer membrane vesicle vaccines. *Proc. Natl. Acad. Sci. U. S. A.* **107**, 3099–104 (2010).
23. Söderblom, T. *et al.* Effects of the Escherichia coli toxin cytolysin A on mucosal immunostimulation via epithelial Ca<sup>2+</sup> signalling and Toll-like receptor 4. *Cell. Microbiol.* **7**, 779–88 (2005).
24. Kulp, A. & Kuehn, M. J. Biological functions and biogenesis of secreted bacterial outer membrane vesicles. *Annu Rev Microbiol* **64**, 163–184 (2010).
25. Kuehn, M. J. & Kesty, N. C. Bacterial outer membrane vesicles and the host – pathogen interaction. *Genes Dev.* 2645–2655 (2005).
26. Wai, S. N., Takade, A., Amako, K. & March, A. The Release of Outer Membrane Vesicles from Strains of Enterotoxigenic Escherichia coli. **39**, 451–456 (1995).
27. Horstman, A. L. & Kuehn, M. J. Bacterial surface association of heat-labile enterotoxin through lipopolysaccharide after secretion via the general secretory pathway. *J. Biol. Chem.* **277**, 32538–32545 (2002).
28. Rowe, G. E. & Welch, R. A. Assays of hemolytic toxins. *Methods Enzymol.* **235**, 657–667 (1994).
29. Chen, M., Khalid, S., Sansom, M. S. P. & Bayley, H. Outer membrane protein G: Engineering a quiet pore for biosensing. *Proc. Natl. Acad. Sci. U. S. A.* **105**, 6272–7 (2008).
30. Gouaux, J. E. *et al.* Subunit stoichiometry of staphylococcal alpha-hemolysin in crystals and on membranes: a heptameric transmembrane pore. *Proc. Natl. Acad. Sci. U. S. A.* **91**, 12828–31 (1994).
31. Yamashita, K. *et al.* Crystal structure of the octameric pore of staphylococcal gamma-hemolysin reveals the beta-barrel pore formation mechanism by two components. *Proc. Natl. Acad. Sci. U. S. A.* **108**, 17314–9 (2011).
32. De, S. & Olson, R. Crystal structure of the Vibrio cholerae cytolysin heptamer reveals common features among disparate pore-forming toxins. *Proc. Natl. Acad. Sci. U. S. A.* **108**, 7385–90 (2011).
33. Eifler, N. *et al.* Cytotoxin ClyA from Escherichia coli assembles to a 13-meric pore independent of its redox-state. *EMBO J.* **25**, 2652–61 (2006).
34. Walker, B., Braha, O., Cheley, S. & Bayley, H. An intermediate in the assembly of a pore-forming protein trapped with a genetically-engineered switch. *Chem. Biol.* **2**, 99–105 (1995).
35. Milne, J. C., Furlong, D., Hanna, P. C., Wall, J. S. & Collier, R. J. Anthrax protective antigen forms oligomers during intoxication of mammalian cells. *J. Biol. Chem.* **269**, 20607–20612 (1994).
36. Shepard, L. A., Shatursky, O., Johnson, A. E. & Tweten, R. K. The mechanism of pore assembly for a cholesterol-dependent cytolysin: Formation of a large prepore complex precedes the insertion of the transmembrane hairpins. *Biochemistry* **39**, 10284–10293 (2000).
37. Hunt, S. *et al.* The formation and structure of Escherichia coli K-12 haemolysin E pores. *Microbiology* **154**, 633–642 (2008).
38. Hille, B. *Ion Channels of Excitable Membranes*. **3rd editio**, (2001).
39. Soskine, M. *et al.* An engineered ClyA nanopore detects folded target proteins by selective external association and pore entry. *Nano Lett.* **12**, 4895–900 (2012).
40. von Rhein, C. *et al.* ClyA cytolysin from Salmonella: distribution within the genus, regulation of expression by SlyA, and pore-forming characteristics. *Int. J. Med. Microbiol.* **299**, 21–35 (2009).
41. Thompson, J. R., Cronin, B., Bayley, H. & Wallace, M. I. Rapid assembly of a

- multimeric membrane protein pore. *Biophys. J.* **101**, 2679–83 (2011).
42. Fass, D. Disulfide Bonding in Protein Biophysics. *Annu. Rev. Biophys.* **41**, 63–79 (2012).
  43. Atkins, A. *et al.* Structure-function relationships of a novel bacterial toxin, hemolysin E. The role of alpha G. *J. Biol. Chem.* **275**, 41150–5 (2000).
  44. Petosa, C., Collier, R. J., Klimpel, K. R., Leppla, S. H. & Liddington, R. C. Crystal structure of the anthrax toxin protective antigen. *Nature* **385**, 833–838 (1997).
  45. Opota, O. *et al.* Monalysin, a novel  $\beta$ -pore-forming toxin from the drosophila pathogen *pseudomonas entomophila*, contributes to host intestinal damage and lethality. *PLoS Pathog.* **7**, (2011).
  46. Oscarsson, J. *et al.* Molecular analysis of the cytolytic protein ClyA (SheA) from *Escherichia coli*. *Mol. Microbiol.* **32**, 1226–38 (1999).
  47. Ishihama, Y. *et al.* Protein abundance profiling of the *Escherichia coli* cytosol. *BMC Genomics* **9**, 102 (2008).

## CONCLUSIONS AND FUTURE WORK

### C.1 What is on the horizon for OmpG?

We could successfully detect biotin binding proteins using the OmpG nanopore by covalently attaching a chemical ligand onto loop 6 (L6).<sup>1-4</sup> We can further extend the utility of the OmpG nanopore by assessing other analyte targets and chemical ligands. For example, other strategies we could apply are labeling the OmpG with (i) an oligonucleotide to detect complimentary nucleic acids or nucleic acid binding proteins (ii) engineer high affinity peptide sequences into loop 6 of OmpG to detect specific protein analytes.

Thus far, we have exploited the dynamics of L6 to detect target proteins. We found that some targets can interact with the OmpG through electrostatic interactions *i.e.* through a sampling mechanism.<sup>2</sup> Another area we can explore is determining whether proteins that can sample OmpG can be detected using loops other than L6. The findings of this exploration would be useful in engineering a new generation of high affinity OmpG sensors that have multiple binding sites engineered into several loops.

We successfully exploited OmpG's intrinsic ionic properties based on loop 6 to develop a sensitive nanopore sensor, however, the underlying mechanisms for OmpG's gating behavior is also of interest to us. It has been shown in previous studies and in our work, that the gating behavior of OmpG is highly altered by conditions of pH and to a lower extent the applied voltage.<sup>5-9</sup> To further develop the OmpG platform, we need more than just a basic understanding of L6 dynamics. Probing the molecular mechanisms contributing to OmpG's ionic behavior will be essential in designing the appropriate mutations and alterations to its structure so that function is not compromised.

## C.2 What is in the future for ClyA?

Many aspects of pore forming toxin (PFT) oligomerization and assembly kinetics remain a puzzle.<sup>10,11</sup> Recent work on ClyA from Benjamin Schuler's lab has characterized the assembly dynamics of various ClyA proteins when triggered by detergent DDM.<sup>12,13</sup> Since detergent is not the biological relevant membrane target of ClyA, assembly studies on biological membranes could give more insight into the native assembly mechanism of pore-forming toxins that are secreted as soluble monomers.

In addition, the Schuler group revealed that the soluble ClyA oligomers that we observed in chapter 5 are in fact intermediates of an off-pathway assembly mechanism.<sup>14</sup> We also found, through electron microscopy characterization that ClyA<sub>O8</sub> and ClyA<sub>O9</sub> do not form pre-pore structures but instead fibril like structures (Figure F.1). We believe these structures could dissociate in the presence of detergent or membrane to re-associate and form active transmembrane pores (Figure F.2). Thus, we characterized a stable misfolded intermediate in the protein folding funnel for ClyA. The motivation for the study of ClyA<sub>O8</sub> and ClyA<sub>O9</sub> was due to the evidence that ClyA proteins are secreted in outer membrane vesicles (OMVs). In these OMVs ClyA exists as ring like structures indicative of oligomeric pores.<sup>15</sup> Later studies had engineered OMVs loaded with ClyA as delivery vehicles into the cell.<sup>16,17</sup> However, the mechanism of ClyA assembly and attack via OMV secretion is still not well understood and is an area for further investigation in our lab since ClyA<sub>O8</sub> and ClyA<sub>O9</sub> were found to be non-native structures.

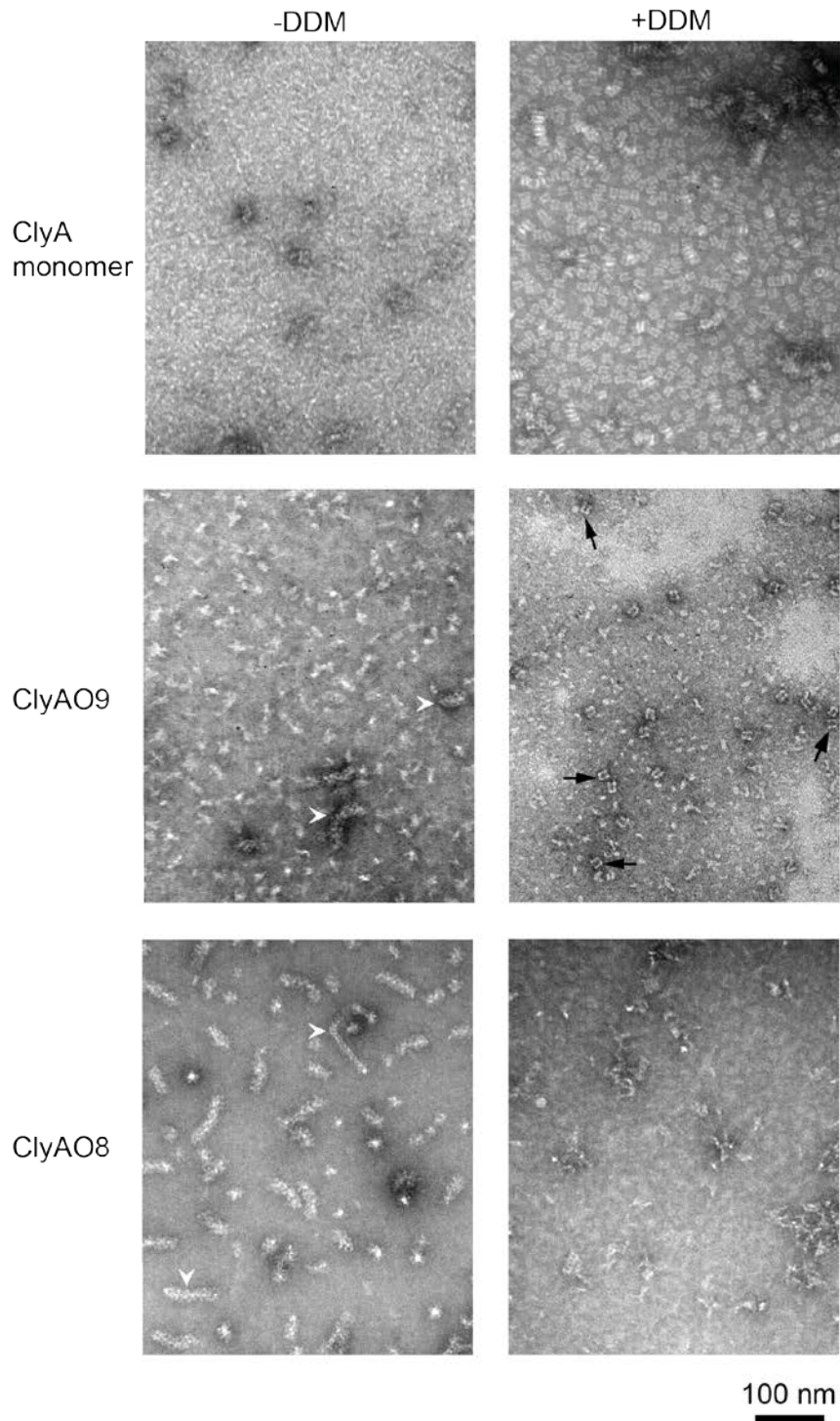
An area that has not been explored is the study of the stability or dissociation kinetics of the transmembrane pore. Researchers have found that multimeric protein complexes can have the ability to exchange subunits.<sup>18,19</sup> Currently, protomer exchange of a PFT has not been studied and is unknown whether it occurs. Very stable PFTs such as alpha-hemolysin which are SDS stable are unlikely to exchange

protomers, however, PFTs like ClyA which are not SDS resistant, could undergo such a mechanism.

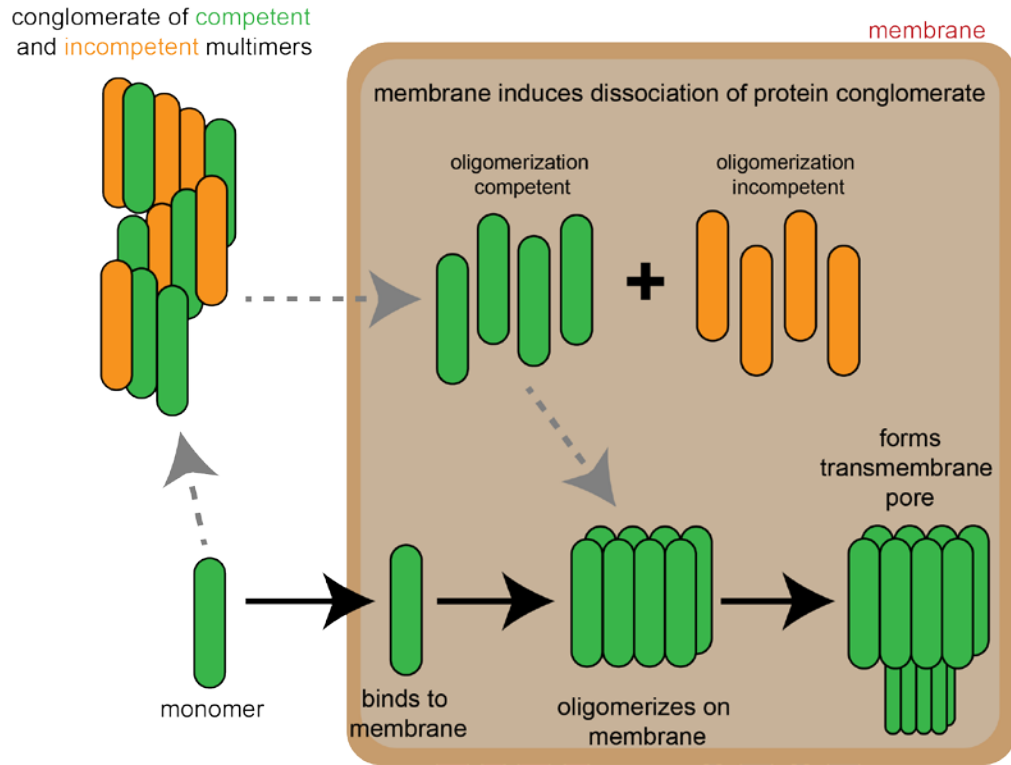
A recent study revealed that the C-terminus of ClyA was critical for pore formation and stability<sup>20</sup> which was not apparent or overseen in previous studies.<sup>21-24</sup> The b-tongue in ClyA is a hydrophobic rich region that is solvent exposed and it is still not quite clear what is its role and thus this can be further investigated.

In conclusion, there are many biochemical and biophysical questions to explore using these OmpG and ClyA as models.





**Figure C.1. Negative stain electron microscopy of ClyA proteins.** Structures of monomer, ClyA<sub>08</sub> and ClyA<sub>09</sub> in with and without detergent. ClyA<sub>08</sub> and ClyA<sub>09</sub> form fibrillar like structures in the absence of detergent. However in the presence of DDM the fibrillar like structures have dissociated and in the case of ClyA<sub>09</sub> some pore structures have formed. White arrowheads indicate the protein conglomerates while black arrows point to pores.



**Figure C.2. CiyA assembly mechanisms.** On-pathway (black arrows) and off-pathway (grey arrows) oligomerization mechanisms of CiyA revealed by studies of the Schuler and Chen labs.

### C.3 References

1. Fahie, M., Chisholm, C. & Chen, M. Resolved Single-Molecule Detection of Individual Species within a Mixture of anti-Biotin Antibodies Using an Engineered Monomeric Nanopore. *ACS Nano* **9**, 1089–1098 (2015).
2. Fahie, M. A. & Chen, M. Electrostatic Interactions between OmpG Nanopore and Analyte Protein Surface Can Distinguish between Glycosylated Isoforms. *J. Phys. Chem. B* **119**, 10198–10206 (2015).
3. Fahie, M. A., Yang, B., Mullis, M., Holden, M. A. & Chen, M. Selective detection of protein homologues in serum using an OmpG nanopore. *Anal. Chem.* **87**, 11143–11149 (2015).
4. Fahie, M. A., Yang, B., Pham, B. & Chen, M. Tuning the Selectivity and Sensitivity of an OmpG Nanopore Sensor by Adjusting Ligand Tether Length. *ACS Sensors* **1**, 614–622 (2016).
5. Zhuang, T., Chisholm, C., Chen, M. & Tamm, L. K. NMR-based conformational ensembles explain pH-gated opening and closing of OmpG channel. *J. Am. Chem. Soc.* **135**, 15101–13 (2013).
6. Damaghi, M. *et al.* pH-dependent interactions guide the folding and gate the transmembrane pore of the beta-barrel membrane protein OmpG. *J. Mol. Biol.* **397**, 878–82 (2010).
7. Korkmaz-Ozkan, F., Köster, S., Kühlbrandt, W., Mäntele, W. & Yildiz, O. Correlation between the OmpG secondary structure and its pH-dependent alterations monitored by FTIR. *J. Mol. Biol.* **401**, 56–67 (2010).
8. Yildiz, O., Vinothkumar, K. R., Goswami, P. & Kühlbrandt, W. Structure of the monomeric outer-membrane porin OmpG in the open and closed conformation. *EMBO J.* **25**, 3702–13 (2006).
9. Chen, M., Li, Q.-H. & Bayley, H. Orientation of the monomeric porin OmpG in planar lipid bilayers. *Chembiochem* **9**, 3029–36 (2008).
10. Lee, A. A., Senior, M. J., Wallace, M. I., Woolley, T. E. & Griffiths, I. M. Dissecting the self-assembly kinetics of multimeric pore-forming toxins. *Interface* **13**, 20150762 (2016).
11. Cosentino, K., Ros, U. & García-Sáez, A. J. Assembling the puzzle: Oligomerization of  $\alpha$ -pore forming proteins in membranes. *Biochim. Biophys. Acta - Biomembr.* **1858**, 457–466 (2016).
12. Roderer, D. *et al.* Characterization of Variants of the Pore-Forming Toxin ClyA from *Escherichia coli* Controlled by a Redox Switch. *Biochemistry* **53**, 6357–6369 (2014).
13. Benke, S. *et al.* The assembly dynamics of the cytolytic pore toxin ClyA. *Nat. Commun.* **6**, 1–13 (2015).
14. Roderer, D., Benke, S., Schuler, B. & Glockshuber, R. Soluble Oligomers of the Pore-forming Toxin Cytolysin A from *Escherichia coli* Are Off-pathway Products of Pore. *J. Biol. Chem.* **291**, 5652–5663 (2016).
15. Wai, S. N. *et al.* Vesicle-mediated export and assembly of pore-forming oligomers of the enterobacterial ClyA cytotoxin. *Cell* **115**, 25–35 (2003).
16. Kim, J.-Y. *et al.* Engineered bacterial outer membrane vesicles with enhanced functionality. *J. Mol. Biol.* **380**, 51–66 (2008).
17. Chen, D. J. *et al.* Delivery of foreign antigens by engineered outer membrane vesicle vaccines. *Proc. Natl. Acad. Sci. U. S. A.* **107**, 3099–104 (2010).
18. Sobott, F., Benesch, J. L. P., Vierling, E. & Robinson, C. V. Subunit Exchange of Multimeric Protein Complexes: Real-Time monitoring of subunit exchange between small heat shock proteins by using electrospray mass spectrometry. *J.*

- Biol. Chem.* **277**, 38921–38929 (2002).
19. Stratton, M. *et al.* Activation-triggered subunit exchange between CaMKII holoenzymes facilitates the spread of kinase activity. *Elife* **3**, e01610 (2014).
  20. Sathyanarayana, P., Desikan, R., Ayappa, K. G. & Visweswariah, S. S. The Solvent-Exposed C-Terminus of the Cytolysin A Pore-Forming Toxin Directs Pore Formation and Channel Function in Membranes. *Biochemistry* [acs.biochem.6b00593](https://doi.org/10.1021/acs.biochem.6b00593) (2016). doi:10.1021/acs.biochem.6b00593
  21. Atkins, A. *et al.* Structure-function relationships of a novel bacterial toxin, hemolysin E. The role of alpha G. *J. Biol. Chem.* **275**, 41150–5 (2000).
  22. Wai, S. N. *et al.* Characterization of Dominantly Negative Mutant ClyA Cytotoxin Proteins in *Escherichia coli*. *J. Bacteriol.* **185**, 5491–5499 (2003).
  23. Ludwig, A. *et al.* Mutations affecting export and activity of cytolysin A from *Escherichia coli*. *J. Bacteriol.* **192**, 4001–11 (2010).
  24. Oscarsson, J. *et al.* Molecular analysis of the cytolytic protein ClyA (SheA) from *Escherichia coli*. *Mol. Microbiol.* **32**, 1226–38 (1999).

## BIBLIOGRAPHY

- Aksimentiev A, Schulten K. Imaging alpha-hemolysin with molecular dynamics: ionic conductance, osmotic permeability, and the electrostatic potential map. *Biophys J*. 2005;88(6):3745-3761.
- Apetrei A, Asandei A, Park Y, Hahm KS, Winterhalter M, Luchian T. Unimolecular study of the interaction between the outer membrane protein OmpF from *E. coli* and an analogue of the HP(2-20) antimicrobial peptide. *J Bioenerg Biomembr*. 2010;42(2):173-180.
- Apetrei A, Ciuca A, Lee J, Seo CH, Park Y, Luchian T. A Protein Nanopore-Based Approach for Bacteria Sensing. *Nanoscale Res Lett*. 2016;11(1):501.
- Arnaut V, Langecker M, Simmel FC. Nanopore force spectroscopy of aptamer-ligand complexes. *Biophys J*. 2013;105(5):1199-1207.
- Astier Y, Kainov DE, Bayley H, Tuma R, Howorka S. Stochastic detection of motor protein-RNA complexes by single-channel current recording. *ChemPhysChem*. 2007;8(15):2189-2194.
- Atkins A, Wyborn NR, Wallace AJ, et al. Structure-function relationships of a novel bacterial toxin, hemolysin E. The role of alpha G. *J Biol Chem*. 2000;275(52):41150-41155.
- Baran K, Dunstone M, Chia J, et al. The Molecular Basis for Perforin Oligomerization and Transmembrane Pore Assembly. *Immunity*. 2009;30(5):684-695.
- Barati Farimani A, Dibaeinia P, Aluru NR. DNA Origami-Graphene Hybrid Nanopore for DNA Detection. *ACS Appl Mater Interfaces*. 2017;9(1):92-100.
- Bayley H, Cremer PS. Stochastic sensors inspired by biology. *Nature*. 2001;413(6852):226-230.
- Bayley H. Membrane-protein structure: Piercing insights. *Nature*. 2009;459:4-5.
- Behlau M, Mills DJ, Quader H, Kühlbrandt W, Vonck J. Projection structure of the monomeric porin OmpG at 6 Å resolution. *J Mol Biol*. 2001;305(1):71-77.
- Bell NAW, Keyser UF. Specific Protein Detection Using Designed DNA Carriers and Nanopores. *J Am Chem Soc*. 2015;137(5):2035-2041.
- Benke S, Roderer D, Wunderlich B, Nettels D, Glockshuber R, Schuler B. The assembly dynamics of the cytolytic pore toxin ClyA. *Nat Commun*. 2015;6:1-13.
- Benner S, Chen RJA, Wilson NA, et al. Sequence-specific detection of individual DNA polymerase complexes in real time using a nanopore. *Nat Nanotechnol*. 2007;2(11):718-724.

Benz R, Bauer K. Permeation of hydrophilic molecules through the outer membrane of gram-negative bacteria. *Eur J Biochem.* 1988;171(1):1-19.

Benz R, Popp B, Petra Wiesner, Schmid A. The mitochondrial porins. *Prog Cell Res.* 1995;5:107-112.

Benz R. Biophysical properties of porin pores from mitochondrial outer membrane of eukaryotic cells. *Experientia.* 1990;46(2):131-137.

Bezrukov SM, Vodyanoy I, Parsegian VA. Counting polymers moving through a single ion channel. *Nature.* 1994;370(6487):279-281.

Bhakdi S, Trantum-Jensen J. Alpha-Toxin of *Staphylococcus aureus*. *Microbiol Rev.* 1991;55(4):733-751.

Biesemans A, Soskine M, Maglia G. A Protein Rotaxane Controls the Translocation of Proteins Across a ClyA Nanopore. *Nano Lett.* 2015;15(9):6076-6081.

Bischofberger M, Gonzalez MR, van der Goot FG. Membrane injury by pore-forming proteins. *Curr Opin Cell Biol.* 2009;21(4):589-595.

Boersma AJ, Brain KL, Bayley H. Real-time stochastic detection of multiple neurotransmitters with a protein nanopore. *ACS Nano.* 2012;6(6):5304-5308.

Booth PJ, Clarke J. Membrane protein folding makes the transition. *Proc Natl Acad Sci U S A.* 2010;107(9):3947-3948.

Bradley KA, Mogridge J, Mourez M, Collier RJ, Young JA. Identification of the cellular receptor for anthrax toxin. *Nature.* 2001;414(6860):225-229.

Bradley KA, Young JAT. Anthrax toxin receptor proteins. *Biochem Pharmacol.* 2003;65(3):309-314.

Braha O, Gu LQ, Zhou L, Lu X, Cheley S, Bayley H. Simultaneous stochastic sensing of divalent metal ions. *Nat Biotechnol.* 2000;18(9):1005-1007.

Braha O, Walker B, Cheley S, et al. Designed protein pores as components for biosensors. *Chem Biol.* 1997;4(7):497-505.

Branton D, Deamer DW, Marziali A, et al. The potential and challenges of nanopore sequencing. *Nat Biotechnol.* 2008;26(10):1146-1153.

Burns JR, Al-Juffali N, Janes SM, Howorka S. Membrane-spanning DNA nanopores with cytotoxic effect. *Angew Chemie - Int Ed.* 2014;53(46):12466-12470.

Burns JR, Göpfrich K, Wood JW, et al. Lipid-bilayer-spanning DNA nanopores with a bifunctional porphyrin anchor. *Angew Chemie - Int Ed.* 2013;52(46):12069-12072.

Burns JR, Seifert A, Fertig N, Howorka S. A biomimetic DNA-based channel for the ligand-controlled transport of charged molecular cargo across a biological membrane. *Nat Nanotechnol.* 2016;advance on(2):1-16.

Burns JR, Stulz E, Howorka S. Self-Assembled DNA Nanopores That Span Lipid Bilayers. *Nano Lett.* 2013;13(6):2351-2356.

Butler TZ, Pavlenok M, Derrington IM, Niederweis M, Gundlach JH. Single-molecule DNA detection with an engineered MspA protein nanopore. *Proc Natl Acad Sci.* 2008;105(52):20647-20652.

Carlsen AT, Zahid OK, Ruzicka J a, et al. Selective Detection and Quantification of Modified DNA with Solid- State Nanopores. *Nano Lett.* 2014;14:5488-5492.

Cheley S, Gu LQ, Bayley H. Stochastic sensing of nanomolar inositol 1,4,5-trisphosphate with an engineered pore. *Chem Biol.* 2002;9(7):829-838.

Cheley S, Xie H, Bayley H. A genetically encoded pore for the stochastic detection of a protein kinase. *ChemBioChem.* 2006;7(12):1923-1927.

Chen DJ, Osterrieder N, Metzger SM, et al. Delivery of foreign antigens by engineered outer membrane vesicle vaccines. *Proc Natl Acad Sci U S A.* 2010;107(7):3099-3104.

Chen DJ, Osterrieder N, Metzger SM, et al. Delivery of foreign antigens by engineered outer membrane vesicle vaccines. *Proc Natl Acad Sci U S A.* 2010;107(7):3099-3104.

Chen JQ, Zhan YF, Wang W, Jiang SN, Li XY. The engineered *Salmonella typhimurium* inhibits tumorigenesis in advanced glioma. *Onco Targets Ther.* 2015;8:2555-2563.

Chen K, Bell NAW, Kong J, Tian Y, Keyser UF. Direction- and Salt-Dependent Ionic Current Signatures for DNA Sensing with Asymmetric Nanopores. *Biophysj.* 2017;112(1):1-15.

Chen M, Khalid S, Sansom MSP, Bayley H. Outer membrane protein G: Engineering a quiet pore for biosensing. *Proc Natl Acad Sci U S A.* 2008;105(17):6272-6277.

Chen M, Li Q-H, Bayley H. Orientation of the monomeric porin OmpG in planar lipid bilayers. *Chembiochem.* 2008;9(18):3029-3036.

Clarke J, Wu H, Jayasinghe L, Patel A, Reid S, Bayley H. Continuous base identification for single-molecule nanopore DNA sequencing. *Nat Nanotechnol.* 2009;4(4):265-270.

Conlan S, Bayley H. Folding of a monomeric porin, OmpG, in detergent solution. *Biochemistry.* 2003;42(31):9453-9465.

Conlan S, Zhang Y, Cheley S, Bayley H. Biochemical and Biophysical Characterization of OmpG: A Monomeric Porin †. *Biochemistry.* 2000;39(39):11845-11854.

Cornell B a, Braach-Maksvytis VL, King LG, et al. A biosensor that uses ion-channel switches. *Nature.* 1997;387(6633):580-583.

Cortajarena AL, Goñi FM, Ostolaza H. Glycophorin as a receptor for *Escherichia coli* alpha-hemolysin in erythrocytes. *J Biol Chem.* 2001;276(16):12513-12519.

- Cosentino K, Ros U, García-Sáez AJ. Assembling the puzzle: Oligomerization of  $\alpha$ -pore forming proteins in membranes. *Biochim Biophys Acta - Biomembr.* 2016;1858(3):457-466.
- Costa TRD, Felisberto-Rodrigues C, Meir A, et al. Secretion systems in Gram-negative bacteria: structural and mechanistic insights. *Nat Rev Microbiol.* 2015;13(6):343-359.
- Damaghi M, Bippes C, Köster S, et al. pH-dependent interactions guide the folding and gate the transmembrane pore of the beta-barrel membrane protein OmpG. *J Mol Biol.* 2010;397(4):878-882.
- Darvish A, Goyal G, Kim M. Sensing, capturing, and interrogation of single virus particles with solid state nanopores. *SPIE Sens Technol + Appl.* 2015;9490:94900M.
- De S, Olson R. Crystal structure of the *Vibrio cholerae* cytolysin heptamer reveals common features among disparate pore-forming toxins. *Proc Natl Acad Sci U S A.* 2011;108(18):7385-7390.
- Dekker C. Solid-state nanopores. *Nat Nanotechnol.* 2007;2(4):209-215.
- del Castillo FJ, Leal SC, Moreno F, del Castillo I. The *Escherichia coli* K-12 sheA gene encodes a 34-kDa secreted haemolysin. *Mol Microbiol.* 1997;25(1):107-115.
- Deng W, Marshall NC, Rowland JL, et al. Assembly, structure, function and regulation of type III secretion systems. *Nat Rev Microbiol.* 2017.
- Derrington IM, Butler TZ, Collins MD, et al. Nanopore DNA sequencing with MspA. *Proc Natl Acad Sci U S A.* 2010;107(37):16060-16065.
- Ding S, Gao C, Gu LQ. Capturing single molecules of immunoglobulin and ricin with an aptamer-encoded glass nanopore. *Anal Chem.* 2009;81(16):6649-6655.
- Douglas Hanahan, Weinberg RA. The hallmarks of cancer. *Cell.* 2000;100(1):57-70.
- Dube DH, Bertozzi CR. Glycans in cancer and inflammation--potential for therapeutics and diagnostics. *Nat Rev Drug Discov.* 2005;4(6):477-488.
- Durand G, Seta N. Protein glycosylation and diseases: Blood and urinary oligosaccharides as markers for diagnosis and therapeutic monitoring. *Clin Chem.* 2000;46(6):795-805.
- Eifler N, Vetsch M, Gregorini M, et al. Cytotoxin ClyA from *Escherichia coli* assembles to a 13-meric pore independent of its redox-state. *EMBO J.* 2006;25(11):2652-2661.
- Fagerlund A, Lindbäck T, Storset AK, Granum PE, Hardy SP. *Bacillus cereus* Nhe is a pore-forming toxin with structural and functional properties similar to the ClyA (HlyE, SheA) family of haemolysins, able to induce osmotic lysis in epithelia. *Microbiology.* 2008;154(3):693-704.



Fahie M, Chisholm C, Chen M. Resolved Single-Molecule Detection of Individual Species within a Mixture of anti-Biotin Antibodies Using an Engineered Monomeric Nanopore. *ACS Nano*. 2015;9(2):1089-1098.

Fahie M, Chisholm C, Chen M. Resolved Single-Molecule Detection of Individual Species within a Mixture of anti-Biotin Antibodies Using an Engineered Monomeric Nanopore. *ACS Nano*. 2015;9(2):1089-1098.

Fahie M, Romano F, Chisholm C, Heuck AP, Zbinden M, Chen M. A non-classical assembly pathway of Escherichia coli pore forming toxin cytolysin A. *J Biol Chem*. 2013;288(43):31042-31051.

Fahie MA, Chen M. Electrostatic Interactions between OmpG Nanopore and Analyte Protein Surface Can Distinguish between Glycosylated Isoforms. *J Phys Chem B*. 2015;119(32):10198-10206.

Fahie MA, Yang B, Mullis M, Holden MA, Chen M. Selective detection of protein homologues in serum using an OmpG nanopore. *Anal Chem*. 2015;87(21):11143-11149.

Fahie MA, Yang B, Pham B, Chen M. Tuning the Selectivity and Sensitivity of an OmpG Nanopore Sensor by Adjusting Ligand Tether Length. *ACS Sensors*. 2016;1(5):614-622.

Fajardo DA, Cheung J, Ito C, Sugawara E. Biochemistry and Regulation of a Novel Escherichia coli K-12 Porin Protein , OmpG , Which Produces Unusually Large Channels. *J Bacteriol*. 1998;180(17):4452-4459.

Faller M, Niederweis M, Schulz GE. The Structure of a Mycobacterial Outer-Membrane Channel. *Science*. 2004;303(5661):1189-1192.

Fass D. Disulfide Bonding in Protein Biophysics. *Annu Rev Biophys*. 2012;41:63-79.

Firnkes M, Pedone D, Knezevic J, et al. Electrically Facilitated Translocations of Proteins through Silicon Nitride Nanopores : Conjoint and Competitive Action of Diffusion,. *Nano Lett*. 2010;10(6):2162-2167.

Fologea D, Ledden B, McNabb DS, Li J. Electrical characterization of protein molecules by a solid-state nanopore. *Appl Phys Lett*. 2007;91(5):53901-1-53901-53903.

Franceschini L, Brouns T, Willems K, Carlon E, Maglia G. DNA Translocation through Nanopores at Physiological Ionic Strengths Requires Precise Nanoscale Engineering. *ACS Nano*. 2016;10(9):8394-8402.

Franceschini L, Soskine M, Biesemans A, Maglia G. A nanopore machine promotes the vectorial transport of DNA across membranes. *Nat Commun*. 2013;4:2415.

Freedman KJ, Haq SR, Edel JB, Jemth P, Kim MJ. Single molecule unfolding and stretching of protein domains inside a solid-state nanopore by electric field. *Sci Rep*. 2013;3:1638.

Freedman KJ, Jurgens M, Prabhu A, et al. Chemical, thermal, and electric field induced unfolding of single protein molecules studied using nanopores. *Anal Chem*. 2011;83(13):5137-5144.

Fuentes JA, Villagra N, Castillo-Ruiz M, Mora GC. The Salmonella Typhi hlyE gene plays a role in invasion of cultured epithelial cells and its functional transfer to *S. Typhimurium* promotes deep organ infection in mice. *Res Microbiol*. 2008;159(4):279-287.

Garrido-cardenas JA, Garcia-maroto F, Alvarez-bermejo JA, Manzano-agugliaro F. DNA Sequencing Sensors : An Overview. *Sensors (Basel)*. 2017;17 (3)(588):1-15.

Gilbert RJC, Serra MD, Froelich CJ, Wallace MI, Anderluh G. Membrane pore formation at protein-lipid interfaces. *Trends Biochem Sci*. 2014;39(11):510-516.

Goodrich CP, Kirmizialtin S, Huyghues-Despointes BM, et al. Single-molecule electrophoresis of  $\beta$ -hairpin peptides by electrical recordings and Langevin dynamics simulations. *J Phys Chem B Lett*. 2007;111(13):3332-3335.

Gouaux JE, Braha O, Hobaugh MR, et al. Subunit stoichiometry of staphylococcal alpha-hemolysin in crystals and on membranes: a heptameric transmembrane pore. *Proc Natl Acad Sci U S A*. 1994;91(26):12828-12831.

Green NM. Avidin and streptavidin. *Methods Enzymol*. 1990;184(1978):51-67.

Green NM. Avidin. *Adv Protein Chem*. 1975;29:85-133. doi:10.1016/S0065-3233(08)60411-8.

Grosse W, Psakis G, Mertins B, et al. Structure-Based Engineering of a Minimal Porin Reveals Loop-Independent Channel Closure. *Biochemistry*. 2014;53:4826-4838.

Gu LQ, Bayley H. Interaction of the noncovalent molecular adapter, beta-cyclodextrin, with the staphylococcal alpha-hemolysin pore. *Biophys J*. 2000;79(4):1967-1975.

Gu LQ, Braha O, Conlan S, Cheley S, Bayley H. Stochastic sensing of organic analytes by a pore-forming protein containing a molecular adapter. *Nature*. 1999;398(6729):686-690.

Guo BY, Zeng T, Wu HC. Recent advances of DNA sequencing via nanopore-based technologies. *Sci Bull*. 2015;60(3):287-295.

Gurnev PA, Oppenheim AB, Winterhalter M, Bezrukov SM. Docking of a Single Phage Lambda to its Membrane Receptor Maltoporin as a Time-resolved Event. *J Mol Biol*. 2006;359(5):1447-1455.

Halverson KM, Panchal RG, Nguyen TL, et al. Anthrax biosensor, protective antigen ion channel asymmetric blockade. *J Biol Chem*. 2005;280(40):34056-34062.

Han A, Schürmann G, Mondin G, et al. Sensing protein molecules using nanofabricated pores. *Appl Phys Lett*. 2006;88(9):1-4.

Han X, Aslanian A, Yates JR. Mass spectrometry for proteomics. *Curr Opin Chem Biol.* 2008;12(5):483-490.

Hanahan D, Weinberg RA. Hallmarks of cancer: the next generation. *Cell.* 2011;144(5):646-674.

Haque F, Li J, Wu HC, Liang XJ, Guo P. Solid-state and biological nanopore for real-time sensing of single chemical and sequencing of DNA. *Nano Today.* 2013;8(1):56-74.

Harrington L, Cheley S, Alexander LT, Knapp S, Bayley H. Stochastic detection of Pim protein kinases reveals electrostatically enhanced association of a peptide substrate. *Proc Natl Acad Sci U S A.* 2013;110(47):E4417-26.

Harsman A, Schock A, Hemmis B, et al. OEP40, a regulated glucose-permeable  $\beta$ -barrel solute channel in the chloroplast outer envelope membrane. *J Biol Chem.* 2016;291(34):17848-17860.

Hart GW, Slawson C, Ramirez-Correa G, Lagerlof O. Cross talk between O-GlcNAcylation and phosphorylation: roles in signaling, transcription, and chronic disease. *Annu Rev Biochem.* 2011;80:825-858.

Heng JB, Aksimentiev A, Ho C, et al. Stretching DNA using the electric field in a synthetic nanopore. *Nano Lett.* 2005;5(10):1883-1888.

Henrickson SE, Dimarzio EA, Wang Q, Stanford VM, Kasianowicz JJ. Probing single nanometer-scale pores with polymeric molecular rulers. *J Chem Phys.* 2010;132(13).

Henrickson SE, Misakian M, Robertson B, Kasianowicz JJ. Driven DNA transport into an asymmetric nanometer-scale pore. *Phys Rev Lett.* 2000;85(14):3057-3060.

Heuck AP, Moe PC, Johnson BB. The cholesterol-dependent cytolysin family of gram-positive bacterial toxins. *Subcell Biochem.* 2010;51:551-577.

Hille B. *Ion Channels of Excitable Membranes.* Vol 3rd edition.; 2001.

Ho C-W, Van Meervelt V, Tsai K-C, De Temmerman P-J, Mast J, Maglia G. Engineering a nanopore with co-chaperonin function. *Sci Adv.* 2015;1(11):e1500905.

Horstman AL, Kuehn MJ. Bacterial surface association of heat-labile enterotoxin through lipopolysaccharide after secretion via the general secretory pathway. *J Biol Chem.* 2002;277(36):32538-32545.

Howorka S, Cheley S, Bayley H. Sequence-specific detection of individual DNA strands using engineered nanopores. *Nat Biotechnol.* 2001;19(7):636-639.

Howorka S, Nam J, Bayley H, Kahne D. Stochastic detection of monovalent and bivalent protein-ligand interactions. *Angew Chemie - Int Ed.* 2004;43(7):842-846.

Howorka S, Siwy Z. Nanopore analytics: sensing of single molecules. *Chem Soc Rev.* 2009;38(8):2360-2384.

Howorka S, Siwy Z. Nanopores and Nanochannels: From Gene Sequencing to Genome Mapping. *ACS Nano*. 2016;10(11):9768-9771.

Howorka S, Siwy ZS. Nanopores as protein sensors. *Nat Biotechnol*. 2012;30(6):506-507.

Hunt S, Green J, Artymiuk PJ. Hemolysin E (HlyE, ClyA, SheA) and Related Toxins. *Adv Exp Med Biol*. 2010;677:116-126.

Hunt S, Moir AJG, Tzokov S, Bullough PA, Artymiuk PJ, Green J. The formation and structure of Escherichia coli K-12 haemolysin E pores. *Microbiology*. 2008;154(2):633-642.

Hwang WL, Chen M, Cronin B, Holden M a, Bayley H. Asymmetric droplet interface bilayers. *J Am Chem Soc*. 2008;130(18):5878-5879.

Iacovache I, Bischofberger M, van der Goot FG. Structure and assembly of pore-forming proteins. *Curr Opin Struct Biol*. 2010;20(2):241-246.

Iacovache I, van der Goot FG, Pernot L. Pore formation: An ancient yet complex form of attack. *Biochim Biophys Acta - Biomembr*. 2008;1778(7-8):1611-1623.

Iacovache I, Van Der Goot FG. A bacterial big-MAC attack. *Nat Struct Mol Biol*. 2004;11(12):1163-1164.

Ishihama Y, Schmidt T, Rappsilber J, et al. Protein abundance profiling of the Escherichia coli cytosol. *BMC Genomics*. 2008;9(1):102.

Ivankin A, Carson S, Kinney SRM, Wanunu M. Fast, label-free force spectroscopy of histone-DNA interactions in individual nucleosomes using nanopores. *J Am Chem Soc*. 2013;135(41):15350-15352.

Jain M, Fiddes IT, Miga KH, Olsen HE, Paten B, Akeson M. Improved data analysis for the MinION nanopore sequencer. *Nat Methods*. 2015;12(4):351-356.

Japrun D, Dogan J, Freedman KJ, et al. Single-molecule studies of intrinsically disordered proteins using solid-state nanopores. *Anal Chem*. 2013;85(4):2449-2456.

Jiang S-N, Phan TX, Nam T-K, et al. Inhibition of tumor growth and metastasis by a combination of Escherichia coli-mediated cytolytic therapy and radiotherapy. *Mol Ther*. 2010;18(3):635-642.

Kabachinski G, Schwartz TU. The nuclear pore complex - structure and function at a glance. *J Cell Sci*. 2015;128(3):423-429.

Kasianowicz JJ, Balijepalli AK, Etedgui J, et al. Analytical applications for pore-forming proteins. *Biochim Biophys Acta - Biomembr*. 2016;1858(3):593-606.

Kasianowicz JJ, Brandin E, Branton D, Deamer DW. Characterization of individual polynucleotide molecules using a membrane channel. *Proc Natl Acad Sci U S A*. 1996;93(24):13770-13773.

- Kasianowicz JJ, Henrickson SE, Weetall HH, Robertson B. Simultaneous multianalyte detection with a nanometer-scale pore. *Anal Chem*. 2001;73(10):2268-2272.
- Kasianowicz JJ, Robertson JWF, Chan ER, Reiner JE, Stanford VM. Nanoscopic porous sensors. *Annu Rev Anal Chem (Palo Alto Calif)*. 2008;1:737-766.
- Kim J-Y, Doody AM, Chen DJ, et al. Engineered bacterial outer membrane vesicles with enhanced functionality. *J Mol Biol*. 2008;380(1):51-66.
- Kleinschmidt JH. Folding of  $\beta$ -barrel membrane proteins in lipid bilayers - Unassisted and assisted folding and insertion. *Biochim Biophys Acta - Biomembr*. 2015;1848(9):1927-1943.
- Korkmaz F, Köster S, Yildiz O, Mäntele W. In situ opening/closing of OmpG from *E. coli* and the splitting of  $\beta$ -sheet signals in ATR-FTIR spectroscopy. *Spectrochim Acta A Mol Biomol Spectrosc*. 2012;91:395-401.
- Korkmaz-Ozkan F, Köster S, Kühlbrandt W, Mäntele W, Yildiz O. Correlation between the OmpG secondary structure and its pH-dependent alterations monitored by FTIR. *J Mol Biol*. 2010;401(1):56-67.
- Kouokam JC, Wai SN. Outer membrane vesicle-mediated export of a pore-forming cytotoxin from *Escherichia coli*. *Toxin Rev*. 2008;25(1):31-46.
- Kowalczyk SW, Kapinos L, Blosser TR, et al. Single-molecule transport across an individual biomimetic nuclear pore complex. *Nat Nanotechnol*. 2011;6(7):433-438.
- Kudr J, Skalickova S, Nejdil L, et al. Fabrication of solid-state nanopores and its perspectives. *Electrophoresis*. 2015;36(19):2367-2379.
- Kuehn MJ, Kesty NC. Bacterial outer membrane vesicles and the host – pathogen interaction. *Genes Dev*. 2005;(Beveridge 1999):2645-2655.
- Kulp A, Kuehn MJ. Biological functions and biogenesis of secreted bacterial outer membrane vesicles. *Annu Rev Microbiol*. 2010;64:163-184.
- Kumar S, Tao C, Chien M, et al. PEG-Labeled Nucleotides and Nanopore Detection for Single Molecule DNA Sequencing by Synthesis. *Sci Rep*. 2012;2(684):1-8.
- Lai X, Arencibia I, Johansson A, et al. Cytocidal and Apoptotic Effects of the ClyA Protein from *Escherichia coli* on Primary and Cultured Monocytes and Macrophages. *Infect Immun*. 2000;68(7):4363-4367.
- Laohakunakorn N, Keyser UF. Electroosmotic flow rectification in conical nanopores. *Nanotechnology*. 2015;26(27):275202.
- Lee AA, Senior MJ, Wallace MI, Woolley TE, Griffiths IM. Dissecting the self-assembly kinetics of multimeric pore-forming toxins. *Interface*. 2016;13:20150762.
- Leippe M. Pore-forming toxins from pathogenic amoebae. *Appl Microbiol Biotechnol*. 2014;98(10):4347-4353.

- Li J, Stein D, McMullan C, Branton D, Aziz MJ, Golovchenko J A. Ion-beam sculpting at nanometre length scales. *Nature*. 2001;412(6843):166-169.
- Li T, Liu L, Li Y, Xie J, Wu HC. A universal strategy for aptamer-based nanopore sensing through host-guest interactions inside  $\alpha$ -hemolysin. *Angew Chemie - Int Ed*. 2015;54(26):7568-7571.
- Li W, Bell NAW, Hernández-Ainsa S, et al. Single protein molecule detection by glass nanopores. *ACS Nano*. 2013;7(5):4129-4134.
- Liang B, Tamm LK. Structure of outer membrane protein G by solution NMR spectroscopy. *Proc Natl Acad Sci U S A*. 2007;104(41):16140-16145.
- Lim YP. Mining the Tumor Phosphoproteome for Cancer Markers. *Clin Cancer Res*. 2005;11(9):3163-3169.
- Liu X, Jiang S, Piao L, Yuan F. Radiotherapy combined with an engineered *Salmonella typhimurium* inhibits tumor growth in a mouse model of colon cancer. *Exp Anim*. 2016;65(June):413-418.
- Los FCO, Randis TM, Aroian R V, Ratner AJ. Role of pore-forming toxins in bacterial infectious diseases. *Microbiol Mol Biol Rev*. 2013;77(2):173-207.
- Luchian T, Shin SH, Bayley H. Single-molecule covalent chemistry with spatially separated reactants. *Angew Chemie - Int Ed*. 2003;42(32):3766-3771.
- Ludwig A, Bauer S, Benz R, Bergmann B, Goebel W. Analysis of the SlyA-controlled expression, subcellular localization and pore-forming activity of a 34 kDa haemolysin (ClyA) from *Escherichia coli* K-12. *Mol Microbiol*. 1999;31(2):557-567.
- Ludwig A, Rhein C Von, Bauer S, et al. Molecular analysis of cytolysin A (ClyA) in pathogenic *Escherichia coli* strains. *J Bacteriol*. 2004;186(16):5311-5320.
- Ludwig A, Völkerink G, von Rhein C, et al. Mutations affecting export and activity of cytolysin A from *Escherichia coli*. *J Bacteriol*. 2010;192(15):4001-4011.
- Lukyanova N, Saibil HR. Friend or foe: the same fold for attack and defense. *Trends Immunol*. 2008;29(2):51-53.
- Ma T, Trinh M a, Wexler AJ, et al. Suppression of eIF2 $\alpha$  kinases alleviates Alzheimer's disease-related plasticity and memory deficits. *Nat Neurosci*. 2013;16(9):1299-1305.
- Maingi V, Burns JR, Uusitalo JJ, Howorka S, Marrink SJ, Sansom MSP. Stability and dynamics of membrane-spanning DNA nanopores. *Nat Commun*. 2017;8:14784.
- Maingi V, Lelimosin M, Howorka S, Sansom MSP. Gating-like Motions and Wall Porosity in a DNA Nanopore Scaffold Revealed by Molecular Simulations. *ACS Nano*. 2015;9(11):11209-11217.

Majd S, Yusko EC, Billeh YN, Macrae MX, Yang J, Mayer M. Applications of biological pores in nanomedicine, sensing, and nanoelectronics. *Curr Opin Biotechnol*. 2010;21(4):439-476.

Majd S, Yusko EC, MacBriar AD, Yang J, Mayer M. Gramicidin pores report the activity of membrane-active enzymes. *J Am Chem Soc*. 2009;131(44):16119-16126..

Mann M, Jensen ON. Proteomic analysis of post-translational modifications. *Nat Biotechnol*. 2003;21(3):255-261.

Manrao EA, Derrington IM, Laszlo AH, et al. Reading DNA at single-nucleotide resolution with a mutant MspA nanopore and phi29 DNA polymerase. *Nat Biotechnol*. 2012;30(4):349-353.

Manrao EA, Derrington IM, Pavlenok M, Niederweis M, Gundlach JH. Nucleotide discrimination with DNA immobilized in the MSPA nanopore. *PLoS One*. 2011;6(10):1-7.

Mazor Y, Borovikova A, Nelson N. The Structure of the plant photosystem I supercomplex at 2.6 Å resolution. *Nat Plants*. 2017;3:17014.

McBroom AJ, Johnson AP, Vemulapalli S, Kuehn MJ. Outer membrane vesicle production by *Escherichia coli* is independent of membrane instability. *J Bacteriol*. 2006;188(15):5385-5392.

McMorrán LM, Brockwell DJ, Radford SE. Mechanistic studies of the biogenesis and folding of outer membrane proteins in vitro and in vivo: What have we learned to date? *Arch Biochem Biophys*. 2014;564:265-280.

McMullen A, de Haan HW, Tang JX, Stein D. Stiff filamentous virus translocations through solid-state nanopores. *Nat Commun*. 2014;5(May):4171.

Meervelt V Van, Soskine M, Maglia G. Detection of Two Isomeric Binding Configurations in a Protein Aptamer Complex with a Biological Nanopore. *ACS Nano*. 2014;8(12):12826-12835.

Meller a, Nivon L, Brandin E, Golovchenko J, Branton D. Rapid nanopore discrimination between single polynucleotide molecules. *Proc Natl Acad Sci U S A*. 2000;97(3):1079-1084.

Merstorf C, Cressiot B, Pastoriza-Gallego M, et al. Wild type, mutant protein unfolding and phase transition detected by single-nanopore recording. *ACS Chem Biol*. 2012;7(4):652-658.

Messenger L, Burns JR, Kim J, et al. Biomimetic Hybrid Nanocontainers with Selective Permeability. *Angew Chemie - Int Ed*. 2016;55(37):11106-11109.

Milne JC, Furlong D, Hanna PC, Wall JS, Collier RJ. Anthrax protective antigen forms oligomers during intoxication of mammalian cells. *J Biol Chem*. 1994;269(32):20607-20612.

Misra R, Bensont SA. A Novel Mutation , cog , which results in production of a new porin protein (OmpG) of Escherichia coli K-12. J B. 1989;171(8):4105-4111.

Mohammad MM, Iyer R, Howard KR, McPike MP, Borer PN, Movileanu L. Engineering a rigid protein tunnel for biomolecular detection. J Am Chem Soc. 2012;134(22):9521-9531.

Mohammad MM, Movileanu AEL. Excursion of a single polypeptide into a protein pore : simple physics , but complicated biology. Eur Biophys J. 2008;37(6):913-925.

Morita-Yamamuro C, Tsutsui T, Sato M, et al. The Arabidopsis gene CAD1 controls programmed cell death in the plant immune system and encodes a protein containing a MACPF domain. Plant Cell Physiol. 2005;46(6):902-912.

Movileanu L, Howorka S, Braha O, Bayley H. Detecting protein analytes that modulate transmembrane movement of a polymer chain within a single protein pore. Nat Biotechnol. 2000;18(10):1091-1095.

Movileanu L, Schmittschmitt JP, Scholtz JM, Bayley H. Interactions of peptides with a protein pore. Biophys J. 2005;89(2):1030-1045.

Movileanu L. Interrogating single proteins through nanopores: challenges and opportunities. Trends Biotechnol. 2009;27(6):333-341.

Mueller M, Grauschopf U, Maier T, Glockshuber R, Ban N. The structure of a cytolytic alpha-helical toxin pore reveals its assembly mechanism. Nature. 2009;459(7247):726-730.

Niedzwiecki DJ, Lanci CJ, Shemer G, Cheng PS, Saven JG, Drndić M. Observing Changes in the Structure and Oligomerization State of a Helical Protein Dimer Using Solid-State Nanopores. ACS Nano. 2015;9(9):8907-8915.

Nir I, Huttner D, Meller A. Direct Sensing and Discrimination among Ubiquitin and Ubiquitin Chains Using Solid-State Nanopores. Biophys J. 2015;108(9):2340-2349.

Nivala J, Marks DB, Akeson M. Unfoldase-mediated protein translocation through an  $\alpha$ -hemolysin nanopore. Nat Biotechnol. 2013;31(3):247-250.

Nivala J, Mulroney L, Li G, Schreiber J, Akeson M. Discrimination among Protein Variants Using an Unfoldase-Coupled Nanopore. ACS Nano. 2014;8(12):12365-12375.

Nomura DK, Dix MM, Cravatt BF. Activity-based protein profiling for biochemical pathway discovery in cancer. Nat Rev Cancer. 2010;10(9):630-638.

Noutoshi Y, Kuromori T, Wada T, et al. Loss of necrotic spotted lesions 1 associates with cell death and defense responses in Arabidopsis thaliana. Plant Mol Biol. 2006;62(1-2):29-42.

Olofsson A, Hebert H, Thelestam M. The Projection Structure of Perfringolysin-O (Clostridium-Perfringens Omicron-Toxin). FEBS Lett. 1993;319(1-2):125-127.



- Olson R, Gouaux E. Crystal structure of the *Vibrio cholerae* cytolysin (VCC) pro-toxin and its assembly into a heptameric transmembrane pore. *J Mol Biol.* 2005;350(5):997-1016.
- Opota O, Vallet-Gély I, Vincentelli R, et al. Monalysin, a novel  $\beta$ -pore-forming toxin from the drosophila pathogen *pseudomonas entomophila*, contributes to host intestinal damage and lethality. *PLoS Pathog.* 2011;7(9).
- Oscarsson J, Mizunoe Y, Li L, Lai XH, Wieslander a, Uhlin BE. Molecular analysis of the cytolytic protein ClyA (SheA) from *Escherichia coli*. *Mol Microbiol.* 1999;32(6):1226-1238.
- Oscarsson J, Mizunoe Y, Uhlin BE, Haydon DJ. Induction of haemolytic activity in *Escherichia coli* by the *s/yA* gene product. *Mol Microbiol.* 1996;20(1):191-199.
- Oscarsson J, Westermarck M, Löfdahl S, et al. Characterization of a Pore-Forming Cytotoxin Expressed by *Salmonella enterica* Serovars Typhi and Paratyphi A. *Infect Immun.* 2002;70(10):5759-5769.
- Ota K, Butala M, Viero G, Serra MD, Sepcic K, Macek P. MACPF/CDC Proteins - Agents of Defence, Attack and Invasion. *Subcell Biochem.* 2014;80:271-291.
- Oukhaled A, Bacri L, Pastoriza-Gallego M, Betton JM, Pelta J. Sensing proteins through nanopores: Fundamental to applications. *ACS Chem Biol.* 2012;7(12):1935-1949.
- Oukhaled G, Mathe J, Biance AL, et al. Unfolding of proteins and long transient conformations detected by single nanopore recording. *Phys Rev Lett.* 2007;98(15):158101.
- Panchal RG, Cusack E, Cheley S, Bayley H. Tumor protease-activated, pore-forming toxins from a combinatorial library. *Nat Biotechnol.* 1996;14(7):852-856.
- Parker MW, Feil SC. Pore-forming protein toxins: From structure to function. *Prog Biophys Mol Biol.* 2005;88(1):91-142.
- Pastoriza-Gallego M, Rabah L, Gibrat G, et al. Dynamics of unfolded protein transport through an aerolysin pore. *J Am Chem Soc.* 2011;133(9):2923-2931.
- Payet L, Martinho M, Pastoriza-Gallego M, et al. Thermal Unfolding of Proteins Probed at the Single Molecule Level Using Nanopores. *Anal Chem.* 2012;84(9):4071-4076.
- Peraro MD, van der Goot FG. Pore-forming toxins: ancient, but never really out of fashion. *Nat Rev.* 2016;14:77-92.
- Petosa C, Collier RJ, Klimpel KR, Leppla SH, Liddington RC. Crystal structure of the anthrax toxin protective antigen. *Nature.* 1997;385(6619):833-838.
- Plesa C, Ruitenbergh JW, Witteveen MJ, Dekker C. Detection of Single Proteins Bound along DNA with Solid-State Nanopores. *Nano Lett.* 2015;15:3153-3158.

- Poole K, Jr TRP, Hancock REW. Phosphate-selective porins from the outer membranes of fluorescent *Pseudomonas* sp. *Can J Microbiol.* 1987;33(1):63-69.
- Potrich C, Tomazzolli R, Serra MD, Anderluh G, Malovrh P, Mac P. Cytotoxic Activity of a Tumor Protease-Activated Pore-Forming Toxin. *Bioconjugate Chem.* 2005;16:369-376.
- Rai AK, Paul K, Chattopadhyay K. Functional mapping of the lectin activity site on the  $\beta$ -prism domain of vibrio cholerae cytolysin: implications for the membrane pore-formation mechanism of the toxin. *J Biol Chem.* 2013;288(3):1665-1673.
- Reboul CF, Whisstock JC, Dunstone MA. Giant MACPF/CDC pore forming toxins: A class of their own. *Biochim Biophys Acta - Biomembr.* 2016;1858(3):475-486.
- Reiner JE, Balijepalli A, Robertson JWF, Campbell J, Suehle J, Kasianowicz JJ. Disease detection and management via single nanopore-based sensors. *Chem Rev.* 2012;112(12):6431-6451.
- Reiner JE, Balijepalli A, Robertson JWF, Drown BS, Burden DL, Kasianowicz JJ. The effects of diffusion on an exonuclease nanopore-based DNA sequencing engine. *J Chem Phys.* 2012;137(21):214903.
- Reiner JE, Kasianowicz JJ, Nablo BJ, Robertson JWF. Theory for polymer analysis using nanopore-based single-molecule mass spectrometry. *Proc Natl Acad Sci USA.* 2010;107(27):12080-12085.
- Reingold J, Starr N, Maurer J, Lee MD. Identification of a new *Escherichia coli* She haemolysin homolog in avian *E. coli*. *Vet Microbiol.* 1999;66(2):125-134.
- Reiß P, Koert U. Ion-channels: Goals for function-oriented synthesis. *Acc Chem Res.* 2013;46(12):2773-2780.
- Robertson JWF, Rodrigues CG, Stanford VM, Rubinson KA, Krasilnikov O V, Kasianowicz JJ. Single-molecule mass spectrometry in solution using a solitary nanopore. *Proc Natl Acad Sci U S A.* 2007;104(20):8207-8211.
- Roderer D, Benke S, Mu M, et al. Characterization of Variants of the Pore-Forming Toxin ClyA from *Escherichia coli* Controlled by a Redox Switch. *Biochemistry.* 2014;53:6357-6369.
- Roderer D, Benke S, Schuler B, Glockshuber R. Soluble Oligomers of the Pore-forming Toxin Cytolysin A from *Escherichia coli* Are Off-pathway Products of Pore. *J Biol Chem.* 2016;291(11):5652-5663.
- Rodriguez-Larrea D, Bayley H. Multistep protein unfolding during nanopore translocation. *Nat Nanotechnol.* 2013;8(4):288-295.
- Rodriguez-Larrea D, Bayley H. Protein co-translocational unfolding depends on the direction of pulling. *Nat Commun.* 2014;5:4841.

- Rojko N, Dalla Serra M, MačEk P, Anderluh G. Pore formation by actinoporins, cytolysins from sea anemones. *Biochim Biophys Acta - Biomembr.* 2016;1858(3):446-456.
- Roosen-Runge F, Hennig M, Zhang F, et al. Protein self-diffusion in crowded solutions. *Proc Natl Acad Sci U S A.* 2011;108(29):11815-11820.
- Rosado CJ, Kondos S, Bull TE, et al. The MACPF/CDC family of pore-forming toxins. *Cell Microbiol.* 2008;10(9):1765-1774.
- Rosen CB, Rodriguez-Larrea D, Bayley H. Single-molecule site-specific detection of protein phosphorylation with a nanopore. *Nat Biotechnol.* 2014;32(2):179-181.
- Rosenthal JA, Huang C, Doody AM, et al. Mechanistic insight into the Th1-biased immune response to recombinant subunit vaccines delivered by probiotic bacteria-derived outer membrane vesicles. *PLoS One.* 2014;9(11):1-24.
- Rotem D, Jayasinghe L, Salichou M, Bayley H. Protein detection by nanopores equipped with aptamers. *J Am Chem Soc.* 2012;134(5):2781-2787.
- Rowe GE, Welch RA. Assays of hemolytic toxins. *Methods Enzymol.* 1994;235(1983):657-667.
- Ryan RM, Green J, Williams PJ, et al. Bacterial delivery of a novel cytolysin to hypoxic areas of solid tumors. *Gene Ther.* 2009;16(3):329-339.
- Santelli E, Bankston L a, Leppla SH, Liddington RC. Crystal structure of a complex between anthrax toxin and its host cell receptor. *Nature.* 2004;430(7002):905-908.
- Sathyanarayana P, Desikan R, Ayappa KG, Visweswariah SS. The Solvent-Exposed C-Terminus of the Cytolysin A Pore-Forming Toxin Directs Pore Formation and Channel Function in Membranes. *Biochemistry.* 2016:acs.biochem.6b00593.
- Schleiff E, Becker T. Common ground for protein translocation : access control for mitochondria and chloroplasts. *Nat Rev Mol Cell Biol.* 2011;12(1):48-59.
- Schön P, García-Sáez AJ, Malovrh P, Bacia K, Anderluh G, Schwille P. Equinatoxin II permeabilizing activity depends on the presence of sphingomyelin and lipid phase coexistence. *Biophys J.* 2008;95(2):691-698.
- Schulz GE. The structure of bacterial outer membrane proteins. *Biochim Biophys Acta.* 2002;1565(2):308-317.
- Seeger-Nukpezah T, Geynisman DM, Nikonova AS, Benzing T, Golemis EA. The hallmarks of cancer: relevance to the pathogenesis of polycystic kidney disease. *Nat Rev.* 2015;11(9):515-534.
- Seifert A, Göpfrich K, Burns JR, Fertig N, Keyser UF, Howorka S. Bilayer-Spanning DNA Nanopores with Voltage- Switching between Open and Closed State. *ACS Nano.* 2015;9(2):1117-1126.

Sexton LT, Horne LP, Sherrill SA, Bishop GW, Baker LA, Martin CR. Resistive-pulse studies of proteins and protein/antibody complexes using a conical nanotube sensor. *J Am Chem Soc.* 2007;129(43):13144-13152.

Shepard LA, Shatursky O, Johnson AE, Tweten RK. The mechanism of pore assembly for a cholesterol-dependent cytolysin: Formation of a large prepore complex precedes the insertion of the transmembrane  $\beta$ -hairpins. *Biochemistry.* 2000;39(33):10284-10293.

Shi W, Friedman AK, Baker LA. Nanopore Sensing. *Anal Chem.* 2017;89(1):157-188.

Shin S, Luchian T, Cheley S, Braha O, Bayley H. Kinetics of a Reversible Covalent-Bond-Forming Reaction Observed at the Single-Molecule Level. *Current.* 2002;(19):3707-3709.

Silva AMN, Vitorino R, Domingues MRM, Spickett CM, Domingues P. Post-translational modifications and mass spectrometry detection. *Free Radic Biol Med.* 2013;65:925-941.

Simpson AA, Tao Y, Leiman PG, et al. Structure of the bacteriophage phi29 DNA packaging motor. *Nature.* 2000;408(6813):745-750.

Singh PR, Bárcena-Uribarri I, Modi N, et al. Pulling peptides across nanochannels: Resolving peptide binding and translocation through the hetero-oligomeric channel from *nocardia farcinica*. *ACS Nano.* 2012;6(12):10699-10707.

Singh Y, Klimpel KR, Arora N, Sharma M, Leppla SH. The Chymotrypsin-sensitive Site , FFD315 , in Anthrax Toxin Protective Antigen Is Required for Translocation of Lethal Factor. *J Biol Chem.* 1994;269(46):29039-29046.

Siwy Z, Trofin L, Kohli P, Baker LA, Trautmann C, Martin CR. Protein biosensors based on biofunctionalized conical gold nanotubes. *J Am Chem Soc.* 2005;127(14):5000-5001.

Slade DJ, Lovelace LL, Chruszcz M, Minor W, Lebioda L, Sodetz JM. Crystal Structure of the MACPF Domain of Human Complement Protein C8 $\alpha$  in Complex with the C8 $\gamma$  Subunit. *J Mol Biol.* 2008;379(2):331-342.

Sobott F, Benesch JLP, Vierling E, Robinson C V. Subunit Exchange of Multimeric Protein Complexes: Real-Time monitoring of subunit exchange between small heat shock proteins by using electrospray mass spectrometry. *J Biol Chem.* 2002;277(41):38921-38929.

Söderblom T, Oxhamre C, Wai SN, et al. Effects of the *Escherichia coli* toxin cytolysin A on mucosal immunostimulation via epithelial Ca<sup>2+</sup> signalling and Toll-like receptor 4. *Cell Microbiol.* 2005;7(6):779-788.

Song L, Hobaugh MR, Shustak C, Cheley S, Bayley H, Gouaux JE. Structure of staphylococcal alpha-hemolysin, a heptameric transmembrane pore. *Science.* 1996;274(5294):1859-1866.

Soskine M, Biesemans A, De Maeyer M, Maglia G. Tuning the Size and Properties of ClyA Nanopores Assisted by Directed Evolution. *J Am Chem Soc.* 2013;135(36):13456-13463.

- Soskine M, Biesemans A, Maglia G. Single-molecule analyte recognition with ClyA nanopores equipped with internal protein adaptors. *J Am Chem Soc.* 2015;137(17):5793-5797.
- Soskine M, Biesemans A, Moeyaert B, Cheley S, Bayley H, Maglia G. An engineered ClyA nanopore detects folded target proteins by selective external association and pore entry. *Nano Lett.* 2012;12(9):4895-4900.
- Stefureac R, Long Y-T, Kraatz H-B, Howard P, Lee JS. Transport of alpha-helical peptides through alpha-hemolysin and aerolysin pores. *Biochemistry.* 2006;45(30):9172-9179.
- Stefureac RI, Lee JS. Nanopore analysis of the folding of zinc fingers. *Small.* 2008;4(10):1646-1650.
- Stoddart D, Heron AJ, Klingelhoefer J, Mikhailova E, Maglia G, Bayley H. Nucleobase recognition in ssDNA at the central constriction of the alpha-hemolysin pore. *Nano Lett.* 2010;10(9):3633-3637.
- Stoloff DH, Wanunu M. Recent trends in nanopores for biotechnology. *Curr Opin Biotechnol.* 2013;24(4):699-704.
- Stratton M, Lee IH, Bhattacharyya M, et al. Activation-triggered subunit exchange between CaMKII holoenzymes facilitates the spread of kinase activity. *Elife.* 2014;3:e01610.
- Subbarao G V, van den Berg B. Crystal structure of the monomeric porin OmpG. *J Mol Biol.* 2006;360(4):750-759.
- Sutherland TC, Long YT, Stefureac RI, Bediako-Amoa I, Kraatz HB, Lee JS. Structure of peptides investigated by nanopore analysis. *Nano Lett.* 2004;4(7):1273-1277.
- Talaga DS, Li J. Single-molecule protein unfolding in solid state nanopores. *J Am Chem Soc.* 2009;131(25):9287-9297.
- Tamm LK, Hong H, Liang B. Folding and assembly of beta-barrel membrane proteins. *Biochim Biophys Acta - Biomembr.* 2004;1666(1-2):250-263.
- Tejuca M, Anderluh G, Dalla Serra M. Sea anemone cytolysins as toxic components of immunotoxins. *Toxicon.* 2009;54(8):1206-1214.
- Thompson JR, Cronin B, Bayley H, Wallace MI. Rapid assembly of a multimeric membrane protein pore. *Biophys J.* 2011;101(11):2679-2683.
- Tilley SJ, Saibil HR. The mechanism of pore formation by bacterial toxins. *Curr Opin Struct Biol.* 2006;16(2):230-236.
- Tweten RK. Cholesterol-Dependent Cytolysins, a Family of Versatile Pore-Forming Toxins. *Infect Immun.* 2005;73(10):6199-6209.

Tzokov SB, Wyborn NR, Stillman TJ, et al. Structure of the hemolysin E (HlyE, ClyA, and SheA) channel in its membrane-bound form. *J Biol Chem*. 2006;281(32):23042-23049.

Visudtiphole V, Chalton DA, Hong Q, Lakey JH. Determining OMP topology by computation, surface plasmon resonance and cysteine labelling: The test case of OMPG. *Biochem Biophys Res Commun*. 2006;351(1):113-117.

von Rhein C, Bauer S, López Sanjurjo EJ, Benz R, Goebel W, Ludwig A. ClyA cytolysin from *Salmonella*: distribution within the genus, regulation of expression by SlyA, and pore-forming characteristics. *Int J Med Microbiol*. 2009;299(1):21-35.

Wai SN, Lindmark B, Söderblom T, et al. Vesicle-mediated export and assembly of pore-forming oligomers of the enterobacterial ClyA cytotoxin. *Cell*. 2003;115(1):25-35.

Wai SN, Takade A, Amako K, March A. The Release of Outer Membrane Vesicles from Strains of Enterotoxigenic *Escherichia coli*. *Microbiol. and Immunol*. 1995;39(7):451-456.

Wai SN, Westermarck M, Oscarsson J, et al. Characterization of Dominantly Negative Mutant ClyA Cytotoxin Proteins in *Escherichia coli*. *J Bacteriol*. 2003;185(18):5491-5499.

Walker B, Braha O, Cheley S, Bayley H. An intermediate in the assembly of a pore-forming protein trapped with a genetically-engineered switch. *Chem Biol*. 1995;2(2):99-105.

Wallace AJ, Stillman TJ, Atkins A, et al. *E. coli* hemolysin E (HlyE, ClyA, SheA): X-ray crystal structure of the toxin and observation of membrane pores by electron microscopy. *Cell*. 2000;100(2):265-276.

Wang H, Ying Y, Li Y, Kraatz H, Long Y. Nanopore Analysis of  $\beta$ -Amyloid Peptide Aggregation Transition Induced by Small Molecules. *Anal Chem*. 2011;83(5):1746-1752.

Wang HY, Gu Z, Cao C, Wang J, Long YT. Analysis of a single alpha-synuclein fibrillation by the interaction with a protein nanopore. *Anal Chem*. 2013;85(17):8254-8261.

Wang S, Haque F, Rychahou PG, Evers BM, Guo P. Engineered nanopore of phi29 dna-packaging motor for real-time detection of single colon cancer specific antibody in serum. *ACS Nano*. 2013;7(11):9814-9822.

Wang S, Haque F, Rychahou PG, Evers BM, Guo P. Engineered nanopore of phi29 dna-packaging motor for real-time detection of single colon cancer specific antibody in serum. *ACS Nano*. 2013;7(11):9814-9822.

Wang Y, Montana V, Grubišić V, Stout RF, Parpura V, Gu LQ. Nanopore sensing of botulinum toxin type B by discriminating an enzymatically cleaved peptide from a synaptic protein synaptobrevin 2 derivative. *ACS Appl Mater Interfaces*. 2015;7(1):184-192.

Wanunu M, Morrison W, Rabin Y, Grosberg AY, 1D AM. Electrostatic Focusing of Unlabeled DNA into Nanoscale Pores using a Salt Gradient. *Nat Nanotechnol*. 2010;5(2):160-165.

- Wanunu M. Nanopores: A journey towards DNA sequencing. *Phys Life Rev.* 2012;9(2):125-158.
- Weeber EJ, Levy M, Sampson MJ, et al. The role of mitochondrial porins and the permeability transition pore in learning and synaptic plasticity. *J Biol Chem.* 2002;277(21):18891-18897.
- Wei R, Gatterdam V, Wieneke R, Tampé R, Rant U. Stochastic sensing of proteins with receptor-modified solid-state nanopores. *Nat Nanotechnol.* 2012;7(4):257-263.
- Wendell D, Jing P, Geng J, et al. Translocation of double stranded DNA through membrane adapted phi29 motor protein nanopore. *Nat Nanotechnol.* 2009;4(11):765-772.
- Westphal D, Dewson G, Menard M, et al. Apoptotic pore formation is associated with in-plane insertion of Bak or Bax central helices into the mitochondrial outer membrane. *Proc Natl Acad Sci U S A.* 2014;111(39):E4076-E4085.
- Wloka C, Van Meervelt V, van Gelder D, et al. Label-Free and Real-Time Detection of Protein Ubiquitination with a Biological Nanopore. *ACS Nano.* 2017;acs.nano.6b07760.
- Wolfe AJ, Mohammad MM, Cheley S, Bayley H, Movileanu L. Catalyzing the translocation of polypeptides through attractive interactions. *J Am Chem Soc.* 2007;129(45):14034-14041.
- Wong CT a, Muthukumar M. Polymer capture by electro-osmotic flow of oppositely charged nanopores. *J Chem Phys.* 2007;126(16):1-6.
- Wu H, Chen Y, Zhou Q, et al. Translocation of Rigid Rod-Shaped Virus through Various Solid-State Nanopores. *Anal Chem.* 2016;88(4):2502-2510.
- Wu HC, Bayley H. Single-molecule detection of nitrogen mustards by covalent reaction within a protein nanopore. *J Am Chem Soc.* 2008;130(21):6813-6819.
- Wyborn NR, Clark A, Roberts RE, et al. Properties of haemolysin E (HlyE) from a pathogenic *Escherichia coli* avian isolate and studies of HlyE export. *Microbiology.* 2004;150(5):1495-1505.
- Xie H, Braha O, Gu LQ, Cheley S, Bayley H. Single-molecule observation of the catalytic subunit of cAMP-dependent protein kinase binding to an inhibitor peptide. *Chem Biol.* 2005;12(1):109-120.
- Xu JJ. Visualizing nanopore blinkings in parallel: a high-throughput nanopore array potential for ultra-rapid DNA sequencing. *Sci Bull.* 2015;60(23):2067-2068.
- Yamaji-Hasegawa A, Hullin-Matsuda F, Greimel P, Kobayashi T. Pore-forming toxins: Properties, diversity, and uses as tools to image sphingomyelin and ceramide phosphoethanolamine. *Biochim Biophys Acta - Biomembr.* 2016;1858(3):576-592.

- Yamashita K, Kawai Y, Tanaka Y, et al. Crystal structure of the octameric pore of staphylococcal  $\gamma$ -hemolysin reveals the  $\beta$ -barrel pore formation mechanism by two components. *Proc Natl Acad Sci U S A*. 2011;108(42):17314-17319.
- Yildiz O, Vinothkumar KR, Goswami P, Kühlbrandt W. Structure of the monomeric outer-membrane porin OmpG in the open and closed conformation. *EMBO J*. 2006;25(15):3702-3713.
- Yilmaz N, Kobayashi T. Assemblies of pore-forming toxins visualized by atomic force microscopy. *Biochim Biophys Acta - Biomembr*. 2016;1858(3):500-511.
- Young ID, Ibrahim M, Chatterjee R, et al. Structure of photosystem II and substrate binding at room temperature. *Nature*. 2016;540(7633):453-457.
- Young JA, Collier RJ. Anthrax toxin: receptor binding, internalization, pore formation, and translocation. *Annu Rev Biochem*. 2007;76:243-265.
- Young MJ, Bay DC, Hausner G, Court DA. The evolutionary history of mitochondrial porins. *BMC Evol Biol*. 2007;7(1):31.
- Yusko EC, Johnson JM, Majd S, et al. Controlling protein translocation through nanopores with bio-inspired fluid walls. *Nat Nanotechnol*. 2011;6(4):253-260.
- Yusko EC, Prangko P, Sept D, Rollings RC, Li J, Mayer M. Single-particle characterization of A $\beta$  oligomers in solution. *ACS Nano*. 2012;6(7):5909-5919.
- Zhang S, Udho E, Wu Z, Collier RJ, Finkelstein A. Protein translocation through anthrax toxin channels formed in planar lipid bilayers. *Biophys J*. 2004;87(6):3842-3849.
- Zhao J, Patwa TH, Lubman DM, Simeone DM. Protein biomarkers in cancer: natural glycoprotein microarray approaches. *Curr Opin Mol Ther*. 2008;10(6):602-610.
- Zhao Q, De Zoysa RSS, Wang D, Jayawardhana DA, Guan X. Real-time monitoring of peptide cleavage using a nanopore probe. *J Am Chem Soc*. 2009;131(18):6324-6325.
- Zhong J, Chau Y. Antitumor activity of a membrane lytic peptide cyclized with a linker sensitive to membrane type 1-matrix metalloproteinase. *Mol Cancer Ther*. 2008;7(9):2933-2940.
- Zhuang T, Chisholm C, Chen M, Tamm LK. NMR-based conformational ensembles explain pH-gated opening and closing of OmpG channel. *J Am Chem Soc*. 2013;135(40):15101-15113.
- Zhuang T, Tamm LK. Control of the conductance of engineered protein nanopores through concerted loop motions. *Angew Chem Int Ed Engl*. 2014;53(23):5897-5902.